Study of fission of exotic actinides by relativistic reactions

Yiman Yan

▶ **To cite this version:**

Yiman Yan. Study of fission of exotic actinides by relativistic reactions. Nuclear Experiment [nucl-ex]. Université Paris-Saclay, 2016. English. NNT : 2016SACLS258 . tel-01507094

HAL Id: tel-01507094
https://theses.hal.science/tel-01507094

Submitted on 12 Apr 2017

HAL is a multi-disciplinary open access archive for the deposit and dissemination of scientific research documents, whether they are published or not. The documents may come from teaching and research institutions in France or abroad, or from public or private research centers.

L'archive ouverte pluridisciplinaire **HAL**, est destinée au dépôt et à la diffusion de documents scientifiques de niveau recherche, publiés ou non, émanant des établissements d'enseignement et de recherche français ou étrangers, des laboratoires publics ou privés.

NNT : 2016SACLS258

THÈSE DE DOCTORAT
DE
L'UNIVERSITÉ PARIS-SACLAY
PRÉPARÉE À
L'UNIVERSITÉ PARIS SUD

ÉCOLE DOCTORALE N°576
Particules, Hadrons, Énergie, Noyau, Instrumentation, Imagerie, Cosmos et Simulation (PHENIICS)

Spécialité de doctorat : Structure et réactions nucléaires

Par

Mme Yiman YAN

Study of fission of exotic actinides by relativistic reactions

Thèse présentée et soutenue à Orsay, le 28 septembre 2016 :

Directrice de Thèse :
Mme Dominique Jacquet, Directrice de Recherche, CNRS

Composition du Jury :
M. Fadi Ibrahim, Directeur de Recherche, CNRS (IPNO), Président du Jury
Mme Héloïse Goutte, Directrice de Recherche, CEA, Rapporteure
M. Stephan Oberstedt, Directeur de Recherche, Joint Research Center, Rapporteur
M. Julien Taïeb, Chargé de Recherche, CEA, Examinateur
M. Grégoire Kessedjian, Maître de Conférences, INP Grenoble, Examinateur
M. Laurent Audouin, Maître de Conférences, Université Paris Saclay, Encadrant de Thèse
M. Laurent Tassan-Got, Directeur de Recherche, CNRS (IPNO), Invité

CNRS - UNIVERSITÉ PARIS SUD

28 septembre 2016 IPNO-T-16-05

Thèse de Doctorat

École doctorale : Particules, Hadrons, Énergie, Noyau, Instrumentation, Imagerie, Cosmos et Simulation (PHENIICS)

Laboratoire : Institut de physique nucléaire d'Orsay

Discipline : Physique

Présentée et soutenue par

Yiman YAN

Pour obtenir le grade de Docteur ès Sciences

De l'Université Paris Sud

Study of fission of exotic actinides by relativistic reactions

Directrice de thèse : Dominique Jacquet, CNRS

Composition du jury :

Président du jury :	Fadi Ibrahim	-	CNRS (IPNO)
Rapporteurs :	Héloïse Goutte	-	CEA
	Stephan Oberstedt	-	Joint Research Center
Examinateurs :	Julien Taïeb	-	CEA
	Grégoire Kessedjian	-	INP Grenoble
Encadrant de thèse :	Laurent Audouin	-	Université Paris Saclay
Invité :	Laurent Tassan-Got	-	CNRS (IPNO)

Institut de Physique Nucléaire

Acknowledgements

When I start writing this part, all those people who helped, supported and encouraged me of pursuing a doctoral degree, and all the moments I shared with them during the three years of my PhD training come to my mind. Here I want to say to all of them that I am really grateful.

First of all, I want to sincerely thank Laurent Tassan-Got for his dedicated supervision, without which I would not be able to present a manuscript of the current quality in time. I also want to thank him for his detailed and understandable explanations to all kinds of questions I raised, especially those about the nuclear physics. He was always willing to help, and his confidence in me helped me to calm down and motivated me to face the challenges.

I would like to thank Laurent Audouin for his advice in coding, his guidance which helped me to be prepared for the thesis, his corrections of the manuscript, and his assist in all the administrative stuff, especially those requiring a good French level.

I would also like to express thanks to all the jury members for their reading of the manuscript and the suggestions they made during the defense, and particularly to the two reviewers, Héloïse Goutte and Stephan Oberstedt, for their constructive comments and their agreeing to write the report under time pressure.

I want to thank the entire SOFIA team as well. I feel very lucky to be a member of this team, and it was an exciting and precious experience to perform such a complicated nuclear fission experiment with a group of people who are professional, hard-working and enthusiastic about their research work. I really appreciate that I have learned a lot from these people: Julien, Audrey, Gilbert, Benoît, Guillaume, Andreas, Fanny, Beatriz, Carme, Jose-Luis... In particular, I would like to thank Julie, Thomas and Lucie for all the discussions we had to help me solve the problems, and their generous sharing of experience in assembling detectors, coding and data analysis. Besides, I am grateful that the team members shared a pleasant memory of enjoying beers, delicious dinners and karaoke evenings together in the breaks of the experiment period.

I also want to thank all the colleagues in the lab: Maud, my dear "office-mate", with whom I not only shared the office for 3 years, but also exchanged knowledge, ideas and experience; Aurélie, who cared about me, encouraged me and gave me advice on many things; Alice, who patiently helped me on several issues; Claude, a warm-hearted lady who drove me home many times and invited me and my husband to her home; Yonghao, the other Chinese in the group, who introduced me to a number of his friends and with whom I discussed various subjects; Xavier, who was very kind to read my manuscript and give comments; Dominique, who helped me in the paperwork by agreeing to be my director of thesis in an administrative point of view; and I do not forget Claire and Marc.

I would like to thank all the Chinese friends I made in the university: Lousai, for having welcomed me to the lab; Yu, Binsong and Mengze, for their advice and encouragement; Gaoyang, Zizhao, Ying, Yanzhou, Yaqiong, Yiting and Feng, for their help in preparing the "pot" and their accompany in several relaxing parties.

Additionally, many thanks to my best friends — Jinling, Xin and Qi, for their always being available when I need them and their firm confidence in me of successfully obtaining the doctoral degree. In particular, I would like to thank Qi for understanding my situation very well as being a PhD student herself and for the practical suggestions she made.

Finally, I want to say that I am extremely grateful to my family — my parents, my husband, and my parents-in-law, for their patient listening to my worries and concerns, their understanding and support, and their being a source of comfort and inspiration. Especially, I want to thank my husband for his accompany, his efforts to help me in all aspects, and his taking care of me in the very last period of writing this manuscript. Without him, those three years could have been much tougher.

Contents

1 Introduction **1**
1.1 Fission . . . 2
1.1.1 Discovery of fission . . . 2
1.1.2 Fission Models . . . 3
1.1.2.1 Liquid drop model . . . 3
1.1.2.2 Shell model, and shell correction method . . . 8
1.2 Fission yields . . . 11
1.2.1 Motivation to measure fission yields . . . 11
1.2.1.1 Importance of fission yields for theory . . . 11
1.2.1.2 Importance of fission yields for application . . . 12
1.2.2 Experimental techniques . . . 12
1.2.2.1 Radiochemical methods . . . 12
1.2.2.2 2E and 2v methods . . . 13
1.2.2.3 Recoil mass spectrometers . . . 14
1.2.2.4 Experiments using inverse kinematics . . . 15

2 the SOFIA experiment **19**
2.1 Overview of the SOFIA experiment . . . 20
2.2 Overview of the GSI facility . . . 21
2.3 Method of identifying ions . . . 22
2.4 Fission Mechanism . . . 23
2.4.1 Coulomb-induced fission . . . 23
2.4.1.1 Calculation of Coulomb-induced excitation energy . . . 24
2.4.2 Nuclear-induced fission . . . 25
2.4.3 Extraction of Coulomb-induced fission . . . 27
2.5 Two SOFIA experiments . . . 28
2.6 Outline of the following chapters . . . 29

3 Secondary beam identification **31**
3.1 Experimental setup . . . 33
3.1.1 Fragmentation of the primary beam . . . 33
3.1.2 The GSI FRagment Separator . . . 34
3.1.2.1 Overview . . . 34
3.1.2.2 A/Z selection process . . . 35

3.1.2.3 Energy degrader . . . 36
3.1.2.4 Z selection process . . . 37
3.1.3 Triple MUSIC . . . 38
3.1.3.1 General aspects as a MUSIC detector . . . 38
3.1.3.2 Specifics of the Triple MUSIC . . . 39
3.1.4 Scintillation detectors . . . 42
3.1.5 MWPC . . . 44
3.2 Analysis . . . 48
3.2.1 Velocity . . . 48
3.2.2 Nuclear charge . . . 49
3.2.2.1 Alignment of gains of all anodes . . . 49
3.2.2.2 Corrections of energy loss per section . . . 53
3.2.2.3 Combination of corrected energy losses . . . 57
3.2.2.4 Extraction of nuclear charge . . . 64
3.2.3 Mass-over-charge ratio . . . 66
3.2.3.1 Magnetic rigidity measurement . . . 66
3.2.3.2 Position measurements . . . 67
3.2.3.3 Dispersions . . . 68
3.2.3.4 A/q corrections . . . 69
3.2.4 Full identification . . . 72
3.2.5 Performance of new PMTs under extreme counting rate . . . 74

4 Identification of fission fragments 79
4.1 Experimental setup . . . 80
4.1.1 Overview . . . 80
4.1.2 Active target . . . 82
4.1.3 Twin MUSIC . . . 85
4.1.4 ToF wall . . . 87
4.1.5 MWPCs . . . 90
4.2 Analysis . . . 92
4.2.1 Determination of the fission location . . . 92
4.2.1.1 Energy loss in each section . . . 92
4.2.1.2 Principle of the measurement . . . 92
4.2.2 Nuclear charge identification . . . 95
4.2.2.1 Horizontal angle upstream ALADIN . . . 95
4.2.2.2 Tracking . . . 99
4.2.2.3 Trajectory reconstruction . . . 101
4.2.2.4 Time of flight . . . 105
4.2.2.5 Energy loss corrections . . . 106
4.2.2.6 Extraction of Z from ΔE . . . 109
4.2.2.7 Optimization of the nuclear charge distribution . . . 110

5 Extraction of the elemental fission yield and discussion **115**
5.1 Extraction of the elemental fission yield . . . 116
5.1.1 Extraction of Coulomb-induced fission . . . 116
5.1.1.1 Rejection of events in which the total charge is not equal to 92 . 116
5.1.1.2 Subtraction of residual contribution of nuclear-induced fission . 119
5.1.2 Efficiency of the experimental setup . . . 123
5.1.2.1 Limitations due to the Twin MUSIC . . . 123
5.1.2.2 Limitations due to MWPCs . . . 124
5.1.2.3 Limitations due to the ToF wall . . . 124
5.1.2.4 Efficiency of the setup . . . 125
5.1.3 Elemental fission yield . . . 127
5.1.3.1 Elemental yield . . . 127
5.1.3.2 Calculation of uncertainty on the yield . . . 127
5.2 Discussions . . . 132
5.2.1 Comparison with other SOFIA data . . . 132
5.2.2 Mean position of the heavy fragments . . . 132
5.2.3 Comparison with evaluated data . . . 135
5.2.3.1 Library ENDF/B-VII.1 . . . 135
5.2.3.2 Library JEFF 3.1 . . . 136
5.2.4 Evaluation of the elemental yield level at symmetry . . . 136

6 Conclusion **143**

List of Tables **147**

List of Figures **149**

A Scheme of the experimental setup **159**

Chapter 1

Introduction

This chapter is composed of two sections: the first one concentrates on fission, and the second one is focused on the fission yield measurement. Specifically speaking, efforts leading to the discovery of fission and several classical theoretical models developed for the interpretation of the fission process are demonstrated in the first section, while in the second section, the motivation to measure the fission yields and the evolution of the experimental techniques are presented.

1.1 Fission

1.1.1 Discovery of fission

After Chadwick's discovery of the neutron in 1932 [1], numerous experiments were conducted by Fermi and his collaborators to investigate radioactivities induced by the neutron bombardment on a variety of elements [2]. In the experiment concerning uranium, it turned out that radioactive species with at least five half lives were produced. The main attempt was made to identify the product whose half life of the beta decay is 13 minutes. Finally, by using a chemical method, possibilities that the product can be the element of Z = 92, 91, 90, 89, 88, 87, 86, 83 or 82 were excluded. Since at that time, only light charged particles like protons or α particles were known to be emitted from nuclei, the produced radioactive elements were always believed to have atomic numbers close to that of the parent element [3]. Consequently, Fermi concluded that the irradiation of uranium with neutrons may have led to the production of a transuranic element Z = 93 or higher, by the emission of one or more β-particles.

However, the fact that so many various radioactive elements were produced by the irradiated uranium made the conclusion somewhat questionable to the scientific community [4]. Furthermore, Noddack suggested that a new reaction mechanism was possibly responsible for the results: "it is conceivable that the nucleus breaks up into several large fragments, which would of course be isotopes of known elements but would not be neighbors of the irradiated element" [5]. Unfortunately, the advice was ignored. According to Van Assche [6], one of the potential reasons for this was the low credibility of the research work of Noddack et al. resulting from their previous claim on the discovery of the element Z = 43 [7], which could not be confirmed at that time.

In 1938, Hahn and Strassman stated in an article that after the irradiation of uranium by neutrons, some radioactive products can precipitate with the Ba carrier, implying that they are chemically similar to the latter [8]. At the end, the produced element was recognized as radium, and the nuclear reaction was supposed to be ^{238}U(n, 2α)^{231}Ra. However, one year later, these conclusions were revised by the authors themselves after performing a series of elaborate experiments [9]. Surprisingly, the element was actually barium whose atomic number is about half that of uranium, indicating the uranium nuclei could divide into fragments of intermediate mass.

Although this interpretation of the experimental finding did not fit with the previous nuclear knowledge, it was supported by some other experiments. For example, Meitner and

Frisch estimated that if the interpretation was correct, due to the Coulomb repulsion between the two fragments when they were produced, a total kinetic energy of about 200 MeV would be released and shared by them [3], and the prediction was then confirmed experimentally by Frisch with the use of an ionization chamber [10].

Meanwhile, Meitner and Frisch qualitively explained that this brand-new reaction process of heavy nuclei can be resembled to the break of a liquid drop into two smaller drops due to a violent external disturbance [3]. And they named the process as "fission" for its analogy to the division process of living cells [4].

In the same year, Bohr and Wheeler [11] published a paper on a theoretical explanation of the fission mechanism developed from the liquid drop model [12], which will be presented extensively in the following subsection. Some other classical models of fission will also be introduced.

1.1.2 Fission Models

1.1.2.1 Liquid drop model

As the name implies, the liquid drop model macroscopically regards the nucleus as a uniformly charged liquid drop, which has a shape of sphere and is incompressible. The model was first proposed by Gamow in 1930 [12], and then formulated by Weiszäcker to estimate the mass of the nucleus [13].

Binding energy of a spherical nucleus

Based on similar considerations of Weiszäcker's semi-empirical mass formula, the binding energy of the nucleus is computed as a combination of five energy terms:

- the volume energy term E_V, which reflects the strong nuclear force between nucleons. Since the force has a short range, every nucleon only interacts with a constant number of other nucleons in its neighborhood, resulting that this term is proportional to the number of nucleons A.
- the surface energy term E_S, which serves as a correction to the volume term, by taking into account that a nucleon in the vicinity of the surface of the nucleus has fewer nucleons in the surrounding as compared to an interior one and thus is less bounded. Naturally, this term has a negative sign and is proportional to the surface area, which is known to be proportional to $A^{2/3}$.
- the Coulomb energy term E_C, which acts as a reduction of the binding energy due to the Coulomb repulsion between each pair of protons in the nucleus. Since the Coulomb force is a long range force, every proton experiences the repulsion from any other proton, resulting this energy term proportional to the number of pairs of protons $\frac{Z\times(Z-1)}{2}$, with Z the number of protons in the nucleus. Besides, it is known that the Coulomb potential decreases with the increase of the distance between two charges, making this term inversely proportional to the nuclear radius, which is approximately equal to $r_0 \times A^{1/3}$

with r_0 being an empirical constant. In sum, the Coulomb energy term is proportional to $Z \times (Z-1) \times A^{-1/3}$ and has a negative sign in the formula.

- the asymmetry energy term E_A, which reflects the influence of the inequality in the number of protons and neutrons on the binding energy.
  If there were not for the Coulomb energy, for a given quantum state, the proton and neutron energy levels would be comparable. Then in the nucleus having the equal number of protons and neutrons, the highest energy levels independently filled by both types of nucleons would be approximately the same.
  Taking this nucleus as a reference, one can imagine to replace several protons by neutrons to generate a new nucleus with an excess of the latter. According to the Pauli exclusion principle [14], two fermions (like protons or neutrons) can not take the same quantum state. Since all lower energy states have already been occupied, the added neutrons in the new nucleus can only fill those energy states which are even higher than the highest one reached by the neutrons in the original nucleus and hence apparently higher than the ones of the replaced protons, resulting in the new nucleus with a potential energy higher than it used to be in the reference nucleus.
  Therefore, for a given number of nucleons, the difference in the number of protons and neutrons leads the nucleus to be less stable. Finally, it is deduced that this asymmetry term is proportional to $(A-2Z)^2 \times A^{-1}$ and contributes to the formula with a negative sign.
- the pairing energy term E_P, which reflects the effect of the even-odd characteristic of the number of protons and neutrons. If there are an even number of a certain type of nucleons, they will be fully paired. Due to the Pauli exclusion principle, each pair of protons or neutrons have the same quantum numbers except the spin. Since their wave functions are overlapped, implying a stronger interaction between them, the paired particles are bounded more tightly.
  The nucleus having an odd number of nucleons is taken as a reference and the corresponding pairing energy is set to 0. Comparing to this, in the case of an even mass number, the pairing term is proportional to $A^{-1/2}$, and it has a positive (resp. negative) sign when both Z and N (*i.e.* the number of neutrons in the nucleus) are even (resp. odd).

Consequently, the binding energy of a spherical nucleus can be expressed as:

$$\begin{aligned} E_B &= E_V - E_S - E_C - E_A \pm E_P \\ &= C_v A - C_s A^{2/3} - C_c \frac{Z(Z-1)}{A^{1/3}} - C_a \frac{(A-2Z)^2}{A} \pm \frac{C_p}{A^{1/2}} \end{aligned}$$

where C_v, C_s, C_c, C_a and C_p are empirical coefficients for each term.

Deformation energy of a slightly deformed nucleus

To interpret the fission process, Bohr and Wheeler studied the nuclear deformation and estimated the energy demanded for the critical deformation to undergo fission [11]. Since the

nucleus is assumed to be incompressible, its volume and density stay unchanged at deformations. Consequently, the volume energy of the nucleus is conserved. Besides, the asymmetry term and the pairing term only concern the number of nucleons, resulting that they are not affected by the shape deformations, neither. Therefore, solely the surface and Coulomb terms in the formula depend on the deformation of the nucleus, which is described as:

$$R(\theta) = R_0 \left[1 + \alpha_0 + \alpha_2 P_2(cos\theta) + \alpha_3 P_3(cos\theta) + \cdots\right]$$

where θ is the angle of the radius vector, R_0 is the original radius of the spherical nucleus, α_0 is the quantity needed to conserve the volume, α_i with i = 2, 3, ... is a coefficient describing the extent of the multipole deformation (the term concerning α_1 is neglected because it corresponds to a shift of the center of the nucleus and not relevant here), and P_i with i = 2, 3, ... is a Legendre polynomial.

For a small deformation, only the quadrupole term which reflects the elongation of the nucleus is taken into account. Then the deformation is expressed as:

$$R(\theta) = R_0 \left[1 + \alpha_2 P_2(cos\theta)\right]$$

Accordingly, due to such a deformation, the surface and Coulomb energies are changed to:

$$E_S(\alpha_2) = E_S(0)(1 + \frac{2}{5}\alpha_2^2)$$
$$E_C(\alpha_2) = E_C(0)(1 - \frac{1}{5}\alpha_2^2)$$

where $E_S(0)$ and $E_C(0)$ are the surface and Coulomb energies of the original spherical nucleus, respectively.

So the overall deformation energy of the nucleus is:

$$\begin{aligned} E_{def} &= E_{pot}(\alpha_2) - E_{pot}(0) \\ &= E_B(0) - E_B(\alpha_2) \\ &= E_S(\alpha_2) + E_C(\alpha_2) - E_S(0) - E_C(0) \\ &= \frac{2}{5}\alpha_2^2 E_S(0) - \frac{1}{5}\alpha_2^2 E_C(0) \end{aligned}$$

where $E_{pot}(0)$ and $E_{pot}(\alpha_2)$ are the potential energy of a spherical nucleus and that of a deformed one, respectively.

It is observed that at deformations, the surface energy of the nucleus is enhanced as compared to the original value, because any deformation away from a sphere results in a larger nuclear surface, leading the nucleus to a higher potential energy. On the contrary, the Coulomb energy is decreased due to deformations, since the average distance between protons increases in a deformed nucleus.

When we say that a nucleus is stable against deformations, we mean it has the capability

to return to the unchanged shape after it is forced to deform. Since the nucleus always tends to have the lowest potential energy, it can only be stable against small deformations if the potential energy of a spherical nucleus is lower than that of a deformed one, *i.e.* the deformation energy $E_{def} > 0$. Otherwise, the nucleus will stay at this deformation or go to even further deformations.

Therefore, the condition for a spherical nucleus to be stable is $E_C(0) < 2E_S(0)$, which leads to the definition of the fissility parameter [11]:

$$x = \frac{E_C(0)}{2E_S(0)} \simeq \frac{1}{50}\frac{Z^2}{A}$$

Consequently, following the calculations based on the liquid drop model, it shows that nuclei with $Z^2/A > 50$ (*i.e.* $x > 1$) are unstable against even very small deformations, which is confirmed by the fact that when the fissility parameter is close to the unity, solely a slight deformation is required to go to the critical state for fission, as presented in figure 1.1.

From the evolution of nuclear shapes at the saddle point for various x-values, it is clearly seen that with the decrease of this parameter, a higher deformation is needed to reach the saddle point and finally to undergo fission, indicating that more external energy needs to be supplied to the nuclei of low fissilities to undergo fission.

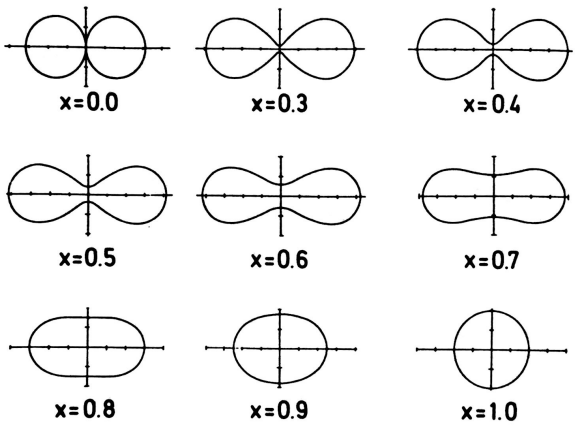

FIGURE 1.1: *Nuclear shapes at the saddle point for various values of x [15].*

Fission barrier

Although the nucleus with $Z^2/A < 50$ is stable against small deformations, when it reaches a critical deformation, the decrease in the Coulomb energy begins to overwhelm the increase in the surface energy, resulting that the potential energy of the nucleus starts to decrease. Then the nucleus is not able to recover from the deformation itself, *i.e.* it becomes unstable, and it will continue deforming and finally fission.

As seen from figure 1.2, the deformation energy of the nucleus is a net outcome of both the change in the surface energy and that in the Coulomb one. It exhibits a maximum value at a

certain deformation, which is the critical state for fission and corresponds to the saddle point of the nucleus, as indicated by the triangle in the figure. The maximum of the deformation energy is regarded as the fission barrier, suggesting that fission only occurs if the excitation energy acquired by the nucleus is beyond this value.

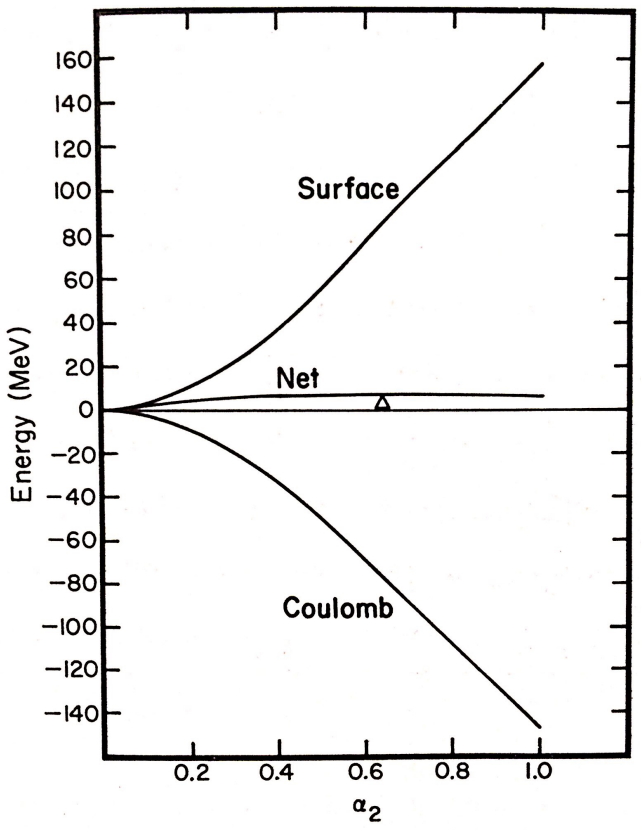

FIGURE 1.2: *Correlations of the surface, Coulomb and net deformation energies to the quadrupole deformation (α_2). The triangle indicates the position of the saddle point of the nucleus. The fissility parameter in this example is equal to 0.76, approximately corresponding to ^{252}Cf. The figure is cited from [4].*

Although the liquid drop model offers a theoretical interpretation of the fission process and it provides satisfactory estimates of some properties of nuclei such as the fission barrier, it is inadequate to explain some other basic nuclear features. Specifically speaking, this quite simple model is not able to explain the appearance of magic numbers of neutrons and protons, and the enhanced stability of nuclei associated with these numbers.

More importantly, it cannot explain the asymmetric division in the fission of most actinides. Additionally, according to the liquid drop model, ground states of all stable nuclei are spherical, which is actually opposite to the observation. Furthermore, the existence of fission isomers cannot be explained by the model, neither.

The lack of these explanations can solely be made up by taking into account the microscopic effects of nuclei such as those incorporated by the nuclear shell model.

1.1.2.2 Shell model, and shell correction method

In 1948, Mayer published a paper in which she summarized experimental facts indicating that the stability of nuclei with 50 and 82 protons and 50, 82 and 126 neutrons is enhanced [16], which provided an evidence for the nuclear shell model. Then the model was developed independently by both Mayer [17] and the group of Haxel, Jensen and Suess [18].

In this model, each nucleon is assumed to move in a potential well generated by its interaction with all other nucleons. The protons and neutrons are independent to each other, but both follow the Schrödinger equation from which single-particle energy levels are calculated. If we take the shell model potential as a combination of a spherically symmetric potential and a spin-orbit interaction, the ordering of successive energy levels can be correctly obtained, and magic numbers of protons and neutrons leading to a particular stability of the nucleus can be also successfully estimated.

Since it is observed that nuclei having different numbers of protons and neutrons than those corresponding to closed shells exhibit large deformations, Nilsson extended the shell model to deformed nuclei [19], by regarding the potential in which each nucleon moves as non-spherical. And he developed diagrams to show single-particle energy levels as a function of the nuclear deformation, as presented in figure 1.3.

According to the Pauli exclusion principle, the nucleons occupy available energy levels from the lowest one upwards, by assigning two protons (neutrons) to each proton (neutron) energy level. So, the simplest calculation for the total energy of a nucleus is to add up the lowest Z proton and N neutron level energies [4]. If the total energy is calculated as a function of deformation, the equilibrium deformation can be then obtained by finding the minimum of the former. Besides, it is also possible to obtain fission barriers by calculating the total energy of the nucleus at larger deformations.

However, the total energy calculated in this way over a large range of nuclei turns out to be much less precise as compared to that derived from the liquid drop model. In view of such a failure of the shell model, Strutinsky proposed the shell correction method in which shell effects are added as a correction to the liquid drop model [20]. This hybrid approach is also named as the macroscopic-microscopic method, literally suggesting that both macroscopic (liquid drop model) and microscopic (shell effects) characteristics of the nucleus are considered.

Then the total energy of the nucleus is expressed as the sum of the potential energy computed by the liquid drop model and the shell correction:

$$E = E_{LDM} + \delta U$$

Since shell effects are regarded as the deviation from a uniform distribution of single-particle energy levels, the correction term is then provided by:

$$\delta U = U - \widetilde{U}$$

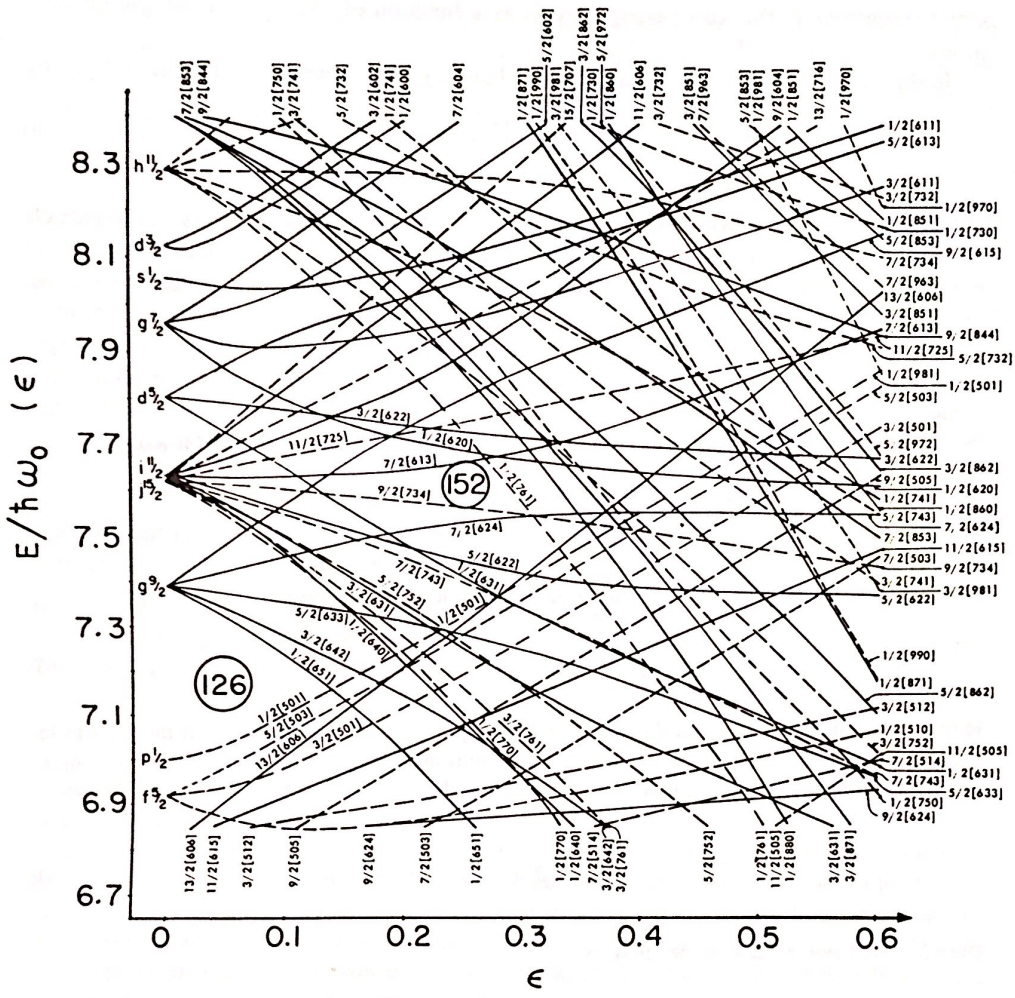

FIGURE 1.3: *Nilsson diagram for single-neutron energy levels as a function of deformation. The figure is cited from [21].*

where U is the sum of single particle energies for the real shell model reflecting a non-uniform density of energy levels, and $\widetilde{U}$ is that for a uniform distribution obtained by averaging true energy levels over a sufficiently wide energy interval.

Due to the existence of big gaps between shells, when the nucleon number corresponds to a closed shell, the occupied energy levels are more compact than average, resulting in a negative shell correction term and thus a lower total energy, which fits the fact that nuclei having magic numbers of protons or/and neutrons are more stable.

The potential energy calculated for a typical actinide nucleus by the Strutinsky hybrid method is schematically presented in figure 1.4. The lowest energy at a deformation corresponds to the known deformed ground state of actinide nuclei, in contrast to the spherical shape predicted by the liquid drop model. The second minimum is due to the strong negative shell correction and it corresponds to fission isomers. As seen from the figure, after adding the shell correction to the liquid model, the fission barrier becomes double humped.

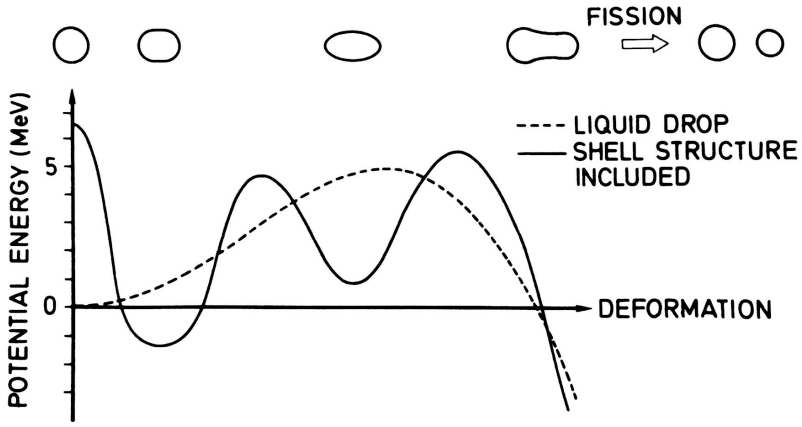

FIGURE 1.4: *Schematic illustration of the fission barrier of a typical actinide nucleus, obtained from both the liquid drop model and the shell correction model. The figure is cited from [21].*

To summarize, by applying such a hybrid approach, problems encountered when using the liquid drop model and the shell model individually are effectively solved.

1.2 Fission yields

Fission of the nucleus is one of the most complicated nuclear reactions in which the nucleus undergoes a large-scale deformation along with a complete reordering of nucleons. To characterize the fission dynamics, various observables have been proposed, among which the SOFIA experiment is mainly interested in the fission yields and the total kinetic energy of the fragments. In addition, the prompt neutron multiplicity can be also obtained.

This part is concentrated on the fission yields. First, the motivation to measure the fission yields will be discussed extensively, and then the experimental techniques dedicated to the fission yield measurement will be introduced.

1.2.1 Motivation to measure fission yields

The motivation for the measurement of fission yields is mainly twofold: on one hand, fission yields predicted by various models are not sufficiently accurate, and data obtained from different libraries often show poor consistency, implying that more experimental data are highly demanded. For example, the difference between elemental yields of thermal-neutron induced fission of ^{235}U, which is one of the most studied reactions, given by the JEFF 3.1.1. and the ENDF/B-VII libraries is about 5% in average and has a maximum value as high as 20% [22]. On the other hand, fission yields are of remarkable interest to both theory of nuclear reaction and structure and application aspects concerning the nuclear reactor, as presented in the following part.

1.2.1.1 Importance of fission yields for theory

As mentioned before, without taking into account the single-particle shell structure of nucleons, the asymmetric distributions of fission fragments of actinides cannot be explained, suggesting that fission fragment distributions can help to interpret the nuclear structure. It is known that nuclei having magic numbers of protons or/and neutrons exhibit enhanced stability, making themselves preferred in the production of fission fragments. Therefore, fission yields can give a clue to the shell structure and fission modes.

Additionally, fission is considered as an efficient way to produce neutron-rich isotopes, whose properties are crucial to understand the nucleosynthesis r-process. And yields of these products can be used to interpret the mass abundance in the universe.

Furthermore, accurate data of fission yield measurements can be used to evaluate the performance of theoretical models of the nuclear fission. Besides, with sufficient experimental data of fission yields, it is possible to find regularities and correlations which can help to interpret the fission process and can be then incorporated in semi-empirical fission models.

1.2.1.2 Importance of fission yields for application

Fission fragments play a key role in the operation of nuclear reactors: they are the source of delayed neutrons, which are very essential for the stability of the chain reaction. Some of them, such as ^{135}Xe, are responsible for the poisoning of the core because they have a high neutron absorption cross section, bringing negative reactivity. Therefore, it is very important to know precisely the amount of the produced fragments.

In addition, the residual power of the reactor comes from the decay heat of the fission fragments. In the case of reactor shutdown, all reactions stop subsequently, as well as the energy released from the reactions. However, the decay heat does not disappear immediately, but decreases gradually with time, implying that cooling is still needed to prevent the core temperature from increasing continuously and thus to avoid the potential core meltdown. In order to take appropriate actions concerning the cooling, it is essential to have a high-precision estimate of the decay heat, which requires exact information on the fission yields, the decay scheme, the half-life and the decay energy of the fission fragments.

Moreover, fission yields are also important for the waste management since precise knowledge of the constitutions of the inventory is necessary for the handling of the used fuel, and they can be very helpful for the design of the next generation of nuclear power plants.

1.2.2 Experimental techniques

In this part, various experimental techniques developed for the measurement of fission yields are presented, in an order which roughly follows their development in history. Additionally, the advantages and drawbacks of these techniques are also discussed.

1.2.2.1 Radiochemical methods

From the discovery of fission to the early 1960's, the predominant techniques applied to acquire the fission yield data were radiochemical methods [23], in which a target of fissile material is first irradiated by neutrons and then dissolved. The fission product of interest is chemically separated from the solution afterwards, and its radioactivity is measured either by a beta counting detector or by a gamma ray spectrometer, providing an estimate of the number of its atoms.

If precise gamma ray spectrometry is used, it is possible to calculate the yield of a product nuclide without performing prior chemical separations [24], because discrete gamma rays are characteristic and can be unambiguously assigned to a given nuclide. However, due to lack of accurate data on decay constants and branching ratios of gamma rays, this spectrometry is solely feasible for a limited number of fission products. Besides, other factors like the necessity to subtract the background activity also make it a difficult counting technique [23].

In order to obtain absolute fission yields, not only the number of fission product atoms but also the number of fissions are required, in addition to the efficiency of the chemical separation and that of the counting used for the radioactivity measurement [24]. Since it is very difficult

and time-consuming to measure all these quantities, the determination of absolute yields for all fission products becomes barely possible. In reality, absolute yields are normally measured for only one or two products and they are set as standard yields. Then for other products, the yields are determined relative to these values. Alternatively, all the fission yields can be determined relative to the yields of the fission products of a standard fissioning nuclide (usually ^{235}U) [24]. In a word, the fission yields measured by radiochemical methods are mostly relative and need to be normalized to acquire the absolute values, introducing an extra systematic uncertainty to the measurement [25].

Moreover, considering the time needed for the irradiation, the target transportation and the chemical separation, usually only yields of fission products with reasonably long half-lives can be measured, or only cumulative yields including generation from precursor decay are measured by radiochemical methods.

1.2.2.2 2E and 2v methods

Later on, targets of fissile materials were irradiated by ion beams instead of conventional ion sources, and fission fragments were measured in flight, giving an access to the measurement of independent yields before β decay of precursors.

The two methods, namely the "double energy 2E" and "double velocity 2v" methods, correspond to measuring the kinetic energy and the velocity of both fission fragments, respectively. Both methods are based on mass and momentum conservation [26]. If the recoil on the compound nucleus caused by the incident ion (usually neutron) is negligible, the fission fragments before the prompt neutron emission make up a two-body system with null momentum. Then according to the conservation rules, fragment masses can be calculated.

Technically, in the 2E method, fragment energies are measured by using a double ionization chamber with a thin target in the center: fission fragments fly away from the target back-to-back, and each enters one half of the ionization chamber wherein its kinetic energy is measured, whereas the velocities are determined by a time-of-flight measurement in the 2v method.

The effect of the prompt neutron emission on the measurements of the fragments is twofold [25]:

- the loss of mass of the fragment, leading to a loss of the fragment kinetic energy,
- and the recoil energy added to the fragment, which is caused by the emission of the neutron.

Measurements of fragment energies are influenced by both aspects, while the measurements of velocities are solely affected by the recoil effect. Since the neutron emission is assumed to be isotropic with respect to the fragments' center of mass, the recoil results in no systematic error [25], implying that velocities of the fragments are unchanged on average. Consequently, the 2v method is more accurate than the 2E method. However, this advantage is usually canceled by the less good resolution of the time-of-flight measurement.

Until today, the combination of the 2E and 2v methods has been implemented in many experiments [27][28][29]. Since the mean value of fragment velocities is conserved prior to and post the neutron evaporation, fragments' pre-neutron masses can be determined from velocity measurements according to the conservation law, while the post-neutron masses are calculated directly from the combination of measured kinetic energies and velocities [29]. Then, by measuring simultaneously pre- and post- neutron fragment masses with the use of the 2v-2E method, it is possible to obtain the prompt neutron multiplicity, as published in [29].

1.2.2.3 Recoil mass spectrometers

The Lohengrin recoil mass spectrometer located at ILL, Grenoble is the most accurate instrument for the measurement of thermal neutron fission yields, with which thermal-neutron induced fission of various nuclei has been studied [30].

The spectrometer stands near to the core of ILL's nuclear reactor, which produces high-flux thermal neutrons. A target of fissile material is placed under the neutron irradiation. One of the two fission products emerging from the target enters the spectrometer. It is first deflected by a magnet and then deviated by a condenser according to its mass-over-charge (A/q) and kinetic-energy-over-charge (E_k/q) ratios, respectively. Due to the combination of the magnetic and electric fields, fission products with a given mass, ionic charge and kinetic energy are selected and finally reach the exit of the spectrometer.

The time of flight throughout the spectrometer for the fission products is about 2 μs, suggesting that products arrive at the detector before β decays and hence independent yields are measured. At the very beginning, mass and isotopic yields of fission products were determined by an ionization chamber coupled to the spectrometer. However, due to the charge state fluctuations, this technique was limited to the very light mass group. Later on, even with some improvements, isotopic yields can only be measured not heavier than Z = 47 [31].

In order to expand the isotopic yield measurement to the heavy mass group, a new technique including γ spectrometry has been developed. Finally, the range of yield measurements is effectively doubled, giving an access to isotopic yields of heavy fragments [30]. However, since the γ rays used to identify the fission products are emitted from γ de-excitation process following β decays [30], the isotopic yields measured by this technique are cumulative yields. In addition, this new method can only be applied to fission products who are γ emitters with accurately known γ-ray ratios and decay constants.

It is known that the fission product with a given mass can be selected by the spectrometer with several combinations of kinetic energy and ionic charge. In principle, to calculate isotopic yields, all kinetic energies and all ionic charges need to be taken into account. However, this method is too time-consuming. Finally, the isotopic yield is obtained by only measuring various kinetic energies at the mean ionic charge and various ionic charges at the mean kinetic energy [30]. According to [32], a systematic uncertainty of less than 1.3% is additionally introduced due to this approximation.

1.2.2.4 Experiments using inverse kinematics

The advent of heavy ion accelerators provided an access to a new type of experimental techniques: instead of making a target of fissile material and irradiating it by a beam of neutrons, photons or charged particles to initiate fission, fissile nuclei are accelerated as a beam and fission is induced in flight by the interaction between the beam and a static target. In the former type of methods, the fissile material is at rest, while in the latter case, nuclei of the fissile material are accelerated. Respectively, the two types of techniques are referred to as direct kinematics and inverse kinematics.

By using inverse kinematics, several problems encountered in the direct kinematics techniques are solved:

- since the fissile material needs to be made as a target in direct kinematics, it is constrained to reasonably long-lived isotopes, whereas in inverse kinematics, fission yields of isotopes with very short half-lives can also be measured. Besides, some difficulties concerning the fissile target such as handling of the target naturally disappear by using fissioning nuclei as a beam.
- in direct kinematics experiments, fission fragments are emitted back-to-back in all directions, making it very difficult to detect both fission fragments simultaneously. In contrast, in inverse kinematics, fission fragments are produced in a narrow cone in the forward direction, which leads to a high detection efficiency for both fragments at the same time. As a consequence, this allows to identify fission products over the whole range.
- the isotopic yield measurement is always limited to light fragments in direct kinematics, because the fissile material is at rest and both fission fragments are produced with low kinetic energies, then the heavy fragment with even lower kinetic energy undergoes charge state fluctuations in the detectors, spoiling the resolution of its atomic number. Conversely, due to the boost of the fissioning system in inverse kinematics, fission fragments can be emitted with very high velocities, permitting to measure isotopic yields for heavy fragments.

There are mainly three facilities in the world wherein accelerated heavy ion beams are available, thus allowing the study of fission in inverse kinematics: GANIL in France, RIKEN in Japan, and GSI in Germany. In these facilities, heavy ions are accelerated to various orders of magnitudes of energies: tens of AMeV, hundreds of AMeV, and a few AGeV respectively. Specific fission experiments are performed accordingly, as presented in the following part.

At GANIL

A ^{238}U primary beam up to 24 AMeV is available in the GANIL facility. In the case of experiments with the VAMOS spectrometer, the uranium beam is accelerated to 6.09 AMeV and then bombarded to a carbon target [33].

The interaction between ^{238}U and ^{12}C gives an access to various fissioning systems ranging from ^{238}U to ^{250}Cm, allowing the fission study of numerous nuclides in one single experiment.

Specifically speaking, with an ^{238}U beam, transfer reactions provide a variety of actinides (^{238}U + ^{12}C $\rightarrow$ actinide + recoil), and fusion reactions produce ^{250}Cm (^{238}U + ^{12}C $\rightarrow$ ^{250}Cm) [34]. An advantage of this approach is that it offers a unique opportunity to investigate neutron-rich actinides with mass number not smaller than 238. Additionally, with this method, it also allows to study fission of very short-lived isotopes which would be impossible to handle as targets or beams.

Since several actinides can be produced as fissioning systems, they need to be identified first, which is realized by the identification of reaction recoils. To be detailed, measurements of the energy loss δE and the residual energy E_{res} of recoils performed by two silicon detectors allow to reconstruct the transfer reactions. As a result, not only the mass and atomic numbers but also the excitation energy of the fissioning system can be obtained under physical assumption on the excitation energy sharing between the outgoing partners.

The fission fragments are identified by means of the VAMOS spectrometer in which measurements of the magnetic rigidity, time of flight, the energy loss and the total energy of the fragments are performed. Due to the boost of the primary beam, the fission fragments are produced forward in a cone of 25°, which is much larger than the acceptance of the spectrometer according to a simulation [34], resulting that a simultaneous identification of both fragments in every single event is not possible.

Finally, the mass and atomic-number identifications of the fragments over the complete range are obtained. However, since the available energy of the primary beam is relatively low at GANIL, the distribution of the ionic charge states of the fission fragments is quite broad, which deteriorates the atomic-number resolution, especially for the heavy fragments.

At RIKEN

With the construction of the SAMURAI spectrometer, a new and powerful method for the fission study based on knockout reactions has been proposed [35], and some tests have already been performed.

A ^{238}U primary beam at 345 AMeV is provided by the Radioactive Ion Beam Factory (RIBF) and then bombarded to a Beryllium target, producing a secondary beam of various nuclides. The nuclide of interest is separated and identified by the BigRIPS fragment separator. The selected nuclei then fly through a liquid Hydrogen target in front of the SAMURAI spectrometer, on which the proton knockout (p, 2p) reaction occurs, producing an excited knockout residue which de-excites via fission afterwards. The excitation energy of the fissioning nucleus can be determined with missing mass spectroscopy (*i.e.* measurement of the two protons).

Benefiting from the large acceptance spectrometer SAMURAI, it should be possible to identify both fission fragments simultaneously. The mass and atomic numbers of the fragments are obtained via Bρ-ΔE-ToF technique. The aim of the experiment is to obtain charge and mass distributions of the fragments as a function of the excitation energy at fission. But the clean identification of the (p, 2p) reactions among the other reactions producing 2 protons, for example (p, 2pxn), has still to be proved to secure the excitation energy determination.

At GSI

The first experiments using inverse kinematics to study fission were conducted in the early 1990's at GSI [36, 37]. A ^{238}U primary beam was accelerated to 750 AMeV and then bombarded to a lead target at the entrance of the fragment separator FRS. The nuclei of ^{238}U were excited due to their electromagnetic interaction with the target nuclei and they de-excited via fission afterwards. Since the high resolution FRS spectrometer has a limited acceptance, only one of the two forward-emitted fission fragments was measured in every single event. The fragments were identified via the ΔE-Bρ-ToF technique by the FRS combined with some detectors on an event-by-event basis, in both mass and nuclear charge. The time of flight throughout the FRS for the fragment ions was about 300 ns [36], which is shorter than any β decay half-life, indicating that the measured isotopic fission yields are independent yields.

Later on, in the second experiments [38], in order to study fission of various nuclides, a ^{238}U primary beam at 1 AGeV was driven to a Beryllium target, on which the fragmentation of ^{238}U nuclei occurred, producing a secondary beam of neutron-deficient actinides and pre-actinides. The created nuclide whose fission was to be studied was selected and identified in both mass and atomic numbers by the FRS, and it was then transmitted to a lead target and underwent fission following a Coulomb excitation. Due to the relativistic boost of the secondary beam, the fission fragments were emitted forward inside a narrow cone of about 60 mrad [38], allowing a simultaneous measurement of both fragments. Finally, elemental yields and total kinetic energies were obtained for the fission fragments.

Our SOFIA experiment was inspired by and based on these pioneering experiments, and it is an upgraded one in view of its aiming at identifying both fission fragments in mass and nuclear charge simultaneously.

Chapter 2

the SOFIA experiment

This chapter will first give an overview of the SOFIA experiment and the GSI facility. Then the method to identify ions with the use of a recoil spectrometer and the fission mechanism, especially the coulomb-induced one, will be introduced. At the end, work accomplished in my PhD and how it will be presented in the following chapters are briefly demonstrated.

2.1 Overview of the SOFIA experiment

SOFIA, Studies On FIssion with Aladin, is an innovative experimental setup developed to measure isotopic (mass and nuclear charge) yields of fission fragments.

As already mentioned in the previous chapter, to avoid inherent drawbacks of the direct kinematics techniques, inverse kinematics is applied in the SOFIA experiment, in which the beam of fissioning nuclides is impinging to a target where fissioning nuclei are excited and then de-excite through fission. Fissions of a broad range of fissioning nuclei, covering many actinides and pre-actinides, are studied.

In SOFIA, nuclear charges are derived from energy loss measurements in an ionization chamber. If ions pass through the chamber with low kinetic energies, they easily collect electrons, resulting in a charge state fluctuation which makes an accurate measurement of nuclear charges very difficult. Therefore, to achieve a good nuclear charge resolution, fission fragments have to be produced with sufficient energies, which means the fissioning system needs to be accelerated to several hundreds of AMeV. Issues concerning the charge state fluctuation will be explained extensively in the part 3.2.2.3.

In order to apply inverse kinematics and produce fission fragments of actinides and pre-actinides with sufficiently high energies, SOFIA experiments are conducted in GSI because it is the sole facility that provides relativistic heavy ion beams.

It is known that with the increase of the excitation energy, shell effects, including asymmetric fission and even-odd staggering, become less obvious. Since the influence of the shell structure on the fission process is essential, low energy fission is of great interest. There are mainly two reaction mechanisms between the projectile nuclei and the target nuclei, which can lead to the excitation of the incident projectile: the nuclear collision and the Coulomb interaction. Since the Coulomb excitation exhibits a relatively lower mean value of the energy as compared to the nuclear-included one, our experiment is focused on the study of the Coulomb-induced fission.

In a word, in the SOFIA experiment, isotopic yields of fission fragments produced in the Coulomb-induced fission of various actinides and pre-actinides are measured by means of a relativistic primary beam and the inverse kinematics technique.

2.2 Overview of the GSI facility

For SOFIA experiments, GSI provided a ^{238}U primary beam at 1 AGeV. The layout of the GSI facility is shown in figure 2.1. The ^{238}U primary beam is first accelerated in the linear accelerator UNILAC, then in the synchrotron SIS-18 to a kinetic energy of 1AGeV. It impinges to a Beryllium target at the exit of the synchrotron and fragmentation reactions take place, producing various nuclei with mass number not larger than 238. The nuclei are then transmitted to the FRagment Separator (FRS).

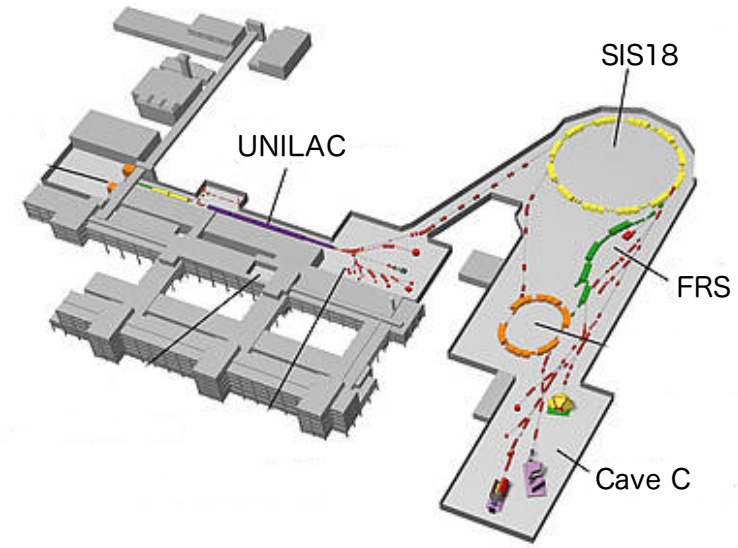

FIGURE 2.1: *Layout of the GSI facility, Court. GSI.*

The FRS is a recoil spectrometer and is structured with two pairs of dipoles. The nuclei, whose fission is going to be studied, are separated and selected from the fragmentation products by the FRS, according to their magnetic rigidity. However, except the nuclei of interest, some other nuclei with similar magnetic rigidity are also chosen. All these selected nuclei make up a cocktail secondary beam which is transmitted to the Cave C, and this can be an opportunity to study the fission of several nuclei. Thus, it is necessary to first identify the fissioning nuclei from the secondary beam, then perform an identification of fission fragments.

In the Cave C, there is A Large Acceptance DIpole magNet (ALADIN), which forms a recoil spectrometer with the accompany of a series of detectors developed by the SOFIA group. This very large acceptance recoil spectrometer is used to identify both fission fragments in nuclear charge and mass simultaneously.

2.3 Method of identifying ions

In the SOFIA experiment, the method of identifying ions is applied twice: to distinguish the fissioning nuclei among secondary beam ions, and to identify fission fragments in mass and elemental number over the whole range.

Ions of the secondary beam are emitted at about 700 AMeV and fission in flight, producing fission fragments also with very high energies. Under such a circumstance, ions of both the fission fragments and the majority of the fissioning nuclides are fully stripped when they go through an ionization chamber, resulting in the ionic charge equal to the product of the nuclear charge (*i.e.* atomic number Z) and the elementary charge. Thus, the nuclear charge can be directly deduced from the measurement of the energy loss, which is proportional to the square of the ionic charge, in an ionization chamber. As for the rest of the fissioning nuclides whose ions are non-fully stripped, it is not straightforward but still possible to extract the nuclear charge from the energy loss measurement. The details will be discussed in section 3.2.2.

The mass number is measured with the use of a recoil spectrometer, which contains dipole magnet(s) and several detectors. When ions fly through the magnet, they are deflected according to their magnetic rigidity (Bρ). The mass number is thus obtained on the basis of the following equation:

$$B\rho = \frac{p}{Q} = \frac{A}{q \times e} u\beta\gamma c \tag{2.1}$$

with:

B	Magnetic field [T]
ρ	Ion's curvature radius [m]
p	Momentum [kg·m/s]
Q	Ionic charge [C]
q	Charge number
e	Elementary charge [C]
A	Mass number
u	Atomic mass unit [kg]
β	Ratio of ion's velocity to the light speed in vacuum
γ	Lorentz factor
c	Speed of light in vacuum [m/s]

From equation 2.1, it is shown that the mass number can be deduced after knowing the ionic charge, velocity items (β and γ) and the magnetic rigidity. Since the nuclear charge and the ionic charge are extracted from the energy loss measurement and velocity items are given by a time-of-flight (ToF) measurement, this method of fully identifying ions in mass A and nuclear charge Z is named as the ΔE - Bρ - ToF technique.

The energy loss measurement is performed by a MUSIC (MUlti-Sampling Ionization Chamber) detector. The magnetic rigidity is the product of the known magnet field and the deflection radius extracted from tracking the ion's trajectory. Complete information of the trajectory

is provided by the combination of a horizontal angle measured in the MUSIC and position measurements given by MWPC (Multi-Wire Proportional Chamber) detector(s). As for the ToF measurement, the detector type is slightly different between the case of secondary beam ions and that of fission fragments. For the secondary beam, the ToF measurement is executed by two scintillation detectors and each of them mainly contains a single plastic scintillator, while it is performed by one scintillation detector and a time-of-flight wall composed of 28 plastic slats for fission fragments, due to the large dispersion of trajectories behind ALADIN.

In a word, the identification of ions, no matter for the secondary beam or for the fission fragments, is achieved by applying the ΔE - Bρ - ToF technique with the use of a recoil spectrometer.

2.4 Fission Mechanism

As already mentioned, the Coulomb-interaction induced fission, rather than the nuclear-collision induced one, is of interest in the SOFIA experiment. However, the latter also occurs in the events, implying that fission triggered by two types of reactions has to be distinguished from each other.

In this section, the mechanism of the Coulomb-induced fission and the calculation procedure to obtain the excitation-energy distribution at such fission are first explained. Then the mechanism of the nuclear-induced fission and a corresponding excitation-energy spectrum are presented. Finally, the method to extract the Coulomb-induced fission is introduced.

2.4.1 Coulomb-induced fission

When the impact parameter between the projectile and the target nuclei is small, the coulomb interaction is less preferred as compared to the nuclear collision. However, when the parameter is larger than the sum of the radii of the interacting nuclei, *i.e.* when the charge distribution of two nuclei do not overlap each other [39], the coulomb interaction becomes the exclusive mechanism to induce fission.

The simplest description of this mechanism is given by the equivalent photon method, which was originally proposed by Fermi [40]. It is claimed that the variable electromagnetic field produced by the passage of a charged particle at one point is equivalent to that at the same point, as if it was struck by light with a proper distribution of frequencies [41]. Therefore, due to the Coulomb field of the target nuclei, when the projectile passes by, it feels like being irradiated by a stream of virtual photons. Then the projectile absorbs these photons, resulting in the excitation of giant multipole resonances. Eventually, the projectile can de-excite through fission, which is possibly preceded by an evaporation of neutron(s), depending on the amplitude of the excitation energy.

2.4.1.1 Calculation of Coulomb-induced excitation energy

On the contrary to the conventional neutron-induced fission experiments, in which the excitation energy is easily given by the sum of the incident kinetic energy and the binding energy of the neutron, it is impossible to measure the excitation energy directly in our experiment. Actually, this is supposed to be one of the main limitations of the inverse kinematics experiments. Instead, the excitation energy is estimated according to the calculation.

Cases of ^{235}U and ^{238}U are taken as an example to show the procedure of calculating the excitation energy at Coulomb-induced fission. The steps corresponding to ^{235}U and ^{238}U are drawn on the left- and right- side of figure 2.2 respectively, and they are numbered by captital and small letters, respectively. The plots in the former case are cited from reference [22], while those in the latter case are cited from [42]. The calculation is implemented step by step:

1. The spectrum of virtual photons equivalent to the electromagnetic field of the target nuclei seen by the projectile is obtained. First, the electromagnetic field is expressed as identical to the radiation of two plane-polarized waves of light, and the relativistic Lorentz factor is computed to take the contraction of the field into account. Then the electromagnetic field is decomposed into multipole components via a Fourier transform. For each multipolarity, a photon spectrum is given accordingly. Relevant formulations can be found in [40]. In both (A) and (a) of figure 2.2, spectra of electric dipole (E1) and electric quadrupole (E2) photons are plotted, and the amplitude of the latter is roughly one order of magnitude larger than that of the former.
2. The cross section of photon absorption is estimated. The absorption of E1 and E2 photons results in the excitation of the electric Giant Dipole Resonance (GDR) and Giant Quadrupole Resonance (GQR), respectively. Excitations of magnetic resonances and higher-order electric resonances are neglected, as they are supposed to be very small [38]. The GDR is seen as the collective oscillation of the protons and the neutrons of the nucleus with opposite phase. The photon absorption cross section of the GDR is described by a Lorentzian for spherical nuclei, while in deformed nuclei, the resonance splits into two components, and the ratio of the resonance energies is equal to that of the main axes of the deformed nucleus [38]. As shown in (B) and (b) of the figure, the absorption of dipole photons is much more preferred, as compared to that of quadrupole photons.
3. The excitation-energy distribution is calculated by the product of the spectrum of virtual photons and the corresponding absorption cross section obtained in the previous steps. Since the probability to excite the GDR is high, a double excitation of this mode (*i.e.* the GDR excited on a GDR state by absorbing two photons) is quite possible, while multiple excitations of the GQR are negligible [38].
4. The profile of the fission probability at various excitation energies is obtained. As mentioned before, excited nuclei can de-excite via two competing processes — nucleon evaporation and fission. Since the proton evaporation can be neglected at such an excitation energy, the nucleon evaporation after the Coulomb excitation actually implies the neutron

removal. From (C) and (c) in the figure, it is noticed that thresholds for the first-, second- and third-chance fission, after the removal of 0, 1 and 2 neutrons, are about 6 MeV, 11 MeV and 18 MeV, respectively.

5. The excitation-energy spectrum at fission is finally provided by the product of quantities acquired in steps (1), (2) and (4). It needs to be kept in mind that in cases of the multi-chance fission, a portion of the original excitation energy is assigned to the neutron evaporation, and thus the excitation energy at fission is reduced by at least 5.3 MeV, which is the value of the binding energy of the neutron.

In (D) and (d) of figure 2.2, the excitation-energy spectra at the Coulomb-induced fission of ^{235}U in the first (at 640 AMeV), second Uranium targets and the lead target, and those for the fission of ^{238}U in the first Uranium target (at 585 AMeV) and the lead target (at 490 AMeV), are plotted respectively [22, 42]. It is observed that for a certain fissioning nucleus (^{235}U or ^{238}U), the shape of the spectrum is strictly the same for all targets, and only the amplitude scales. Indeed, the shape of the three curves for ^{235}U also looks quite similar to that of the two curves for ^{238}U. Therefore, it is reasonable to extrapolate that in our case (^{236}U impinging on two U targets and one lead target at about 670 AMeV), the excitation-energy distributions at fission are similarly shaped, and the mean excitation energy for the Coulomb-induced fission of ^{236}U is about 12 MeV, which is equivalent to that of the compound nucleus formed by ^{235}U absorbing a neutron at roughly 6 MeV.

2.4.2 Nuclear-induced fission

The nuclear collision occurs only when the impact parameter between the projectile and the target nuclei is smaller than the sum of their radii. Due to the violent collision, some nucleons are directly kicked out from the projectile, leaving the residual nuclide with an excitation energy ranging from a few MeV to hundreds of MeV, as seen in figure 2.3 [38], in which the energy distribution of the collision-induced excitation of ^{234}U is taken as an example. Then, the projectile-like nuclide de-excites through two competing processes — fission and nucleon evaporation. Events with a removal of proton(s) due to the abrasion and/or the evaporation are not considered to show the spectrum in the figure.

As above mentioned, the excitation energy is not measured event by event, but only an overall distribution is estimated. It is observed that the energy distribution for the nuclear-induced excitation is less compact as compared to that for the Coulomb-induced one, implying a higher uncertainty in the excitation energy in each event, and thus making it more difficult to interpret the excitation-energy dependent results, like the fission yields. In such a point of view, it also concludes that the Coulomb-induced fission is a better candidate for our study of fission.

Furthermore, due to the abrasion of nucleons in the collision, the resulting excited nuclide already differs from the one which was identified before the target. And the nuclear-induced

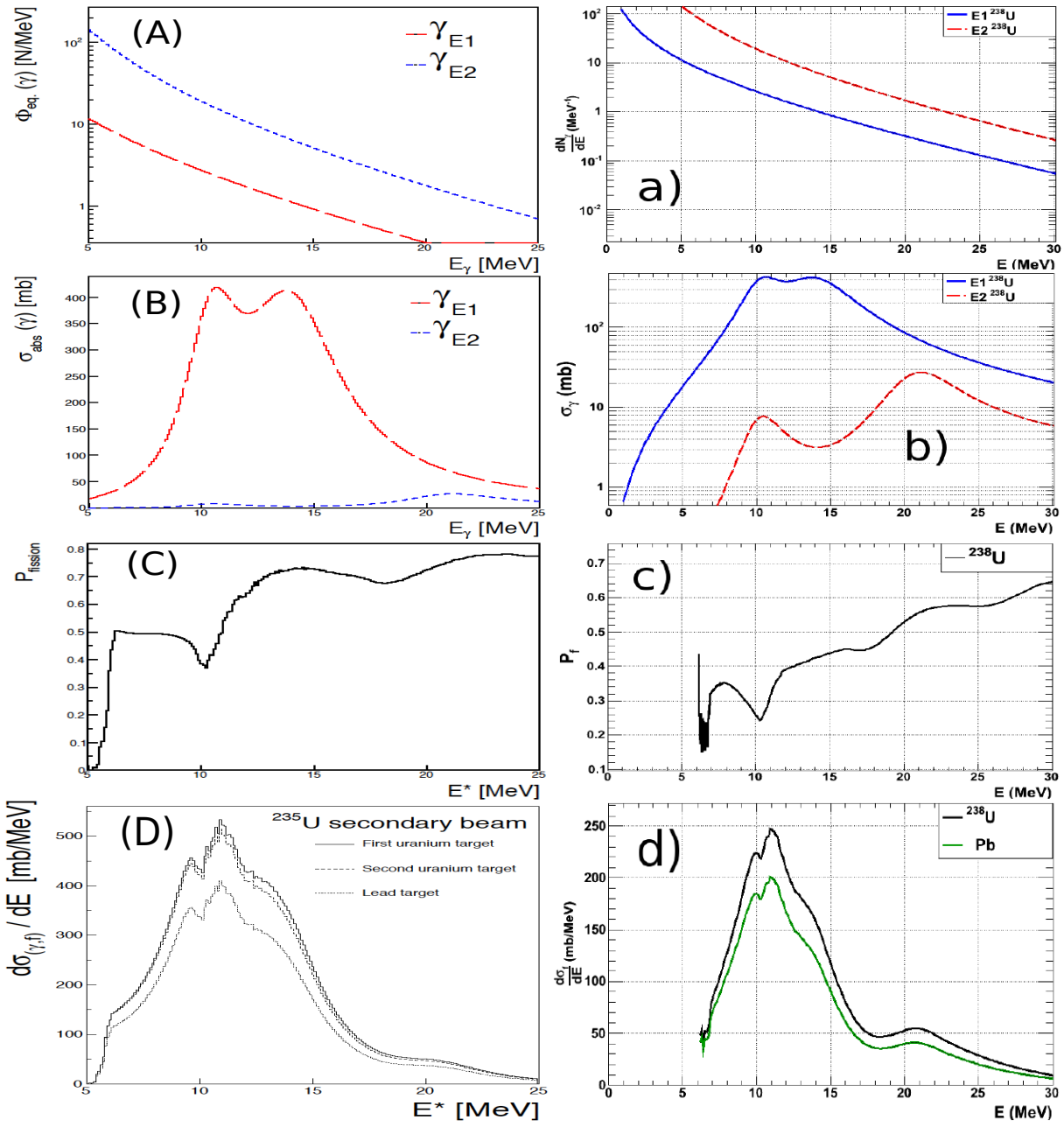

FIGURE 2.2: *Calculation of the excitation-energy distribution at the Coulomb-induced fission. Plots on the left- and right-side of the figure correspond respectively to the fission of ^{235}U and ^{238}U studied in the first SOFIA experiment, and they are cited from [22, 42]. When comparing the plots from both sides for each step, pay attention to the labels of the curves and the scale of the Y-axes; otherwise, one may be misled at the first look.* ***(A), (a)****: Spectra of virtual photons equivalent to the E1 and E2 components of the electromagnetic field of the target nuclei, as seen by the projectile.* ***(B), (b)****: Cross sections of the photon absorption of the projectile. The absorption of electric dipole (E1) and quadrupole (E2) photons mainly lead to the excitation of the Giant Dipole Resonance (GDR) and the Giant Quadrupole resonance (GQR).* ***(C), (c)****: Profile of the fission probability at various excitation energies. Multi-chance fissions preceded by the evaporation of neutron(s) are possible, depending on the value of the excitation energy.* ***(D), (d)****: Excitation-energy distributions at the Coulomb-induced fission. The actual excitation energy is reduced by an amount of energy assigned to the neutron evaporation prior to fission. The distributions are calculated for the fission of ^{235}U and ^{238}U in several targets.*

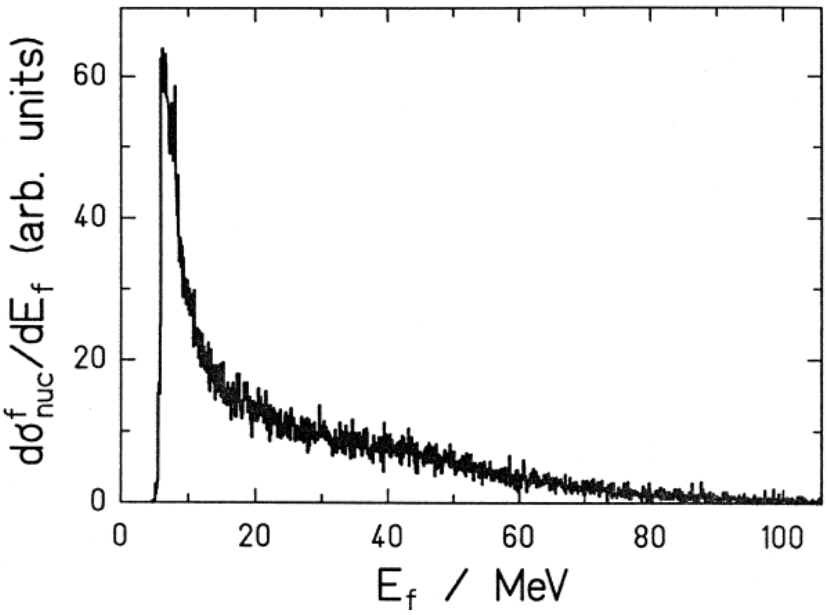

FIGURE 2.3: *"Excitation-energy distribution at fission after nuclear collisions of ^{234}U inside the plastic target, calculated with the ABRABLA code under the condition that all protons of the secondary projectile are still present in the fission fragments. This condition selects very peripheral collisions that only remove neutrons from the secondary projectile." Caption and figure cited from [38]*

.

fission is possibly preceded by a proton removal, not mentioning the competitive neutron evaporation. It is calculated that in the nuclear collisions between the incident ^{234}U nuclei and the nuclei of the plastic target, by selecting very peripheral collisions in which only neutrons are removed from the projectile, an average mass loss of 2.3 occurs in the fissioning nucleus prior to the fission [38].

On the contrary, in the case of the Coulomb-induced fission, no nucleons are removed before the excitation and the proton evaporation which requires very high excitation energy is rather impossible. Although the evaporation of neutron(s) is not negligible, the first-chance fission always dominates firmly. Taking ^{234}U as an example, the Coulomb-excitation induced fission consists of around 80% first-chance fission (^{234}U), 15% second-chance fission (^{233}U), and a slight fraction of higher-chance fission (mainly ^{232}U) [38]. In our case, the measured fission yields also represent a combination of about 3 isotopes (^{236}U, ^{235}U and ^{234}U), which corresponds to an average mass loss less than 2 units.

Therefore, the Coulomb-excitation induced fission is exclusively desired and it needs to be separated from the fission caused by the nuclear collision.

2.4.3 Extraction of Coulomb-induced fission

As already discussed, following a nuclear collision, the projectile is very likely to undergo a removal of proton(s), due to either the abrasion or the evaporation right before or after the excitation respectively. These events can be easily discarded by requiring the sum of nuclear

charges of the fission fragments equal to the charge of the nucleus of the secondary beam. Since the nuclear charge identifications of both the fragments and the secondary beam are performed in every single event, the exclusion of events in which the protons of the projectile are not preserved in the fission fragments is also implemented on an event-by-event basis.

However, the rest of the nuclear-induced fission events, in which only neutrons are removed, still remain. Although in this case, the species (*i.e.* the atomic number) of the fissioning nuclide does not change, the corresponding broad excitation-energy distribution, as already observed in figure 2.3, implies that these events are not wanted, neither. Unfortunately, there is no way to directly separate them from the fission events triggered by the Coulomb interaction. Yet their contribution to the nuclear charge distribution of the fission fragments can be eliminated, finally resulting in an elemental yield of fragments purely from the Coulomb-induced fission.

The subtraction of the contribution is achieved with the use of several low-Z materials (Aluminum), in which almost only the nuclear-induced fission occurs, because the cross section of the Coulomb excitation decreases drastically with the decrease of the material's nuclear charge, resulting that the Coulomb excitation is negligible in very light materials.

According the hypothesis of "limiting fragmentation regime" [43], it is assumed that the contribution of the nuclear-induced fission in various materials can be scaled to each other. Therefore, with a properly weighted charge distribution from the fission events in the Al materials, the influence of the nuclear-induced fission in the high-Z U/Pb targets can be fully subtracted, leading to the extraction of the nuclear charge distribution of the fission fragments from the Coulomb-induced fission. The calculation of the scaling factor and the implementation of the subtraction will be extensively explained later.

Actually, the role of the projectile and the target nuclei in the Coulomb excitation can be exchanged, which means the excitation of the projectile is induced by the electromagnetic field of the target, and vice versa [40]. Similarly, the nuclear collision between the projectile and the target is also mutual and the residual nuclide from the fragmentation of the target nuclei may be excited. Therefore, the following fission of the target and target-like nuclei also needs to be considered.

However, since the targets are at rest, the corresponding fission fragments are produced with very low kinetic energies. The range of these fragments in the U/Pb targets is only a few μm, implying that they can hardly escape from the target in which they are created and thus not recorded in the data. Therefore, the fission fragments identified in this paper are purely produced by the relativistic secondary beam.

2.5 Two SOFIA experiments

The first SOFIA experiment was conducted in August 2012 and a wide range of fissioning systems were measured. Isotopic yields of fission of ^{234}U, ^{235}U, ^{238}U,^{237}Np and ^{238}Np have

been successfully extracted and elemental yields of fission fragments of Protactinium isotopes (^{231}Pa and ^{232}Pa) have also been obtained [22, 42].

In October 2014, some extra beam time was assigned to the SOFIA collaboration for measuring isotopic fission yields of ^{236}U. The fission of ^{236}U has gained interest because it is the compound nucleus formed by ^{235}U capturing one neutron and thermal neutron-induced fission of ^{235}U is the most typical reaction in nuclear reactors. In addition to two shifts' data taking of fission of ^{236}U, a few beam time (about one hour per setting) was given to three different FRS settings centered on ^{207}Fr, ^{194}Bi and ^{187}Tl to explore fissioning behavior of more exotic nuclei.

2.6 Outline of the following chapters

My work in this PhD is focused on the analysis of fission of ^{236}U. At the moment, the elemental (Z) fission yield has been obtained while the isobaric (A) yield has not been achieved yet. Following chapters (chapter 3 to 5) are divided into two parts.

The first part concentrates on the description of the experimental setup and the analysis leading to the identification of ions. Chapter 3 and 4 are dedicated to the identification of the secondary beam and fission fragments respectively. To be detailed:

In chapter 3, the production of the cocktail secondary beam, through the fragmentation of ^{238}U followed by a selection process in FRS dipoles, is presented. Then the working principle of the FRS dipole magnet is explained and detectors used for the secondary beam identification are introduced. At last, measurements leading to the full identification are demonstrated.

With an unambiguous identification of secondary beam ions, the selection of ^{236}U nuclei is then straightforward. ^{236}U ions fly into the Cave C and fission is induced there. In chapter 4, the corresponding experimental setup is first described and measurements applied to fulfill a simultaneous nuclear charge identification of both fission fragments are then stated.

The second part (chapter 5) focuses on the elemental yield of fission fragments, which is extracted from the nuclear charge distribution over the whole range. Discussions on obtained results are also shown in this chapter.

Chapter 3

Secondary beam identification

With the use of the linear accelerator UNILAC and the synchrotron SIS-18, a primary beam of ^{238}U at 1AGeV is provided to SOFIA experiments. The relativistic beam then impinges a Beryllium target at the entrance of the FRS, in which fragmentation reactions occur, producing a variety of radioactive isotopes with a velocity close to that of the projectile.

The FRS is a high resolution spectrometer used for the selection and isotopic separation of ions. The nuclides of interest, whose fissions are to be studied later, can be selected and separated from the fragmentation products, by adjusting magnetic settings of the FRS. However, due to the spread in magnetic rigidities, some nuclides with close elemental and mass numbers are also transmitted to the Cave C. Thus, to correctly assign two fission fragments to the parent nuclide event by event, it is necessary to first identify the fissioning system from the secondary beam.

The first section of this chapter presents the experimental setup for the secondary beam identification, which is schematically plotted in figure 3.1. An overview of the FRS is first given and the selection process is explained. Then detectors involved for the identification of the secondary beam, including the Triple MUSIC, two scintillation detectors and one MWPC detector, are presented.

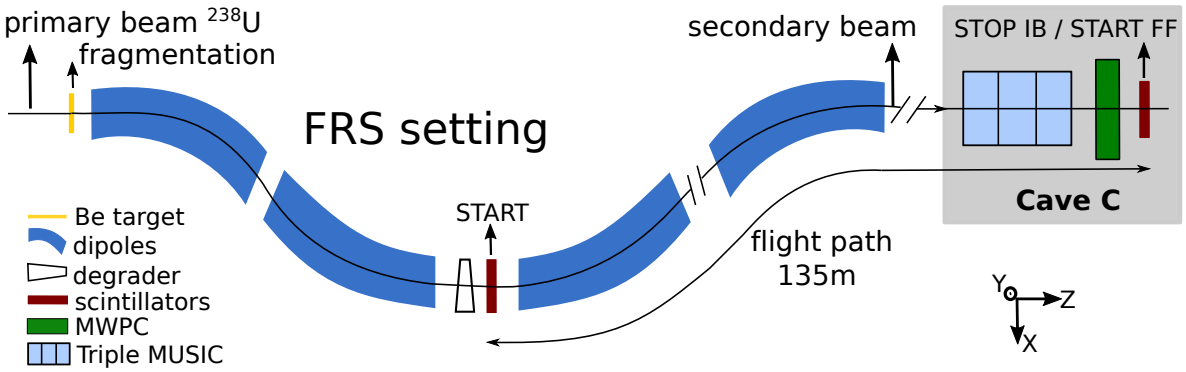

FIGURE 3.1: *Schematic view of the setup used for the secondary beam identification.*

The second section is focused on the analysis procedure leading to the full identification. First, the extraction of the nuclear charge from the energy loss measurement is demonstrated. From equation 2.1 given in chapter 2, it is shown that the mass-over-charge ratio (A/q) can be deduced from measurements of magnetic rigidity and velocity. Then in combination with the previously derived nuclear charge Z, an unambiguous identification of the secondary beam is obtained. Since both A/q and Z are already known, it is possible to compute the mass number A. Finally, the evolution of mass resolution with increasing counting rate is presented, to verify the quality of two new photo-multiplier tubes (PMTs) under high rate.

3.1 Experimental setup

3.1.1 Fragmentation of the primary beam

The nuclides, whose fission is going to be investigated, are first produced via the fragmentation of the primary ^{238}U beam when it penetrates a target, and then selected by the FRS facility. The production target is Beryllium with a thickness of 1036 mg/cm^2, followed by a Niobium foil of 223 mg/cm^2 in the beam direction. Since it is quite unlikely to have non-fully stripped products, the Niobium foil is inserted as a stripper, to minimize the contamination of ionic charge states.

Due to the collision with target nuclei, the relativistic projectile undergoes an abrasion of several nucleons at the first stage of the fragmentation reaction. The residues, populated with some excitation energy, mainly have two channels to de-excite: particle-evaporation or fission. On the left of figure 3.2, cross sections of the reaction of 1AGeV ^{238}U projectiles on hydrogen are shown. It is observed that the majority of fragments are produced in two regions linked by a neck of minima: the vicinity of the projectile and a much wider area down to the lightest nuclide. In the former region, the nuclides are purely produced by fragmentation-evaporation reactions, while with Z going down to the latter region, the fragmentation-fission becomes dominant. As for the nuclides of very low Z, they are mostly produced by the multi-fragmentation.

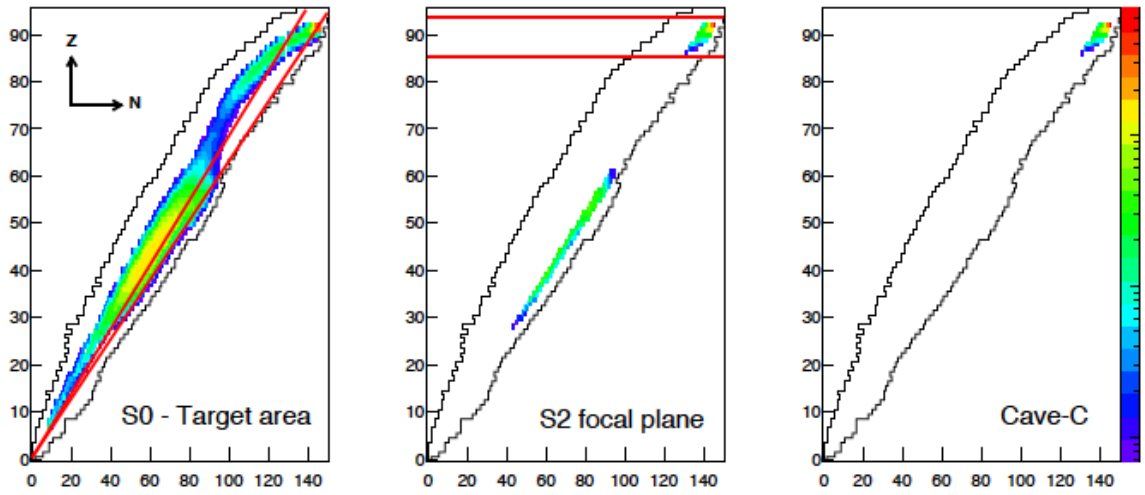

FIGURE 3.2: *Example of the selection process of fragmentation products for a FRS setting centered on ^{235}U, shown on the nuclide chart. The figure is cited from [22]. Left: nuclides produced by the fragmentation of 1AGeV ^{238}U projectiles on hydrogen, according to reference [44]. The red lines represent the A/Z selection performed between the production target and S2. Center: nuclides arrive at S2, after the A/Z selection. The red lines represent the Z selection performed between S2 and the final focal plane. Right: nuclides going through the whole selection process and arrive at the final focal plane at the entrance of the Cave C.*

The kinetic features of the produced fragments are mainly determined by the reaction mechanism (*i.e.* fragmentation-evaporation, fragmentation-fission or multi-fragmentation) and the

slowing down process in the production target, and the relative contribution of both aspects decreases with the increasing energy [45]. Since the incident projectile has a relativistic energy, the influence on the kinematic features of the fragments is relatively small. Consequently, fragments are produced narrow-peaked (*i.e.* with small momentum spread) in the forward direction with velocities close to that of the projectile.

Furthermore, actinides produced by fragmentation-evaporation reactions are what we are interested in. In this case, only a few nucleons are ejected, namely a mass difference of a few units with respect to the projectile. Since the momentum spread scales with the square root of the mass difference, as seen in equation 3.1, it finally results in a limited momentum spread of the fragments.

$$\sigma(p) = 87\sqrt{\Delta A} \quad \mathrm{MeV/c} \tag{3.1}$$

where $\sigma(p)$ is the momentum spread and ΔA is the mass difference with respect to the projectile.

Thus, for the following discussion, we assume that all fragments are emitted with the same velocity.

3.1.2 The GSI FRagment Separator

The GSI fragment separator, which is used for the selection of nuclei of interest and identification of the secondary beam, is an important part of the SOFIA setup.

In this section, an overview of the FRS facility is first given. Then the selection process of ions, on the basis of the Bρ - ΔE - Bρ method, is briefly explained. It consists of two steps: first, an A/q selection based on the magnetic rigidity analysis, and then, another selection in Z according to the energy loss in a dedicated material. Finally, only ions with almost the same A and Z as that of the intended nuclide are delivered till the end of the facility.

A detailed description of the facility and the selection principle can be found in reference [45].

3.1.2.1 Overview

The fragment separator, as shown in figure 3.3, contains two pairs of dipole magnets, in which ions are deflected according to their magnetic rigidity. By adjusting magnetic settings in the dipoles, desired nuclides can be selected and driven up to the end of the facility, whereas other nuclides with different magnetic rigidity, thus flying through different paths, will be expelled out of the system.

The FRS is symmetric around S2, which is the focal plane in between the first and the second pair of dipoles. Every dipole is equipped with a series of quadrupoles, either two or three on each side. These quadrupole magnets are applied to fulfill high requirements of focusing for the beam. Besides, sextupoles are also placed in front of and behind the dipole magnets, for

correcting higher order aberrations and tuning the central focal plane to be perpendicular to the reference beam line. All the sextupoles are not exhibited in figure 3.3 for simplification.

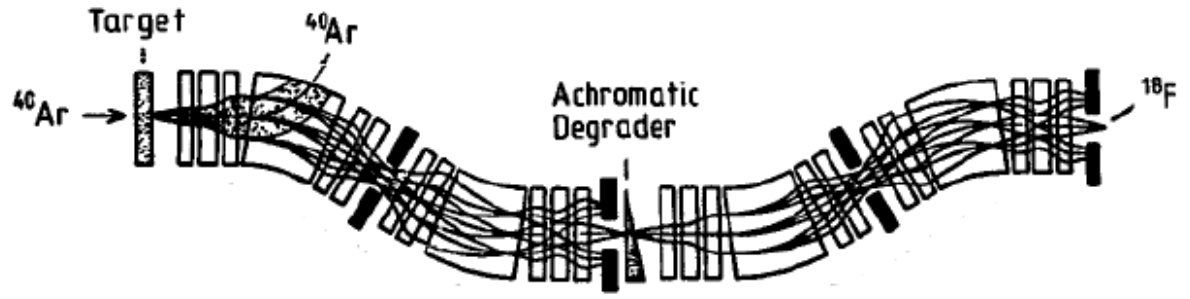

FIGURE 3.3: *Schematic view of the FRS facility. The figure is cited from [45].*

In our experiment, the beam is not transmitted till the S4 focal plane at the end of the FRS. Instead, from the middle of the second section of the FRS, the beam is switched to a transport line up to the Cave C. The section between the S2 and the S8 focal plane at the entrance of the Cave C is the real second part of the magnetic system, which is about 135-meter long, while the second stage of the standard FRS only has a length of about 35 m.

After the first stage of the FRS, ions with different magnetic rigidity end at different positions, along the X direction, at the S2 focal plane, implying that S2 is dispersive. On the contrary, the final focal plane S8 is achromatic because ions are refocused on it, after flying through the second pair of dipoles. In sum, the whole system, from the production target before the FRS to the final focal plane, exhibits overall achromatism.

3.1.2.2 A/Z selection process

The projectile beam undergoes fragmentation when it impinges a target. The fragments produced are then selected by the FRS with a setting centered on the desired nuclide, forming a secondary beam which is transmitted to the Cave C later.

As mentioned before, the whole selection process is based on the Bρ - ΔE - Bρ method. Since the actinides are created nearly with the same velocity, *i.e.* the same $\beta\gamma$ value, the selection according to Bρ at the first stage of the FRS is actually the selection in A/q. In addition, those relativistic actinides produced are mostly fully stripped. Thus, the first selection process is actually a selection in A/Z.

The maximum momentum acceptance of the FRS is approximately 3%, which means a difference of 3% in Bρ in the first section [46]. Still assuming that velocities of fragment ions are almost the same, there is a variation of about 3% in A/Z. A slit can be placed at S2 to expel unwanted nuclides, by adjusting the size of its opening.

In this work, the FRS setting is centered on ^{236}U and its A/Z value is $(A/Z)_0 = 236/92 = 2.5652$. So A/Z values of ions selected by the first section of the FRS are varying within the range $(A/Z)_0 \pm 1.5\% \times (A/Z)_0 = 2.5652 \pm 0.0385$. This range can be indicated by two lines on the nuclide chart, as similarly seen on the left of figure 3.2 [22], in which the selection process of

fragmentation products for a FRS setting centered on ^{235}U is taken as an example. The outcome of the selection, *i.e.* the nuclides transmitted up to the central focal plane S2, is shown on the middle of the same figure. It is noticed that a lot of fission fragments are also selected, implying a future selection is needed.

3.1.2.3 Energy degrader

As already mentioned, the whole magnetic system exhibits an overall achromatism, which means all ions, although separated at S2, are refocused on the final focal plane and thus will be delivered together. However, for our experiment, only ions of the nuclide whose fission is going to be studied need to be selected and transmitted further. Therefore, a spatial separation among fragmentation products at the end of the magnetic system is required. To achieve this, an energy degrader made of Aluminum of 2200 mg/cm^2 is inserted right before S2 and after the first pair of dipoles.

The amount of the energy loss undertaken by the ions inside the degrader depends on:

- the kinetic energy of ions when they reach the degrader: the higher the energy, the lower the energy loss
- the length of the penetrating path: the longer the path, the higher the energy loss
- ions' elemental number

Actually, ions with the same A and Z values are not necessarily produced with the same velocity. They may undergo a slight momentum spread, depending on the reaction mechanism and the slowing down process in the target (which are neglected up to now), and arrive at various positions at the S2 focal plane. The higher (resp. lower) the velocity, the larger (resp. smaller) the Bρ value, and the more right (resp. left) along the X axis of the position at S2.

To ensure that ions of the same nuclide, in spite of a momentum spread, are still refocused on the final focal plane, it is required that for the same nuclide, the energy loss in the degrader is proportional to the kinetic energy upstream the matter. Since the energy loss decreases with increasing kinetic energy, a profiled degrader dedicated to let ions with higher kinetic energy travel via a longer path and thus lose more energy is needed. Since the higher the ions' kinetic energy, the more to the right in the X direction that the ions will arrive on the degrader, the profile of the degrader is designed as wedge-shaped with the thickness increasing gradually along the X axis.

It is known that the energy loss is proportional to the square of the ions' charge. With this extra contribution of the atomic charge, ions of different nuclides are not focused at the same point on the final focal plane, which means they are separated in positions. Thus with the use of the degrader, it permits to select the ions of the desired nuclide.

With a thicker degrader, ions of different Z will end at a wider spread of positions, which eases the selection of the desired nuclide. However, this will also cause more nuclear reactions, resulting in a larger loss of events. Besides, a longer penetrating path in the degrader means further slowing down. As a result, the ions will undergo a larger kinetic straggling. Thus,

the thickness of the degrader needs to be determined properly, to ensure the selection of the wanted nuclide as well as minimizing the nuclear reactions and the kinetic straggling.

3.1.2.4 Z selection process

Since ions flying through the second part of the magnetic system are with close A/Z values, the selection in Bρ is actually a selection in $\beta\gamma$ (*i.e.* velocity). The velocity of the ions is depending on the energy loss inside the degrader which is influenced by the ions' atomic charge. Thus, the selection in Bρ in the second stage (*i.e.* from S2 to S8) is indeed according to ions' elemental numbers. In another word, the second selection in the magnetic system is a Z selection process. It is indicated by red lines on the middle of figure 3.2 and ions arriving at the final focal plane are shown on the right of the same figure.

The FRagment Separator, which is a high resolution spectrometer, is used to select and identify ions. The selection process, based on the Bρ - ΔE - Bρ method, consists of two steps: first, a selection according to the mass-over-charge ratio, and then a selection in the elemental number. However, except ions of the desired nuclide, some ions with similar A and Z values are also selected, forming a secondary beam which is then transmitted to the Cave C and fissions there. Thus, to obtain the fission fragment distribution for the nuclide of interest, it needs to first identify the fissioning system from the secondary beam event by event. The analysis needed to perform the identification and the detectors concerned will be presented in the following sections.

3.1.3 Triple MUSIC

The nuclear charge of the secondary beam is extracted from the energy loss measured in the Triple MUSIC (MUlti-Sampling Ionization Chamber). The detector was designed and constructed by GSI in collaboration with CEA Bruyères-le-Châtel. It is a triple ionization chamber developed on the basis of standard MUSIC detectors used at GSI and specifically upgraded for the SOFIA experiment. A picture of the Triple MUSIC is given in figure 3.4 and some technical information is presented in table 3.1.

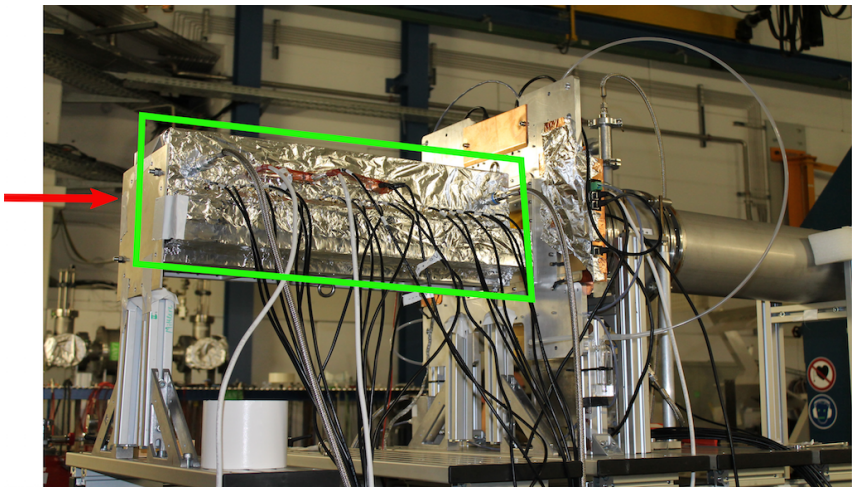

FIGURE 3.4: *Picture of the Triple MUSIC. The red arrow indicates the secondary beam coming from the left side. Inside the green quadrilateral is the Triple MUSIC. The silver wrapping is the Aluminum foil used to form a Faraday cage enclosing the detector to avoid the electromagnetic interference generated by electronic devices in the surrounding. The foil is led to the ground potential.*

In this subsection, general aspects of the Triple MUSIC as a typical MUSIC detector are first described, then specifics of the Triple MUSIC are introduced.

3.1.3.1 General aspects as a MUSIC detector

The Triple MUSIC is composed of a gas-filled chamber with two parallel planes separated by 83 mm. One plane is set on negative high voltage, acting as cathode; while the other plane with positive voltage is served as anode. A frisch grid is inserted between two planes with a distance of 3 mm to the anode.

When an ion passes through the chamber, it ionizes the gas into ions and electrons. The electrons then drift rapidly towards the anode plane, inducing a signal there. The signal is read out by different electric modules and two pieces of information are extracted: the energy deposited by the ion in the gas and the drift time of the electrons reaching the anode.

As mentioned before, the ion's energy loss is proportional to the square of its ionic charge. If the thickness of the gas volume is small, no collision with the gas atoms will occur on the ions' path throughout the gas, and thus the ions' initial charge state will be kept along the path, resulting in well separated energy signals corresponding to various charge states. On the

contrary, in the case with thicker gas, the energy loss signal is broaden because of charge state changes within the volume.

However, with thinner gas, another effect which also deteriorates the energy loss resolution becomes to dominate. It is known that ions' energy deposited in the gaseous material also varies with the kinetic energy. Since in our experiment, secondary beam ions are at relativistic energies and with high charge numbers, a large amount of energy is transferred to the medium, producing a number of so-called delta electrons, which have sufficient energy to induce ionization of more gas atoms. The creation of delta electrons distorts the energy loss spectrum from symmetric Gaussian distribution to Landau distribution with a tail towards high energies. In thinner gas, collisions between ions and material atoms are fewer, resulting in a larger fluctuation in the energy transfer, and thus a more obvious distortion in the energy loss distribution [47]. In another word, the relative resolution of the energy loss is degraded with thinner gas.

Therefore, in order to obtain a satisfactory resolution of the energy loss measurement, the thickness of the gas volume is a trade-off decision between not too thick to undergo too many charge exchange collisions and not too thin to induce large fluctuation in the energy transfer.

3.1.3.2 Specifics of the Triple MUSIC

Since the secondary beam has a relativistic energy, its ions are mostly fully stripped, resulting in the ionic charge equal to the product of the nuclear charge and the elementary charge (*i.e.* $Q = Z \times e$). Thus, the nuclear charge of the secondary beam can be directly extracted from the energy loss. However, some ions are non-fully stripped, leading to $Q \neq Z \times e$. In such a case, the nuclear charge will be wrongly computed by a few units.

Because the probability that ions are non-fully stripped in several measurements is considerably reduced as compared to a single measurement, the anode plane of the Triple MUSIC is divided into 3 identical sections to perform energy loss measurements three times, and finally to enhance the possibility of correctly deriving the nuclear charge.

Figure 3.5 is a sketch of the side view of the Triple MUSIC. It is seen that the anode plane is cut into 3 sections and a Niobium foil is perpendicularly inserted between every two parts. Each section of the plane is segmented into three successive pairs of trapezoidal shaped anodes, sandwiched by two rectangular screening anodes. Every pair consists of two complementary anodes, forming a shape of rectangle. On each effective anode (*i.e.* trapezoidal shaped anode), an energy loss and a drift time are measured.

The point of segmenting the anode plane into a number of anodes is to compute the horizontal angle of the ion's flight path. As mentioned above, the drift time of the electrons arriving at each anode is measured. After knowing the drift velocity, it is straightforward to obtain the distance between the creation point of the electrons and the anode plane. By selecting a reference plane, the ion's horizontal position is then given. Since there are several effective anodes, a series of X positions along the ion's flight path is acquired. Finally, in combination with the distance between anodes, the horizontal angle of the ion's trajectory is computed. Figure 3.6 is a sketch of the top view of the Triple MUSIC and the ion's trajectory is schematically presented.

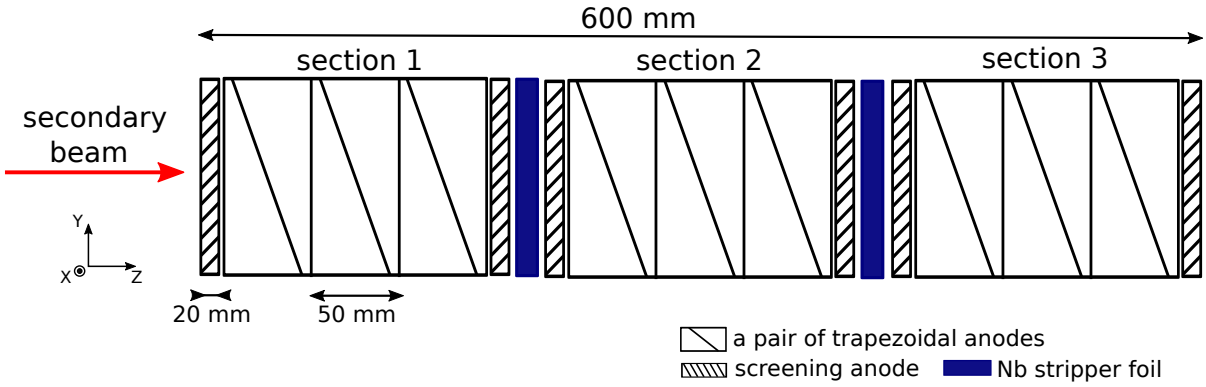

FIGURE 3.5: *Sketch of the side view of the Triple MUSIC.*

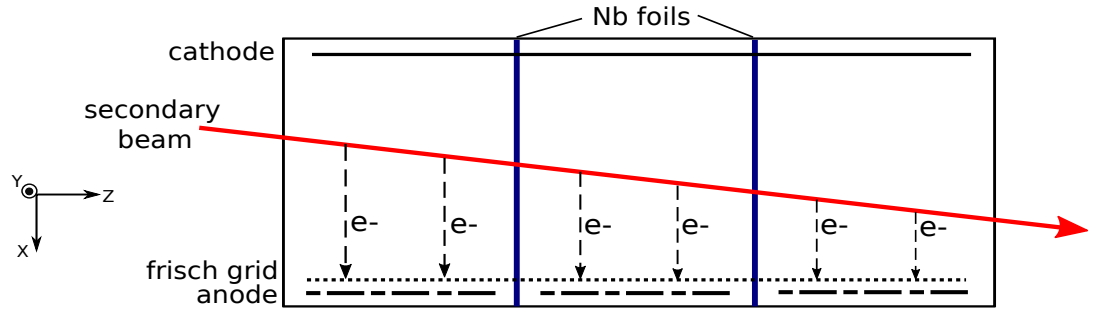

FIGURE 3.6: *Sketch of the top view of the Triple MUSIC.*

It is noticed that each anode is specially designed into a trapezoidal shape rather than a common rectangular shape. By doing this, both the ion's vertical positions and the vertical angle of the trajectory can be obtained: because of the trapezoidal shape, the width of the anode is gradually varied along the Y axis, resulting in the energy loss measured on each anode dependent on the ion's vertical position. Thus, the difference of the energy loss between two complementary anodes in one pair is a signature of the ion's Y position. Since the anode plane is segmented into 9 pairs, a set of Y positions is given. Eventually, combining with the distance between every two pairs, the vertical angle of the ion's flight path can be acquired.

Gas	30% CH_4, 15% CF_4, 15% He, 40% Ar
Pressure	1.02 bar
Voltage of anodes	+650 V
Voltage of cathode plane	-2600 V
Voltage of Frisch grid	+230 V
Distance between cathode and Frisch grid	80 mm
Distance between Frisch grid and anodes	3 mm
External volume	$200 \times 200 \times 600$ mm^3
Strippers	80 μm Niobium

TABLE 3.1: *Technical information of the Triple MUSIC.*

The Triple MUSIC is a triple ionization chamber, which consists of a cathode plane and an anode plane separated by a volume of mixed gases. A frisch grid is inserted between two electrode planes and placed very close to the anode. The anode plane is segmented into 3 sections of 3 pairs of trapezoidal shaped anodes. An energy loss and a drift time are measured on each anode.

By using a combination of 3 independent energy loss measurements, the possibility of deriving the nuclear charge of the secondary beam correctly is enhanced. Besides, benefiting from the fact that the anodes are designed with a trapezoidal shape, the vertical angle of the ion's flight path can be also obtained from the energy loss measurements. In addition, the horizontal angle of the trajectory is computed as well in the Triple MUSIC, through drift time measurements.

3.1.4 Scintillation detectors

The time of flight of the secondary beam is measured by two scintillation detectors, which are separated by about 135 m. The one standing at the central focal plane of the FRS is labeled as the START detector, while the other one standing in the front of the Cave C is labeled as the STOP SB detector. Indeed, the latter is also served as the start detector for the time of flight measurement of both fission fragments.

Each scintillation detector is composed of two PMTs and a plastic scintillator in the middle. Both ends of the plastic slat are connected to PMTs via optical grease. Since the START detector standing at S2 has to stand very high counting rate, special PMTs have been developed accordingly. Their performance under extreme counting rate will be discussed in details in subsection 3.2.5.

A picture of the STOP IB detector is given in figure 3.7. The START detector has the same structure but with a plastic scintillator of different dimensions. The technical information of two detectors is presented in table 3.2.

The ToF system, including these two scintillation detectors and a ToF wall detector at the end of the setup, is built at CEA Bruyères-le-Châtel, France.

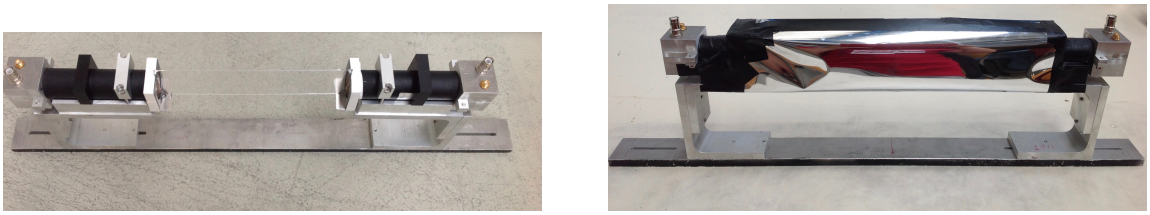

FIGURE 3.7: *Pictures of the STOP IB detector for the time-of-flight measurement of the secondary beam. It is composed of a plastic scintillator and two PMTs. The detector is wrapped by mylar foils, to prevent the disturbance of the light in the environment, as seen in the picture on the right of the figure.*

When radioactive ions penetrate the plastic scintillator, some atoms of the matter are excited, and then de-excite by emitting photons. These photons enter the photo-multiplier tubes coupled to the plastic slat, inducing the photoelectric effect and resulting in the production of a number of electrons. Next, the electrons are multiplied and accelerated by the internal electric field, resulting in a detectable current pulse, which is finally analyzed in an electronic device to timestamp the strike of the ions on the plastic.

In this way, the incident time of the ions given by the PMT on one side depends on the relative position of the striking point on the plastic. The closer the incident position to the PMT, the earlier the determined time of strike. Thus, the plastic scintillator is equipped with two PMTs, one at each end, to cancel the influence of the ions' incident position. In the end, the average value of the time given by each side is taken as the ions' arrival time on the plastic.

Since the time determined by one side relies on the distance between the ions' striking point and the end of the plastic on this side, the time difference between signals from two sides can be used to calibrate the plastic and finally extract the ions' incident position. In other

words, the scintillation detector can also provide position measurements. In our experiment, to fulfill the identification of the secondary beam, the START detector is indeed used for position measurements.

START	
Plastic scintillator	EJ228, not quenched
Plastic dimensions	$220 \times 50 \times 1$ mm^3
Photo-multiplier tubes	Hamamatsu 10580, modified for high counting rate

STOP IB	
Plastic scintillator	EJ232, quenched
Plastic dimensions	$50 \times 32 \times 1$ mm^3
Photo-multiplier tubes	Hamamatsu 6533

TABLE 3.2: *Technical information of scintillation detectors.*

The time of flight of the secondary beam is measured by two scintillation detectors separated by about 135 meters. Each detector is constructed by one plastic scintillator and two photo-multiplier tubes, with the configuration that each end of the plastic is coupled to a PMT. This detector is used not only for recording the time, but also for performing position measurements.

3.1.5 MWPC

In our experiment, position measurements are mainly performed by Multi-Wire Proportional Chambers. The first effective MWPC was built by Charpak and collaborators in 1960s [48] . For the SOFIA experiment, two small MWPCs (200 mm $\times$ 200 mm) and a large one (900 mm $\times$ 600 mm) were designed and constructed at IPN Orsay. Based on the order of their appearance in the setup along the beam direction, three MWPCs are labeled as MWPC0, MWPC1 and MWPC2 accordingly. The MWPC0 standing between the Triple MUSIC and the STOP IB detector, as seen in figure 3.1, is applied for position measurements of the secondary beam; while MWPC1 and MWPC2 downstream the Active Target in which fission occurs, are dedicated to fission fragments. A picture of two little MWPCs is given in figure 3.8 and the technical information is shown in table 3.3.

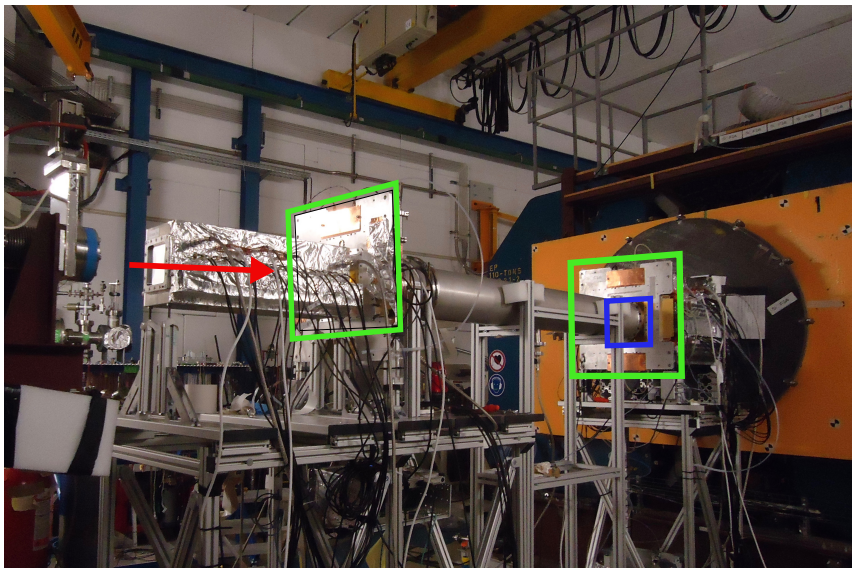

FIGURE 3.8: *Picture of the MWPC0 and MWPC1. The red arrow indicates the beam coming from the left side. Inside the green quadrilaterals are two little MWPCs. The left one (MWPC0) is dedicated for position measurements of the secondary beam, while the right one (MWPC1) is used for that of fission fragments. The blue square presents the active area of the MWPC1.*

Each MWPC is composed of a plane of wires, sandwiched by two foil planes, one segmented horizontally and the other segmented vertically. The wires are placed in parallel and separated by the same distance, on the central plane of two foils perpendicular to the incoming beam. A schematic view of the MWPC is prsented in figure 3.9a .

The wires are set to a high voltage, acting as anodes, while two foils are led to ground potential and serve as cathodes. A non-uniform electric field is formed between anode wires and cathode planes, as shown in figure 3.9b.

The chamber is filled with a mixture of gas. When an ion passes through the MWPC, it ionizes the gas into ions and electrons. Due to the internal electric field, the electrons drift towards anode wires. They are accelerated along the drifting path, and may ionize the gas further. Since the electric field near the anode wires has a $1/r$ dependence (r is the radial

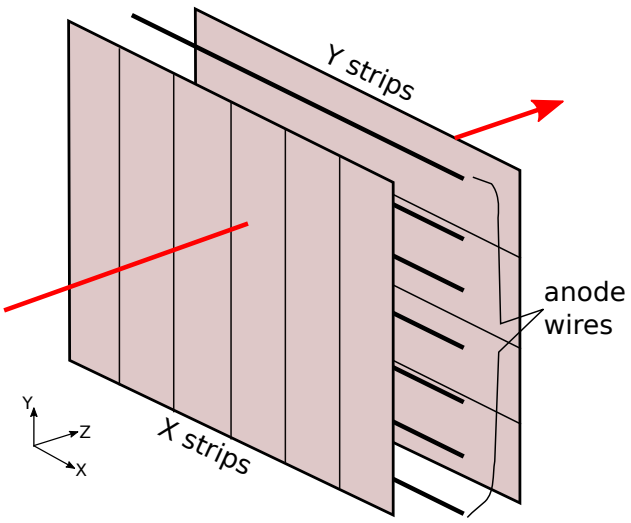

(a) *Sketch of MWPC0*

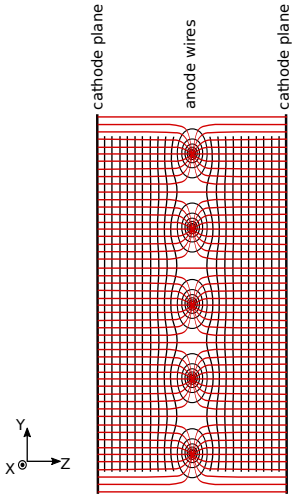

(b) *Electric field lines and equipotentials in a MWPC*

FIGURE 3.9: *Structure of a MWPC and the internal electric field. Left: sketch of the MWPC0 detector. It is composed of a plane of anode wires, sandwiched by two cathode foils. The wires are placed horizontally and two cathodes are segmented vertically and horizontally to measure positions in the X and Y direction, respectively. The red arrow represents the flight path of the secondary beam. Right: Schematic view of the electric field between anode wires and cathode planes. Red lines are electric field lines and black lines represent equipotentials. The right part of this figure is developed on the basis of a figure from [49].*

distance to the anode wire) [50], implying a rapid increase in the field towards the anodes, the electrons entering the very vicinity of wires are significantly accelerated and easily ionize the gas into secondary electrons. This process can be repeated and an avalanche of ions and electrons occurs. Finally, all the electrons are rapidly absorbed by the wires and a large quantity of ions are left around, creating a strong electromagnetic influence on both cathodes.

The cathode plates are segmented into strips and the influence spreads on strips according to their distances to the location of avalanche. The closer the strip to the avalanche spot, the stronger the signal induced. Thus, it is possible to localize the ion from the distribution of amplitudes of signals on various strips. The vertical strips provide information on the horizontal position (*i.e.* the X position), while the horizontal strips help to compute the vertical position (*i.e.* the Y position).

With this technique, the resolution of the position measured along the wires is very good. As previously mentioned, the measurement of magnetic rigidity, which is the product of the magnetic field and the ions' trajectory curvature, is needed to deduce the mass number. Since the ions are only deflected by dipoles in the X direction, the curvature is computed from the horizontal displacement. Consequently, the resolution of the mass is affected by the accuracy of the X position measurement, implying that a high resolution of the X position is required. Thus, in our experiment, anode wires in MWPCs are placed horizontally.

However, in the other direction (vertical in our case), the measured position is more dependent on the position of the anode wire over the ion's position, resulting in a relatively low resolution which has the same order of magnitude as the wire spacing.

Common for 3 MWPCs	
Gas	80% Ar, 20% CO_2
Voltage of anodes	1250 V
Voltage of cathodes	Ground
Wire pitch	2.5 mm
Distance between the cathode plane and wires	2.5 mm
Diameter of wires	25 μm
Width of X strips	3.125 mm
Width of Y strips	5 mm

MWPC0, for the secondary beam identification	
Active surface	200 $\times$ 200 mm^2
Number of X strips	64
Number of Y strips	40

TABLE 3.3: *Technical information of MWPCs.*

Three MWPCs are used in the SOFIA setup for position measurements. Each MWPC is composed of two cathode foils and a plane of anode wires in between. The cathodes are segmented into horizontal and vertical strips to measure positions in the Y and X direction, respectively. The resolution of the X position is more demanding than that of the Y position. Since the position resolution is degraded in the direction perpendicular to the wires, they are placed horizontally, *i.e.* along the X axis, to ensure the accuracy of the X position measurement.

A primary beam of ^{238}U at 1AGeV impinges a Beryllium target and fragmentation reactions take place, producing a broad range of radioactive isotopes. These isotopes are then transmitted to the FRS and the nuclide of interest, ^{236}U in our case, is intended to be selected and spatially separated from other created elements. Yet some nuclides with close atomic and mass numbers are also delivered to the end of the FRS. Finally, a secondary beam of all selected ions fly into the Cave C and fissions there. Thus, to acquire the fission fragment distribution of the desired nuclide, it is necessary to identify the fissioning system from the secondary beam event by event.

The complete identification of the secondary beam is achieved on the basis of the ΔE - Bρ - ToF technique. The energy loss measurement is performed by the Triple MUSIC. In this detector, the horizontal angle of the ion's flight path is also given. In combination with positions measured in a small MWPC and the START scintillation detector, the ion's deflection radius in the FRS can be then computed, and thus the magnetic rigidity is obtained. In addition, the ToF measurement is performed between the START and the STOP IB detectors.

The next section is focused on the analysis based on aforementioned measurements. The procedure leading to the full identification of the secondary beam is presented.

3.2 Analysis

3.2.1 Velocity

The velocity of the secondary beam is extracted from the time-of-flight measurement, which is performed between the START detector at S2 and the STOP IB detector in the front of the Cave C. Actually, the difference of times measured by these two scintillation detectors is the raw time of flight, which needs a calibration prior to being used to compute the velocity.

The calibration process is accomplished by using four primary beam runs with different combinations of materials along the center line of the beam. Since the primary beam deposits different amounts of energy after penetrating different materials, it undergoes various velocities over a fixed trajectory length in four runs, which permits to calibrate the time of flight.

The length of the flight path is computed as:

$$LoF = v \times (ToF_{raw} - \Delta ToF)$$

which leads to:

$$ToF_{raw} = LoF \times \frac{1}{v} + \Delta ToF$$

where v is the overall velocity along the length of flight, ToF_{raw} is the raw value of time of flight and ΔToF is its offset as compared to the real time of flight.

In each run, a raw time of flight (ToF_{raw}) is given by the time difference between measurements in two separated scintillation detectors, and a velocity (v) is computed via the LISE++ simulation [51]. Thus, four points of ($\frac{1}{v}$, ToF_{raw}) are obtained in total, as seen in figure 3.10. By applying a linear fit on these points, the trajectory length (LoF) and the offset of the ToF measurement (ΔToF) can be then directly obtained from the coefficients of the fit function, leading to a calibration of the length of flight and of the time of flight. Finally, the ion's velocity can be extracted on an event-by-event basis.

Various combinations of materials applied in four runs are detailed in table 3.4. The stripper is placed at the entrance of the FRS, while the degrader stands right before the center focal plane S2.

Calibration #	Target [mg/cm^2]	Stripper [mg/cm^2]	Degrader [mg/cm^2]
1	\	\	\
2	\	\	Aluminum, 2200
3	Beryllium, 1036	Niobium, 223	Aluminum, 2200
4	Beryllium, 1036	Niobium, 223	Aluminum, 3200

TABLE 3.4: *Combinations of materials applied in four calibration runs*

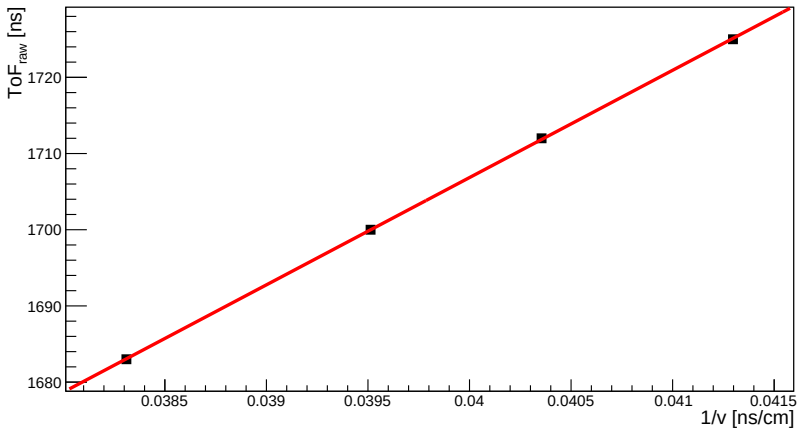

FIGURE 3.10: *Raw time of flight between S2 and Cave C vs. the inverse of the velocity obtained from the simulation in LISE++, for the primary beam. Each point corresponds to one calibration run. The red line represents the linear function used to fit the points.*

3.2.2 Nuclear charge

The nuclear charge of the secondary beam is extracted from energy loss measurements in the Triple MUSIC. The complete procedure consists of 4 steps. First, gains of the energy signal in all anodes are aligned to prepare energy loss measurements for further use. Second, corrections of energy loss dependences in each section are performed. Then, an optimized energy loss is determined by the combination of corrected energy loss measurements in 3 sections. Finally, with its correlation to the energy loss, the spectrum of the nuclear charge is obtained.

3.2.2.1 Alignment of gains of all anodes

Each anode collects a part of the electrons stripped from the gas by the passing projectile, inducing an energy loss measurement. To determine an overall energy loss from all these measurements, an alignment of gains of the energy signal in each anode is required. The alignment of all anodes is achieved in 2 steps: first, the alignment of two complementary anodes in a pair; and then, the alignment of 9 pairs.

As mentioned earlier, each pair composed of two complementarily shaped anodes has a rectangular appearance, which means its width is uniform along the Y axis. Therefore, if gains of two anodes are already aligned, the sum of weighted energy losses in a pair should stay the same whatsoever the ion's Y position. In another word, after setting the gain of one anode as 1, the gain of the other anode has the value which permits the sum of weighted energy signals to be independent on the Y position.

Y position

When an ion passes through a gas-filled chamber, the gas atoms are ionized. The produced electrons then drift perpendicularly towards the anodes. So the amount of electrons collected by an anode is directly proportional to the width of the anode at the incident ion's position.

Therefore, in combination with the geometrical correlation between the anode's width and the Y position, the energy loss measured in various anodes, which is proportional to the amount of collected electrons, can lead to the determination of the ion's Y position.

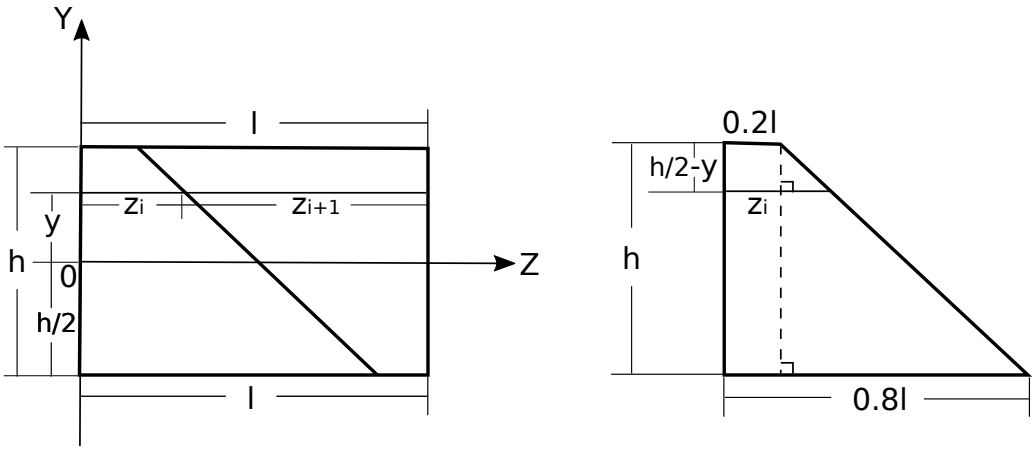

FIGURE 3.11: *Geometric sketch of anodes. Left: sketch of a pair of anodes. Right: sketch of an anode.*

The geometry of a trapezoidal shaped anode is shown on the right of figure 3.11. According to properties of two similar triangles, it is given that:

$$\frac{z_i - \frac{1}{5}l}{\frac{3}{5}l} = \frac{\frac{1}{2}h - y}{h}$$

where y is the ion's vertical position and the reference is set as y = 0 on the centerline of the anode's height, z_i is the width of the anode i at position y, l is the total width of a pair of anodes, and h is the height of an anode: h = 85 mm.

This leads to

$$z_i = \frac{1}{5}l + \frac{3}{5}l \times \left(\frac{1}{2} - \frac{y}{h}\right)$$

Similarly, the width of the anode i+1 at position y is that

$$z_{i+1} = \frac{1}{5}l + \frac{3}{5}l \times \left(\frac{1}{2} + \frac{y}{h}\right)$$

It is then straightforward to infer

$$z_{i+1} - z_i = \frac{6}{5}l \times \frac{y}{h}$$
$$z_{i+1} + z_i = l$$

Next, the ion's vertical position is expressed as:

$$y = \frac{5}{6}h \times \frac{z_{i+1} - z_i}{z_{i+1} + z_i}$$

Since $E_i \propto z_i$, the ion's Y position is finally calculated as:

$$\begin{aligned} y &= \frac{5}{6}h \times \frac{E_{i+1} - E_i}{E_{i+1} + E_i} \\ &= 70.8 \times \frac{E_{i+1} - E_i}{E_{i+1} + E_i} \quad [mm] \end{aligned}$$

where E_i and E_{i+1} are the ion's weighted (*i.e.* with consideration of gains of the amplifiers) energy losses in the anode i and i+1, respectively.

The mean value of the ion's vertical position given by each of the three pairs in section 2 is plotted against that in section 1, as shown in figure 3.12. The resolution of the Y position measured per section is about 1 mm at 1σ.

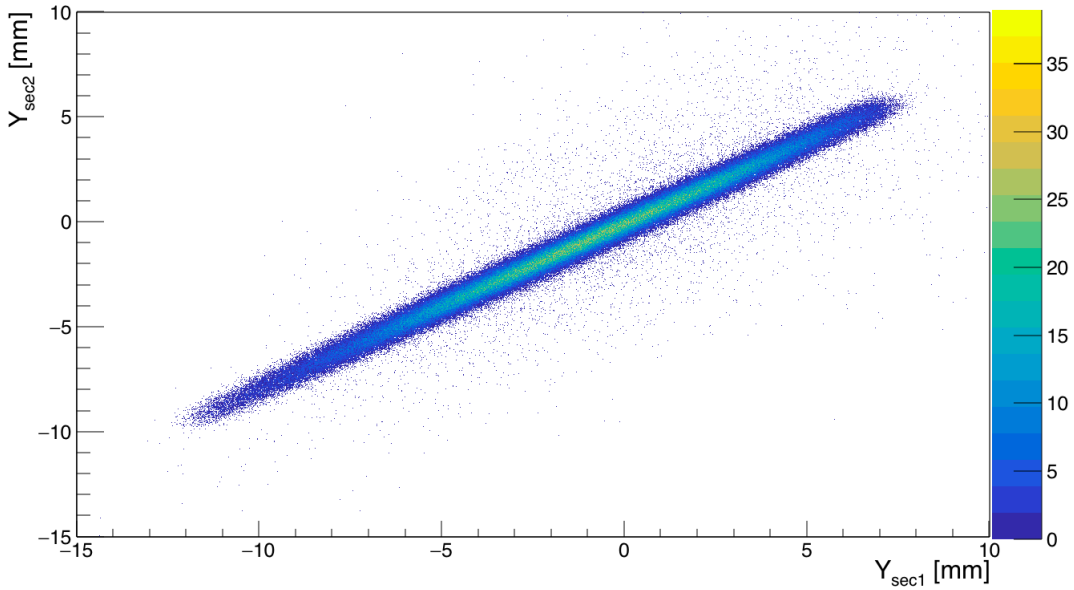

FIGURE 3.12: *Correlation between the average vertical position in section 2 and that in section 1.*

Alignment of gains in a pair

The energy loss increases monotonically with the increasing nuclear charge. To identify a nuclear charge unambiguously, what matters is not the absolute magnitude of the corresponding energy loss, but the relative value as compared to that of other nuclear charges. Therefore, the scaling on energy losses can be canceled by adjusting coefficients of their correlation. In another word, as long as energy signals are scaled in the same way, the nuclear charges can still be obtained correctly.

Thus, instead of calculating both gains to align anodes in a pair, the gain of one anode is regarded as 1 and only the relative gain of the other anode is calculated for simplification. With the properly calculated gain, the sum of weighted energy losses should be independent on the ion's Y position.

The alignment mainly consists of two steps:

1. In each pair, the anodes are numbered as 2i and 2i+1, where i is the number of the pair and i = 0, 1, . . . , 8. For $\forall$ i, anode 2i+1 is chosen as reference and its gain (a_{2i+1}) is set as 1, while a_{2i} is given by several values varying in a small range centered at 1. For each value, E_{2i+1} + $a_{2i} \times E_{2i}$ is calculated versus y = 70.8 $\times \frac{E_{2i+1}-a_{2i}\times E_{2i}}{E_{2i+1}+a_{2i}\times E_{2i}}$ event by event. Their correlation is plotted on the left of figure 3.13, in which a_{2i} = 1 (*i.e.* gains of anodes not aligned yet) is taken as an example. Then this correlation is fitted by a linear function and the slope is computed.
2. Until now, a set of (slope, a_{2i}) points is obtained for each pair. The value of a_{2i} corresponding to slope = 0, which is the relative gain of anode 2i we are looking for, can be then extrapolated from the fit of these points. Finally, with this value, the sum of weighted energy losses is independent of the ion's Y position, which can be verified by plotting and fitting the correlation between E_{2i+1} + $a_{2i} \times E_{2i}$ and y, as seen on the right of figure 3.13.

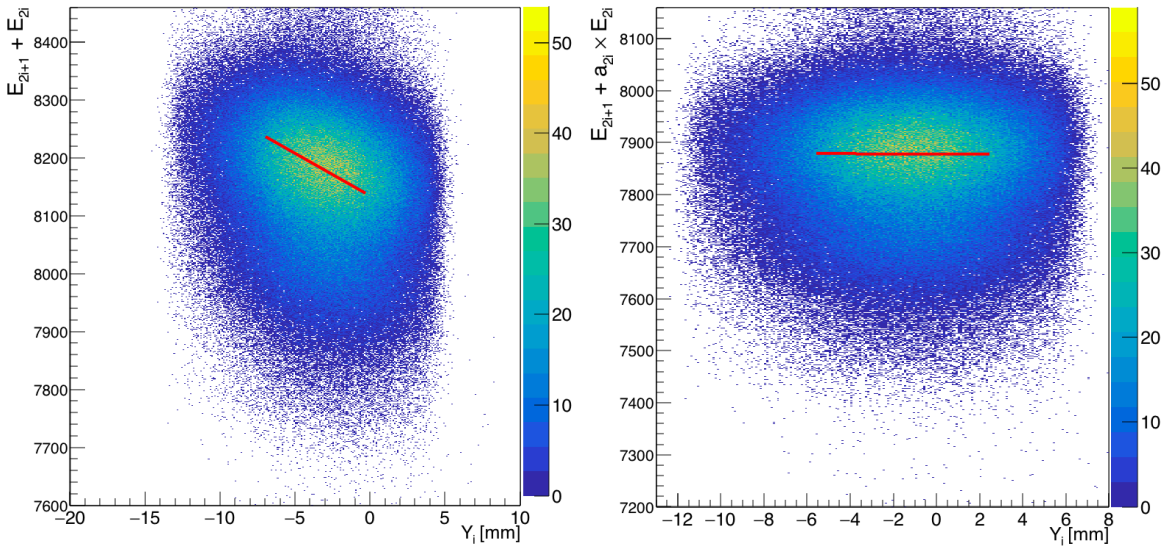

FIGURE 3.13: *Sum of energy losses in a pair vs. ion's Y position in the Triple MUSIC. The red line represents the linear fit. Left: the correlation is shown without taking gains of anodes into account. Right: the gain of one anode is set as 1 and the relative gain of the other anode in the pair is properly calculated. The correlation is shown with energy losses weighted by gains.*

Alignment of gains of pairs

In the previous part, a relative gain is calculated for each pair based on the correlation of energy loss measurements in its two anodes. To fulfill the alignment of all anodes, gains of pairs still need to be aligned. Since the rectangular pair of anodes has the same width, the weighted energy signal given by each pair should be the same. Consequently, the gain of one pair is defined as the ratio of the reference energy to the sum of energy losses measured in two anodes of this pair: $b_i = \frac{E_{ref}}{E_{sum,i}}$, where i is the number of the pair and i = 0, 1, . . . , 8. Finally, with these gains, weighted energy losses measured in all pairs are well aligned, as seen in figure 3.14.

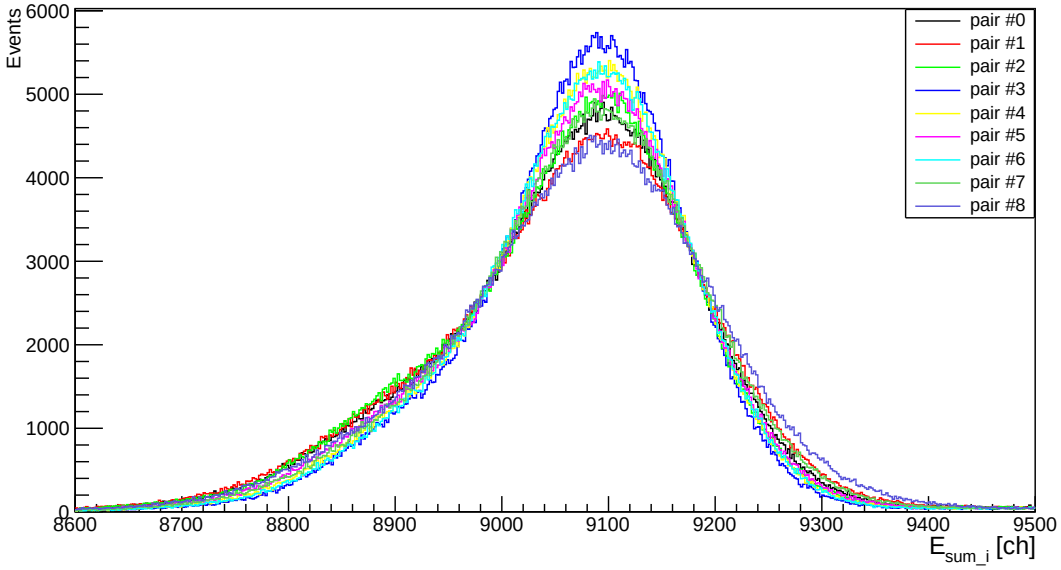

FIGURE 3.14: *Spectra of aligned energy losses, for all pairs of the Triple MUSIC.*

3.2.2.2 Corrections of energy loss per section

The Triple MUSIC contains three successive sections, which are separated by a Niobium foil between every two sections. In each section, the energy loss of the secondary beam is computed as the sum of energy losses measured in three pairs of effective anodes.

Corrections of its dependences on several parameters are applied to reach the best resolution of the energy loss measurement. Two main dependences on the velocity and the drift time are corrected first, and then the minor correction of the horizontal angle is implemented. Corrections of the energy loss in different sections are performed separately.

Velocity

As mentioned before, the amount of the ion's energy deposited in a material for a certain depth depends on its initial kinetic energy. The higher the kinetic energy, the lower the energy loss. This dependence can be corrected by adjusting the correlation between the energy loss and the velocity.

Since the energy loss also depends largely on the drift time, in order to obtain a clear correlation to the velocity, the influence of the drift time has to be minimized. Consequently, only events in which the drift time falls in a reasonably small range are selected. As seen on the left of figure 3.15, a selection of about 20 ns is made on the drift time in a central anode and it is centered at the most probable drift time to ensure statistics.

After limiting the drift time, the correlation showing that the energy loss decreases with the increasing velocity is plotted on the right of figure 3.15.

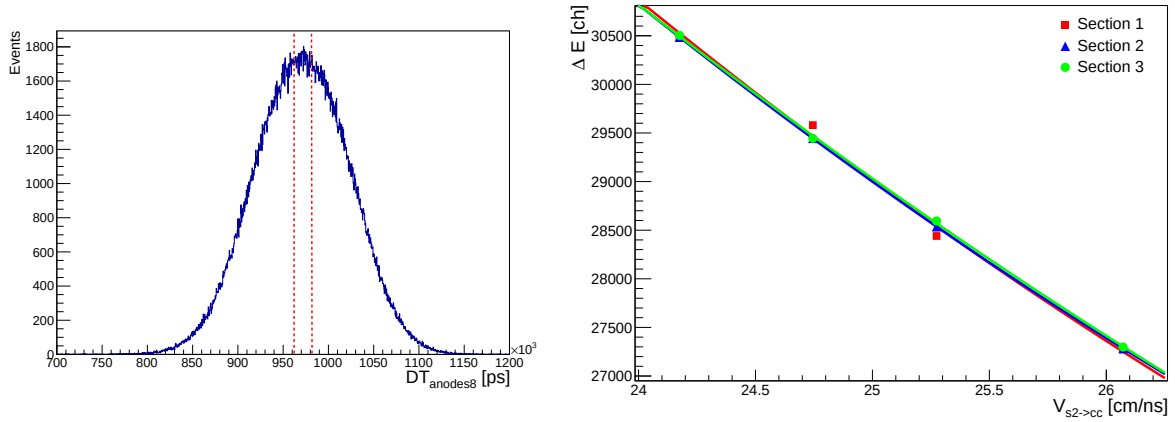

FIGURE 3.15: *Selection on the drift time and correlations between the energy loss and the velocity for 3 sections in the Triple MUSIC. Left: a drift time selection of about 20 ns is made on anode 8. Right: energy loss vs. velocity for 3 sections. For a certain section, four points are corresponding to four calibration runs. A polynomial fit is applied on these points and it is represented by a line with the same color as the signs of the points.*

Drift time

The energy loss is extracted from the signal induced upon the arrival of electrons on the anodes. Along the drifting path, a fraction of electrons are absorbed in the gas. For a certain amount of deposited energy, the longer the drift time towards the anodes, the larger the quantity of absorbed electrons, and thus the smaller the measured energy loss.

The correlation between the energy loss in one section and the drift time is plotted in figure 3.16. Different bands are corresponding to different nuclear charges. Since this dependence is the same for all isotopes, the polynomial fit is first acquired on the basis of one band which covers the largest range, and then applied to correct all data.

Horizontal angle

The energy loss measured in one anode is not the energy deposited in the gas over a fixed length of the anode's width, but that over a distance varying with the horizontal angle of the ion's trajectory. Therefore, the energy loss also depends on the horizontal angle.

The calculation of the horizontal angle is implemented under the assumption that the positioning of detectors is perfect. However, in reality, detectors can be slightly tilted as compared to the planned positioning, making the correlation between the measured energy loss and the calculated horizontal angle more complicated.

This dependence is demonstrated in figure 3.17. A polynomial function is applied for the correction. Instead of being full calibrated, the horizontal angle is roughly represented by the drift time difference between one of the beginning anodes and one anode near the exit, for simplification.

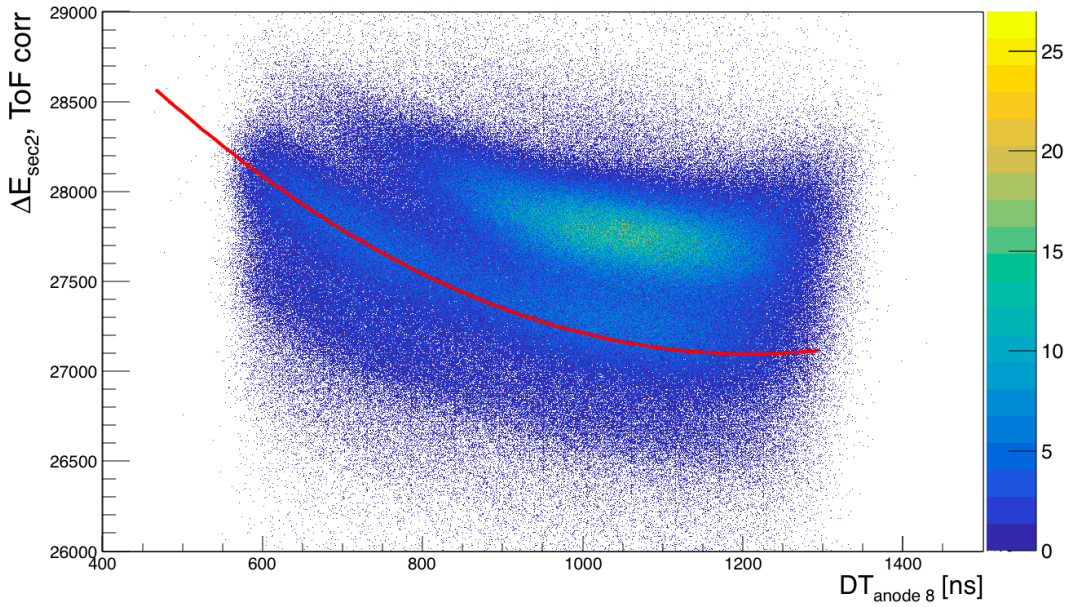

FIGURE 3.16: *Energy loss in section 2 vs. drift time in anode 8. The polynomial fit used to correct the dependence is represented by the red line.*

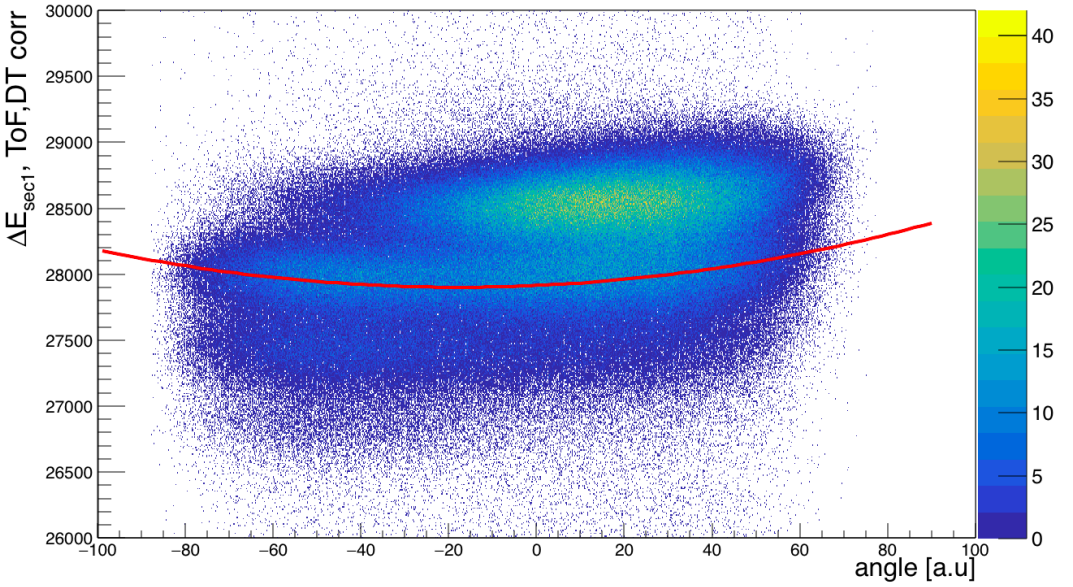

FIGURE 3.17: *Energy loss in section 1 vs. horizontal angle. The angle is simplified as the drift time difference between anode 2 and 14. The polynomial function used for the correction of the dependence is represented by the red line.*

Corrected energy loss per section

Both spectra of the energy loss before and after corrections of all dependences are plotted in figure 3.18. On the spectrum of the corrected energy loss, several peaks appear and each peak corresponds to one element, while the original spectrum of the energy loss has only one blurred peak, showing no capability of separating different elements. Thus, the resolution of the corrected energy loss in each section is significantly improved.

It is noticed that the absolute value of the energy loss is shifted after corrections, which is a result of normalization factors used in the correction procedure, and it depends on the manner how the data are dealt with. But the shift will not affect the identification of elements, because energy losses corresponding to different nuclear charges are scaled in the same way and the influence of the scaling can be easily canceled by adjusting coefficients of the quadratic conversion accordingly.

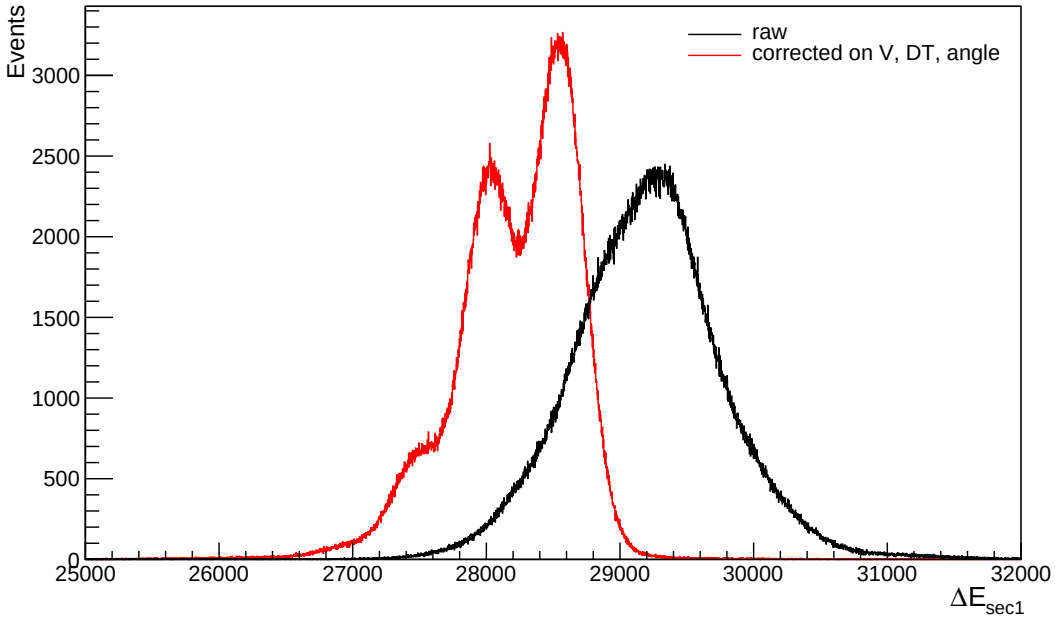

FIGURE 3.18: *Spectra of the energy loss in section 1 of the Triple MUSIC, before and after all corrections.*

3.2.2.3 Combination of corrected energy losses

As previously mentioned, the ion's energy loss measured in an ionization chamber is proportional to the square of its ionic charge Q = q × e = (Z - n_{e^-}) × e, with q, n_{e^-} and e being the ion's charge number, the number of electrons in the ion cloud and the elementary charge, respectively. When an ion penetrates matter, it undergoes charge exchange in collisions with the material atoms. The charge-changing is caused by electron capture (n_{e^-} increases by 1) and electron loss (n_{e^-} decreases by 1) processes.

In figure 3.19, equilibrium charge-state distributions of U, Au and Xe projectiles in the Cu foil are plotted as a function of the projectile energy [52]. In the case of each projectile, it is seen that with increasing projectile energy, the chance to have electrons in the ion cloud (*i.e.* $n_{e^-} \neq 1$) decreases. By comparing three cases, one can conclude that at a given projectile kinetic energy, with the increase of the atomic number of the projectile, more charge states appear and the chance to be non-fully stripped increases.

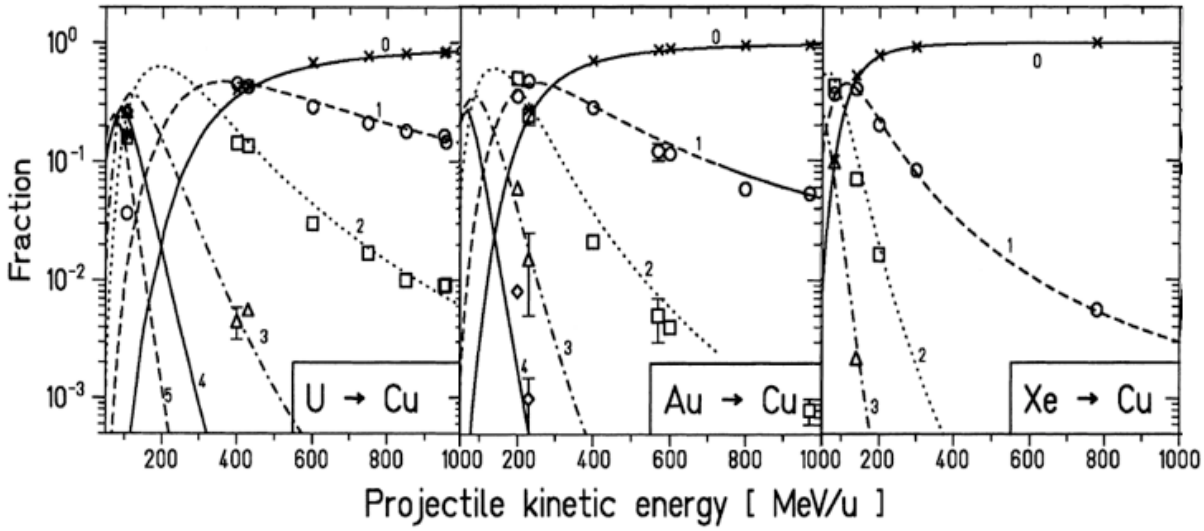

FIGURE 3.19: *Equilibrium charge-state distributions of U, Au, and Xe projectiles in the Cu foil as a function of the projectile energy. Data represented by the curves are from the GLOBAL code. Each curve corresponds to one charge state. The figure is cited from [52].*

It is also noticed that at relativistic energies, the majority of U projectile ions are fully stripped, while the rest can carry up to two electrons in the ion cloud, which is the case of our experiment. Because of the charge state fluctuation, namely the oscillation in n_{e^-}, an extraction of the nuclear charge Z from the energy loss measurement becomes difficult. To solve this problem, two methods can be tried: either to reach the charge state equilibrium or to measure the energy loss of fully stripped ions.

Charge state fluctuations

The fraction of a final charge state q′ of an ion after it goes through a material is determined by five parameters: nuclear charge Z, kinetic energy E, initial charge state q, material species, and

thickness t of the material [53]. If t is large enough, an adequate amount of electron capture and electron loss processes will occur, leading to a statistical charge state equilibrium, in which the final distribution of charge states no longer varies with the initial one. In another word, for a certain material and a known initial energy, as long as t is larger than the minimum thickness to reach the equilibrium, the final charge state distribution solely depends on the nuclear charge Z.

The energy loss of an ion measured in an ionization chamber is $\Delta E \propto \bar{q^2} = \frac{\sum q_i^2 l_i}{\sum l_i}$, where $\bar{q^2}$ is the mean value of the square of ion's charge along the path, l_i is the length of the ith interval between two charge states, and q_i is the ion's charge number on the ith interval until being changed by the next collision. If t is far beyond the minimum thickness, the measured energy loss can be approximated by that in the case of charge state equilibrium, in which the probability of a charge state is only determined by the nuclear charge. Therefore, the energy loss is a unique function of the nuclear charge, which means the latter can be identified from energy loss measurements.

In our experiment, a mixture of gases is used in the ionization chamber and the dominant gas is Ar (45%). According to LISE++, the equilibrium thickness of Ar for ^{236}U projectiles at the initial energy of about 700 AMeV is around 1.6 m. From the above discussion, it is known that the criterion of this method is that the thickness of the material should be much larger than the length at which the charge state equilibrium is achieved. So the ionization chamber should be constructed to a few meters. Considering that the whole experimental area in Cave C is only several meters in depth, this method is not feasible for our experiment.

Results of simulations using the GLOBAL code [52, 54], the CHARGE code [52, 55] and the AMADEUS code [56] for Ar with a thickness of 200 mm (the length of each section of the Triple MUSIC) are presented in table 3.5. It is seen that before reaching the equilibrium, the distribution of final charge states depends largely on the initial one. Besides, it is noticed that results given by the GLOBAL code and the CHARGE code are quite close, while the AMADEUS code shows a general difference of a few percent.

Use of three energy loss measurements, and Nb foils

The nuclear charge can be directly derived from the energy loss only when the ions are fully stripped. In order to enhance the probability of extracting the nuclear charge, three measurements are conducted, since it is more unlikely that ions are non-fully stripped in all measurements, as compared to a single one.

Each section of the Triple MUSIC is preceded by a Niobium foil acting as a stripper. To ensure most ions are fully stripped at the exit of the Niobium foil, no matter what is the charge state distribution at the entrance, the thickness of the foil is selected as around the equilibrium thickness, at which ions reach the charge state equilibrium. In this way, the stripper reboots the ions' initial charge state distribution and prepares most ions to be fully stripped before each measurement. The Niobium material (Z = 41) is chosen because of its high stripping efficiency: at the equilibrium charge state, the fraction of bare ions is relatively higher than that of using

GLOBAL

Entrance charge state	Exit charge state distribution		
	92+	91+	90+
92+	83.9%	15.4%	0.7%
91+	34.3%	60.3%	5.4%
90+	14.5%	47.3%	37.8%

CHARGE

Entrance charge state	Exit charge state distribution		
	92+	91+	90+
92+	84.7%	14.5%	0.8%
91+	33.4%	60.9%	5.7%
90+	15.7%	45.4%	38.9%

AMADEUS

Entrance charge state	Exit charge state distribution		
	92+	91+	90+
92+	87.7%	11.9%	0.4%
91+	28.3%	67.2%	4.5%
90+	9.2%	42.2%	48.6%

TABLE 3.5: *Charge state distribution at the exit of the gas volume in each section of the Triple MUSIC, for different initial charge states. Ions of ^{236}U projectiles are at the energy of 700 AMeV. The gas is 200 mm of Ar. Calculations are conducted by using the GLOBAL code, the CHARGE code and the AMADEUS code.*

many other strippers, as seen in figure 3.20 in which the equilibrium charge-state distribution of the U projectile at different energies is plotted as a function of the atomic number of the stripper foil [52].

In our case, the thickness of the Nb foil is 80 μm. Based on a simulation, the fraction of charge states at the exit of the foil, for different initial charge states, is exhibited in table 3.6. It is observed that with a Nb foil of such thickness, the final charge state distribution is already quite stable whatsoever the charge state at the entrance, implying that ions are very close to the equilibrium charge state.

To verify the gain of using three measurements and Nb strippers, the probability that ions are fully stripped in at least one of the three sections is calculated in a simplified model. As indicated in figure 3.21, fractions of three charge states — 92+, 91+ and 90+, at the entrance of the Triple MUSIC, are labeled as p_{92}, p_{91} and p_{90} respectively. Accordingly, along the beam line, the charge state distribution at the end of each section is recorded as (p'_{92}, p'_{91}, p'_{90}), (p''_{92}, p''_{91}, p''_{90}) and (p'''_{92}, p'''_{91}, p'''_{90}), respectively.

In the model, the gas in each section is simplified as Ar. The charge state at the end of the section is regarded as the one along the path in this section, which means the change of charge

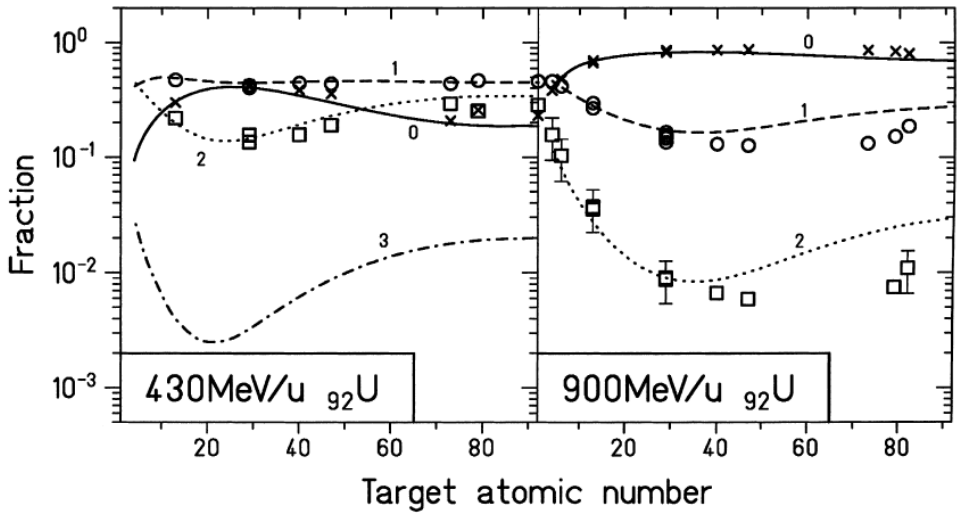

FIGURE 3.20: *Equilibrium charge-state distribution of the U projectile at different energies as a function of the target atomic number. Data corresponding to the curves are from the GLOBAL code, while those represented by the symbols are from the CHARGE code. Each curve and each set of symbols correspond to one charge state. The figure is cited from [52].*

Entrance charge state	Exit charge state distribution		
	92+	91+	90+
92+	74.0%	23.8%	2.2%
91+	69.1%	27.9%	3.0%
90+	64.2%	31.6%	4.2%

TABLE 3.6: *Charge state distribution at the exit of the 80 μm Nb foil preceding each section of the Triple MUSIC, for different initial charge states. Ions of ^{236}U projectiles are at the energy of 700 AMeV. The calculation is conducted with the GLOBAL code.*

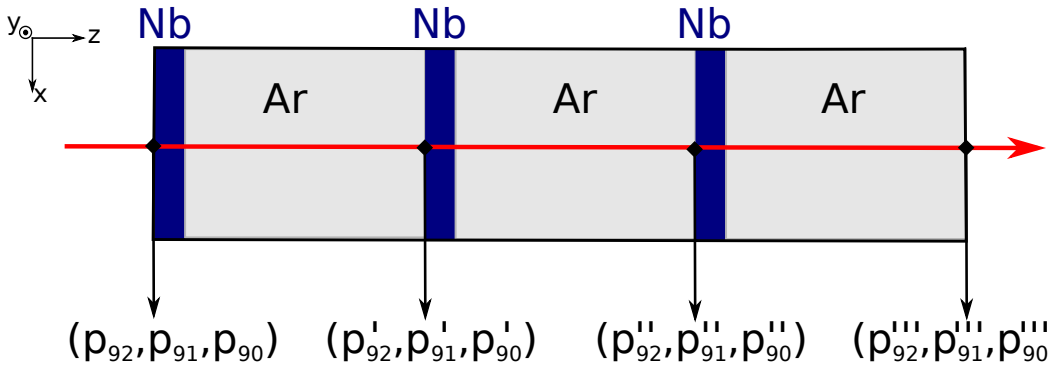

FIGURE 3.21: *Simplified model used for calculating the charge state distribution at the end of each section of the Triple MUSIC. The red arrow indicates that the beam comes from the left.*

states within the section is not considered, even though the final charge state may actually be obtained after a few charge exchanges. Thus, the probability of having bare ions in at least one section is calculated as 1 - (1-p'_{92})(1-p''_{92})(1-p'''_{92}).

For any volume, if the probability of obtaining a charge state at the exit from any charge state at the entrance is taken as one element, all elements make up a 3×3 matrix. Matrices for one Nb foil and a section filled with Ar are labeled as A and B respectively, and their elements are listed in the order as shown in table 3.6 and 3.5 respectively. Then, the charge state distribution at the exit of each section, which can be expressed as an 1×3 matrix, is calculated by the product of several matrices:

$$
\begin{aligned}
P_0 &= (p_{92} \quad p_{91} \quad p_{90}) \\
P_1 &= (p'_{92} \quad p'_{91} \quad p'_{90}) = P_0AB \\
P_2 &= (p''_{92} \quad p''_{91} \quad p''_{90}) = P_0ABAB \\
P_3 &= (p'''_{92} \quad p'''_{91} \quad p'''_{90}) = P_0ABABAB
\end{aligned}
$$

There is a very thick Aluminum degrader at S2, in which ions reach the charge state equilibrium. This equilibrium charge state is served as the starting point of all following probability calculations. The ions then fly through the START detector and several windows, and finally arrive at the Triple MUSIC. After obtaining the probability matrix for each material from simulations, the ions' charge state population at the entrance of the Triple MUSIC P_0 is calculated by the product of these matrices.

With known A, B and P_0, it is straightforward to compute 1 - (1-p'_{92})(1-p''_{92})(1-p'''_{92}). In the case of three sections equipped with 80 μm Nb foils, the probability that ions are fully stripped in at least one section is 97.15%, which is much higher than that in a single measurement: $\sim$ 69%. In this way, the chance of misidentifying the nuclear charge due to the direct extraction from the energy loss measurement is considerably decreased.

To evaluate the effectiveness of the 80 μm Nb foil, behaviors of foils with various thicknesses are compared. Four cases: 40 μm, 80 μm, 160 μm and a thickness (e.g. 350 μm) far beyond the equilibrium thickness are taken into account. Results are presented in table 3.7.

It is shown that with an increasing thickness, the difference of probabilities of having bare ions in at least one of the three measurements is negligible. To understand the situation, another case of a virtual Nb foil of 0 μm is also tested, by assuming that the ion's charge state is the same before and after the Nb layer. According to the model described above, it is calculated that the probability of having fully stripped ions in at least one of the three sections is 96.68%, which is really close to the values of probabilities obtained in other cases. It seems that the Nb stripper is not effective at all, which is opposed to what was observed in our experiment, suggesting that there must be something wrong in the simplified model. Actually, the idea of using the formula 1 - (1-p'_{92})(1-p''_{92})(1-p'''_{92}) to calculate the probability of interest is feasible, but the variables in the formula should be the probabilities of being fully stripped along the path in 3 sections, rather

than those at the end of the sections. Therefore, the model developed here without considering the change of charge states along the path is not valid. In fact, the probability of having bare ions in at least one measurement can only be obtained from full simulations along the path throughout the whole detector.

From the table, it is observed that the nuclear reaction rate increases linearly and the angular straggling also grows steadily. Since the highest angular straggling is just a bit higher than that in the plastic scintillator (0.16 mrad) and much lower as compared to that in the Uranium foil (1.6 mrad) in the Active Target where fission occurs, the value of this parameter is acceptable in all cases of thicknesses. In terms of statistics, the thinnest foil which shows the lowest reaction rate, and thus the least loss of beam intensity is the best option. To conclude, the current Nb foil is not the optimum: it is what was available in the experiment and it already works very effectively.

Thickness of Nb foil	Calculated probability	Reaction rate	Angular straggling
40 μm	97.07%	0.14%	0.21 mrad
80 μm	97.15%	0.27%	0.30 mrad
160 μm	97.17%	0.55%	0.42 mrad
> equilibrium thickness	97.17%	\	\

TABLE 3.7: *Behaviors of Nb foils with various thicknesses. Probabilities are calculated on a basis of simulations in the GLOBAL code. Reaction rates are given by the AMADEUS code, and values of the angular straggling are obtained according to simulations in LISE++.*

Combination of three measurements

As discussed above, ions in the Triple MUSIC are either fully stripped or carrying one or two electrons in the ion cloud. Since bare ions show the highest ionic charge, they transfer more energy to the gaseous medium, as compared to H- and He- like ions. Consequently, the maximum of three measurements is regarded as the energy loss of fully stripped ions, from which the nuclear charge will be directly extracted.

In figure 3.22, the corrected energy loss in the section 2 is plotted against that in the section 1. If energy losses in two sections are identical, like in the area within the graphic cut represented by the black line, their average value is taken; otherwise, the higher value is accepted. Then a comparison between the value taken from the first two measurements and the corrected signal in the section 3 is performed, and the same algorithm is applied to determine the final value.

The spectrum of the energy loss determined by the combination of three measurements is represented by the red line in figure 3.23. It is seen that with further separated peaks, the energy loss resolution is significantly improved, as compared to that of a single measurement (the corrected energy loss in the section 2, whose spectrum is shown by the black line, is taken as an example). Each peak of the energy loss corresponds to one Z value, *i.e.* one element. Data shown here are of all nuclides selected by four FRS settings centered on ^{236}U, ^{207}Fr, ^{194}Bi and

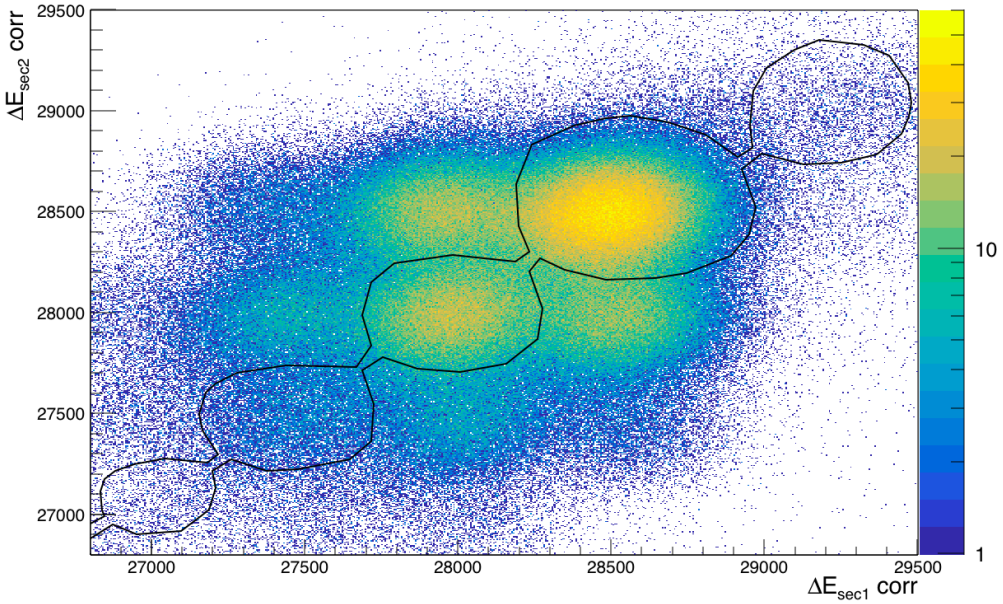

(a) *FRS setting centered on ^{236}U*

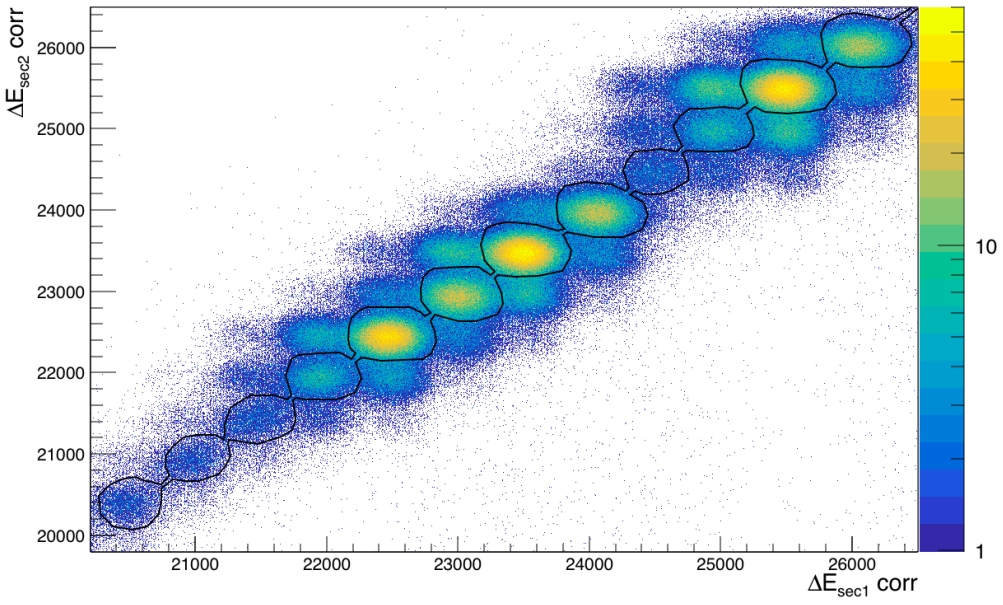

(b) *FRS settings centered on three light nuclei*

FIGURE 3.22: *Corrected energy loss in the section 2 vs. that in the section 1. The black line represents the graphic cut inside which energy losses are identical in two sections. Data of ions selected by FRS settings centered on ^{236}U (top) and some light nuclei (bottom) such as ^{207}Fr, ^{194}Bi and ^{187}Tl are shown.*

^{187}Tl. Since the statistics are quite small in light settings, only about 4% of the data in the ^{236}U setting are used, to make the number of events comparable in all settings, and finally show a spectrum with clear peaks for most elements.

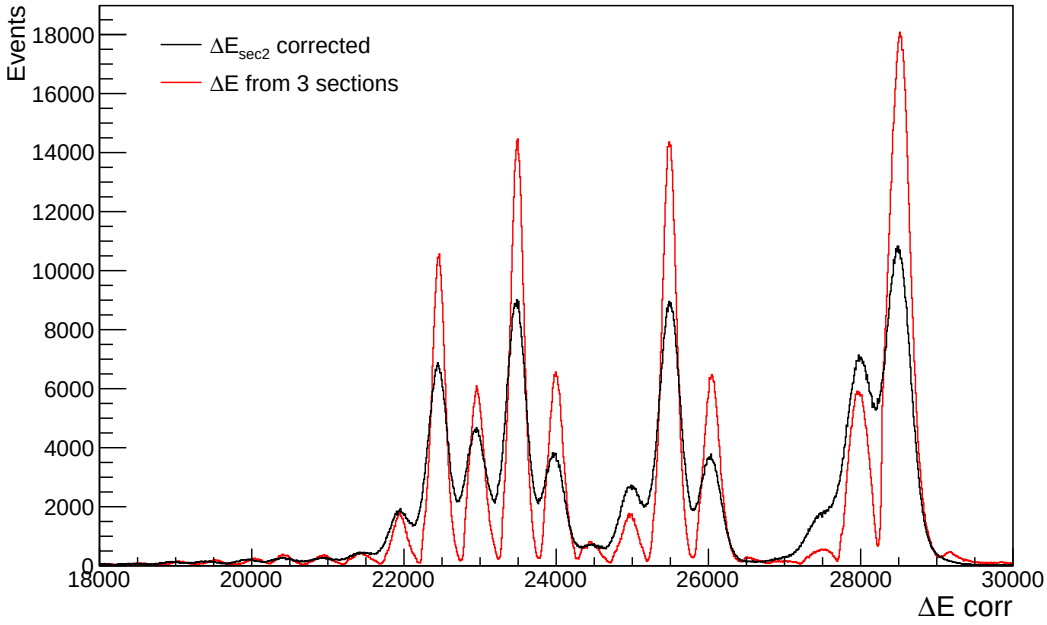

FIGURE 3.23: *Spectrum of the energy loss determined by the combination of three measurements in the Triple MUSIC, comparing to that of the measurement in the section 2. Nuclides selected by all four FRS settings are covered.*

3.2.2.4 Extraction of nuclear charge

The energy spectrum is plotted in the logarithm scale in figure 3.24, to show all peaks, even those with a few statistics, clearly. The most populated peak corresponds to fully stripped ^{236}U ions (nuclear charge 92). Using this peak as a reference, energy peaks corresponding to bare ions of ^{207}Fr (Z = 87), ^{194}Bi (Z = 83) and ^{187}Tl (Z = 81) nuclei, on which three light FRS settings are centered, are easily identified.

From these four peaks, four (Z, ΔE) points are obtained. A polynomial function of order 2 is applied to fit the points, as shown in figure 3.25. Then, for each energy loss given by the Triple MUSIC, the corresponding nuclear charge can be extracted from the quadratic function.

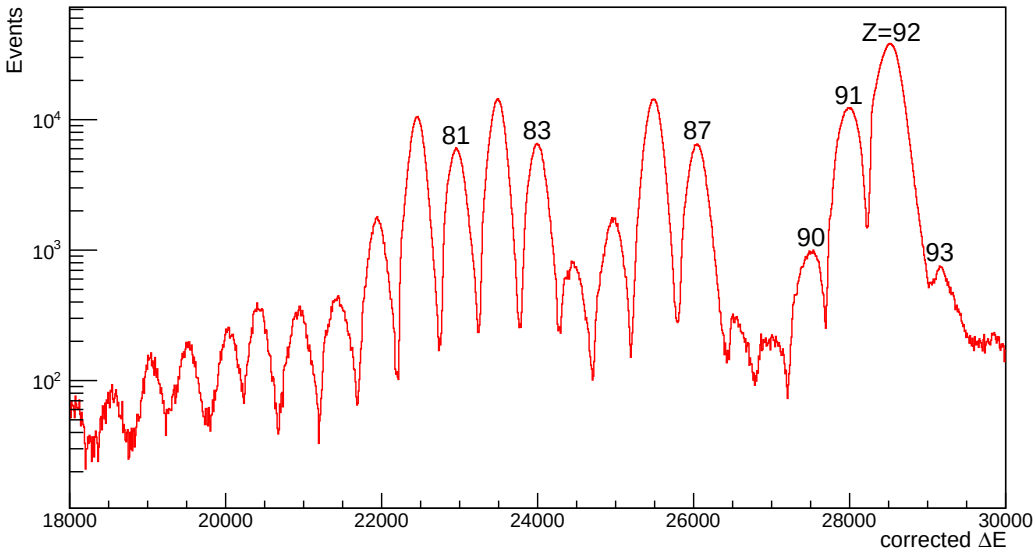

FIGURE 3.24: *Spectrum of the energy loss in the Triple MUSIC of secondary beam ions selected by four FRS settings, shown in the logarithm scale.*

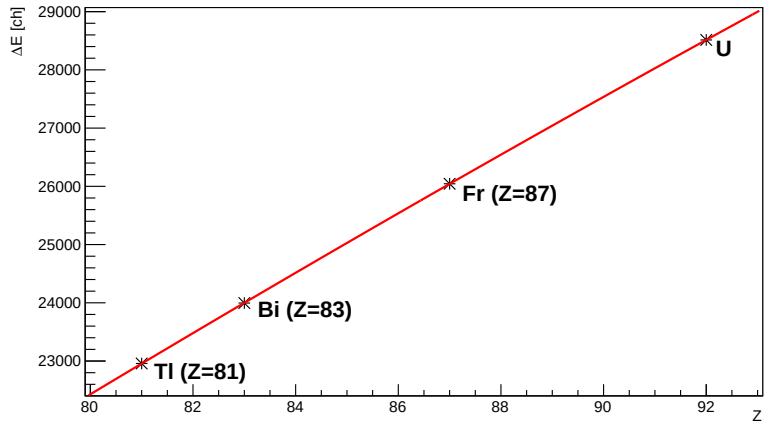

FIGURE 3.25: *Energy loss vs. nuclear charge for secondary beam ions. One point corresponds to one nuclide on which the FRS seting is centered. The red line represents the polynomial function of order 2 used to fit the correlation.*

3.2.3 Mass-over-charge ratio

3.2.3.1 Magnetic rigidity measurement

In the previous part, the identification of the nuclear charge of secondary beam ions has already been achieved. To complete the identification, the mass-over-charge ratio still needs to be computed. According to equation 2.1, A/q $\propto$ Bρ / ($\beta\gamma$). Since velocity terms (*i.e.* $\beta\gamma$) are known from the ToF measurement, the mass-over-charge ratio can be obtained after measuring the magnetic rigidity.

To quantify the position spread due to a variation in the magnetic rigidity, the dispersion D is introduced:

$$D = \frac{\Delta X}{\Delta B\rho} \tag{3.2}$$

with:

ΔX	Distance between the impact position of the ion and that of the reference trajectory
$\Delta B\rho$	Variation in the ion's magnetic rigidity, as compared to the reference value

Literally,

$$\Delta B\rho = \frac{B\rho - (B\rho)_0}{(B\rho)_0} \tag{3.3}$$

where $B\rho$ and $(B\rho)_0$ are magnetic rigidities of the considered ion and the reference one, respectively.

From equation 3.2 and 3.3, the ion's magnetic rigidity measured between S0 and S2 is:

$$B\rho_{S0-S2} = (B\rho_{S0-S2})_0 \times \left(1 + \frac{\Delta X_{S2}}{D_{S0-S2}}\right) \tag{3.4}$$

with:

$(B\rho_{S0-S2})_0$	Magnetic rigidity of the reference ion between S0 and S2
ΔX_{S2}	Distance between the incident position at S2 of the measured ion and that of the reference one
D_{S0-S2}	Dispersion measured between S0 and S2

Between S2 and Cave C, the magnetic rigidity measurement is also performed:

$$B\rho_{S2-CaveC} = (B\rho_{S2-CaveC})_0 \times \left(1 + \frac{\Delta X_{S2}}{D_{S0-S2}} - \frac{\Delta X_{CaveC}}{D_{S2-CaveC}}\right) \tag{3.5}$$

with:

$(B\rho_{S2-CaveC})_0$	Magnetic rigidity of the reference ion between S2 and Cave C
ΔX_{CaveC}	Distance between the incident position at Cave C of the measured ion and that of the reference one
$D_{S2-CaveC}$	Dispersion measured between S2 and Cave C

Since the time-of-flight is measured between S2 and Cave C, the corresponding magnetic rigidity (*i.e.* $B\rho_{S2-CaveC}$) is needed to derive the mass-over-charge ratio. Consequently, position measurements at S2 and Cave C and dispersions in both sections of the FRS are required, according to equation 3.5.

3.2.3.2 Position measurements

As mentioned earlier, the ion's incident position at S2 is measured by the START scintillation detector, while the position at Cave C is obtained by using the MWPC0 detector.

Position measured by the scintillation detector, at S2

The time difference between signals given by two PMTs at both ends is a signature of the ion's impact position on the plastic scintillator. As long as the correlation between the position and the time difference is established, the position measurement can be performed on an event-by-event basis. To acquire the correlation, a pair of Time Projection Chambers (TPCs) downstream the START detector are used, and three position calibration runs are executed. By adjusting the center position of the opening of the slits, ions centered at various positions on the scintillator are transmitted in different runs.

In each run, two horizontal positions are given by the pair of TPCs, one per TPC. With the known distance between TPCs along the beam axis, the horizontal angle of the ions' trajectory is derived. Then, in combination with the distance between the plastic scintillator and one TPC, the horizontal position of the beam spot on the plastic is obtained. Since a time difference is measured by the START detector in each run, three points of (time difference, position) are acquired in total. The correlation is described by a linear function applied to fit the points. Finally, with the time information directly given by the scintillation detector, the position is extrapolated from the linear correlation event by event.

Position measured by the MWPC, at Cave C

As previously stated, in the MWPC detectors, the ion's impact position is derived from the profile of induced signals on cathode strips. Vertical strips are applied to extract the horizontal position, while horizontal strips are used for the vertical position.

The position reconstruction is achieved in two steps:

1. to identify the strip with the maximum signal, which is the closest one to the avalanche spot. Thus, the ion's incident location is supposed to be within the range of this strip.
2. to derive the precise position from the distribution of signals on the identified strip and neighboring strips.

The ion's relative position on the identified strip, which is regarded as the position of the centroid of the distribution of signals, can be reconstructed by various algorithms. A detailed description of several centroid-finding algorithms is given in reference [57]. Generally, there are three categories of methods:

- the center of gravity method, in which the centroid is calculated by weighting the position of each strip with the induced signal. There is no limit on the number of signals.
- the ratio method, which is based on the comparison of ratios of the maximum signal to that on the left- and right- neighboring strip. Namely, this method is developed for using three strips.
- and the use of functions. Since the resolution is degraded when the function is applied to fit the signal distribution on more than three strips, 3-parameter functions, such as the Gaussian function and the hyperbolic secant squared (SECHS) function, are commonly used.

In this paper, the optimum algorithm with the use of the "SECHS" function is applied:

$$Q(x) = \frac{a_1}{cosh^2(\pi(x - a_2)/a_3)}$$

where x is the position of the considered strip, a_1 is an normalization factor, a_2 is the position of the centroid, and a_3 is an indicator of the distribution:

$$a_3 = \frac{\pi\omega}{cosh^{-1}\left(\left(\sqrt{Q_{max}/Q_{left}} + \sqrt{Q_{max}/Q_{right}}\right)/2\right)}$$

with ω being the width of one strip, Q_{max} the maximum signal, Q_{left} the signal on the left neighboring strip, and Q_{right} the signal on the right side.

Then the ion's incident position can be obtained, with the extraction of the center of the distribution:

$$a_2 = \frac{a_3}{\pi} \times tanh^{-1}\left(\frac{\sqrt{Q_{max}/Q_{left}} - \sqrt{Q_{max}/Q_{right}}}{2sinh(\pi\omega/a_3)}\right)$$

3.2.3.3 Dispersions

Equation 3.5 can be expressed as:

$$\frac{B\rho_{S2-CaveC} - (B\rho_{S2-CaveC})_0}{(B\rho_{S2-CaveC})_0} = \frac{\Delta X_{S2}}{D_{S0-S2}} - \frac{\Delta X_{CaveC}}{D_{S2-CaveC}}$$

that is to say:

$$\Delta B\rho_{S2-CaveC} = \frac{\Delta X_{S2}}{D_{S0-S2}} - \frac{\Delta X_{CaveC}}{D_{S2-CaveC}} \tag{3.6}$$

It is calculated from equation 2.1 that $B\rho = 3.107 \times \beta\gamma \times \frac{A}{q}$. Since A and q are known for the ^{238}U primary beam and the value of $\beta\gamma$ is given by the ToF measurement between S2 and Cave C, ions' magnetic rigidity can be computed event by event. Then the variation of the magnetic rigidity as compared to the reference value $(B\rho_{S2-CaveC})_0$ is obtained.

According to equation 3.6, $\Delta B\rho_{S2-CaveC}$ varies with the ion's positions measured at both S2 and Cave C. Since two positions are independent on each other, as seen in figure 3.26, after

limiting one position to a reasonably small range, the variation of the magnetic rigidity becomes a pure function of the other position. Consequently, the corresponding dispersion can be obtained from the slope of their linear correlation.

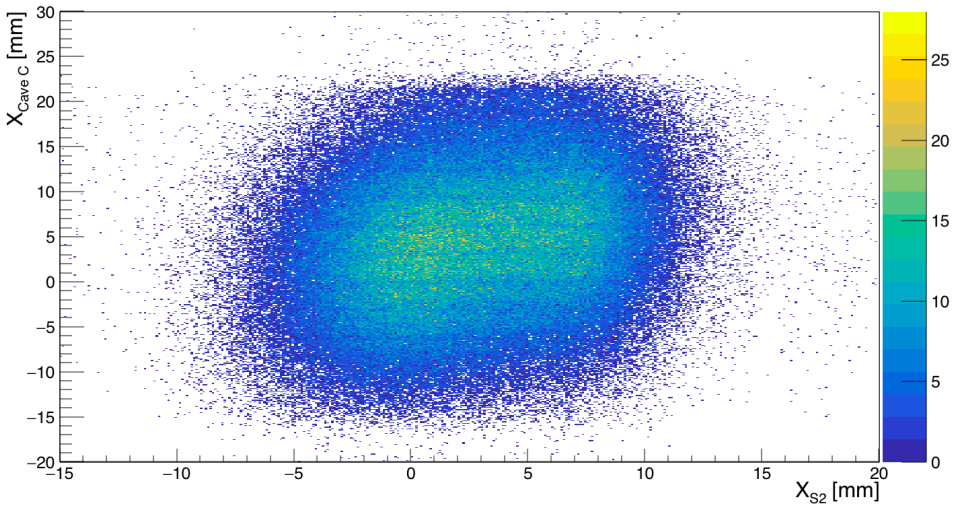

FIGURE 3.26: *Ion's position measured at Cave C vs. that measured at S2.*

Then the ion's mass-over-charge ratio can be measured by:

$$\begin{aligned}\frac{A}{q} &= \frac{B\rho_{S2-CaveC}}{3.107 \times \beta\gamma} \\ &= \frac{(B\rho_{S2-CaveC})_0 \times \left(1 + \frac{\Delta X_{S2}}{D_{S0-S2}} - \frac{\Delta X_{CaveC}}{D_{S2-CaveC}}\right)}{3.107 \times \beta\gamma}\end{aligned}$$

If dispersions are properly calculated, the measured mass-over-charge ratio should be independent on both positions. As seen in figure 3.27, there is no dependence of A/q on two measured positions, verifying that both dispersions are well obtained and can be used further for the identification of secondary beam ions.

3.2.3.4 A/q corrections

The standing place of the MWPC0, which is used for the position measurement of secondary beam ions, is restricted by the room left by other detectors, making itself not necessarily coincide with the location of the focal plane [58]. Therefore, the magnetic rigidity measurement which depends on the position measured by the MWPC0 varies with the horizontal angle, resulting in a dependence of the ion's mass-over-charge ratio on the angle.

At this moment, the ion's mass-over-charge ratio is ready to be obtained, with the velocity given by the ToF measurement between S2 and Cave C, and the magnetic rigidity derived from the combination of dispersions and position measurements. Yet some dependences of the ratio, such as the dependence on the horizontal angle of the trajectory at the entrance of Cave C, remain to be corrected.

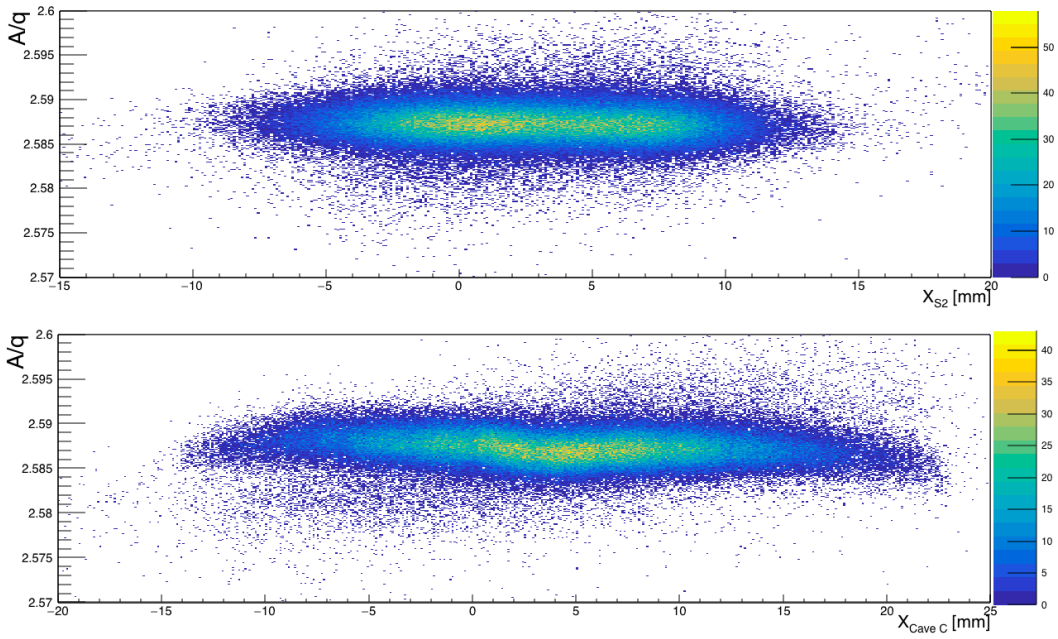

FIGURE 3.27: *Correlations between the mass-over-charge ratio and positions for secondary beam ions. Top: A/q vs. position measured at S2. Bottom: A/q vs. position measured at Cave C.*

On the top of figure 3.28, the correlation between A/q and the horizontal angle and the spectrum of A/q before corrections are plotted, while on the bottom of the figure, the correlation and the spectrum after corrections are shown. As seen from the figure, the spectrum of the corrected mass-over-charge ratio exhibits more separated peaks, implying an improvement in the resolution.

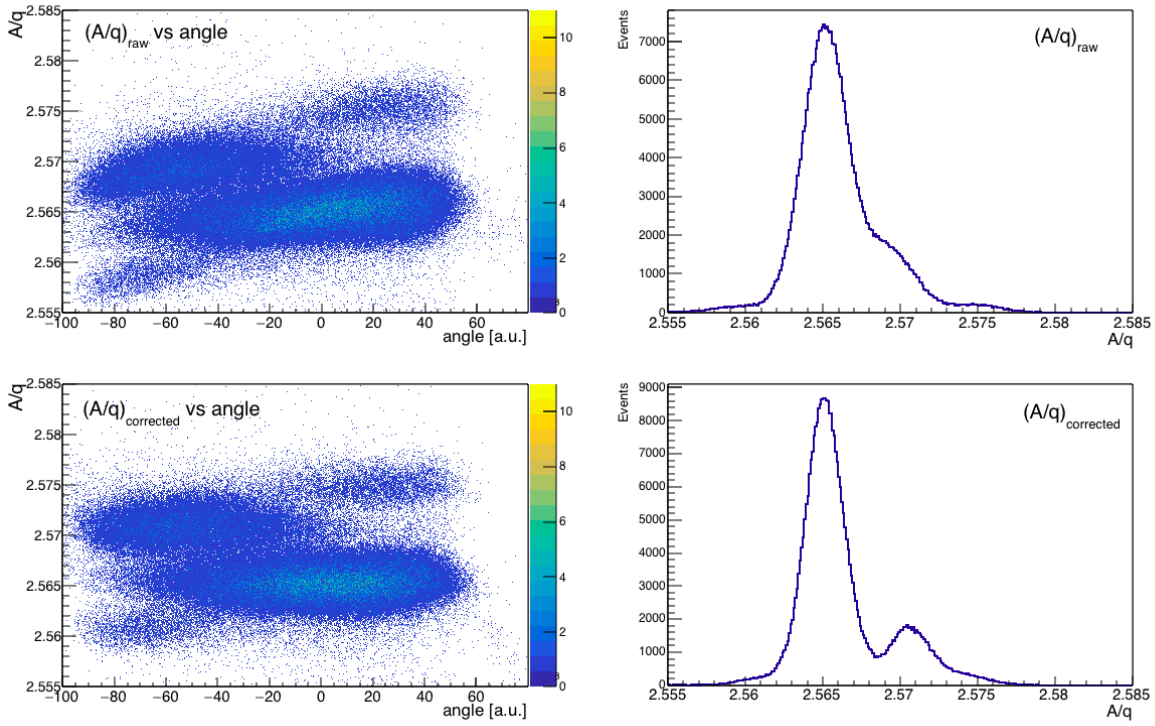

FIGURE 3.28: *Mass-over-charge ratio of secondary beam ions, for an FRS setting centered on* ^{236}U*. Left: Mass-over-charge ratio vs. horizontal angle. Right: Spectrum of the mass-over-charge ratio. Top: Correlation and spectrum before corrections. Bottom: Optimized correlation and spectrum.*

3.2.4 Full identification

As previously pointed, there is a small chance that ions are non-fully stripped in all three sections of the Triple MUSIC, resulting in a mis-identification of the nuclear charge Z. However, the uncertainty of the elemental number can be eliminated by the measurement of the mass-over-charge ratio. Then an unambiguous identification of the ion is achieved by the combination of Z and A/q.

Actually, in order to acquire a complete identification, both the atomic number and mass of the ion should be measured. And by definition, the mass is the product of Z and A/Z, rather than that of Z and A/q. Thus, an ion is fully identified by measurements of both Z and A/Z. However, in our case, the combination of Z and A/q is already enough to distinguish ions without ambiguity.

It is known that A/q is derived from the magnetic rigidity measurement and ToF measurement performed between S2 and the entrance of the Cave C. Ions transmitted throughout this part are constrained by the magnetic setting of the FRS adjusted for the selection of bare ions of the desired nuclide, which means ions carrying two or more electrons are expelled from the beam line. Besides, ions are at relativistic energies, implying that the majority of them are fully stripped and only a small fraction have one electron in the ionic cloud.

If ions are fully stripped along the beam line between S2 and Cave C, A/q is equal to A/Z. Of course ions can be correctly identified by measurements of Z and A/q. Otherwise, if ions are H-like (*i.e.* q = Z -1), since A/Z $\approx$ 2.5 for secondary beam ions, the mass computed as the product of Z and A/q will lead to a deviation of about 2.5 units from the real value. Let's take ^{236}U as an example, the mass of ions with one electron will be wrongly estimated as $92 \times \frac{236}{91} = 238.6$. Since the fake mass drops half a unit away from any possible mass value, namely an integer number, corresponding events can be easily recognized on the identification map (A/q, Z). Consequently, the combination of Z and A/q distinguishes ions unambiguously under both circumstances.

The secondary beam identification map for the FRS setting centered on ^{236}U is presented on the top of figure 3.29. As labeled on the figure, by combining the information on Z and A/q, events corresponding to nuclei of ^{236}U, ^{237}U, ^{233}Pa and ^{234}Pa are clearly recognized. However, there are still two bunches of events (recorded as (1) and (2)) which seem to be puzzling at the first look.

In order to clarify the situation, two graphical cuts on events concerning ions whose atomic number is identified as 91 and 92 are applied to the identification map, and projections of the correlation of Z vs. A/q on the X-axis (*i.e.* A/q spectra) corresponding to events enclosed by two cuts are drawn on the bottom of figure 3.29. The graphical cut and the spectrum of the ratio represented by the black line correspond to the case of Z being estimated as 92, while those indicated by the red line correspond to the case of 91.

On the A/q spectrum plotted with the black line, there are two peaks corresponding to ^{236}U and ^{237}U and a shoulder in between corresponding to the bunch of events labeled as (2) on the identification map. As for the spectrum with the red full line, there are three clear peaks,

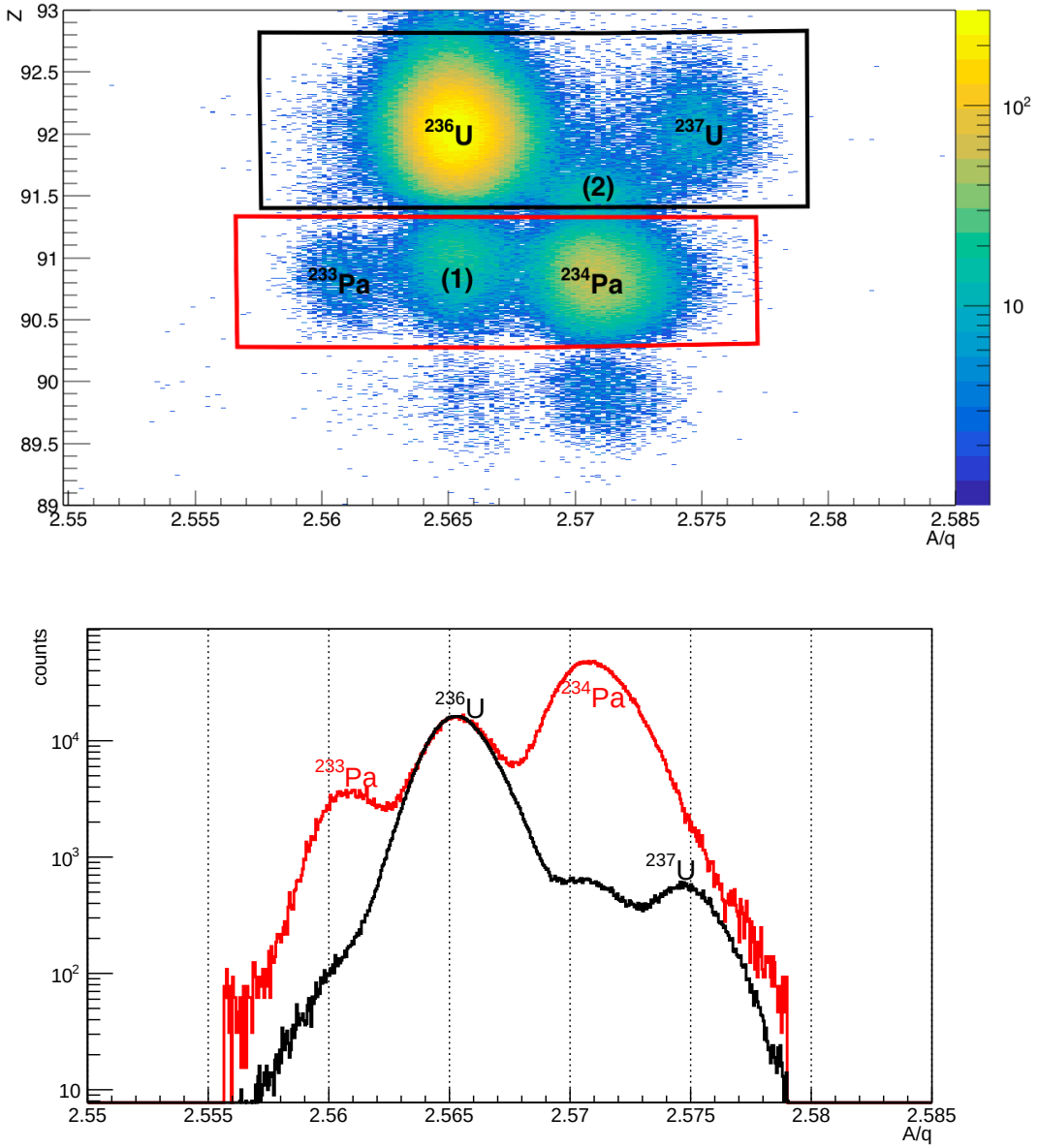

FIGURE 3.29: *Top: Secondary beam identification map (A/q, Z), for the FRS setting centered on ^{236}U. Bottom: Spectra of the mass-over-charge ratio shown in the logarithm scale, the ion's nuclear charge is identified as 92 on the spectrum with the black line, and that is estimated as 91 with the red line.*

with two of them corresponding to ^{233}Pa and ^{234}Pa, and the other one corresponding to events recorded as (1).

As seen on the figure, the latter peak is aligned strictly with the peak of ^{236}U mentioned above, implying this peak also represents ions of ^{236}U. These ions are mis-identified as Protactinium isotopes because they are non-fully stripped in all three sections of the Triple MUSIC. The point of view that ions in the events (1) are mis-identified can also be concluded by the fact that if they are indeed protactinium isotopes, no meaningful mass number is possible, since there is no another integer between 233 and 234.

Similarly, ions in events (2) shown between those of ^{236}U and ^{237}U on the identification map are actually not Uranium isotopes. Since the corresponding shoulder-like peak is aligned very well with the peak of ^{234}Pa on the spectrum with the red line, these ions are of the isotope ^{234}Pa indeed.

As discussed earlier, a very good resolution is reached in the nuclear charge with the use of the Triple MUSIC. However, there are still a fraction of events in which the ion's atomic number is not estimated properly. And this is exactly the case for events (2), in which the ions' mean atomic number is measured as 91.5, rather than 91 nor 92.

Now let's look at the peaks of ^{236}U on the spectra again. Don't be mis-guided by the amount of events in which ions of ^{236}U are mis-identified as Protactinium isotopes. Because the number of events in each bin of the spectrum with the red line is scaled by 14 times to show the alignment of two peaks of ^{236}U. In fact, the fraction of mis-identified ions is just a few percent of all the ions of ^{236}U.

As a conclusion, by combining measurements of the nuclear charge (Z) and the mass-over-charge ratio (A/q), ions are identified unambiguously. Even though in some cases, ions are mis-identified in the atomic number at the beginning, they can be finally identified correctly, with the information on the mass-over-charge ratio.

In figure 3.30, the secondary beam identification map, for three FRS settings centered on ^{187}Tl, ^{194}Bi and ^{207}Fr, is shown. Events concerning the nuclides of interest have been indicated on the map.

3.2.5 Performance of new PMTs under extreme counting rate

To finally have enough statistics for fission events of ^{236}U in a short time, the primary beam of ^{238}U with a very high intensity is required, because only a small fraction of nuclei of ^{238}U produce ^{236}U ions, and then just a few among them fission in Cave C. However, events with a rate of several hundreds of thousand Hz is already a challenge for detectors, and their behaviors are degraded under high counting rate.

In the first SOFIA experiment in 2012, two PMTs of the START detector at S2 were equipped with partly active divider whose last 3 stages over 8 are active, and they performed very well, leading to a good mass resolution for secondary beam ions, until a counting rate of about 1 MHz in S2.

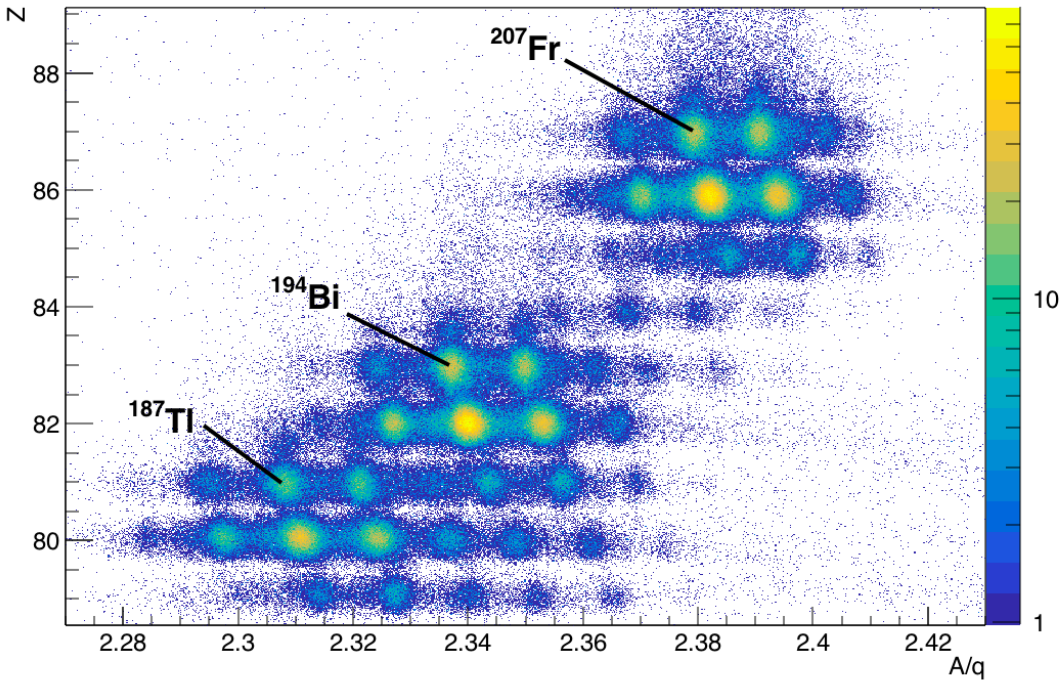

FIGURE 3.30: *Secondary beam identification map (A/q, Z), for three FRS settings centered on ^{187}Tl, ^{194}Bi and ^{207}Fr.*

In the experiment in 2014, in order to bear higher rate, the START scintillator was mounted with two new PMTs, which are upgraded by decreasing the divider resistor value by a factor of 5 to increase the steady current.

To evaluate the performance of new PMTs, mass resolutions of secondary beam ions with various counting rates at S2 are tested. Profiles of counting rates at S2 for FRS settings centered on ^{236}U and ^{187}Tl are presented respectively in figure 3.31. Since the cross section of producing the ^{187}Tl nuclei from the fragmentation of ^{238}U is smaller than that of producing ^{236}U, a ^{238}U primary beam with a higher intensity is needed to produce the same amount of ^{187}Tl as ^{236}U. Consequently, more fission fragments are transmitted to the S2 focal plane in the setting of ^{187}Tl, resulting in a much higher overall counting rate, as observed in figure 3.31.

The evolution of mass spectra of Thallium isotopes is presented in figure 3.32. Four cases of counting rates have been taken into consideration. The sigma of the Gaussian fit on the peak of ^{187}Tl is the representative of the mass resolution to be compared. The larger the value of the sigma, the worse the mass resolution. Values of the sigma in different cases are listed in table 3.8 and the correlation between the sigma and the counting rate is plotted in figure 3.33. It is observed that in cases of counting rate lower than 3 MHz, the mass resolution stays at a quite good level, while it deteriorates rapidly with the increase of the rate beyond that value.

Values of the sigma under different counting rates at S2 for the ^{236}U setting are also recorded in table 3.8, and the corresponding correlation is plotted in figure 3.33. It seems that the mass

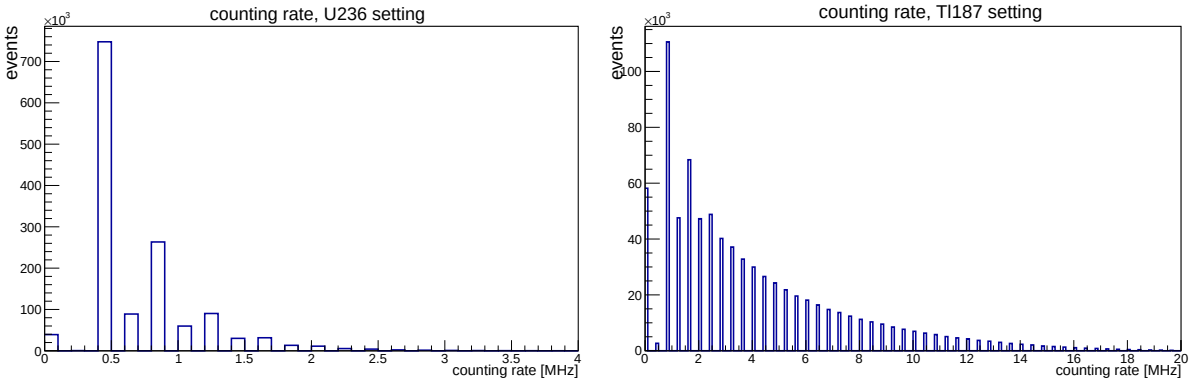

FIGURE 3.31: *Profiles of counting rates at S2. Left: for the FRS setting of ^{236}U. Right: for the FRS setting of ^{187}Tl.*

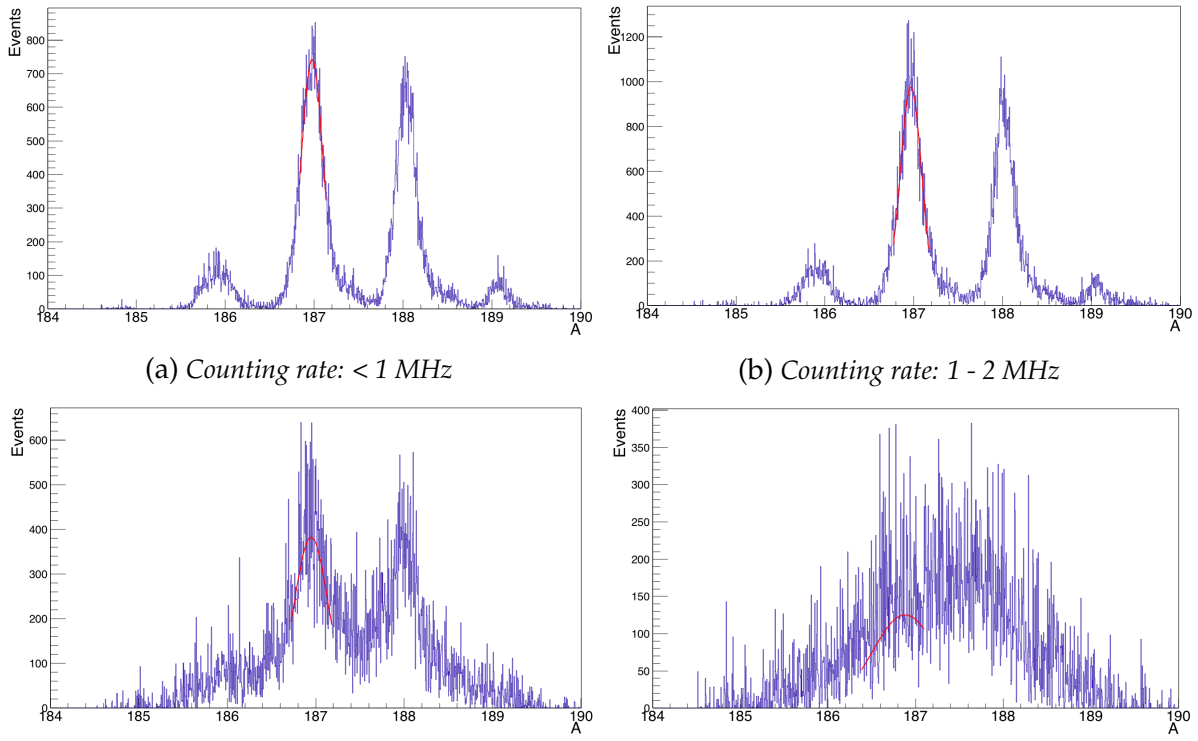

(a) *Counting rate: < 1 MHz*

(b) *Counting rate: 1 - 2 MHz*

(c) *Counting rate: 2 - 3 MHz*

(d) *Counting rate: 3 - 4 MHz*

FIGURE 3.32: *Evolution of mass spectra of Thallium isotopes with various counting rates at S2.*

resolution is slightly degraded with increasing counting rates, yet still remains at a good level with rates below 3 MHz, which is consistent with the evolution of mass resolutions in the ^{187}Tl setting.

In a word, the performance of the new PMTs is excellent, because even though the mass resolution is getting a bit worse with increasing counting rates at S2, it is still satisfying until a rate of 3 MHz which is far beyond the limit of most detectors.

^{187}Tl setting		^{236}U setting	
Counting rate [MHz]	Sigma	Counting rate [MHz]	Sigma
< 1	0.122	< 1	0.108
1 - 2	0.123	1 - 2	0.170
2 - 3	0.176	2 - 3	0.194
3 - 4	0.373		
> 4	0.527		

TABLE 3.8: *Evolution of mass resolutions with various counting rates at S2, in FRS settings centered on ^{187}Tl and ^{236}U.*

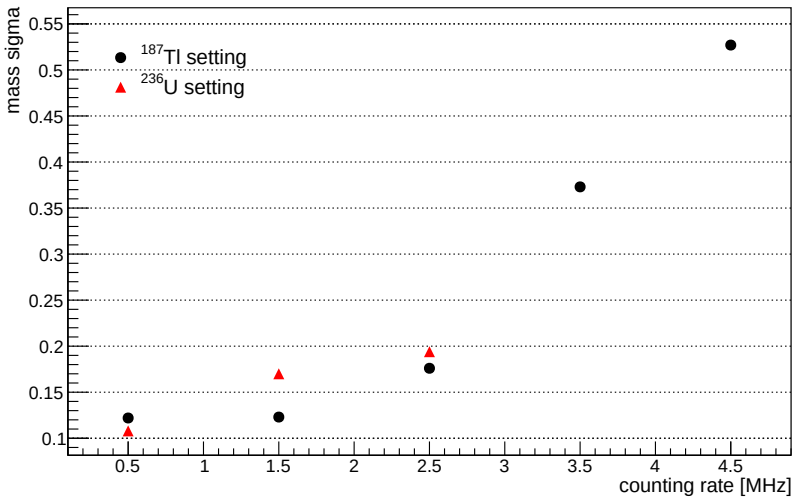

FIGURE 3.33: *Correlation between the mass resolution and the counting rate at S2, for both the ^{187}Tl setting and the ^{236}U setting.*

Chapter 4

Identification of fission fragments

As mentioned in previous chapters, secondary beam ions enter the Cave C and fission in this area, which is equipped with a recoil spectrometer, dedicated for the identification of fission fragments, and consisting of a large acceptance magnet ALADIN and a set of detectors developed by the SOFIA collaboration.

Similar to the secondary beam identification, the complete identification of fission fragments is also achieved by applying the ΔE - Bρ - ToF technique. Both fission fragments are identified simultaneously in every single event. In combination with the event-by-event identification of the fissioning system (*i.e.* secondary beam ion), the fission fragment distribution of the nuclei of interest (^{236}U in this paper) can be finally obtained.

In the first section of this chapter, an overview of the experimental setup and detailed descriptions of all detectors concerning the identification of fission fragments are presented. As seen in the schematic view of the setup given in figure 4.1, there are an active target, a Twin MUSIC, two MWPCs, a plastic scintillator and a time-of-flight wall.

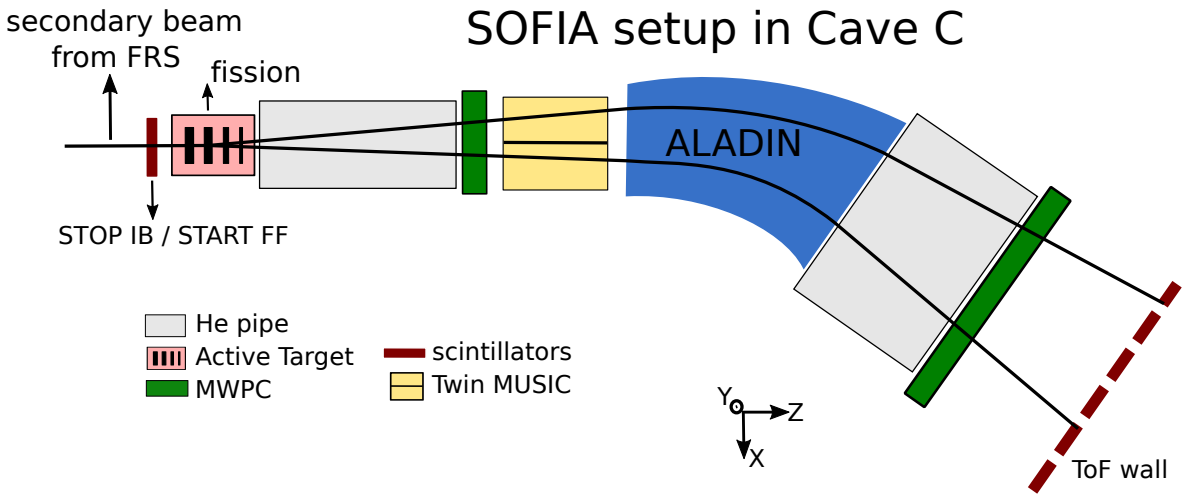

FIGURE 4.1: *Schematic view of the setup in the Cave C, used for the identification of fission fragments.*

The second section concentrates on the analysis of measurements performed by the above mentioned detectors, which leads to the nuclear charge identification of fission fragments of the ^{236}U isotope. Before stepping into the identification procedure, how to locate in which layer in the active target that fission occurs is explained in details.

4.1 Experimental setup

4.1.1 Overview

Secondary beam ions enter the Cave C with an energy of about 715 AMeV. The fission is triggered in flight, and fission fragments are emitted with a very high kinetic energy in the forward direction in the laboratory frame, permitting a high detection efficiency of the setup and a simultaneous identification of both fragments.

At such a high energy, all fission fragments, even the heaviest ones (Z = 62) are fully stripped, making it much easier and more accurate to extract the nuclear charge of the fragments from their energy loss measured in an ionization chamber.

However, since fission fragments fly in a very high velocity in the Cave C whose depth is just several meters, the time-of-flight resolution is really demanding. Besides, the requirement in the resolution of position measurements is also very high. Consequently, it is quite a challenge to develop detectors which can meet the demand on the fission fragment identification.

As seen in figure 4.1, the secondary beam comes from the left side and fission is induced in the active target, producing two fragments in the forward direction, towards ALADIN and up to the ToF wall.

The Twin MUSIC is a double ionization chamber, consisting of two identical parts sharing a cathode plane. Each fragment goes through one side of the MUSIC detector, permitting energy loss measurements of both fragments at the same time, and thus leading to a simultaneous nuclear charge identification of two fission products.

In the Twin MUSIC, the horizontal angle of each fragment's trajectory upstream the ALADIN magnet is also given. In combination with two position measurements, which are performed by two MWPCs with one standing upstream ALADIN and the other downstream the magnet, the fragment's trajectory curvature in ALADIN can be extracted. Since the magnetic field of the dipole is a known value, it is then straightforward to compute the magnetic rigidity for each fragment.

The time of flight of fission fragments is measured between a plastic scintillator and a ToF wall composed of 28 scintillation slats.

Based on these above mentioned measurements (ΔE, Bρ and ToF), the mass and the nuclear charge of both fragments can be obtained. Relevant detectors will be described exhaustively in the following sections.

4.1.2 Active target

The active target used in SOFIA experiments was designed and developed by our colleagues in CNRS/CENBG Bordeaux. It has a cylindrical shape, as seen in figure 4.2. The space inside is filled with gas. A sketch of the side view of its inner volume is given in figure 4.3. Along the symmetry axis, there are in total nine layers which are alternatively charged to ground potential or negative high voltage, and thus acting as anodes and cathodes respectively. Some technical information is listed in table 4.1.

FIGURE 4.2: *Picture of the active target. The direction of the secondary beam is as indicated on the picture.*

The active target is named as "target" because it consists of four layers serving as targets in the inverse kinematics which are used to trigger the fission of incident projectile ions (*i.e.* secondary beam ions in our case). As indicated in figure 4.3, the first two targets encountered by the secondary beam are made of Uranium, then it comes the target of Aluminum, and the last one is the lead target. This combination of materials is applied on a basis of various considerations, as explained in the following paragraphs.

When the projectile impinges the target, there are two kinds of mechanisms leading to the fission of incident ions: nuclear interaction and Coulomb excitation. What interests us is the Coulomb-excitation induced fission, in which the projectile nuclei are excited due to the electromagnetic interaction with the target nuclei, and then de-excite through the fission channel. Since the Coulomb field of the target is enhanced with the increase of the elemental number, resulting in a stronger electromagnetic interaction, high-Z materials such as lead (Z = 82) and depleted uranium (99.8% of ^{238}U, Z = 92) are selected for targets.

The fission is roughly regarded as occurring in the middle of the target, leading to that the thicker the target, the more uncertain the measured fission position. Since the measurement of the total kinetic energy (TKE) of both fragments, which is an important observable in the fission

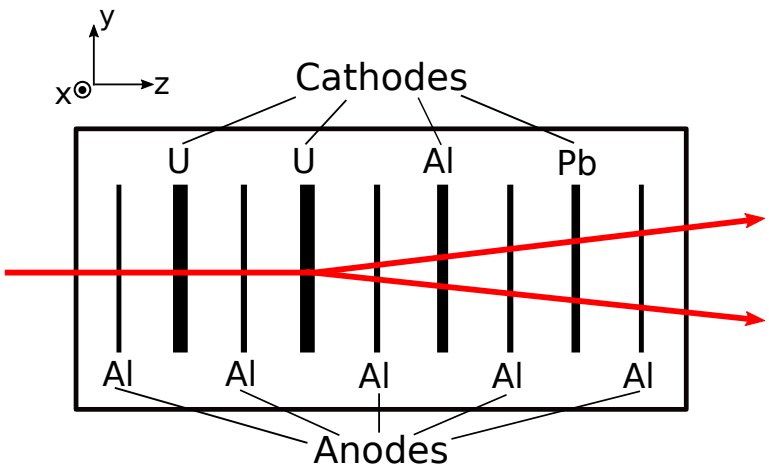

FIGURE 4.3: *Sketch of the side view of the active target. The secondary beam enters the detector from the left side. Two red arrows represent fission fragments. The event that fission occurs in the second Uranium target is taken as an example.*

process, requires accurate information on the fission location, a thin target is needed to avoid degrading the resolution of the TKE measurement. However, it is very difficult to produce thin Uranium targets. As a result, a thin Pb target of 125 μm is used.

It is known that with a higher Z, the cross section of the Coulomb excitation caused by the Uranium target is larger than that in the case of the lead target. In order to ensure the statistics of the Coulomb-excitation induced fission events, two relatively thick U targets (each of 600 μm) are also applied.

As mentioned before, a fraction of the fission events in the U and Pb targets are triggered by the nuclear interaction. The majority of the nuclear contribution to the charge distribution of fission fragments can be easily removed by requiring that the sum of nuclear charges of two fragments is equal to the charge of the nucleus of the secondary beam, while the rest can only be subtracted with the scaled nuclear charge distribution from purely nuclear-induced fission in some low-Z materials. In the first SOFIA experiment, the subtraction of the remaining nuclear contribution is realized with the use of several Aluminum anodes (Z = 13), while an Al target with a thickness of 500 μm is inserted in the second experiment, to obtain a better measurement of the nuclear charge distribution of fission fragments from purely nuclear-induced fission with more statistics.

Except these four targets acting as cathodes, five Aluminum foils are also placed in the active target, acting as anodes. As shown in figure 4.3, every target is sandwiched by two Al anodes, and each cathode is separated from surrounding anodes by gas, making the active target a detector composed of successive ionization chambers.

When a particle penetrates the active target, it ionizes the gas atoms into ions and electrons. The latter drift towards the nearest anode, inducing a signal which is proportional to the energy deposited by the particle in the two ionization chambers sharing that anode. Since the sum of energy losses of two fragments is almost half of the energy loss of the secondary beam, signals

given by the anodes before or after the fission location will be significantly different. Then, by comparing all signals, questions like whether there is a fission event and if yes, in which foil fission occurs can be clearly answered.

Voltage of cathodes	-400 V
Distance between anode and cathode	15 mm
Cathodes 1 and 2	600 μm depleted U
Cathode 3	500 μm Al
Cathode 4	125 μm Pb
Anodes 1 and 5	15 μm Al
Anodes 2, 3 and 4	50 μm Al

TABLE 4.1: *Technical information of the active target.*

The active target consists of nine foils, alternatively acting as anodes and cathodes. Each cathode is surrounded by two anodes and the gap between each cathode and anode is filled with gas, making the active target a detector equipped with multiple ionization chambers. Fission can be triggered by the interaction between the beam nuclei and four targets, which are also cathodes of the active target. Then the fission location is derived from the comparison among signals given by the anodes, which are proportional to the energy loss of the secondary beam or fission fragments.

In a word, the active target serves both a target which induces the fission of the secondary beam, and a detector which aims at locating the fission position.

4.1.3 Twin MUSIC

Similar to the Triple MUSIC, the Twin MUSIC was also constructed at the GSI detector lab, and is developed based on the standard MUSIC detectors. A picture of the Twin MUSIC is given in figure 4.4. However, unlike the Triple MUSIC which consists of 3 successive sections with independent cathodes, the Twin MUSIC is a double ionization chamber, which is composed of two identical parts sharing a central cathode plane, as seen in figure 4.5. The Twin MUSIC is designed in this way to have one fragment flying on one side of the detector, and thus enabling a simultaneous measurement of both fragments.

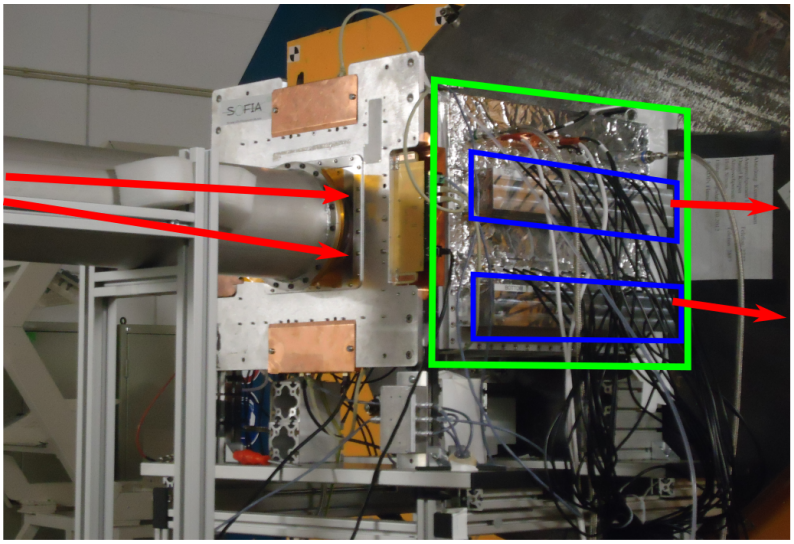

FIGURE 4.4: *Picture of the Twin MUSIC. Red arrows represent trajectories of two fission fragments, starting from the left side of the figure. Inside the green quadrilateral is the detector observed from its right-hand side. The silver wrapping is the Aluminum foil used to form a Faraday cage enclosing the detector to get rid of the electromagnetic interference generated by electronic devices in the surrounding. The foil is led to the ground potential. Inside two blue quadrilaterals are thick Aluminum boxes dedicated to protecting preamplifiers which are directly connected to anodes and very sensitive to electromagnetic waves.*

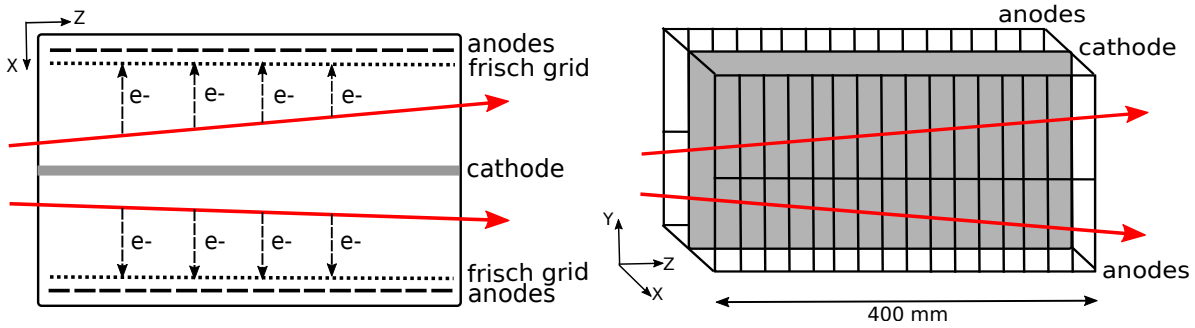

(a) *Top view of the Twin MUSIC* (b) *Side view of the Twin MUSIC*

FIGURE 4.5: *Sketches of the top view and side view of the Twin MUSIC. Red arrows represent the trajectories of the fission fragments.*

On both sides of the Twin MUSIC, it is filled with a mixture of gases. Two anode planes are inserted near the boundaries of the detector, with one on each side. Both planes are parallel to the cathode plane and separated from it by a distance of 113 mm. In each volume of the detector, a frisch grid is placed very close to the anode plane in the gap between two electrodes. Technical information of the detector is provided in table 4.2.

Both anode planes are segmented into two parts along the Z axis, making the Twin MUSIC composed of 4 identical sections. This segmentation is an improvement in the detector and it is introduced to recover events in which two fragments fly on one side of the cathode plane. Besides, each half of the anode plane is segmented vertically (*i.e.* along the Y axis) into 18 anodes, with 16 effective ones in the middle and 2 screening anodes on both ends.

Similar to the case in the Triple MUSIC, when an ion of one fragment penetrates the Twin MUSIC, a signal is induced on each effective anode in the vicinity of the trajectory and two quantities can be extracted: the ion's energy loss along the path, and the drift time of electrons emitted from the ionization of the gas atoms triggered by the ion.

As explained in subsection 3.1.3, since all possible fragments are fully stripped, their nuclear charges can be directly extracted from the energy loss measurements in the Twin MUSIC. In addition, it is also mentioned that the measurement of the drift time is equivalent to that of the X position, implying a set of X positions are available for each fragment. Then, by adding the distance between two effective anodes, the horizontal angle of each fragment's trajectory can be obtained.

Gas	P75 = 75% CH_4 + 24.5% Ar + 0.5% CO_2
Pressure	1.02 bar
Distance between cathode and Frisch grid	110 mm
Distance between Frisch grid and anodes	3 mm
Active volume	$110 \times 220 \times 400$ mm^3
External volume	$430 \times 480 \times 550$ mm^3

TABLE 4.2: *Technical information of the Twin MUSIC.*

The Twin MUSIC is a double ionization chamber, which is made up of two identical volumes sharing a central cathode plane, permitting simultaneous and independent measurements of both fragments. In each volume, an anode plane is separated from the cathode plane by mixed gases and a frisch grid is inserted between two electrode planes. Each anode plane is divided into two parts along the Z axis and every half plane is segmented into several anodes along the Y axis.

On each effective anode, an energy loss and a drift time are given. Then nuclear charges of both fragments can be directly extracted from measured energy losses and the horizontal angle of each fragment's trajectory can be derived from the drift time measurements.

4.1.4 ToF wall

Time-of-flight measurements of fission fragments are performed between a plastic scintillator and the ToF wall, which are separated by a distance of about 8.3 m. The scintillator is labeled as STOP IB / START FF, because it serves as both the STOP detector and the START detector for the time-of-flight measurement of the secondary beam and fission fragments, respectively. It is already described in subsection 3.1.4, as referred to the STOP IB detector. Therefore, this part will focus on the discussion of the ToF wall. A picture is given in figure 4.6.

FIGURE 4.6: *Pictures of the ToF wall, which is used for time of flight measurements of fission fragments. Left: vertical plastic slats and associated PMTs, with half of them placed on the top of plastics, while the rest at the bottom. Right: the operational detector is protected by the black wrapping from the interference of the light in the surrounding.*

The ToF wall consists of 28 plastic slats and each of them is attached to two PMTs, with one at each end, making the ToF wall a set of scintillation detectors. As compared to the START detector, each scintillation detector here is enlarged in dimensions and placed vertically. Accordingly, by combining times provided by the pair of PMTs coupled to the hit plastics, each fragment's incident time and vertical position can be derived.

The ToF wall is the last detector in the setup, implying that it is even further placed along the longitudinal axis than the MWPC2. So it is also constructed with a quite large surface, permitting a high detection efficiency of fission fragments which are extensively spread in X and Y positions. And the active surface is segmented into numerous slats to realize simultaneous and unambiguous measurements of both fragments.

It is known that a broad range (from Z $\approx$ 30 to 62) of fission fragments are produced in our experiment. And measurements of light fragments are more a challenge to the ToF wall as compared to heavy ones, for mainly two reasons:

- light fragments deposit less energy in the scintillator, leading to the fact that fewer photons are produced. Considering that the intensity of photons decreases along the propagation of the light, even fewer photons will reach the PMTs at both ends of each plastic slat. Then weaker signals are induced and they may fail to trigger the associated constant fraction discriminators to obtain the time information.
- and they are further spread in positions with relatively higher transverse velocities, implying that it's more likely for light fragments to reach one extreme of the plastic slat and induce photons there. Then after the attenuation of the photons' intensity along the complete slat, it may be problematic for them to be detected by the PMT at the opposite extreme.

Therefore, to enhance the probability that light fragments are also measurable for PMTs at both ends, all the plastic scintillators used in the first SOFIA experiment were replaced by those with longer attenuation length.

Except being used for time of flight measurements and providing information on vertical positions for fission fragments, the ToF wall also serves to trigger the data acquisition. Since the main goal of the SOFIA experiments is to obtain fission yields, we are solely interested in fission events. Consequently, in order to maximize fission involved data and avoid unnecessary burden due to irrelevant events, data collected in all detectors are recorded only when fission occurs. And an obvious proof of a fission event is that two slats of the ToF wall are struck nearly at the same time, leading to that four meaningful signals in total (two for each slat, *i.e.* each fragment) are induced on PMTs. Therefore, the trigger condition is set as a multiplicity of four in all PMTs of the ToF wall.

It is noted in table 4.3 that two types of PMTs are applied in the ToF wall: Hamamatsu 6533 and 10580. The performance of the former is more satisfactory than that of the latter, while the latter is less costly. Finally, the latter type is used only at the edges of the ToF wall, which are rarely hit by fragments, and thus the overall performance of the ToF wall is barely degraded. The same as the START and STOP IB detector, the ToF wall is also developed in CEA Bruyères-le-Châtel, France.

Plastic scintillator	EJ228
Plastic dimensions	$5 \times 31.5 \times 660$ mm^3
Active surface	$5 \times 900 \times 660$ mm^3
Photo-multiplier tubes	Hamamatsu 6533 in the center Hamamatsu 10580 at edges

TABLE 4.3: *Technical information of the ToF wall.*

The ToF wall consists of 28 vertical plastic slats, and each of them is couple to two PMTs, with one on the top and the other at the bottom. The incident time and the vertical position of both fission fragments are measured in the ToF wall. Furthermore, this detector also supplies the trigger for data acquisition by requiring that four signals in total are induced in its PMTs.

4.1.5 MWPCs

As already mentioned, two MWPCs labeled as MWPC1 and MWPC2 are used for position measurements of two fission fragments. Since the structure and the working principle of a typical MWPC have been presented in subsection 3.1.5, here I will just introduce a few differences in the design between these two MWPCs and the MWPC0 which is dedicated to measuring positions of the secondary beam:

- the plate of X strips in the MWPC1 is segmented horizontally into two identical parts. When two fission fragments hit one MWPC, both plates of X and Y strips will provide two X and Y positions respectively. since measurements of X and Y positions are performed independently and they don't associate with each other themselves, it is problematic to assign a pair of X- and Y- position to one fragment. In most cases, fission fragments are emitted in a situation that one fragment is in the half space beyond the beam axis, while the other fragment is in the other half space below the axis. Then by segmenting the plane of X strips into upper and lower halves, the X position measured in the upper half plane automatically corresponds to the maximum value of Y positions, while that given by lower X strips pairs to the minimum Y position, resulting in an easier association of X and Y positions. For the rest of cases such as both fragments hit the same half plane, the association of positions needs more information from other detectors and it will be explained in details later in this chapter.
- the MWPC2 is equipped with more X and Y strips, leading to a much larger active area. It is known that fission fragments are emitted within a narrow cone in the forward direction, implying that they have velocities along the transverse axes. Therefore, with an increasing displacement in the longitudinal direction, the fission fragments are further spread in X and Y positions. Besides, the MWPC2 stands downstream the ALADIN and the trajectory deflection in the magnet leads to an enhanced spread in fragments' positions. Consequently, the MWPC2 is designed with an enlarged surface to ensure a high detection efficiency.

Since the common technical information of three MWPCs (like the wire pitch and the width of X and Y strips) and specifications of the MWPC0 are already given, and the MWPC1 is almost the same as the MWPC0 except an extra cut in the plate of X strips, only the geometry data of the MWPC2 remain to be listed, as seen in table 4.4. And a picture of the MWPC2 is given in figure 4.7.

Active surface	900×600 mm^2
Number of X strips	287
Number of Y strips	120

TABLE 4.4: *Technical information of the MWPC2.*

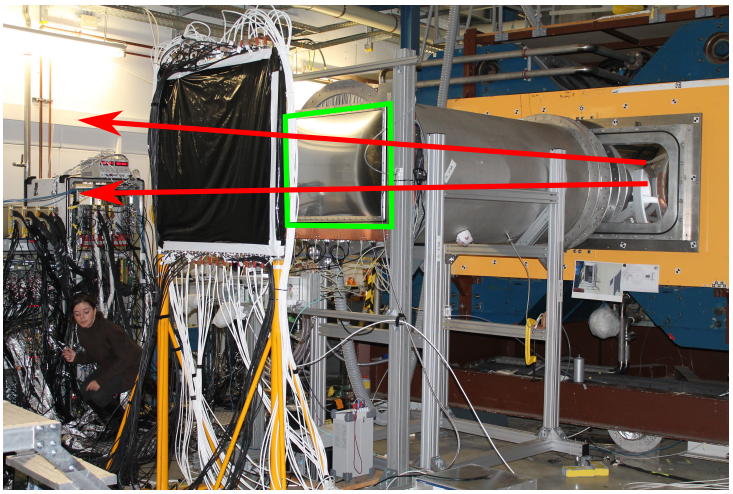

FIGURE 4.7: *Picture of the MWPC2. Red arrows indicate two fission fragments coming from the right side of the figure. Inside the green quadrilateral is the MWPC2.*

As compared to the MWPC0, slight differences in design are introduced to the other two MWPCs, to make them suitable for position measurements of fission fragments. The plane of X strips in the MWPC1 is divided into upper and lower halves, to ease the association of X and Y positions for each fragment. And the MWPC2 is enlarged in the active surface, to enable simultaneous measurements of fragments which are quite spread in positions.

4.2 Analysis

4.2.1 Determination of the fission location

As already mentioned, the resolution of the measurement of the total kinetic energy of the fission fragments is affected by the precision of the measured fission location. Provided that one is capable to know in which layer fission occurs, the resolution will be improved by using several targets instead of a rather thick one-piece target in the active target.

Besides, the fission location also reflects the mechanism of the excitation leading to the fission events: whether it is induced solely by the nuclear collision (in the Al target and all anodes), or also by the Coulomb interaction (in the U/Pb targets).

Therefore, it is essential to measure the fission location prior to the data analysis. In this part, the principle how the fission events are located will be explained.

4.2.1.1 Energy loss in each section

It is known that there are 9 layers in total in the active target: 4 targets acting as cathodes, and the rest acting as anodes. Each cathode is sandwiched by two anodes, and the gap between every pair of the anode and cathode is filled with 15 mm of gas, forming a set of successive ionization chambers.

When a charged particle penetrates the active target, along its path, the electrons created in each section (*i.e.* the gap between an anode and a cathode) are collected by the nearest anode.

For a certain section, the energy deposited by the passage of the secondary beam is:

$$\begin{aligned} \Delta E_{SB} &\propto Z_{SB}^2 \\ &= \Delta E_0 \end{aligned}$$

While if the fission has already happened, the energy loss will be measured as that of the fission fragments:

$$\begin{aligned} \Delta E_{FF} &\propto Z_{FF1}^2 + Z_{FF2}^2 \\ &\approx (Z_{SB}/2)^2 + (Z_{SB}/2)^2 \\ &= 0.5 \times \Delta E_0 \end{aligned}$$

It is noticed that the energy loss of the fission fragments in each section is approximately half of that of the secondary beam, implying an obvious change in the signals induced on the anodes upstream/downstream the fission location.

4.2.1.2 Principle of the measurement

As seen in figure 4.8, every central anode (A2, A3 and A4) is shared by two ionization chambers, and thus it collects electrons produced in both sections, inducing a signal corresponding to the

sum of energy losses in the two gaps. Consequently, the energy loss measured by these anodes will be one of the three values:

- $2 \times \Delta E_0 = \Delta E_0 + \Delta E_0$, which is equivalent to the energy loss of the secondary beam measured in both sections. It means that either no fission occurs in the active target, or the potential fission will take place in the layers downstream the considered anode.
- $\Delta E_0 = 0.5 \times \Delta E_0 + 0.5 \times \Delta E_0$, which is equal to the energy loss of the fission fragments measured in two sections, implying that fission has already taken place in the layers upstream this anode.
- $1.5 \times \Delta E_0 = \Delta E_0 + 0.5 \times \Delta E_0$, which is the combination of the energy loss of the beam in one section and that of the fission fragments in the following section, revealing that fission occurs in the considered anode.

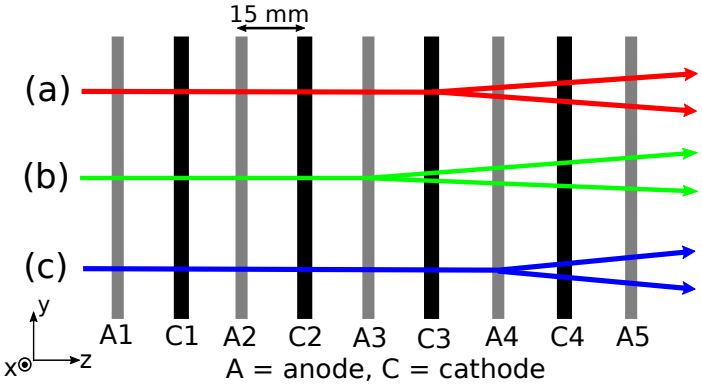

FIGURE 4.8: *Scheme of the alternative alignment of anodes and cathodes in the active target. The secondary beam enters the detector from the left side of the figure. Three cases of fission events with various locations are labeled: (a) in the third cathode (i.e. target), (b) in the third anode, and (c) in the forth anode.*

In contrast, both the first and the last anodes are dedicated to one ionization chamber, so the energy loss measured by each of them has only two possible values: either ΔE_0 or $0.5 \times \Delta E_0$, corresponding respectively to the energy loss of the beam or that of the fission fragments measured in one section. In the case of A1, these values indicate no fission occurs or fission has already happened upstream and/or inside the anode, respectively. Similarly, for the anode A5, two values imply that fission has not or has occurred upstream, respectively.

Consequently, the cathode (*i.e.* target) in which fission takes place can be revealed by the comparison of signals given by the two surrounding anodes, as listed in table 4.5. On the contrary, whether fission occurs in the central anodes are directly reflected by the signals induced on themselves.

Therefore, it is apparent to disentangle the fission events induced in the target C3 (case (a) in the examples), the upstream anode A3 (case (b)) and the downstream anode A4 (case (c)), from the correlation between the signals provided by the anodes, as presented in figure 4.9.

fission in	$\Delta E_{anode-up}$	$\Delta E_{anode-down}$
C2, C3	$2 \times \Delta E_0$	ΔE_0
C1	ΔE_0	ΔE_0
C4	$2 \times \Delta E_0$	$0.5 \times \Delta E_0$

TABLE 4.5: *Energy losses measured in the anodes upstream/downstream the cathode (i.e. target) in which fission occurs. ΔE_0 represents the energy loss of the secondary beam measured in one section.*

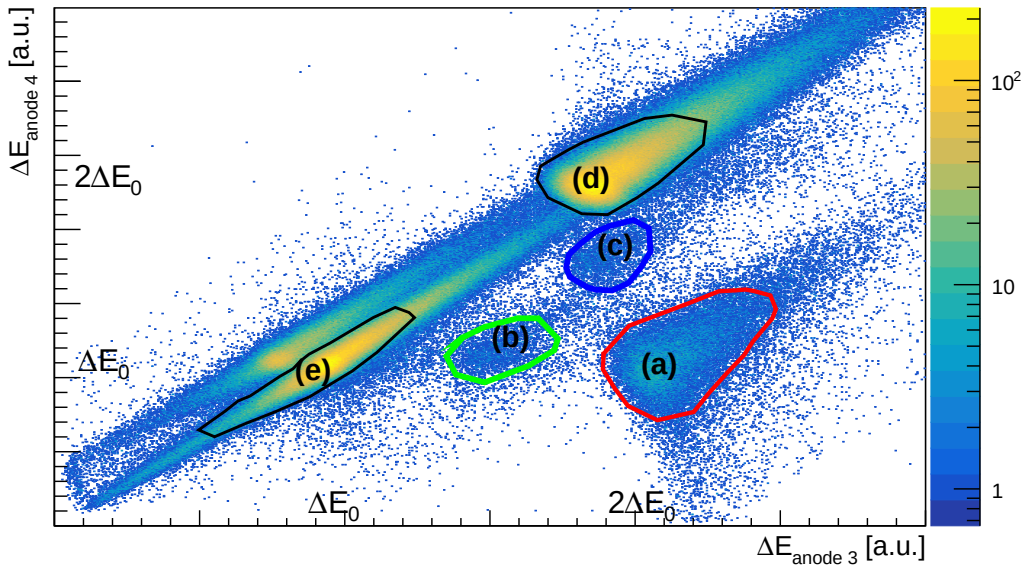

FIGURE 4.9: *Correlation of energy losses measured in the anode 3 and 4. Each spot represents one situation of fission events occurring at various locations. In cases (a), (b) and (c), in which layer fission occurs can be unambiguously revealed, and they are consistent with the examples labeled accordingly in figure 4.8. On the contrary, it can only conclude that no fission takes place up to the anode 4 (included) and fission has already happened upstream the anode 3, in cases (d) and (e) respectively. And to further locate in which layer fission occurs, energy losses measured in other anodes are required.*

4.2.2 Nuclear charge identification

It is known that the nuclear charges of the fission fragments are extracted from simultaneous energy loss measurements performed in the Twin MUSIC. In order to acquire a satisfactory resolution of the nuclear charge, the energy loss measurement needs to be optimized prior to the extraction, through a set of corrections.

The main corrections to be executed are the adjustments of the dependences of the energy loss on the fragment's velocity and its X position in the Twin MUSIC. In our experiment, each fragment's velocity is obtained from a time-of-flight measurement, in combination with the computation of the trajectory length. In order to reconstruct the trajectory, several ingredients are demanded: the horizontal angle of the flight path upstream the ALADIN magnet, and positions measured in two MWPCs.

In this part, the procedure leading to the nuclear charge identification of the fission fragments is explained extensively, in an order which follows that of the real analysis:

- first, the X positions of each fragment in the Twin MUSIC are measured, and its velocity is obtained from the combination of the tracking as well as the reconstruction of the trajectory and the calibrated time-of-flight.
- second, corrections of the dependences of the energy loss measured in the Twin MUSIC, on the above mentioned velocity and X position and other quantities, are performed.
- finally, the nuclear charge of each fragment is extracted from the optimized energy loss by applying a quadratic equation.

4.2.2.1 Horizontal angle upstream ALADIN

As mentioned before, provided that the drift velocity of the electrons in the gas is known, the drift time measured on the anodes can be converted into horizontal positions (*i.e.* X positions). There are 16 anodes in each section of the Twin MUSIC, permitting a measurement of 16 X positions which reflects the evolution of the flight path for each fragment. Then in combination with the distance between every two anodes along the longitudinal axis, the horizontal angle of the trajectory upstream the ALADIN magnet can be obtained.

X positions measured in Twin MUSIC

In principle, the maximum of possible values of the drift time is that of the electrons created at the location of the cathode plane, as indicated in figure 4.10. On the spectrum of the drift time, it is also apparent to recognize the value corresponding to the position of the frisch grid. Since the distance between the central cathode and the frisch grid is already known as 110 mm according to the design, the drift velocity of the electrons for each anode can be given by:

$$v_{drift} = \frac{D_{C-FG}}{\Delta dt}$$

where D_{C-FG} is the distance between the cathode and the frisch grid, and Δdt is the corresponding difference in the drift time.

Then the fragment's X position can be derived from the drift time measured in each anode on an event-by-event basis:

$$x = \pm(dt_C - dt) \times v_{drift}$$

where dt_C is the drift time corresponding to the location of the central cathode, dt is drift time measured in every single event, and the sign of the equation depends on the side of the Twin MUSIC the fragment flies through. The cathode plane is located at X = 0 to be the reference. The sign is "+" ("-") for the fragment on the right (left) side, to let the right- (left-) hand positions be positive (negative).

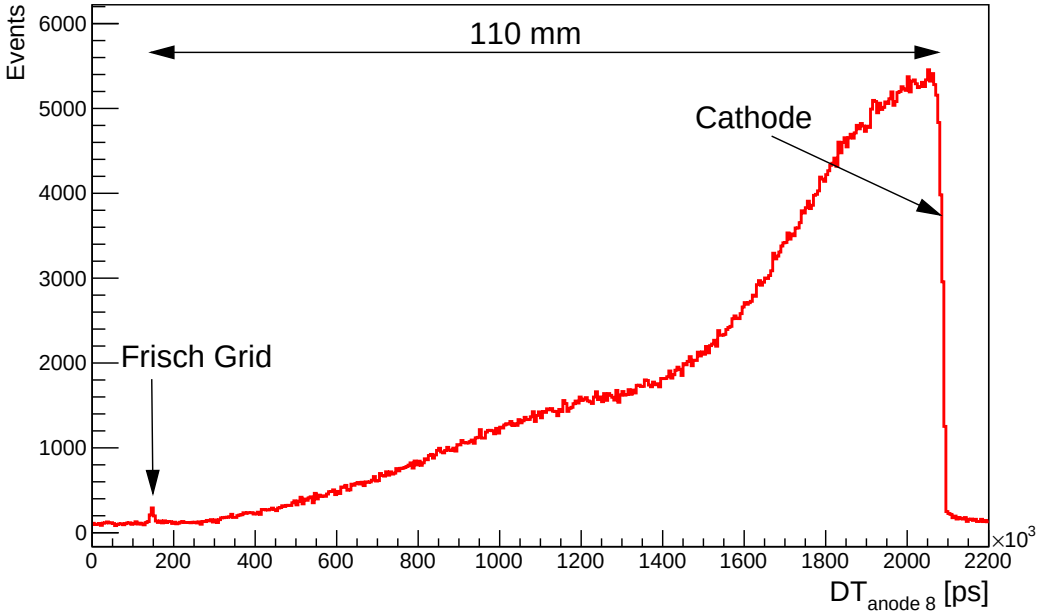

FIGURE 4.10: *Drift time (DT) spectrum for anode 8 in the Twin MUSIC. Values corresponding to the locations of the cathode and the frisch grid are indicated. The interval between these two drift time values corresponds to the distance between the locations, which is about 110 mm.*

X position optimization

As indicated in figure 4.11, 16 X positions are measured and the trajectory is described via a linear fit, from which the horizontal angle is extracted. The deviation of the measured position x_{raw} from the one given by the linear fit x_{cal} is notated as δx.

A linear correlation between δx and x_{raw} is observed from figure 4.12. This obvious dependence is supposed to be caused by the rough estimation of the drift velocity at the first step,

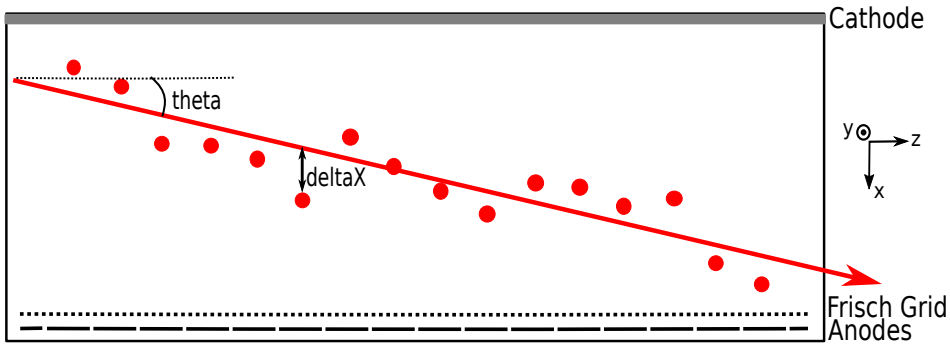

FIGURE 4.11: *Example of the position measurement in one section of the Twin MUSIC. Red circles represent measured positions in each anode. The large arrow corresponds to the trajectory of one fragment calculated from these positions via a linear fit. Then the horizontal angle θ of the trajectory with respect to the cathode plane is extracted. The deviation of the measured position to that given by the linear fit is notated as δx.*

implying that an refinement in the velocity is still needed:

$$\begin{aligned}\delta x &= x_{raw} - x_{cal} \\ &= \pm(dt_C - dt) \times (v_{raw} - v_{cal}) \\ &= \frac{x_{raw}}{v_{raw}} \times (v_{raw} - v_{cal}) \\ &= \frac{(v_{raw} - v_{cal})}{v_{raw}} \times x_{raw}\end{aligned}$$

So the slope of the correlation between δx and x_{raw} is equal to $a = (v_{raw} - v_{cal})/v_{raw}$, from which the optimized velocity v'_{raw} is expressed as:

$$v'_{raw} = v_{cal} = (1 - a) \times v_{raw}$$

Then the drift velocity in each anode is adjusted accordingly, and all X positions are recalculated. After that, the distribution of the fit residual (*i.e.* δx) in each anode is plotted and the mean value is acquired via a Gaussian fit, which is the offset to be subtracted to complete the optimization of the X position.

Extraction of horizontal angle

The distributions of the deviation between the optimized measurement of the X position and the calculated one are well aligned to each other and all are centered at 0, as seen in figure 4.13. The width of the distribution represents the resolution of the measured position in the anode. The central anodes show a good resolution with a mean value per anode equal to about 55 μm FWHM, while the rest exhibit a much broader distribution, implying a degraded resolution. It is seen that anode 1 and 16 show the worst resolution, which is caused by the fact that they are at the extremes of the Twin MUSIC, and thus suffering more from the noises in the surrounding.

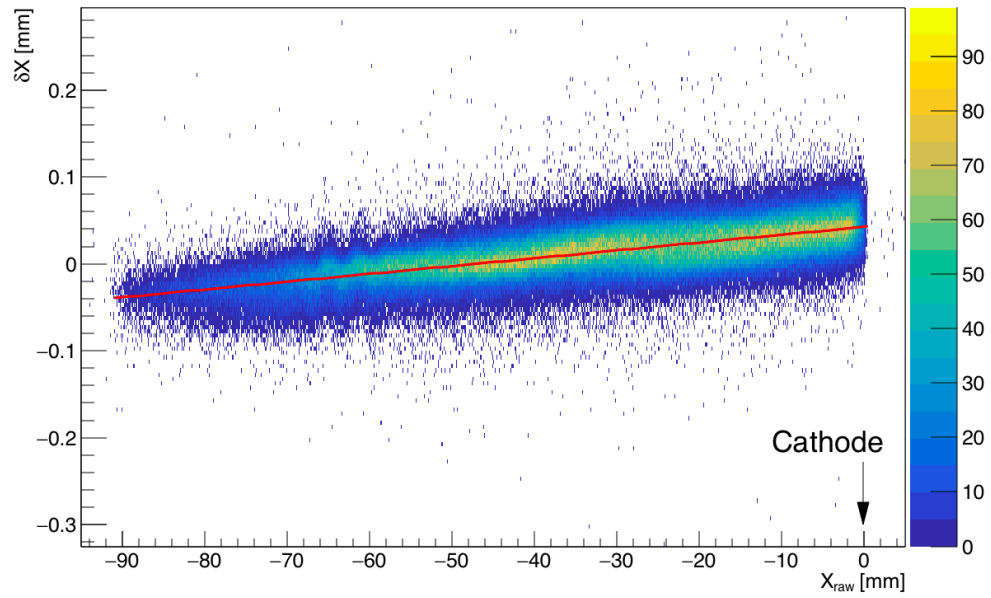

FIGURE 4.12: *Correlation between the fit residual (i.e. deviation of the measured position to that calculated by a fit of all measured positions) and the raw measured position for one anode. The dependence is described by a linear fit, which is represented by a red line on the figure.*

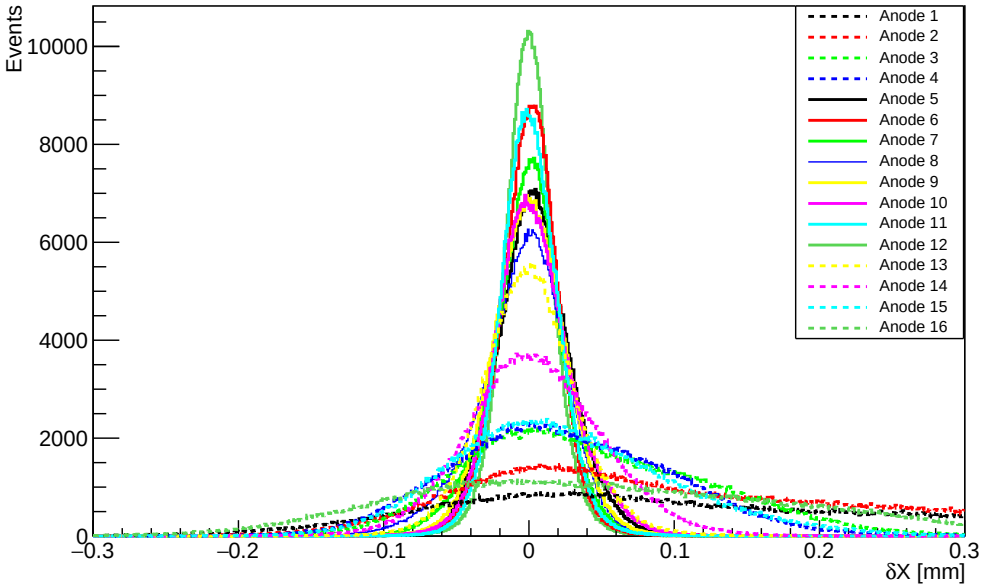

FIGURE 4.13: *Spectra of the fit residual for each anode in one section of the Twin MUSIC, after the optimization of measured X positions.*

Eventually, only positions measured in the 8 central anodes which show a good resolution are used to extract the horizontal angle of the trajectory for each fragment.

4.2.2.2 Tracking

The tracking of one fragment's trajectory is achieved by the measurements of the horizontal angle (by the Twin MUSIC), and vertical (*i.e.* along the Y axis) and horizontal (*i.e.* along the X axis) positions upstream (by the MWPC1) and downstream (by the MWPC2) the ALADIN dipole.

As mentioned before, the X and Y positions are measured independently on two pads of each MWPC, and they are not paired automatically. So, the first two parts of this section are concentrated on the association of X and Y positions in both MWPCs. Then two angles are given in the Twin MUSIC, and two pairs of X and Y positions are measured in each MWPC. Finally, one horizontal angle, and two pairs of positions both upstream and downstream the ALADIN, are assigned for each fission fragment on an event-by-event basis.

Association of X and Y positions in MWPC2

The association of the X and Y positions in the MWPC2 is realized due to the fact that this detector stands right in front of the vertically segmented ToF wall.

By comparing the signals, which two slats are hit can be easily known, leading to a rough estimation of the X positions. Besides, the Y position of each fragment is provided by the time difference of signals induced on two PMTs at both ends of the hit slat. Therefore, the X and Y positions are coupled automatically in the ToF wall.

Since the MWPC2 is located very close to the ToF wall, the correspondence in both X (left or right) and Y (top or bottom) positions is maintained between two detectors. Then it is straightforward to associate the X and Y positions in the MWPC2.

Counting the vertical slats in the ToF wall from left to right, the first hit slat is labeled as slat 1, and the Y position of the fragment impinging on this slat is notated as Y_{slat1}. Accordingly, the second hit slat and the corresponding Y position are recorded as slat 2 and Y_{slat2}, respectively. The minimum and the maximum of the two X positions provided by the MWPC2 are labeled as $X2_{min}$ and $X2_{max}$, respectively. Similarly, the Y positions of both fragmented are notated as $Y2_{min}$ and $Y2_{max}$.

The comparison between Y_{slat1} and Y_{slat2} guides to the association of X and Y positions measured in the MWPC2:

- if $Y_{slat1} < Y_{slat2}$, the left fragment at the bottom, the right fragment on the top, as seen in figure 4.14. The positions are assigned to the fragments as ($X2_{min}$, $Y2_{min}$) and ($X2_{max}$, $Y2_{max}$).
- if $Y_{slat1} > Y_{slat2}$, the left fragment on the top, the right fragment at the bottom. The positions are assigned to the fragments as ($X2_{min}$, $Y2_{max}$) and ($X2_{max}$, $Y2_{min}$).

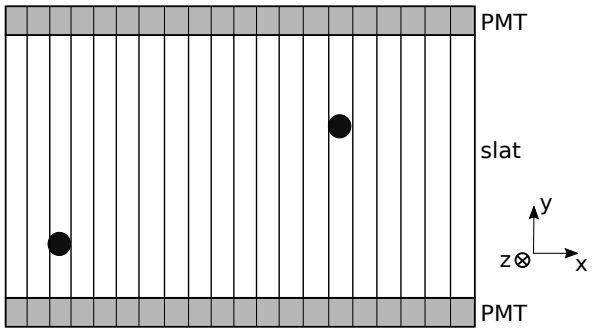

FIGURE 4.14: *Example of the layout of the incident positions on the ToF wall. Both the Y and the rough X positions of the fragment can be extracted from the hit plastic slat, and they are associated automatically, making themselves a reference for the association of the X and Y positions measured in the MWPC2, which stands right upstream the ToF wall.*

Association of X and Y positions in MWPC1

Benefiting from horizontally dividing its X-strips into halves, the MWPC1 itself is sufficient to associate the measured X and Y positions in most cases, because normally one fragment strikes the upper half plane of the X-strips and the other strikes the lower half plane.

The X positions measured by the upper and lower X-strips are notated as $X1_{up}$ and $X1_{down}$, and two Y positions are named as $Y1_{min}$ and $Y1_{max}$ depending on their relative values.

The comparison between $X1_{up}$ and $X1_{down}$ clarifies the situation as follows:

- if $X1_{up} < X1_{down}$, the left fragment on the top, the right fragment at the bottom, as seen in figure 4.15.
- if $X1_{up} > X1_{down}$, the left fragment at the bottom, the right fragment on the top.

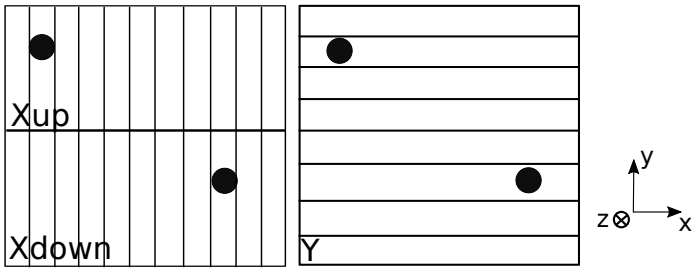

FIGURE 4.15: *Example of the association of the X and Y positions, which are measured independently by different planes in the MWPC1. One fragment hits the upper half plane of the X-strips, and the other one hits the lower part. The association is pretty straightforward in this case.*

However, regardless of the result of the comparison, $X1_{up}$ and $X1_{down}$ are necessarily paired to $Y1_{max}$ and $Y1_{min}$, respectively. That is to say in the events two fragments penetrate different half planes of the X-strips, the positions are always attributed as ($X1_{up}$, $Y1_{max}$) and ($X1_{down}$, $Y1_{min}$) to the fragments.

In the rest cases, both fragments hit the same half plane of the X-strips, the association of X and Y positions then becomes quite complicated and the information from other detectors is also needed. In the analysis of this PhD, these cases have not been considered yet.

Tracking

Until now, the association of X and Y positions has been realized in both MWPCs. And two pairs of positions (one from each MWPC) are assigned to each fragment, according to the consistency in the Y positions upstream and downstream the ALADIN, *i.e.* the upper fragment in the MWPC1 remains the upper one in the MWPC2.

In order to perform the tracking, a horizontal angle measured in the Twin MUSIC still needs to be attributed to each fragment. It is known that the Twin MUSIC consists of four identical sections, with two on each side of the central cathode plane (one up and one down). The two fragments fly through different sections of the Twin MUSIC, making themselves well separated in the X or/and Y position. Since the Twin MUSIC stands right behind the MWPC1, the relativity in both X and Y positions is kept for each fragment between two detectors. Then it is very straightforward to assign a horizontal angle and a pair of positions measured in the MWPC1 to one fragment.

For example, if the fragments penetrate the left-up and the left-down sections in the Twin MUSIC, the horizontal angle measured in the former (resp. latter) section should be attributed to the upper (resp. lower) fragment in the MWPC1.

Finally, an horizontal angle upstream the ALADIN, and a pair of X and Y positions measured in both MWPCs are assigned to each fragment. Based on these quantities, a complete trajectory can be reconstructed. And the reconstruction method will be explained extensively in the next part.

4.2.2.3 Trajectory reconstruction

As already mentioned, each fragment is attributed with two pairs of X and Y positions and a horizontal angle. According to the geometric correlations between these quantities and the known parameters, *i.e.* the locations of the detectors as well as the ALADIN magnet along the beam axis and some angles, the trajectory of each fragment can be reconstructed, as seen in figure 4.16.

The geometric model shown in the figure is developed on the basis of the one used in [22], and it has been adjusted accordingly for the upgraded experimental setup. The total trajectory length is computed step by step as follows [22].

Positions upstream and inside ALADIN

The position of the fragment at the center of the magnet is inferred as:

$$x_C = \frac{1}{1+\tan\alpha\times\tan\theta}\times(x_A+(z_{ALADIN}-z_{MWPC1})\times\tan\theta)$$
$$z_C = z_{ALADIN}-x_C\times\tan\alpha$$

where x_A is the horizontal position measured in the MWPC1, and θ is the angle measured in the Twin MUSIC for the fragment.

Then the fragment's position at the entrance of the magnet is expressed as :

$$x_B = x_C-\frac{L}{2}\times\frac{\sin\theta}{\cos(\theta-\alpha)}$$
$$z_B = z_C-\frac{L}{2}\times\frac{\cos\theta}{\cos(\theta-\alpha)}$$

where L is the effective length of the ALADIN magnet: L = 1400 mm.

Positions downstream ALADIN

The positions of the fragment measured by the MWPC2 in the (X, Y, Z) frame are notated as (X_E, Y_E, Z_E). They are transformed to the laboratory frame as:

$$x_E = (z_{MWPC2}-z_{ALADIN})\times\sin\beta+X_E\times\cos\beta$$
$$y_E = Y_E$$
$$z_E = z_{ALADIN}+(z_{MWPC2}-z_{ALADIN})\times\cos\beta-X_E\times\sin\beta$$

leading to:

$$\eta = \arctan\left(\frac{x_E-x_C}{z_E-z_C}\right)$$

Then the position at the ToF wall can be derived:

$$x_F = x_E+\frac{(z_{ToFW}-z_{MWPC2})\times\sin\eta}{\cos(\eta-\beta)}$$
$$z_F = z_E+\frac{(z_{ToFW}-z_{MWPC2})\times\cos\eta}{\cos(\eta-\beta)}$$

and the position at the exit of the magnet is:

$$x_D = x_C+\frac{L}{2}\times\frac{\sin\eta}{\cos(\eta-\alpha)}$$
$$z_D = z_C+\frac{L}{2}\times\frac{\cos\eta}{\cos(\eta-\alpha)}$$

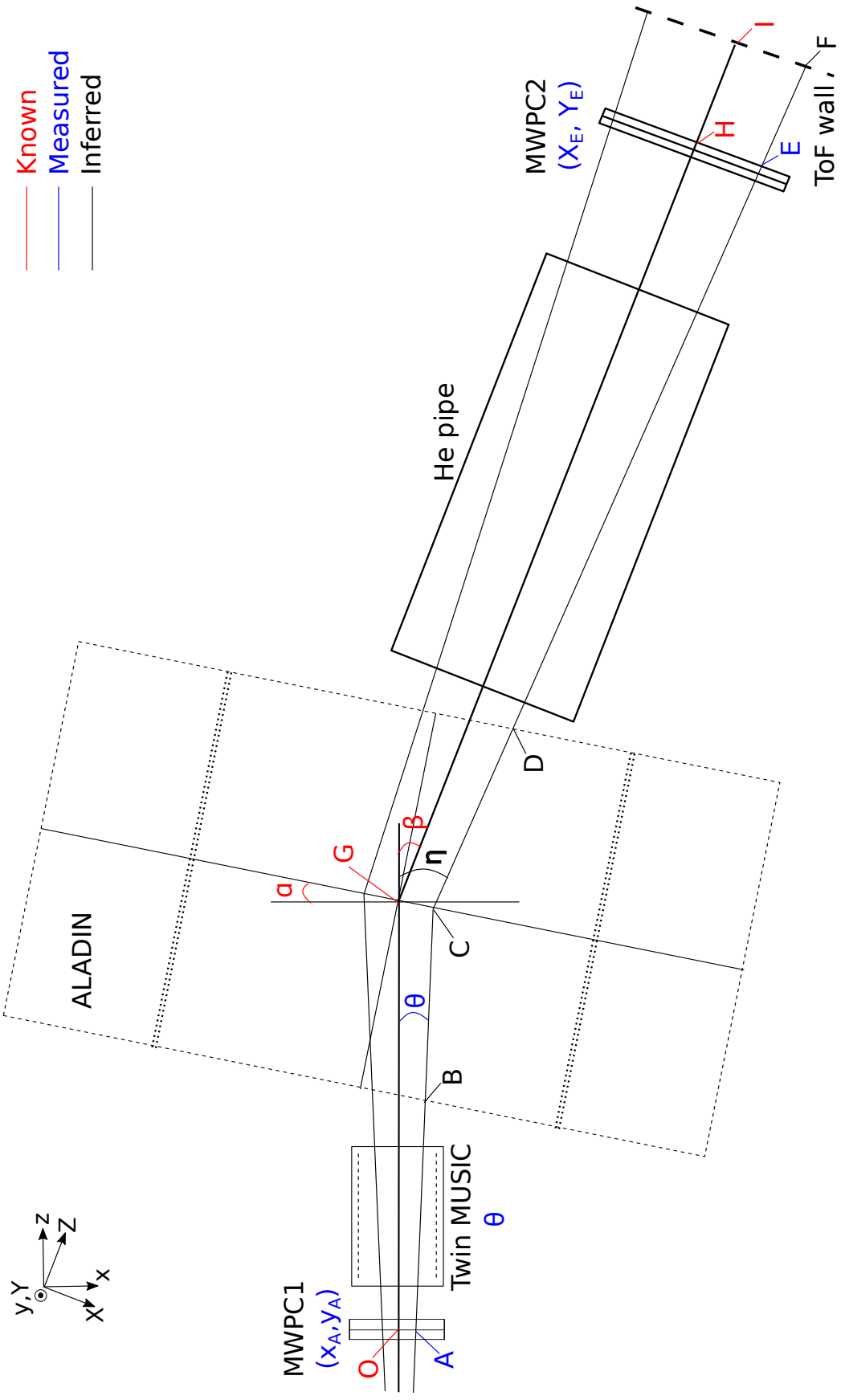

FIGURE 4.16: *Geometric model used for the trajectory reconstruction of the fragments.*

The known angles are α = 7.2° and β = 0.23 rad, and the values of the locations of the detectors as well as the ALADIN magnet (*i.e.* z_{MWPC1}, z_{MWPC2}, z_{ToFW} and z_{ALADIN}) are listed in figure A.1.

Trajectory

The trajectory of the fragment on the xz plane (*i.e.* the plane of the model) is defined by:

- the curvature radius:

$$\rho = Abs\left(\frac{L}{2\sin(\frac{\eta-\theta}{2}) \times \cos(\alpha - \frac{(\eta+\theta)}{2})}\right)$$

- the covered angle:

$$\omega = Abs\left(2\sin^{-1}\frac{\sqrt{(z_D - z_B)^2 + (x_D - x_B)^2}}{2 \times \rho}\right)$$

- and the trajectory length:

$$L_{xz} = \frac{z_B - z_{fission}}{\cos\theta} + \rho \times \omega + \frac{z_F - z_D}{\cos\eta}$$

  where $z_{fission}$ is the position of the fission location along the z axis, which is estimated as that of the center point of the layer in which fission occurs.

The position of the fragment along the y axis at the ToF wall is:

$$y_F = (y_E - y_{fission}) \times \left(\frac{z_F - z_{fission}}{z_E - z_{fission}}\right) + y_{fission}$$

where $y_{fission}$ is the y position of the secondary beam at fission, which is approximately equal to that measured in the MWPC0 right ahead of the active target. When the beam is well centered, this term can be neglected.

Finally, after considering the deviation in the y direction, the total length of the fragment's trajectory is computed as:

$$\begin{aligned} L_{tot} &= \sqrt{L_{xz}^2 + (y_F - y_{fission})^2} \\ &= \sqrt{\left(\frac{z_B - z_{fission}}{\cos\theta} + \rho \times \omega + \frac{z_F - z_D}{\cos\eta}\right)^2 + \left((y_E - y_{fission}) \times \left(\frac{z_F - z_{fission}}{z_E - z_{fission}}\right)\right)^2} \end{aligned}$$

4.2.2.4 Time of flight

Time-of-flight calibration

Similar to the case of the secondary beam, as mentioned in subsection 3.2.1, a calibration is also needed to extract the real time of flight for each fission fragment, from the measurements performed between the STOP IB detector and one slat of the ToF wall.

To obtain the offset in the time of flight for each plastic slat (*i.e.* ΔToF_i, i = 0, 1, . . . , 27), a set of runs using the primary beam are implemented. Among the runs, the magnetic field of the ALADIN dipole varies, and thus the beam's trajectory is deflected to different extents, finally leading to a slat-by-slat scan of the complete ToF wall.

It is known that:

$$v_{PB} = \frac{L_i}{ToF_i + \Delta ToF_i}$$

which leads to:

$$\Delta ToF_i = \frac{L_i}{v_{PB}} - ToF_i$$

where L_i is the length of the beam's trajectory ending at the *i*th slat of the ToF wall, v_{PB} is the mean velocity of the primary beam, and ToF_i is the raw time of flight measured between the STOP IB detector and the considered slat.

As already discussed, the time-of-flight calibration for the secondary beam is achieved by using four primary beam runs at various energies, because the trajectory length is not directly measured. However, the length of the trajectory here (L_i) can be computed via a geometric model (see the previous part). Then, after knowing the velocity of the primary beam (v_{PB}) from a simulation in LISE++, the time-of-flight offset for each slat can be derived from the above equation, implying that a single set of sweep runs at the same beam energy is sufficient.

Time of flight of fission fragments

As seen in the scheme of the setup (figure 4.1), the active target in which fission occurs stands between the STOP IB detector and the ToF wall, implying that the time of flight measured by the latter detectors is a sum of that of one fragment and a part of that of the secondary beam.

Since the accuracy of the measured velocity for the fragment is critical to the resolution of the mass identification, the time-of-flight measurement needs to be as precise as possible. Consequently, the portion of the time-of-flight corresponding to the secondary beam has to be excluded, leading to:

$$\begin{aligned} ToF_{FF} &= ToF_{calib.} - ToF_{SB} \\ &= ToF_{calib.} - \frac{(z_{fission} - z_{STOP})}{v_{SB}} \end{aligned}$$

where $ToF_{calib.}$ is the calibrated time-of-flight given by the STOP IB detector and the hit slat of the ToF wall, $z_{fission}$ is the fission location extracted from the measurements performed in the active target, z_{STOP} is the longitudinal position of the STOP IB detector (already known),

and v_{SB} is the velocity of the secondary beam, which is computed from the combination of the measurement between S2 and Cave C and the simulation in LISE++.

As previously presented, the association of X and Y positions measured in the MWPC2 is achieved due to its correlation to the ToF wall, implying that which slat is hit by the fragment is already known when a pair of X and Y positions are attributed to one fragment. Then it is straightforward to assign one time-of-flight to each fragment's trajectory. Finally the velocity can be obtained precisely for both fission fragments.

4.2.2.5 Energy loss corrections

Similar to the situation of the secondary beam, before extracting the nuclear charge of the fission fragments from the energy loss measured in the Twin MUSIC, the latter needs to be corrected first to optimize the resolution of the measurement. In this part, corrections of the dependences of the energy loss on several parameters will be introduced.

Since the main dependences on the velocity and the drift time (equivalent to the X position measurement) have been explained extensively in the part corresponding to the secondary beam, they are only illustrated briefly here, to show the case of the fission fragments.

The energy loss of each fragment in the Twin MUSIC is taken as the sum of the aligned energy losses in the 14 central anodes in the section which is penetrated by the fragment.

Correction of dependence on velocity

The correlation between the raw energy loss and the fragment's velocity is shown on the left of figure 4.17. After the dependence is fully corrected, the correlation is plotted accordingly on the right of the figure. Each band on the plot corresponds to one Z, namely one element.

Correction of dependence on X position in Twin MUSIC

The correlation between the energy loss and the fragment's horizontal position in the Twin MUSIC is presented in figure 4.18. The latter is derived from the drift time measurement, as explained in part 4.2.2.1.

An obvious decrease in the energy loss signal is observed when the fragment is near to the position X = 0 mm, where the cathode plane of the detector stands. The drop is caused by the fact that the ionization electrons produced near the central cathode may be absorbed by the latter or go through it, entering the opposite side of the Twin MUSIC, and thus do not arrive at the anodes on the original side as expected.

Refinement of time-of-flight offsets

It has been discussed in part 4.2.2.4 that the time of flight measured between the STOP IB detector and each slat of the ToF wall is calibrated by using of a set of primary beam runs.

However, the offsets are not as precise as expected, which is reflected by the dependence of the energy loss (already corrected on the velocity and the horizontal position in the Twin

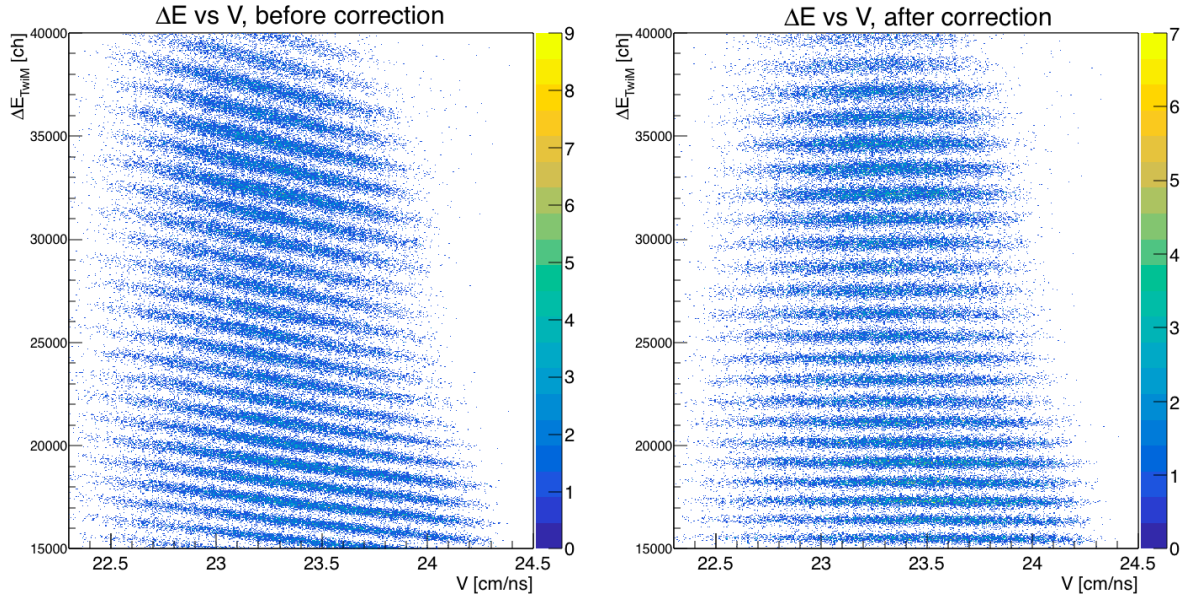

FIGURE 4.17: *Energy loss in the Twin MUSIC vs. velocity for the fission fragments. Left: Correlation before the correction of the dependence of the energy loss on the velocity. Right: Correlation after the correction.*

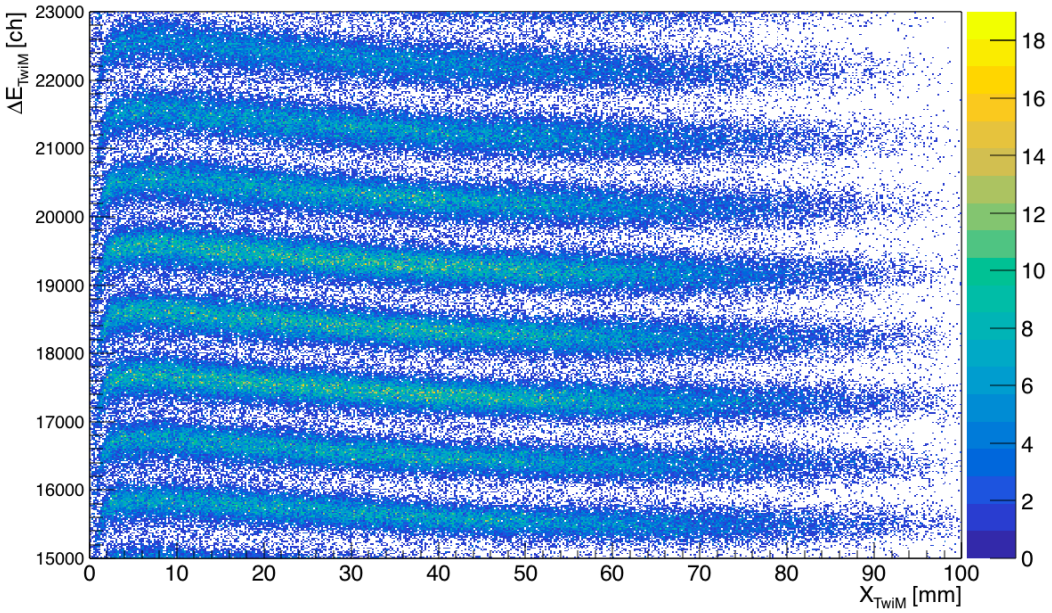

FIGURE 4.18: *Correlation between the energy loss and the fragment's horizontal position in the Twin MUSIC (not corrected yet).*

MUSIC) on the X position measured by the MWPC2 (corresponding to the slat number of the Tof wall), as seen in figure 4.19.

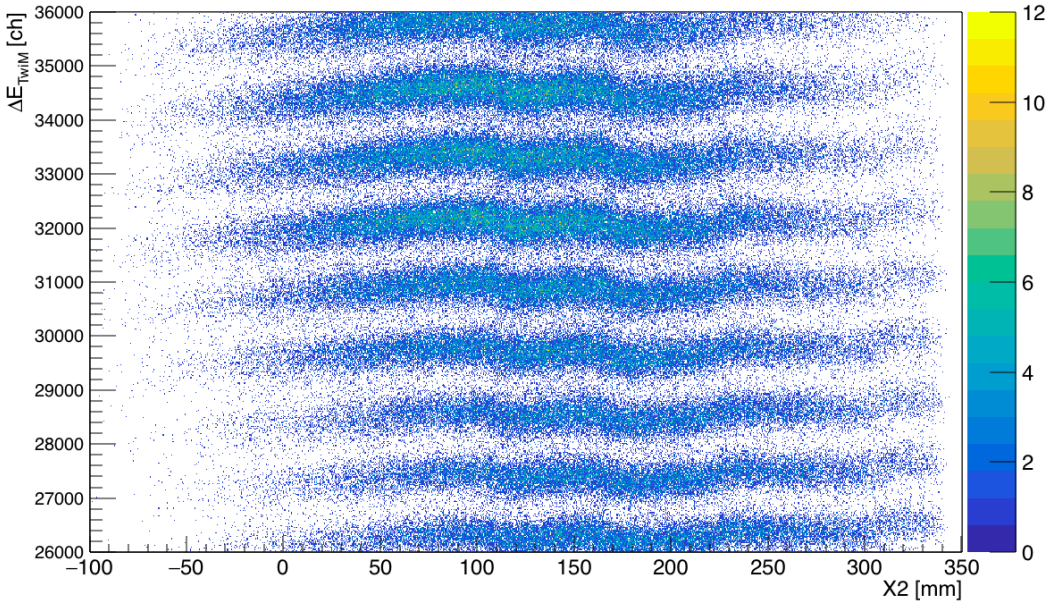

FIGURE 4.19: *Correlation between the energy loss in the Twin MUSIC and the X position measured by the MWPC2 for the fission fragments. This dependence can be corrected by a refinement in the time-of-flight offsets.*

The calibration is not fully achieved for the fission fragments due to the time-walk effect in the ToF wall, *i.e.* the time measurements of the incident particle vary with its energy deposited in the hit slat. Since there is a considerable difference in the amount of the energy deposited by the primary beam and the fission fragments, the offsets obtained with the beam runs are not exactly applicable for the time-of-flight measurement of the fragments.

Therefore, a refinement in the offsets is needed. After that, the observed dependence of the energy loss on the X position measured by the MWPC2 will be corrected.

Correction of dependence on Y position measured by MWPC

A minor dependence of the energy loss on the Y position is also observed, as seen in figure 4.20.

It is said before that the energy loss of the fragment is computed as the sum of the energy losses measured in the 14 central anodes in the section which the fragment passes through. Actually, if the fragments fly on opposite sides (*i.e.* left- and right- side) of the cathode plane, energy losses in the other section on the same side as the penetrated one should be considered as well for each fragment, because when the trajectory is very close to the gap between the upper and lower sections, a portion of the energy is also deposited to the non-penetrated section.

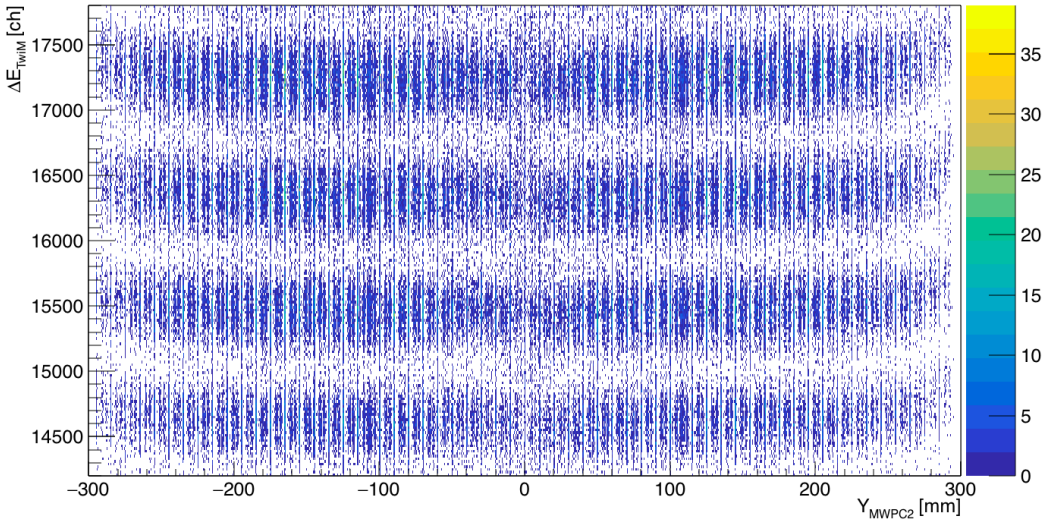

FIGURE 4.20: *Correlation between the energy loss in the Twin MUSIC and the Y position measured by the MWPC2 for the fission fragments.*

For example, one fragment flies through the left up section, while the other fragment flies on the right side of the detector, the energy loss of the former should be computed as:

$$\Delta E = \sum_{i=1}^{14} (\Delta E_{LU_i} + \Delta E_{LD_i})$$

Otherwise, an extra slight dependence will be unintentionally introduced at Y = 0 mm.

4.2.2.6 Extraction of Z from ΔE

At the moment, corrections of the dependence on all the aforementioned parameters have been implemented. The spectrum of the corrected energy loss of the fission fragments is presented in figure 4.21. At the first look of the spectrum, those well separated peaks suggest that a satisfactory resolution of the energy loss signal has been achieved.

It is well known that the even-odd staggering (*i.e.* the elements with an even atomic number are more produced than their neighbours) is expected to be observed in the fragment charge yield of low-energy fission (which is our case) [59]. Since each peak in the energy loss spectrum represents one element (namely one Z), the peak with a larger amplitude as compared to the adjacent ones corresponds to an even-Z, which gives the first hint to the ΔE - Z conversion.

In the figure, only fission events of the ^{236}U secondary beam occurring in the three high-Z targets in the active target are considered. As previously discussed, these fission events are mainly induced by the Coulomb excitation, implying that the number of protons of the secondary beam is conserved in the fission fragments, *i.e.* $Z_{FF1} + Z_{FF2} = Z_{SB}$ = 92. Therefore,

if the conversion is appropriately performed, a dominant peak centered at 92 should be observed on the charge-sum spectrum of the fission products. Based on this criterion, an absolute calibration of the nuclear charge of the fragments can be finally achieved.

Specifically speaking, the calibration is implemented in the following manner:

1. The highest peak in the heavy fragment group (*i.e.* the group showing relatively larger energy losses) on the energy loss spectrum is associated with a reasonable even-Z, like 50, as a start. Then, other peaks are associated with some Z values accordingly.
2. The points exhibiting the pairs of (Z, ΔE) values acquired in the previous step are plotted, as seen in figure 4.22. A second order polynomial function is applied to fit the tendency of these points, which is represented by the black curve in the figure.
3. According to the fit function, the nuclear charges of the fission fragments are derived from their energy losses on an event-by-event basis. Then it is straightforward to obtain the charge-sum spectrum of the fragments.
4. If the starting even-Z is 2 units smaller than the true value, a shift of 4 units as compared to 92 will be noticed in the mean value of the dominant peak on the charge-sum spectrum, because both the light and heavy fragments are underestimated by 2 units in every single event. Then, according to the deviation of the main peak from 92, the real value of the starting Z can be easily deduced.
5. With the updated starting even-Z, the first three steps are repeated. Finally, a remarkably enhanced peak at 92 is observed on the charge-sum spectrum, confirming that the absolute calibration of the nuclear charge of the fission products is properly achieved.

The resulting nuclear charge distribution of the fission fragments is drawn in figure 4.23, showing an excellent resolution for the light fragments with a value of 0.35 FWHM at Z = 39, and a slightly degraded resolution for the heavy ones with 0.42 FWHM at Z = 53.

4.2.2.7 Optimization of the nuclear charge distribution

It is noted that after applying common corrections to all the fission fragments, the corrected energy loss signal is completely independent on the X position in the Twin MUSIC for the light fragments, while a slight dependence still remains for the heavy fragments, as respectively seen on the left- and right- side of figure 4.24, implying that the correlation between the raw energy loss and the X position varies gradually with the energy loss itself (or to say the fragment's nuclear charge, since each band corresponds to one Z).

This charge-dependent feature of the dependence of the energy loss on a certain quantity is believed to be caused by the cross-talk between the left and right sides of the Twin MUSIC: a fraction of the electrons produced due to the ionization of the gas atoms cross the central cathode plane and arrive at the anodes on the opposite side, inducing signals on them. The existence of the cross-talk effect is confirmed by the unexpected correlation between the energy loss of one fragment on one side of the Twin MUSIC and the X position of the other fragment on the opposite side, as seen in figure 4.25.

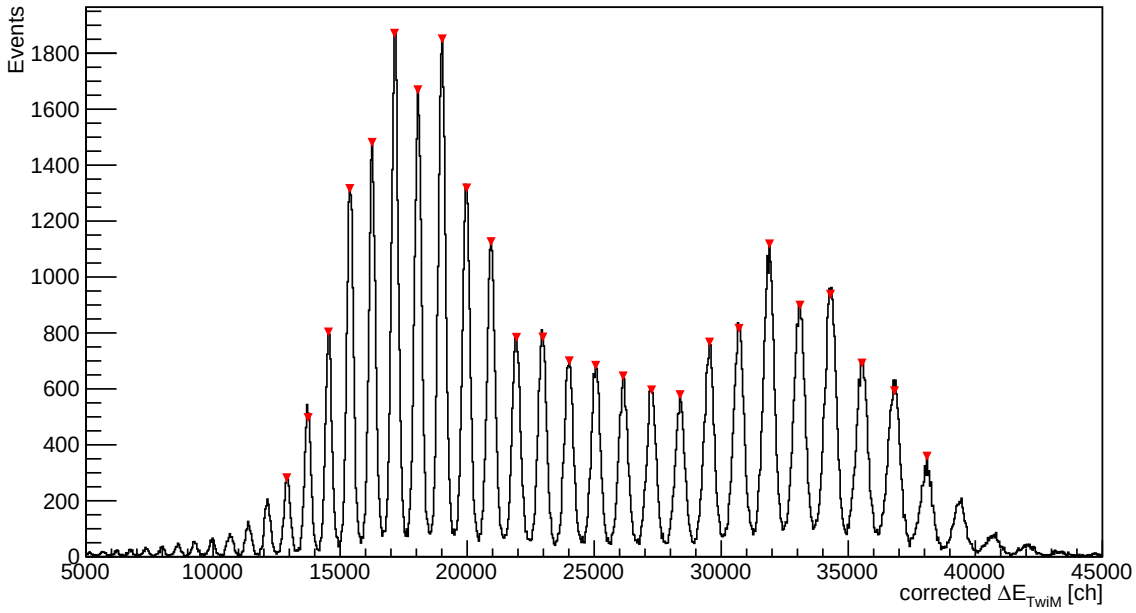

FIGURE 4.21: *Spectrum of the optimized energy loss signal of the fission fragments. Only fission events of ^{236}U occurring in the three high-Z foils in the active target are taken into account.*

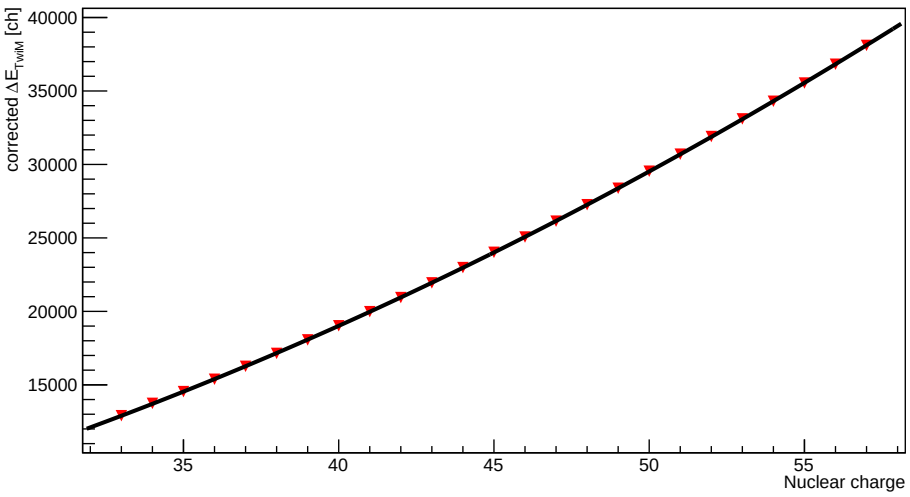

FIGURE 4.22: *Correlation between the energy loss and the nuclear charge for the fission fragments, after their correspondence is correctly established. The black curve represents the quadratic function used to fit the correlation. Each point on the plot corresponds to one peak indicated by a red triangle on the above energy loss spectrum.*

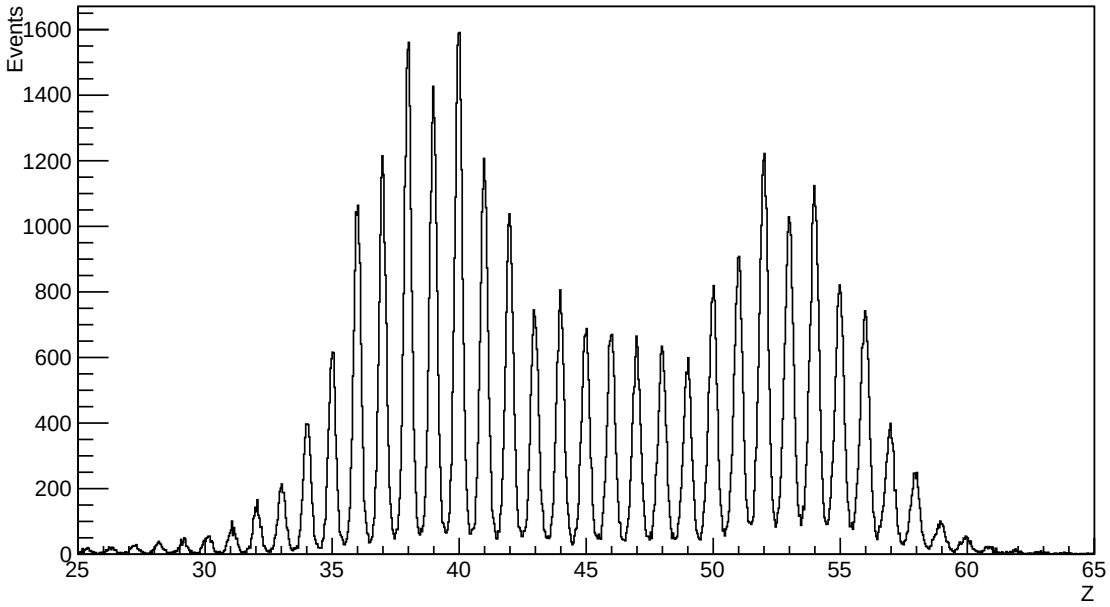

FIGURE 4.23: *Spectrum of the nuclear charge of the fission products. Only fission events of ^{236}U occurring in the three high-Z foils in the active target are taken into account.*

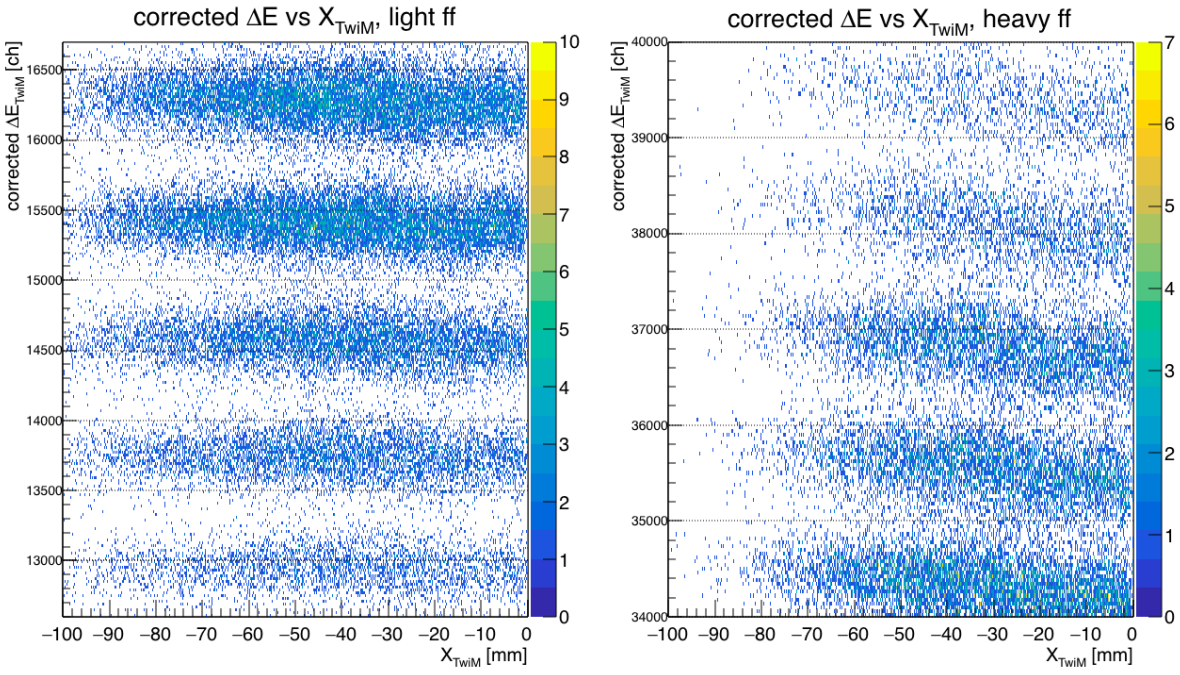

FIGURE 4.24: *Corrected energy loss vs. X position in the Twin MUSIC, for the light fragments (left) and the heavy fragments (right).*

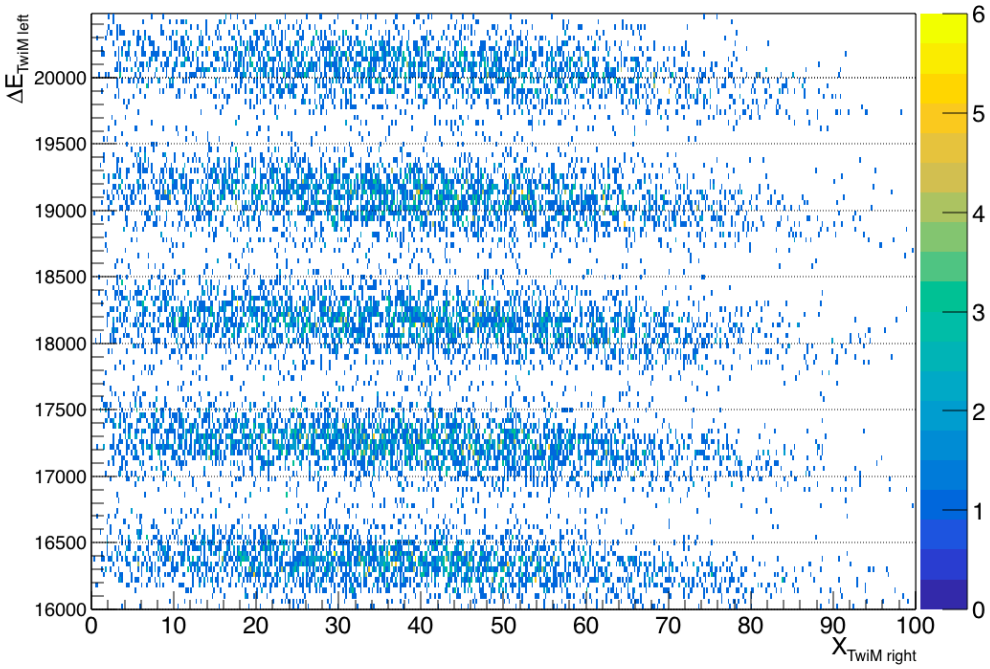

FIGURE 4.25: *Energy loss of the fragment on the left side of the Twin MUSIC vs. X position of the other fragment on the right side, which gives a proof of the cross-talk effect.*

It seems that the former quantity decreases with the increasing amplitude of the latter, which can be explained by the fact that the further away the fragment from the cathode (X = 0 mm), the less probable that the ionization electrons drift across it, and thus a smaller extra energy signal is induced on the other side of the detector.

The influence on the measured energy loss of a light fragment due to the cross-talk is more obvious than that for a heavy fragment: on one hand, its complementary fragment is a heavy one, resulting in more ionization electrons, and thus a larger extra signal is introduced to the light fragment; on the other hand, its original energy loss is relatively small, making itself more sensitive to the extra energy signal of a certain amplitude.

However, it is above mentioned that the residual dependence is observed on the heavy fragments rather than the light ones, because the correlations of the raw energy loss of a light fragment to the considered parameters are always chosen as a reference to cover the full range, and the corrections are implemented accordingly. As a result, the correlations concerning the light fragments are properly corrected, while they are over-corrected for the heavy fragments, leading to the adjusted energy loss still gently dependent on the parameters, which is assumed to be partly responsible for the fact that the resolution of the measured nuclear charge of the heavy fragments is less satisfactory as compared to that of the light ones.

So, to avoid the deterioration of the nuclear charge resolution, the cross-talk effect has to be considered. Yet because of its charge-dependent characteristic, it is very tricky to apply a direct correction to this effect (*i.e.* to the dependence of the energy loss of one fragment on

the X position of the other fragment in the Twin MUSIC). There are two possible approaches: either to correct every band of the dependence separately with various functions, or to develop a universal function whose coefficients vary with the energy signal.

Alternatively, I did not correct the cross-talk effect, but chose to eliminate its negative influence on the nuclear charge resolution:

1. Instead of obtaining the correlation between the corrected energy loss and the X position in the Twin MUSIC over the whole X range for all the fragments, as seen in figure 4.24, the correlation is obtained as a combination of several sub-correlations with each covering a small range of the X position, just like the original plot is segmented vertically into slices.
2. Every sub-correlation is projected onto the energy loss coordinate, resulting in several energy loss spectra of the fragments, each associated with a X sub-range. The light fragments peaks are all aligned, but the heavy ones are not.
3. For each energy loss spectrum, a quadratic function describing the correlation between the energy loss and the nuclear charge is obtained accordingly.
4. In every single event, according to its X position in the Twin MUSIC, each fragment is attributed with a quadratic function. Based on the function, the nuclear charge of the fragment is then extracted from its energy loss.
   For a certain fragment, since the quadratic function is assigned to it depending on its X position, even though the energy loss varies with the latter (*i.e.* the residual dependence), the nuclear charge can still be correctly derived on an event-by-event basis. Consequently, the final nuclear charge resolution would not be deteriorated by the non-fully corrected energy loss.

This approach proves to be effective: the resolution for the heavy fragments is eventually improved to 0.39 FWHM at Z = 53 instead of 0.42.

Chapter 5

Extraction of the elemental fission yield and discussion

5.1 Extraction of the elemental fission yield

In the previous chapter, the nuclear charge distribution of the fission fragments of ^{236}U over the whole range has been obtained. Based on this, the extraction of the elemental fission yield will be performed.

There are mainly two mechanisms leading to the fission events which occur in the targets in the SOFIA experiment: nuclear collision and Coulomb excitation. As already discussed in subsection 2.4.2, it is impossible to measure the excitation energy event by event in our case, and only an average value is estimated from the excitation energy spectrum. Since the spectrum is more compact for the Coulomb excitation, implying a relatively lower deviation from the mean value of the energy in each event, we can have a better control on the excitation energy in this case. Consequently, we are solely interested in the Coulomb-induced fission. Therefore, the first part of this section is dedicated to the extraction of the nuclear charge distribution of the fragments which are purely produced by the Coulomb-induced fission. Then the efficiency of the experimental setup is taken into account. Because if the efficiency differs for various fragments, it will influence the shape of the elemental fission yield spectrum. Finally, the elemental yield of the fragments produced in the fission events following the Coulomb excitation is presented, and the calculation of the associated uncertainties is explained.

5.1.1 Extraction of Coulomb-induced fission

5.1.1.1 Rejection of events in which the total charge is not equal to 92

In the nuclear-induced fission event, due to the violent collision between the projectile and target nuclei, some nucleons (protons and/or neutrons) are abraded from the projectile, resulting in a residual nuclide with an excitation energy up to a few hundreds of MeV. Considering of such a high excitation energy, then the proton evaporation may occur before the projectile-like nuclide de-excites through fission. That is to say, in the fission events following the nuclear collision, it is possible to undergo a removal of proton(s) due to the abrasion and/or the evaporation, leading to the number of protons of the fissioning nucleus lower than that of the secondary beam. Therefore, the total charge of the two fission fragments is less than that of the ^{236}U secondary beam, namely 92.

On the contrary, in the Coulomb-induced fission, there is no abrasion process, and the available excitation energy is not sufficient to undertake the proton evaporation, implying that all the protons of the secondary beam remain in the fissioning system. Therefore, the total charge of the fragments produced in the Coulomb-induced fission is equal to 92.

Consequently, a fraction of the fission events induced by the nuclear collision can be easily rejected by requiring that the total charge of the fission fragments equals to that of the secondary beam. Since the nuclear charges of both fission fragments are identified simultaneously event by event, this rejection is also performed on an event-by-event basis.

It is known that the value directly derived from each fragment's energy loss in the Twin MUSIC via a quadratic conversion is taken as the nuclear charge of the fragment, implying that

the true nuclear charge, which is an integer, is represented by a real number. This is the reason for the appearance of Gaussian-shaped peaks in the nuclear charge distribution of fission fragments obtained in the previous chapter. Each peak is centered at an integer and approximately covers a unit, as seen in figure 4.23.

Now the question arises: should we sum the two real numbers directly derived from the energy loss $Z_1 + Z_2$ to get the total charge of the fission fragments Z_s, or should we add the integer numbers $I(Z_1) + I(Z_2)$, where $I(Z_1)$ and $I(Z_2)$ are the closest integers of Z_1 and Z_2 respectively? In other words, when the condition that total charge of the fragments is equal to 92 is applied, should we perform $Z_s = I(Z_1 + Z_2)$ or $Z_s = I(Z_1) + I(Z_2)$?

In figure 5.1, the correlation between measured nuclear charges (real numbers, *i.e.* Z_1 and Z_2) of both fission fragments of ^{236}U nuclei is presented. As indicated in the figure, each diagonal series of spots corresponds to one total charge, *i.e.* one fissioning system.

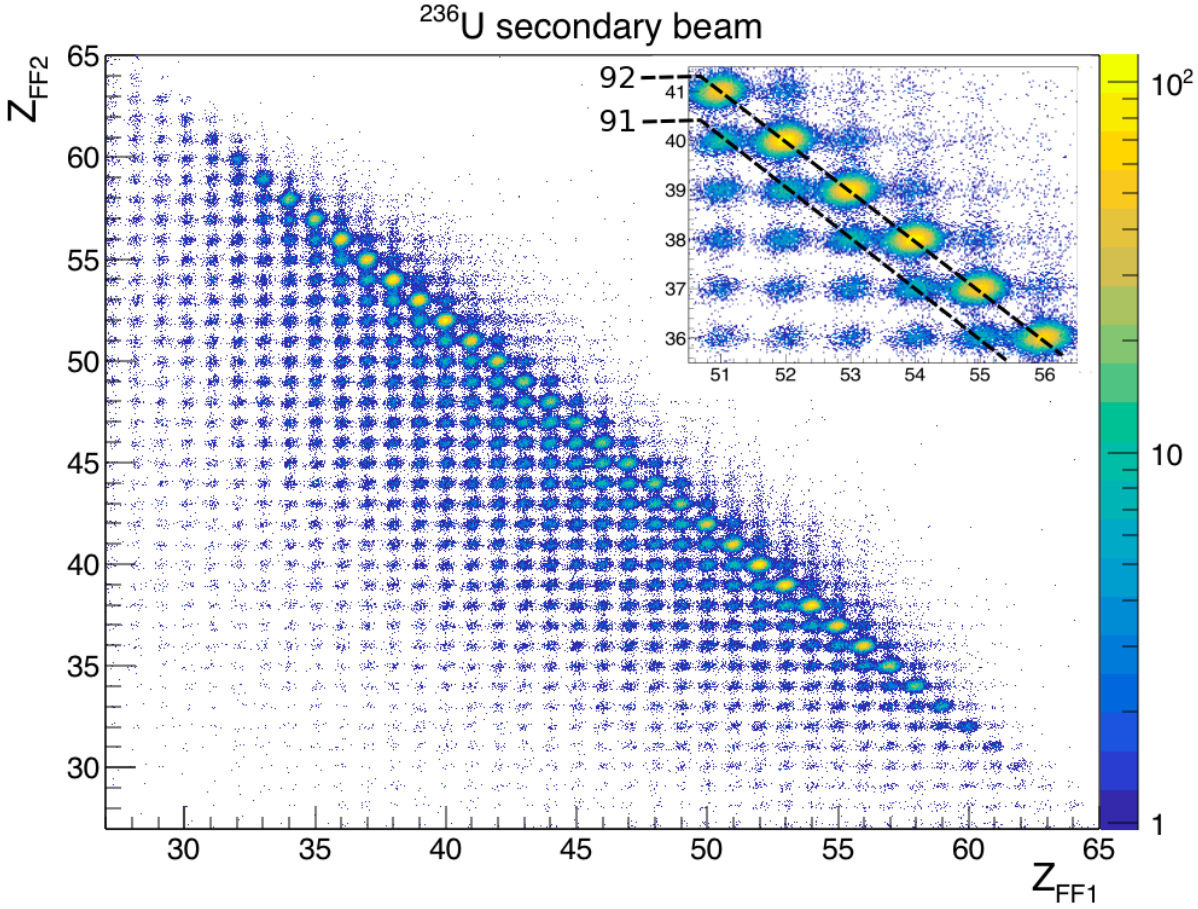

FIGURE 5.1: *Correlation between measured nuclear charges of both fission fragments of the ^{236}U secondary beam. Fission events occurring in the targets in the Active Target are considered. Each diagonal series of spots corresponds to one fissioning system.*

If the total charge of the fragments is taken as $Z_s = I(Z_1 + Z_2)$, then applying the condition $Z_s = 92$ is equivalent to select the events limited by two diagonal lines $Z_1 + Z_2 = 91.5$ and $Z_1 + Z_2 = 92.5$ in figure 5.1. The result is shown on the top of figure 5.2.

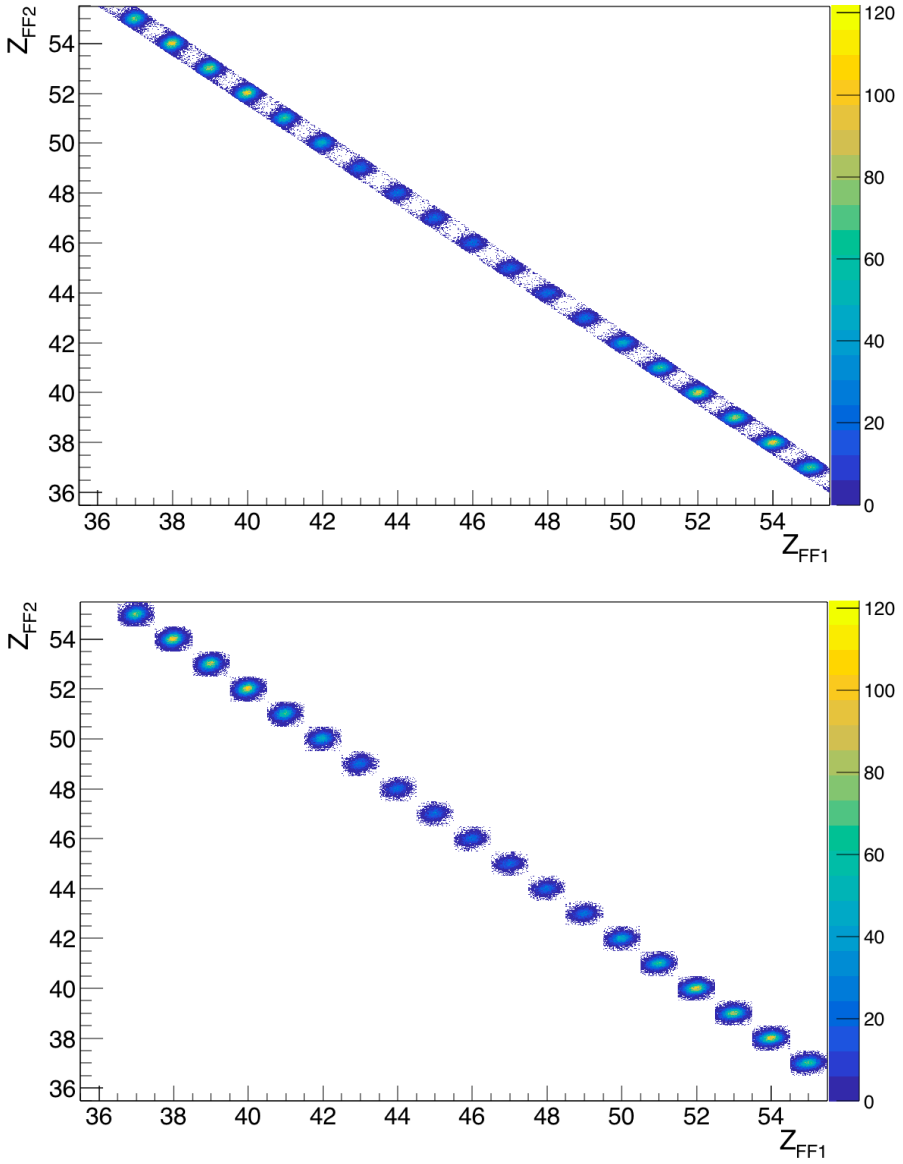

FIGURE 5.2: *Selection of events in which the total charge of the fragments is equal to 92. Top: the sum of nuclear charges directly derived from each fragment's energy loss (real numbers) is used to get the total charge. Bottom: the sum of the closest integers of the above mentioned nuclear charges is taken as the total charge.*

It is clearly seen that in the gap between spots representing the desired events in which $Z_s = 92$, there are tails of events coming upwards ($Z_s = 91$) and downwards ($Z_s = 93$). In addition, at both the lower and upper edges, a fraction of the $Z_s = 92$ events are cut out, and they will appear in the selection of $Z_s = 91$ and $Z_s = 93$ events respectively.

When the sum of integers is used, the result of the selection of the $Z_s = 92$ events is presented on the bottom of figure 5.2. It is noticed that the tails of events coming upwards and downwards vanish, and the $Z_s = 92$ spots are less truncated by the selection.

Therefore, the algorithm of taking the total charge of the fragments as $Z_s = I(Z_1) + I(Z_2)$ is definitely better. Finally, the condition $I(Z_1) + I(Z_2) = 92$ is imposed to reject a part of the nuclear-induced fission events in which a number of protons are removed from the projectile and/or projectile-like nuclei prior to fission.

5.1.1.2 Subtraction of residual contribution of nuclear-induced fission

In some nuclear-induced fission events, only neutrons are emitted in the abrasion and evaporation processes, implying that the total charge of the fission fragments is the same as that of the secondary beam (92 here). In our analysis, it is impossible to distinguish such cases from those following the Coulomb excitation event by event. In order to subtract the residual contribution of these events to the nuclear charge distribution of fission fragments, a relatively low-Z target (Aluminum) in which the Coulomb excitation is negligible is used in the active target.

Then, two sets of data are available: on one hand, the nuclear charge distribution of fragments produced in the fission events following both the nuclear collision and the Coulomb excitation (U/Pb targets); on the other hand, the distribution corresponding to the fission events solely induced by the nuclear collision (Al target). Provided the ratio of the amount of nuclear-induced fission events in which the total charge of the fragments equals to 92 occurring in the U/Pb targets over that corresponding to the Al target is known, the latter set of data can be taken as a reference to extract the nuclear charge distribution of fragments purely produced by the Coulomb-induced fission. In the following part, how this ratio is determined will be explained.

Spectra of the sum of nuclear charges of the two fission fragments produced in the U/Pb targets and in the Al target from the ^{236}U secondary beam are presented on the top and middle of figure 5.3, respectively. The ratio of the amounts of fission events corresponding to each total charge value in the U/Pb targets and in the Al target is calculated. The ratios are then plotted as a function of the total charge, as seen on the bottom of the figure.

The correlation between the ratio and the sum of charges can be interpreted part by part:

- at Z_s = 92, the ratio is significantly higher than all other values. Because for Z_s < 92, the fission events in both the U/Pb targets and the Al target are nearly 100% induced by the nuclear interaction (also called fragmentation), in contrast, for Z_s = 92, in the Al target, almost all the fissions are still triggered by the nuclear collision, while in the U/Pb targets, a large extra amount of fission events are induced by the Coulomb excitation.

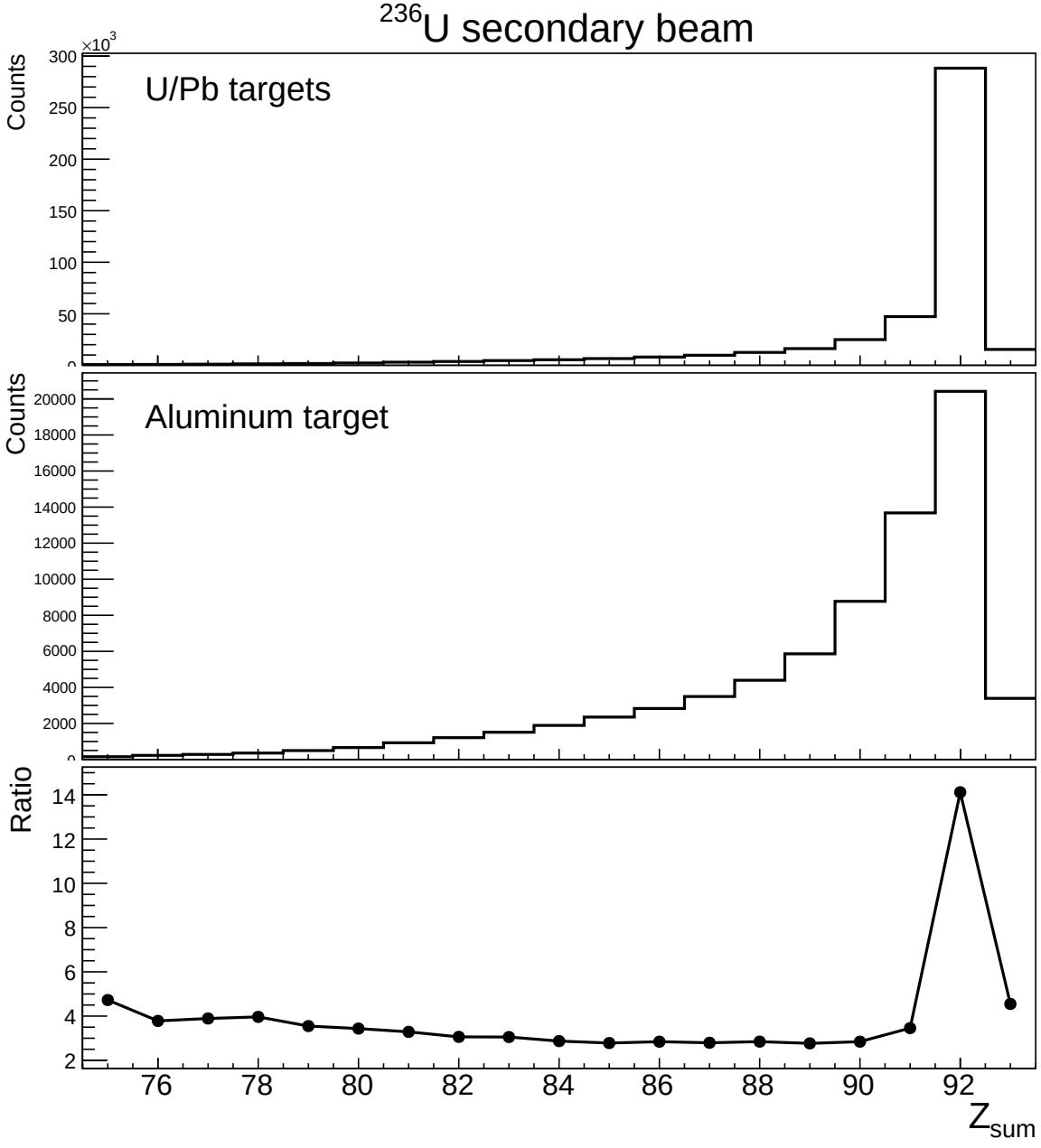

FIGURE 5.3: *Charge-sum spectra of the fission fragments produced in the U/Pb targets (on the top) and in the Al target (in the middle) from the ^{236}U secondary beam. The ratio of the two spectra is plotted at the bottom.*

- for $84 \leq Z_s \leq 90$, the ratios approximately stay as a constant. Since the fissioning elements with an atomic number between 84 and 90 are purely produced by the fragmentation of the projectile, this is an expected outcome: according to the combination of the limiting fragmentation regime and the factorization concept, at a kinetic energy of a few hundreds of MeV, the fragmentation mode of the projectile is independent of the target, implying that the proportions of the fragmentation products of the projectile which subsequently fission are the same regardless of the target [60]. Then the ratio of the amounts of a certain fissioning element in the U/Pb targets and in the Al target remains constant.
- for Z_s < 84, the ratios start to deviate from the constant level observed in the previous case. This is a clear evidence that the limiting fragmentation regime is only an approximation, although it is rather good. In our case, since we are interested in the contribution of nuclear reactions at Z_s = 92, we should focus on the ratios obtained close to Z_s = 92 and we do not care about the discrepancy below 84.
- at Z_s = 93, the ratio also differs from the constant level. The production of the fissioning element of Z = 93 is known to come from the charge-exchange reaction where the nuclear charge of the projectile increases by one unit (also called charge-pickup reaction). There are mainly two processes leading to such a reaction: one is the quasi-elastic collision between a target proton and a projectile neutron. The proton takes over all the kinetic energy of the neutron and ends up in the projectile-like nuclide, while the neutron goes to the target; the other is the excitation of a projectile neutron, resulting in a delta baryon which then decays into a proton and a negative pion [61]. Since the charge-pickup reaction is inherently different from the fragmentation process, it is normal to have a different ratio as compared to the constant level.
- at Z_s = 91, the value of the ratio drops between that corresponding to the case of Z_s = 93 and the constant level. This is due to the fact that the fissioning element of Z = 91 is mainly produced by the fragmentation of the projectile, but it is also produced by the charge-exchange reaction where the nuclear charge of the product is one unit lower than that of the projectile.

Finally, the ratio obtained at Z_s = 90 (notated as R_{90} for the following discussion) is used to subtract the residual contribution of the nuclear-induced fission events in which the total charge of the fragments is conserved in the U/Pb targets.

The charge-sum spectrum of the fission fragments produced in the Al target scaled by this ratio is plotted in the logarithm scale in figure 5.4 (red line), together with the original charge-sum spectrum corresponding to the U/Pb targets (black line). It is observed that the two spectra coincide perfectly between Z_s = 84 and Z_s = 90, while for Z_s < 84, with the decrease of the total charge, the deviation between both spectra becomes more obvious, indicating that the limiting fragmentation regime is not valid for the fragmentation residues quite away from the projectile.

Similar to the cases of $84 \leq Z_s \leq 90$, the amount of nuclear-induced fission events for Z_s = 91 and 92 in the U/Pb targets should be precisely represented by the scaled amount of these events in the Al target. The difference between the two spectra at Z_s = 91 is due to the

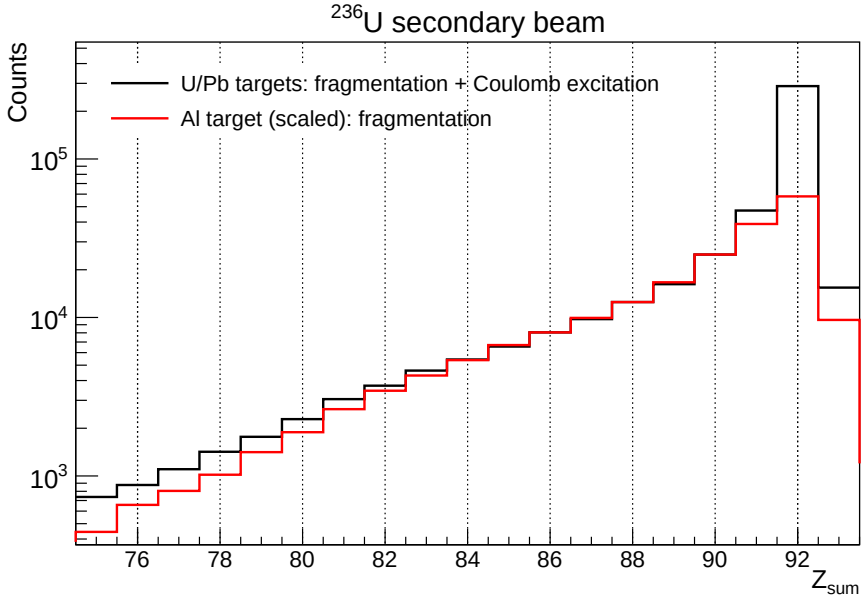

FIGURE 5.4: *Charge-sum spectrum of the fission fragments of the ^{236}U secondary beam produced in the U/Pb targets, and the appropriately scaled spectrum for the Al target. Both spectra are plotted in the logarithm scale.*

contribution of the charge-exchange reaction, while the difference at Z_s = 92 is mainly caused by the existence of the Coulomb-induced fission in the U/Pb targets.

Actually, the production of the fissioning element of Z = 92 is also subject to the charge-exchange reaction: either by the quasi-elastic scattering between a target proton (resp. neutron) and a projectile proton (resp. neutron), or by the excitation of a projectile nucleon, ending at the emission of a nucleon of the same type and a neutral pion. However, there is no way to subtract the contribution of the charge-exchange reaction experimentally. We cannot rely on the Al target for this, because the fragmentation and the charge-exchange reaction are not scaled with the same factor in the U/Pb targets and in the Al target. So we have to live with it and we just subtract the fragmentation contribution, based on the use of the Al target.

The fragmentation weight of the events in which the total charge of the fragments is conserved in the U/Pb targets is given by the ratio of the scaled charge-sum spectrum for the Al target over the spectrum for the U/Pb targets at Z_s = 92. The value is 20.15%.

After imposing the condition of Z_s = 92, the nuclear charge spectrum of the fission fragments produced in the U/Pb targets is plotted in figure 5.5 (black line). It is obtained by incrementing the histogram for each fragment of the detected pair. By construction, the distribution is symmetrical around Z = 46 as the sum is constrained to 92. This spectrum is a combined outcome of the contribution from both the Coulomb-induced fission and the fragmentation fission. Under the same condition, the charge spectrum for the Al target is obtained, and then scaled by the factor R_{90}. The scaled spectrum represents the residual contribution of fragmentation fissions in the U/Pb targets, and it is also plotted in the figure (red line). Finally, the comparison between the charge spectrum for the U/Pb targets and the scaled one for the Al target

gives the nuclear charge spectrum of the fragments purely produced by the Coulomb-induced fission (blue line in the figure).

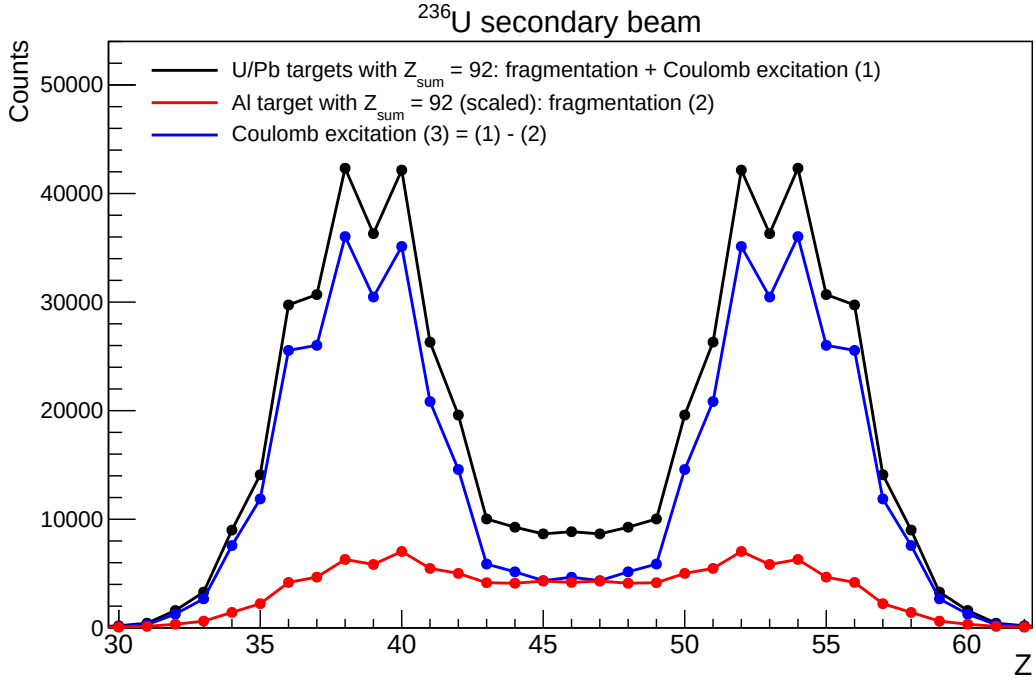

FIGURE 5.5: *Nuclear charge spectra of the fission fragments produced in the U/Pb targets and in the Al target (scaled) from the ^{236}U secondary beam. Both spectra are obtained under the condition that the total charge of the fragments is equal to 92. The comparison of the two spectra gives the charge spectrum of the fission fragments purely produced by the Coulomb-induced fission.*

5.1.2 Efficiency of the experimental setup

In this subsection, the limitations on the setup efficiency due to various detectors are discussed first. Then, the resulting efficiency is presented as a function of the nuclear charge of the fission fragments.

5.1.2.1 Limitations due to the Twin MUSIC

The nuclear charges of both fission fragments are identified simultaneously through energy loss measurements in the Twin MUSIC. In most cases, each fragment goes through one of the four sections of the detector, and energy loss measurements are performed independently for the two fragments. However, there is still possibility that both fragments enter the same section of the Twin MUSIC. In this case, it is impossible to distinguish the two fragments and measure their energy losses correctly. Therefore, such events would be lost.

5.1.2.2 Limitations due to MWPCs

A slight limitation due to MWPCs comes from the sizes of the active surfaces of both the MWPC1 and the MWPC2. Besides, it is known that there is a Helium pipe right ahead of the MWPC1 in the Cave C. If a fission fragment hits the wall of the pipe, it will be stopped there and fail to arrive at the ToF wall.

5.1.2.3 Limitations due to the ToF wall

Benefiting from the fact that the ToF wall is vertically segmented into 28 slats, the two fission fragments can be measured simultaneously, with each hitting one plastic slat. However, there is still small chance that both fragments hit the same slat. Under such a circumstance, signals can be induced on at most two PMTs. As a result, it would fail to trigger the data acquisition and the event would be lost.

It is known that as compared to the heavy fragments, the light ones deposit less energy in the plastic slats of the ToF wall ($\Delta E \propto Z^2$), resulting in weaker signals on the associated PMTs. Therefore, the measurements of light fragments are more sensitive to the amplification in the PMTs: if the amplification is not very powerful, the signals induced by the heavy fragments may be still sufficient to trigger the constant fraction discriminator, while those induced by the light fragments will fail.

As mentioned in subsection 4.1.4, two types of PMTs are used in the ToF wall: PMT Hamamatsu 6533 and PMT Hamamatsu 10580. The former one is more accurate for timing measurements than the latter, but it is much more expensive. Finally, in order not to degrade the overall performance of the ToF wall, the latter type of PMTs are only placed at the side regions which are not frequently hit by the fragments and they are essentially reached by light fragments for which the mass identification, based on the time of flight, is easier.

Since the MWPC2 stands right in front of the ToF wall, the vertical position of the fragments measured by the MWPC2 is also a representative of their position on the ToF wall. Correlations between the vertical position and the nuclear charge for the fragments impinging the plastic slats coupled to PMTs H6533 and PMTs H10580 are presented on the left and right of figure 5.6, respectively. Since the situation is the same for all plastic slats equipped with the same type of PMTs, the correlation obtained for one selected slat is taken as an example in each case.

From the comparison of correlations, it is observed that in the case of PMTs H6533, the fragments over the whole range are properly measured, while in the case of PMTs H10580, only heavy fragments are completely measured, and with the decrease in the nuclear charge of the fragments, the signals induced on the PMTs become weaker, leading to a more obvious loss of events. It is also noticed that light fragments occupy a larger height of the ToF wall than the heavy ones. This is because the light fragments are emitted with higher transverse velocities, resulting that they are more spread in positions.

Additionally, it seems that the higher the height of the ToF wall one light fragment reaches, the smaller the possibility that it can be measured by the detector. The reason is as follows: when the incident position of the light fragment is close to one extreme of the plastic slat (*i.e.*

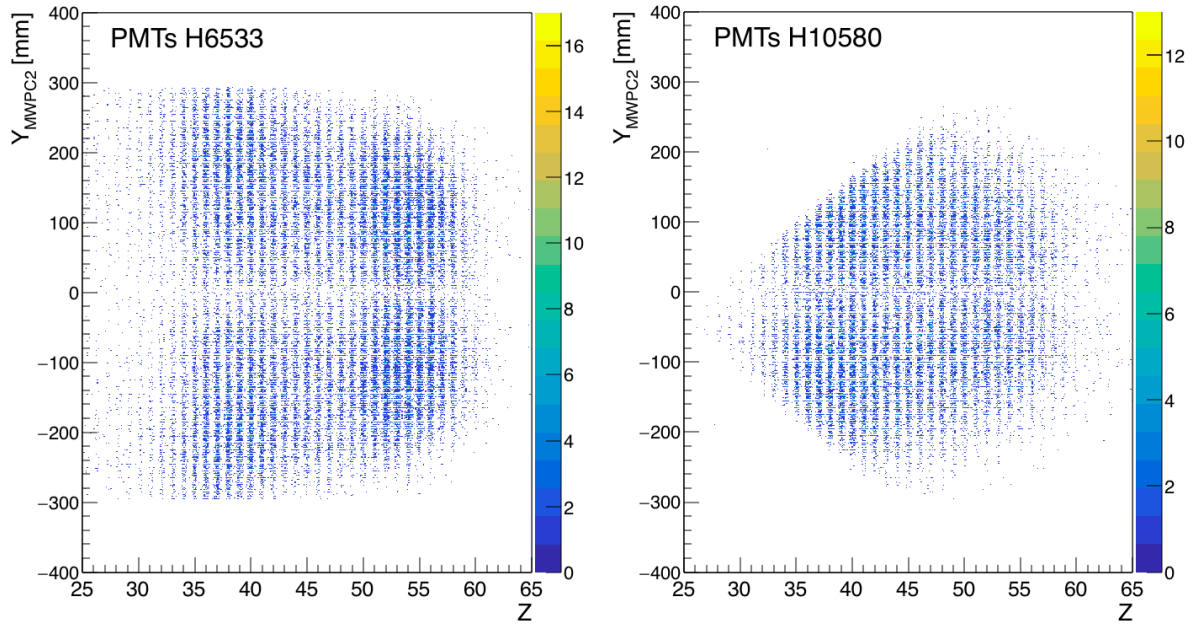

FIGURE 5.6: *Correlations between the vertical position measured in the MWPC2 and the nuclear charge of the fragments for the ToF wall plastics associated with two types of PMTs: PMTs H6533 (left) and PMTs H10580 (right).*

one PMT), it needs to go through a longer length to reach the opposite PMT, which means it will undergo more light attenuation. As a result, it is more likely to fail to induce a sufficient signal on this PMT. Therefore, the incident time of this light fragment cannot be measured.

Since only events in which both fragments are measured are taken into account, although the heavy fragment itself can be measured by the ToF wall, the loss of the measurement of the complementary light fragment will result in a lower efficiency for both of them, as compared to that for the fragments produced in the symmetric fissions.

The correlation between the vertical position and the horizontal position of the fragments measured in the MWPC2 is shown in figure 5.7. As above explained, the position distribution of the fragments on the MWPC2 can be regarded as a representative of their distribution on the ToF wall.

From the position distribution, it is seen that fragments measured in the middle of the ToF wall cover the full height of the detector, while on the left and right sides, a loss of events is observed in the vicinity of the top and the bottom of the detector. This is because PMTs H10580 with which light fragments reaching very high height of the plastic slats cannot be measured are used at the side regions of the ToF wall.

5.1.2.4 Efficiency of the setup

The efficiency of the setup was obtained by Lucie Grente after performing a series of simulations with the CONFID code [62]. All above mentioned limitations have been considered:

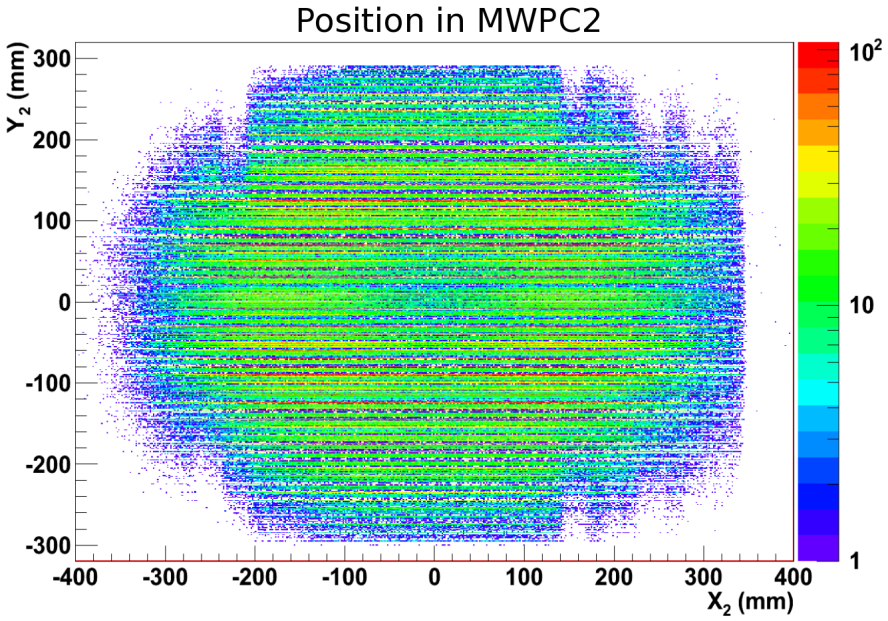

FIGURE 5.7: *Correlation between the vertical position and the horizontal position of the fragments measured in the MWPC2. This position distribution is also a representative of the fragments' distribution on the ToF wall. Court. Lucie Grente.*

- two fission fragments flying through the same section of the Twin MUSIC
- fragments passing too close to the cathode plane of the Twin MUSIC
- geometrical cut and dimensions of MWPCs and the He pipe
- two fragments hitting the same plastic slat of the ToF wall
- attenuation in the ToF Wall as a function of the nuclear charge of the fragments

The obtained efficiency for each pair of fission fragments is presented in figure 5.8 versus the charge of one fragment of the pair. Again by definition due to the pair selection, the efficiency dependence is symmetrical around Z = 46. It is clearly seen that with the increase of the nuclear charge asymmetry, the efficiency drops steadily.

The mean efficiency of the setup for the fragments produced in the Coulomb-induced fission of ^{236}U nuclei is estimated as 90%. There are about 10% events missing: 6% due to the light attenuation in the plastics of the ToF Wall, 4% caused by the fact that fragments passing too close to the cathode in the Twin MUSIC, and less than 1% due to geometrical cuts and dimensions of the detectors (*Court.* Lucie Grente).

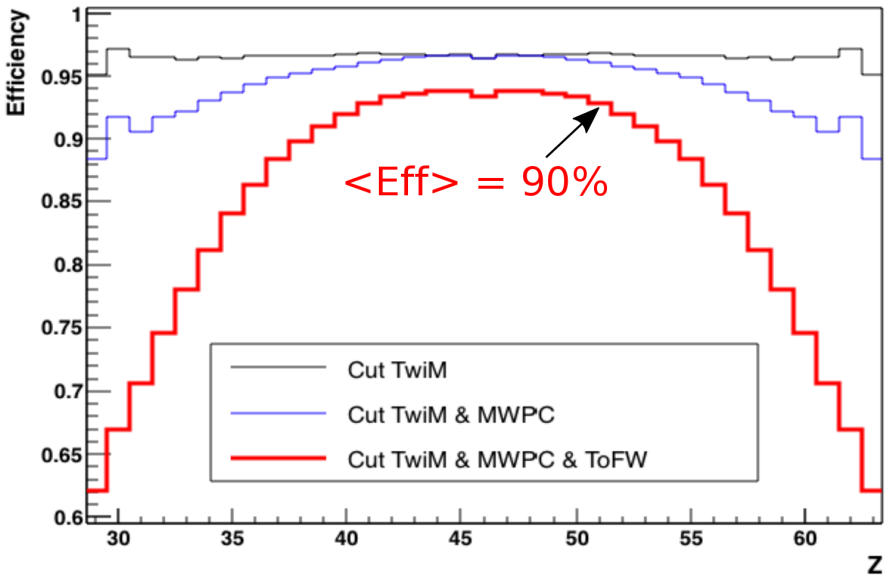

FIGURE 5.8: *Efficiency of the setup for the fragments produced in the Coulomb-induced fission of ^{236}U secondary beam. The evolution of the efficiency after considering limitations due to various detectors is also presented. Court. Lucie Grente.*

5.1.3 Elemental fission yield

5.1.3.1 Elemental yield

At the end of the part 5.1.1.2, the nuclear charge spectrum of the fission fragments purely produced by the Coulomb-induced fission of ^{236}U secondary beam has been given. Then by normalizing the total number of counts over all the fragments to 200%, the raw elemental fission yield is obtained (black line in figure 5.9).

As already explained, in order to get the real elemental yield, the efficiency which varies with the nuclear charge of the fragments has to be taken into account. Finally, the yield Y_k (in %) for the fragment of $Z = k$ is obtained by the formula:

$$Y_k = 200 \times \frac{\frac{N_k}{\epsilon_k}}{\sum_{i=1}^{91} \frac{N_i}{\epsilon_i}} \tag{5.1}$$

where N_i and ϵ_i are the number of counts and the efficiency for the fragment of $Z = i$ produced by the Coulomb-induced fission of ^{236}U secondary beam, respectively.

The final elemental fission yield is also plotted in the figure (red line).

5.1.3.2 Calculation of uncertainty on the yield

Since the yield is calculated by equation 5.1, the uncertainty on the yield comes from the uncertainties on N_i and ϵ_i. By definition N_i and ϵ_i are symmetrical around 46, so that this applies

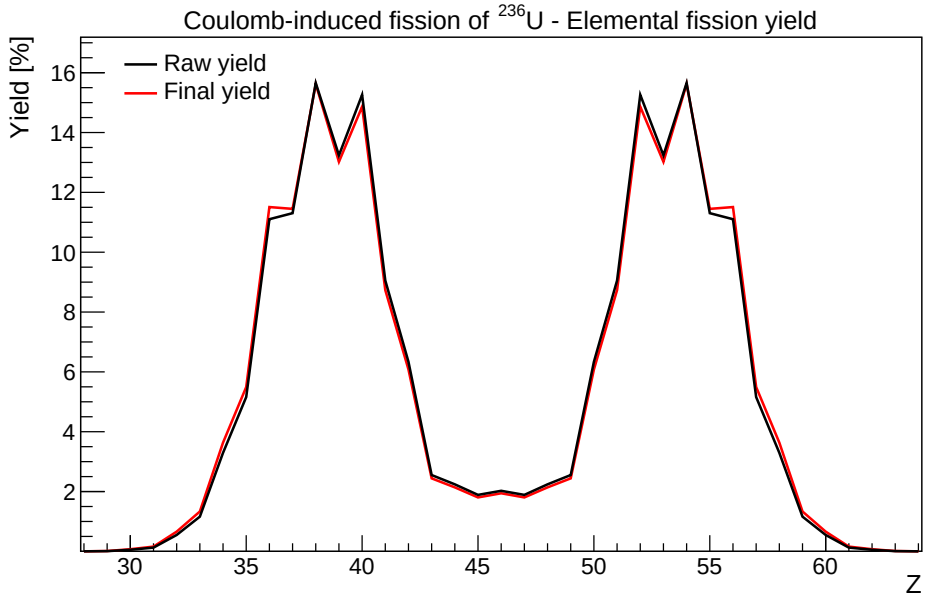

FIGURE 5.9: *Elemental yields of the fragments produced by the Coulomb-induced fission of ^{236}U secondary beam.*

to Y_k too. For convenience it is simpler to restrict to the lower Z (including 46), so that we can write:

$$Y_k = 100 \times \frac{\frac{N_k}{\epsilon_k}}{\sum_{i=1}^{45} \frac{N_i}{\epsilon_i} + \frac{1}{2}\frac{N_{46}}{\epsilon_{46}}} \tag{5.2}$$

where k runs over [1, 46], and we have $Y_{92-k} = Y_k$.

Uncertainties on N_i and ϵ_i

The N_i are counting numbers. If we would perform several times the same experiment we would get different sets of N_i. But N_i result from the subtraction of the fragmentation contribution so that:

$$N_i = N_i(UPb) - N_i(Al) * \rho \tag{5.3}$$

where $N_i(UPb)$ and $N_i(Al)$ are numbers of counts for the fragment of $Z = i$ produced in the U/Pb targets and in the Al target respectively (with the condition $Z_s = 92$ imposed), ρ is the scaling factor applied to the data concerning the Al target before the fragmentation subtraction (notated as R_{90} in the part 5.1.1.2, ρ = 2.84).

$N_i(UPb)$ and $N_i(Al)$ follow independent Poisson distributions, so that:

$$\sigma^2_{N_i(x)} = <\delta N_i(x)^2> = N_i(x) \tag{5.4}$$

where $\sigma_{N_i(x)}$ and $\delta N_i(x)$ are the standard deviation and the statistical fluctuation on $N_i(x)$ respectively, with x for UPb or Al.

By differentiating equation 5.3 we get:

$$dN_i = dN_i(UPb) - dN_i(Al) * \rho \tag{5.5}$$

By squaring and averaging over different measurements we get:

$$<\delta N_i^2> = <\delta N_i(UPb)^2> + \rho^2 <\delta N_i(Al)^2> - 2\rho <\delta N_i(UPb)\delta N_i(Al)> \tag{5.6}$$

As the fluctuations on data corresponding to UPB and Al are independent, the last term is null and we get:

$$\sigma_{N_i}^2 = N_i(UPb) + \rho^2 N_i(Al) = N_i' \tag{5.7}$$

There is no correlation between the N_i except when the two N_i correspond to the same event (their sum is equal to 92) or the two N_i are identical. Therefore we have:

$$<\delta N_i \delta N_j> = \begin{cases} 0 & \text{if } j \neq i \text{ and } j \neq 92 - i \\ N_i' = N_j' & \text{if } j = i \text{ or } j = 92 - i \end{cases} \tag{5.8}$$

This is why it is convenient to use the form in equation 5.2 of the yield, because no correlation between the terms will show up.

The uncertainty on the efficiency behaves in a totally different way because it is not statistical but systematic. It does not come from statistical fluctuations but from some lack of knowledge of some parameters: transverse fission velocity, centering of the beam. As a result, the uncertainties between points are fully correlated: we expect that if the true efficiency is higher than the nominal value for a given Z, it will be higher for the others too. Mathematically this is translated as:

$$<\delta\epsilon_i \delta\epsilon_j> = \sigma_{\epsilon_i}\sigma_{\epsilon_j} \tag{5.9}$$

In addition, since the statistical fluctuations on N_i and the errors on ϵ_i are fully uncorrelated we have:

$$<\delta N_i \delta\epsilon_i> = 0 \tag{5.10}$$

Uncertainty on the yield

The first step consists of deriving equation 5.2 against variations of N_i and ϵ_i. Then the result is squared and averaged (over a representative ensemble of samples), using the relations in equation 5.8 and 5.9 to get the standard deviation σ_Y of the yield.

The derivation of 5.2 gives:

$$\frac{dY_k}{Y_k} = \frac{dN_k}{N_k} - \frac{d\epsilon_k}{\epsilon_k} - \frac{\sum\limits_{i<46} \frac{dN_i}{\epsilon_i} - \sum\limits_{i<46} \frac{N_i}{\epsilon_i^2} d\epsilon_i + \frac{1}{2}\frac{dN_{46}}{\epsilon_{46}} - \frac{1}{2}\frac{N_{46}}{\epsilon_{46}^2} d\epsilon_{46}}{\sum\limits_{i<46} \frac{N_i}{\epsilon_i} + \frac{1}{2}\frac{N_{46}}{\epsilon_{46}}} \tag{5.11}$$

We have to extract the dN_k term from the last term in equation 5.11 to regroup it with the first term of the right side part. Two cases have to be considered according to $k = 46$ or $k \neq 46$.

$$\frac{dY_{46}}{Y_{46}} = \left(\frac{1}{N_{46}} - \frac{1}{2\epsilon_{46} \sum\limits_{i<46} \frac{N_i}{\epsilon_i} + N_{46}} \right) dN_{46} - \frac{\sum\limits_{i<46} \frac{dN_i}{\epsilon_i}}{\sum\limits_{i<46} \frac{N_i}{\epsilon_i} + \frac{1}{2}\frac{N_{46}}{\epsilon_{46}}} - \frac{d\epsilon_{46}}{\epsilon_{46}} + \frac{\sum\limits_{i<46} \frac{N_i}{\epsilon_i^2} d\epsilon_i + \frac{1}{2}\frac{N_{46}}{\epsilon_{46}^2} d\epsilon_{46}}{\sum\limits_{i<46} \frac{N_i}{\epsilon_i} + \frac{1}{2}\frac{N_{46}}{\epsilon_{46}}} \tag{5.12}$$

and for $k \neq 46$:

$$\begin{aligned} \frac{dY_k}{Y_k} = \left(\frac{1}{N_k} - \frac{1}{\epsilon_k \left(\sum\limits_{i<46} \frac{N_i}{\epsilon_i} + \frac{1}{2}\frac{N_{46}}{\epsilon_{46}} \right)} \right) dN_k - \frac{\sum\limits_{i<46, i\neq k} \frac{dN_i}{\epsilon_i} + \frac{1}{2}\frac{dN_{46}}{\epsilon_{46}}}{\sum\limits_{i<46} \frac{N_i}{\epsilon_i} + \frac{1}{2}\frac{N_{46}}{\epsilon_{46}}} \\ - \frac{d\epsilon_k}{\epsilon_k} + \frac{\sum\limits_{i<46} \frac{N_i}{\epsilon_i^2} d\epsilon_i + \frac{1}{2}\frac{N_{46}}{\epsilon_{46}^2} d\epsilon_{46}}{\sum\limits_{i<46} \frac{N_i}{\epsilon_i} + \frac{1}{2}\frac{N_{46}}{\epsilon_{46}}} \end{aligned} \tag{5.13}$$

Now we can square the above expressions and average over the fluctuations, taking into account the relations in equation 5.7, 5.8, 5.9 and 5.10:

$$\begin{aligned} \frac{\sigma^2_{Y_{46}}}{Y_{46}^2} = \frac{<\delta Y_{46}^2>}{Y_{46}^2} = \left(\frac{1}{N_{46}} - \frac{1}{2\epsilon_{46} \sum\limits_{i<46} \frac{N_i}{\epsilon_i} + N_{46}} \right)^2 N'_{46} + \frac{\sum\limits_{i<46} \frac{N'_i}{\epsilon_i^2}}{\left(\sum\limits_{i<46} \frac{N_i}{\epsilon_i} + \frac{1}{2}\frac{N_{46}}{\epsilon_{46}} \right)^2} \\ + \left(-\frac{\sigma_{\epsilon_{46}}}{\epsilon_{46}} + \frac{\sum\limits_{i<46} \frac{N_i}{\epsilon_i^2} \sigma_{\epsilon_i} + \frac{1}{2}\frac{N_{46}}{\epsilon_{46}^2} \sigma_{\epsilon_{46}}}{\sum\limits_{i<46} \frac{N_i}{\epsilon_i} + \frac{1}{2}\frac{N_{46}}{\epsilon_{46}}} \right)^2 \end{aligned} \tag{5.14}$$

and for $k \neq 46$:

$$\begin{aligned} \frac{\sigma^2_{Y_k}}{Y_k^2} = \frac{<\delta Y_k^2>}{Y_k^2} = \left(\frac{1}{N_k} - \frac{1}{\epsilon_k \left(\sum\limits_{i<46} \frac{N_i}{\epsilon_i} + \frac{1}{2}\frac{N_{46}}{\epsilon_{46}} \right)} \right)^2 N'_k + \frac{\sum\limits_{i<46, i\neq k} \frac{N'_i}{\epsilon_i^2} + \frac{1}{4}\frac{N'_{46}}{\epsilon_{46}^2}}{\left(\sum\limits_{i<46} \frac{N_i}{\epsilon_i} + \frac{1}{2}\frac{N_{46}}{\epsilon_{46}} \right)^2} \\ + \left(-\frac{\sigma_{\epsilon_k}}{\epsilon_k} + \frac{\sum\limits_{i<46} \frac{N_i}{\epsilon_i^2} \sigma_{\epsilon_i} + \frac{1}{2}\frac{N_{46}}{\epsilon_{46}^2} \sigma_{\epsilon_{46}}}{\sum\limits_{i<46} \frac{N_i}{\epsilon_i} + \frac{1}{2}\frac{N_{46}}{\epsilon_{46}}} \right)^2 \end{aligned} \tag{5.15}$$

Finally, the relative uncertainty on the elemental yield σ_Y/Y is plotted against the nuclear charge of the fragments, as seen in figure 5.10. It is observed that for the most populated fragments, the relative uncertainty is lower than 1%, and for those produced in the symmetric fissions with relatively low statistics, an accuracy of the relative uncertainty lower than 3.5% is also achieved.

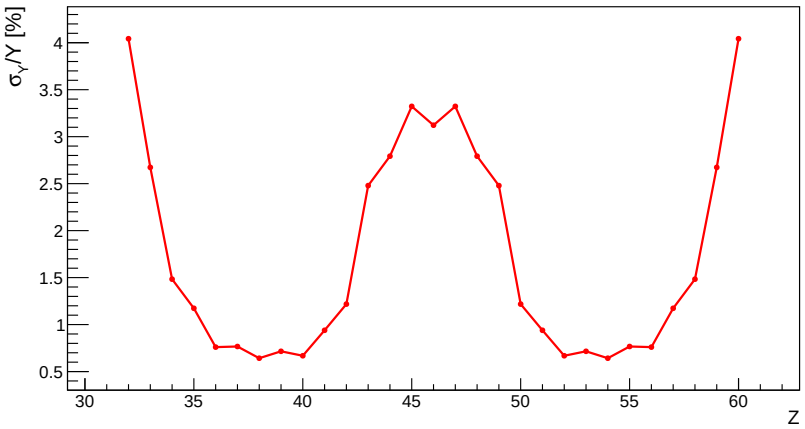

FIGURE 5.10: *Relative uncertainty on the elemental yield of the fragments produced by the Coulomb-induced fission of ^{236}U secondary beam.*

5.2 Discussions

5.2.1 Comparison with other SOFIA data

The elemental yield obtained in this paper for the Coulomb-induced fission of ^{236}U nuclei is compared to the fission yields of ^{234,235}U [22] and ^{238}U [42] measured in the first SOFIA experiment in 2012.

As seen in figure 5.11, for any considered fragment, the elemental yield always varies as a function of the mass number of the fissioning nucleus, indicating that the measured data for the four Uranium isotopes are consistent to each other.

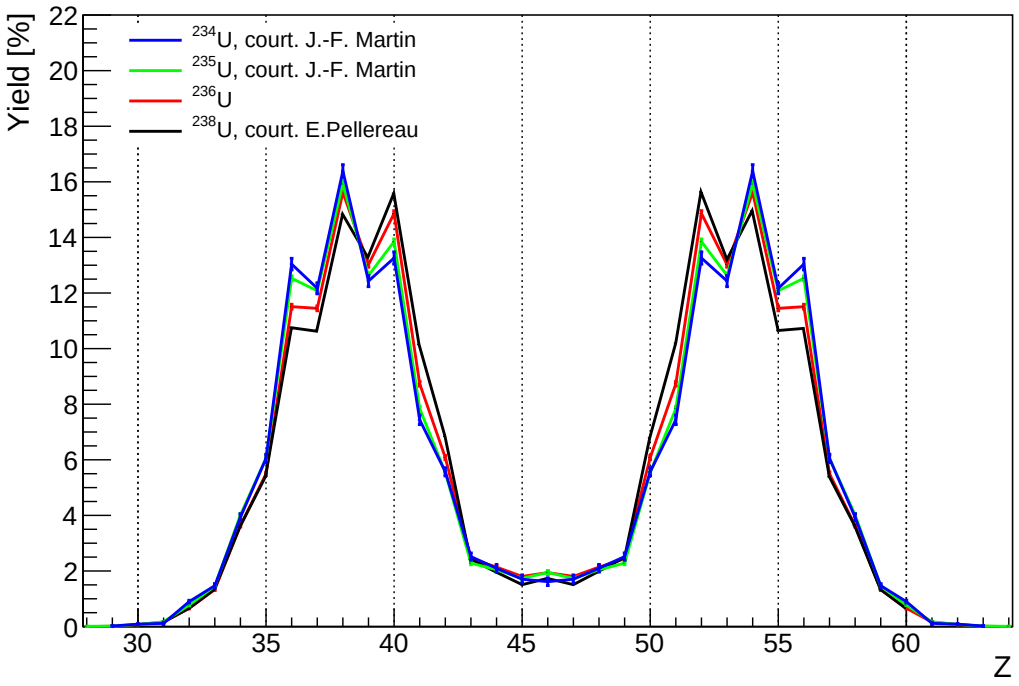

FIGURE 5.11: *Elemental yields of the fragments produced by the Coulomb-induced fission of various Uranium isotopes.*

5.2.2 Mean position of the heavy fragments

It has been observed for a long time that in the actinide region, with the increase of the mass number of the fissioning nucleus, the average mass of the heavy-group fragments remains almost constant, while that of the light-group fragments increases accordingly [63]. Then one question arises: whether the stability of the heavy fragments is more determined by their neutron or proton shells?

This issue has already been discussed by K.-H. Schmidt in an experiment which was a precursor of the SOFIA program [38]. It was found that with 4 neutrons added in the Uranium isotopes, the mean Z-value of the heavy fragments is centered around 54, while the mean N-value increases by 2 units. This observation was then taken as an argument to suspect the role of the

neutron shells on the heavy fragments peak, and the stability of the proton shells was proposed instead. However, in this experiment, the neutron number of the heavy fragments was not directly measured, but deduced from the unchanged-charge-density (UCD) assumption which takes the N/Z ratio of the heavy fragments the same as that of the fissioning nucleus.

Now since the neutron numbers of the fragments for the Coulomb-induced fission of ^{234,235}U [22] and ^{238}U [42] have been measured, it is possible to have a further interpretation on this topic.

Isotonic yields of the fragments for the three U isotopes are presented in figure 5.12. It is seen that the neutron number stays fairly constant for the heavy peaks. The mean N-values for the heavy fragments of three isotopes are listed in table 5.1. An increase of 1.5 units occurs when 4 neutrons are added. Similarly, it is calculated that with the fissioning nucleus passing from ^{234}U to ^{238}U, the average number of neutrons in the light fragments increases by 1.9 units. As mentioned before, the excited nucleus may undergo the neutron evaporation before it de-excites through fission, and the number of evaporated neutrons depends on the excitation energy. Since the mean N-values for the fragments are obtained on the basis of measurements after the probable neutron evaporation, their change among various fissioning isotopes is determined by both the difference in the total number of neutrons in the fissioning nucleus and that in the number of evaporated ones. It is noticed that with 4 neutrons added in the fissioning nucleus, only 3.4 (*i.e.* 1.5 + 1.9) neutrons in total are kept in the fragments. This is due to the fact that as compared to the case of ^{234}U, the ^{238}U nuclei are excited to a higher energy, resulting in an evaporation of 0.6 more neutrons in average.

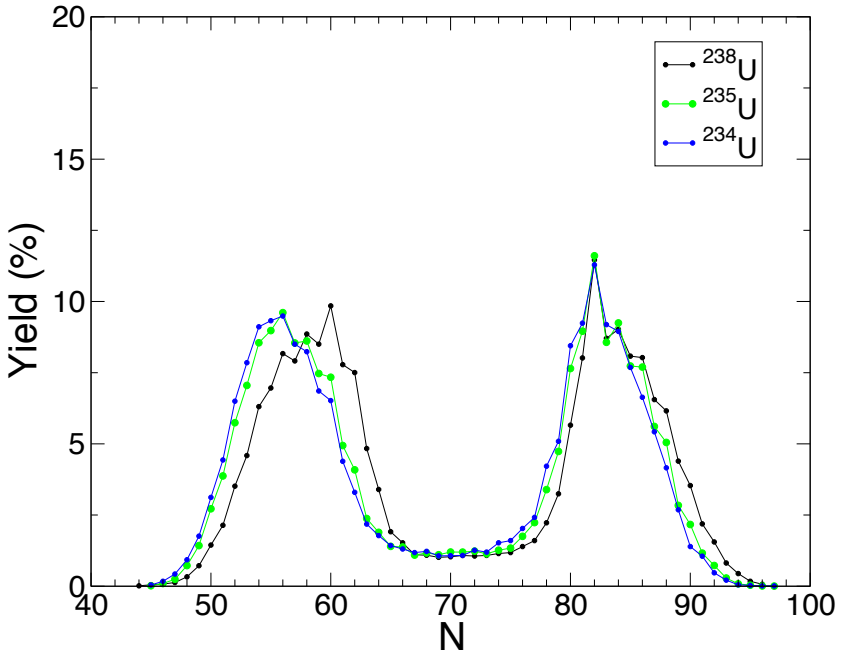

FIGURE 5.12: *Elemental yields of the fragments produced by the Coulomb-induced fission of various Uranium isotopes. Data concerning ^{234,235}U and ^{238}U are found in [22] and [42], respectively.*

isotope	mean N-value
^{234}U	82.2
^{235}U	82.6
^{238}U	83.69

TABLE 5.1: *Mean N-value for the heavy fragments of three Uranium isotopes. Numbers for ^{234,235}U and ^{238}U are calculated from data found in [22] and [42], respectively.*

It is observed that passing from ^{234}U to ^{238}U, the increase in the mean N-value of the heavy fragments is smaller than that for the light ones. Even if considering the extreme case where all the 0.6 more evaporated neutrons would be assigned to the heavy fragments, the former quantity can only be slightly larger than the latter one. We interpret this as a clear sign of the influence of the neutron shells: the spherical closed shell at N = 82 where the maximum of the isotonic yield occurs, and the deformed shell at N = 88. Because otherwise, the sharing of the added neutrons by the fragments would be simply proportional, resulting that the average number of neutrons in the heavy fragments increases much more than that in the light ones.

The average numbers of protons in the heavy fragments for various U isotopes are also calculated, as seen in table 5.2. A drop of 0.28 protons is observed for an increase of 4 neutrons in the fissioning nucleus. This decrease is caused by the fact that the protons have to follow neutrons to keep a reasonable N/Z ratio: since the added neutrons go mainly to the light fragments, their average proton number increases too. For the compensation, the number of protons in the heavy peaks decreases. However, the evolution of the proton number does not simply follow the N/Z ratio, because the decrease of the proton number for the heavy fragments is only about half of what the N/Z ratio would suggest. This may be the sign that the stability of the Z = 54 shell also plays a role.

isotope	mean Z-value
^{234}U	53.64
^{235}U	53.61
^{236}U	53.46
^{238}U	53.36

TABLE 5.2: *Mean Z-value for the heavy fragments of four Uranium isotopes. Numbers for ^{234,235}U and ^{238}U are calculated from data found in [22] and [42], respectively.*

At the mean time, it is interesting to see in figure 5.12 that for three U isotopes, the maximum isotonic yield of the fragments lies at N = 82: since 82 is a magic number for neutrons, an enhanced production of the pre-fragment (fragment before the evaporation) having 82 neutrons is expected. But if sufficient excitation energy is stored in the pre-fragment, it should release the energy through neutron emission, resulting that the neutron number of the produced fragment deviates from 82. In other words, a peak or a bump at lower N for the fragments should be observed. The fact that the peak is at N = 82 means that there is no evaporation for this

pre-fragment, and therefore it is cold.

The situation that the excitation energy in this pre-fragment is very low is not difficult to understand: an important source of the excitation energy for most pre-fragments is the conversion of the deformation energy into internal heat when the highly deformed pre-fragment attempts to reach a more stable state, and it is not available for the spherical doubly magic ^{132}Sn which is hardly deformed.

5.2.3 Comparison with evaluated data

As already mentioned, the mean excitation energy in the Coulomb-induced fission of ^{236}U is estimated as around 12 MeV, which approximates to the excitation energy caused by the absorption of a neutron at a kinetic energy of 5.5 MeV.

The elemental yield for the Coulomb-induced fission of ^{236}U is compared to the evaluated data for the fission of ^{235}U capturing a neutron at energies of 14 MeV and 0.5 MeV (from the American ENDF/B-VII.1 library [64]), or 14 MeV and 0.4 MeV (from the European JEFF 3.1 library [65]).

Results of the comparison are discussed in the following part.

5.2.3.1 Library ENDF/B-VII.1

The comparison to the evaluated data from the ENDF/B-VII.1 library is presented in figure 5.13, in both the linear scale (left) and the logarithm scale (right).

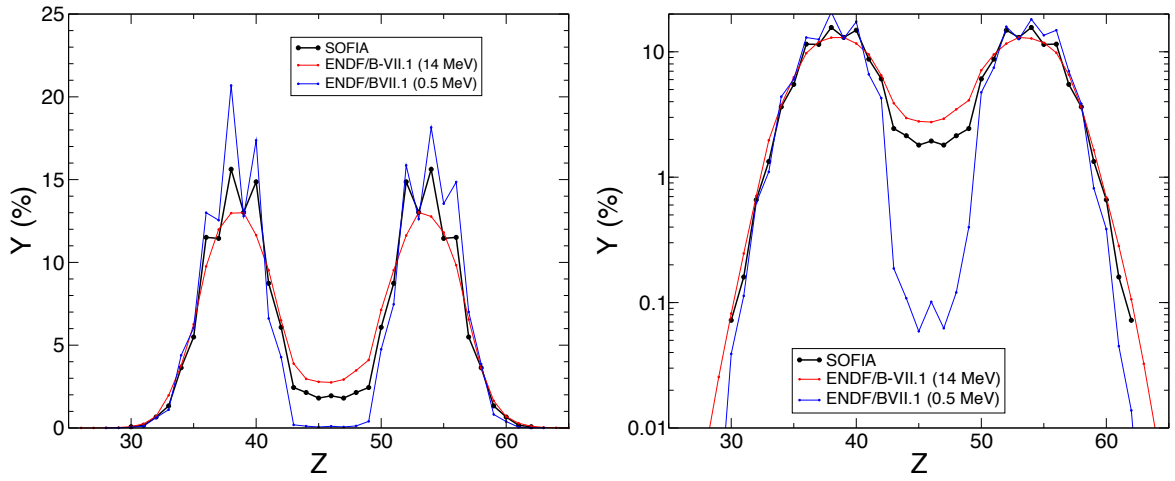

FIGURE 5.13: *Comparison between elemental yields for the Coulomb-induced fission of ^{236}U and for the neutron-induced fission of ^{235}U. Data in the latter case are from evaluation files in the ENDF/B-VII.1 library.*

Let us first look at the plot in the linear scale. The data are consistent: our yield level at the symmetric region is intermediate, which fits to the intermediate excitation energy (12 MeV as compared to 7 MeV for the 0.5 MeV set, and 20.5 MeV for the 14 MeV set). The even-odd effect on the bumps is also intermediate.

With the log scale, we see the symmetric region and the tails better. It is observed that the upper and lower tails are in agreement with the 14 MeV set (excitation energy of 20.5 MeV). This is not surprising because fragments corresponding to those tails are produced by the fission at high excitation energies of the Coulomb excitation, which are probably higher than the average value of 12 MeV.

Overall, the ENDF/B-VII.1 data seem to be of high quality, although covering only a few energy points.

5.2.3.2 Library JEFF 3.1

The comparison to the evaluated data from the JEFF 3.1 library is also presented in both the linear scale and the logarithm scale, as seen in figure 5.14.

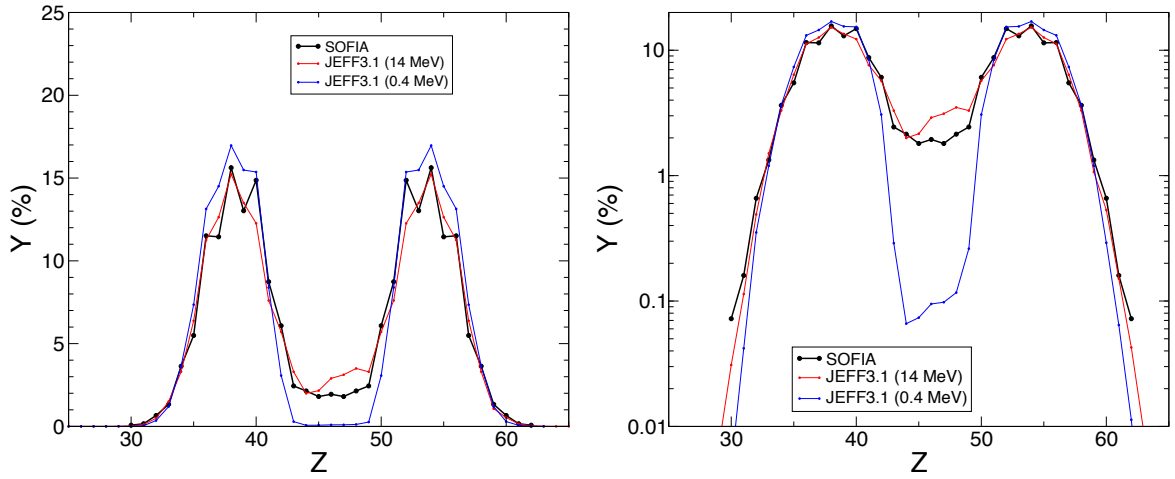

FIGURE 5.14: *Comparison between elemental yields for the Coulomb-induced fission of ^{236}U and for the neutron-induced fission of ^{235}U. Data in the latter case are from evaluation files in the JEFF 3.1 library.*

On the plot in the linear scale, we notice a few problems immediately: the yield spectrum concerning the data of the 0.4 MeV set should exhibit a stronger even-odd effect, while it actually has a smaller one as compared to our result, and the shape of the spectrum, even the one at 14 MeV, is hardly reconcilable with ours at the top of the bumps. Additionally, in the symmetric region, the JEFF data are not symmetric as they should be.

As seen with the log scale, the tails on the spectrum at 14 MeV are close to our results, although they tend to drop steeper.

To conclude, the JEFF database is in overall agreement with our data, but it seems that it still needs some revisions on the fission yield topic.

5.2.4 Evaluation of the elemental yield level at symmetry

It is well known that the yield at symmetry in fission of ^{236}U is strongly dependent on the excitation energy. The higher the excitation energy, the higher the production at symmetry. Hence one question arises: is the yield at symmetry for the Coulomb-induced fission of ^{236}U

observed in the SOFIA experiment consistent with what is known from the neutron-induced fission of ^{235}U?

Yield at symmetry vs. excitation energy

To make this study, the knowledge of the dependence of the production at symmetry on the excitation energy is needed. The experimental data are scarce. The ENDF/B-VII.1 and JEFF3.1 libraries provide data for only 3 neutron energies (thermal, 0.5 MeV, 14 MeV for ENDF/B-VII.1, thermal, 0.4 MeV and 14 MeV for JEFF3.1). An old measurement from Glendenin is also available for 7 excitation energies [66], as shown in figure 5.15 where the numbers label the neutron energy in the unit of MeV.

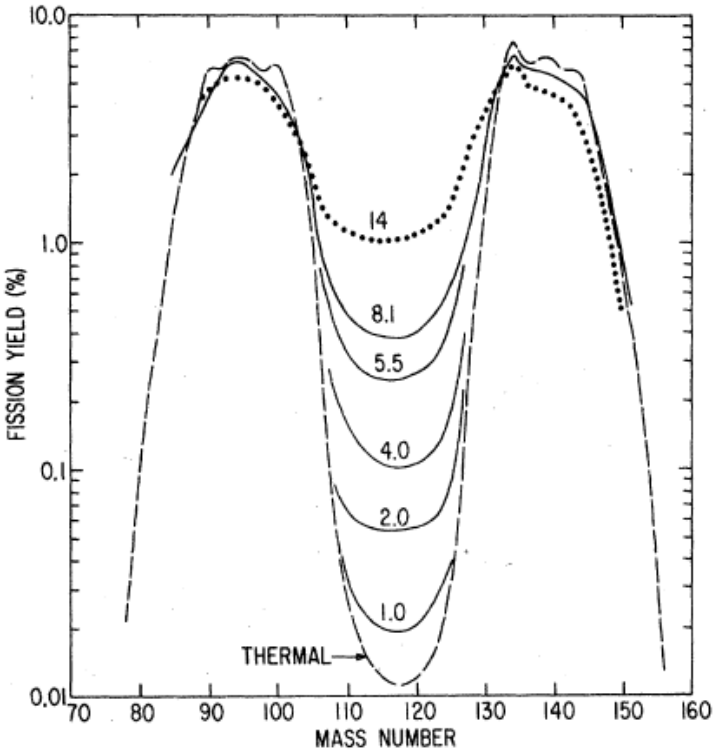

FIGURE 5.15: *Mass yield of fragments produced in the neutron-induced fission of ^{235}U at various neutron energies. The figure is cited from [66].*

These data are used to define the excitation energy dependence. The yield at symmetry is plotted against the excitation energy, as seen in figure 5.16, where the excitation energy is the neutron energy plus 6.55 MeV (the separation energy of the neutron in ^{236}U).

A quasi-exponential dependence for the 5 first points and a reduction of the increase for the 2 last ones are observed in the figure. This can be easily understood from the neutron-induced fission cross section which is plotted in figure 5.17, where the black curve represents the cross section and the vertical blue bars indicate where the databases give the fission yield.

It is clearly seen that at thermal and 0.5 MeV neutron energy, the fission occurs at the energy marked by the associated excitation energy. It is no more the case at 14 MeV neutron energy, because the fission may occur after the emission of 1 or even 2 neutrons, and hence at

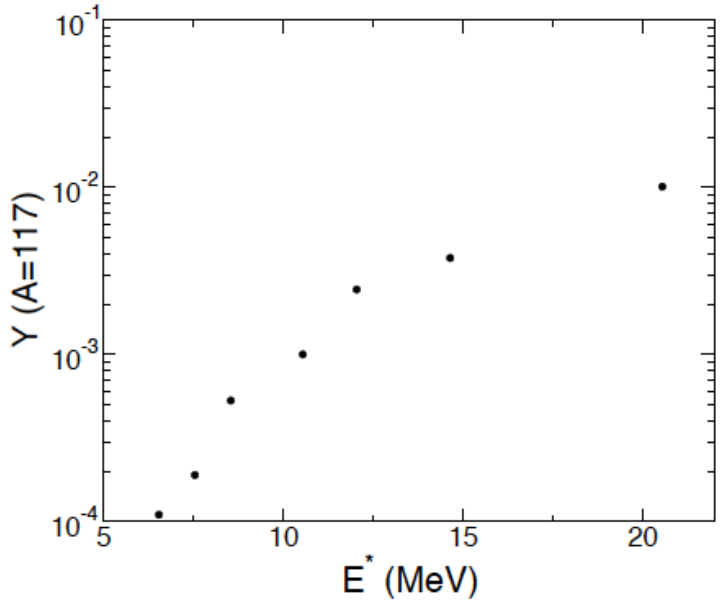

FIGURE 5.16: *Correlation between mass yield at symmetry for* $^{235}U(n, f)$ *and the initial excitation energy.*

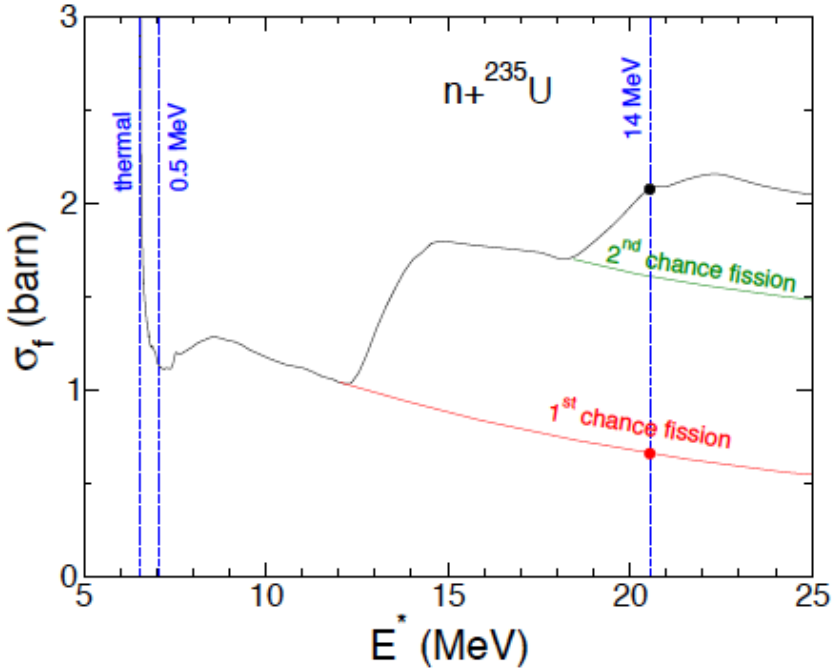

FIGURE 5.17: *Correlation between the neutron-induced fission cross section and the excitation energy.*

lower excitation energy. The contributions of the first-chance fission (fission at the initial excitation energy) and also the second-chance fission (fission after the emission of 1 neutron) are approximately drawn in the figure by the red curve and the green curve, respectively.

We see that at 14 MeV, only one third of the fissions occur at 20.55 MeV, while the rest two thirds occur at lower energy after the neutron emission. Although all fissions produce fragments, only the first-chance fission contributes to the symmetric part of the yield. Even at E_n = 8.1 MeV (E^* = 14.6 MeV), only half of the fissions contribute to the symmetric part. This explains why the 2 last points in figure 5.16 are lower than the trend.

From figure 5.17, it is possible to extract the attenuation factor ($\rho = \sigma_f/\sigma_{1stchance}$, where σ_f and $\sigma_{1stchance}$ are cross sections for all kinds of fission and only the first-chance fission, respectively) with the excitation energy. This factor is shown in figure 5.18.

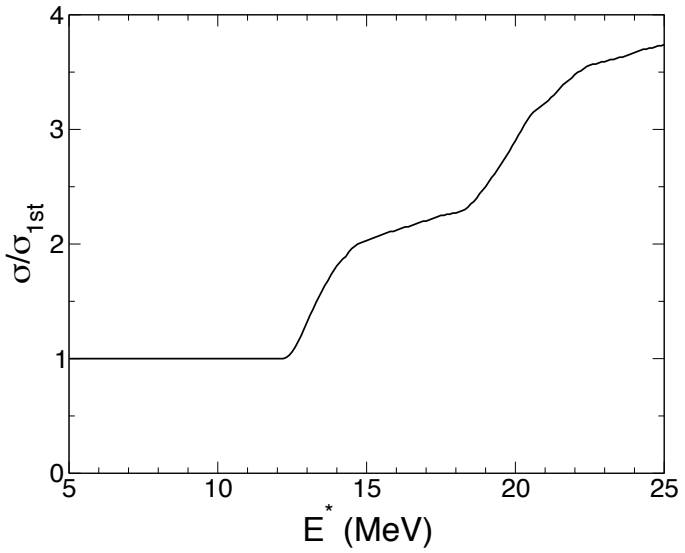

FIGURE 5.18: *Correlation between the attenuation factor of the neutron-induced fission cross section and the excitation energy.*

In the case of Glendenin's data, we expect a smoother tendency for $Y' = Y \times \rho$, because this quantity is really related to the excitation energy at fission rather the initial excitation energy. This quantity is plotted as a function of the excitation energy in figure 5.19.

It is seen that the trend of the correlation is well represented by the formula:

$$Y'_s = Y'_{s0} \exp\left(-\frac{B}{T}\right) = \exp\left(a_0 - \frac{a_1}{\sqrt{E^*}}\right) \tag{5.16}$$

Another formula is also shown, although it seems less accurate:

$$Y'_s = \exp\left(a_0 - \frac{a_1}{E^*}\right) \tag{5.17}$$

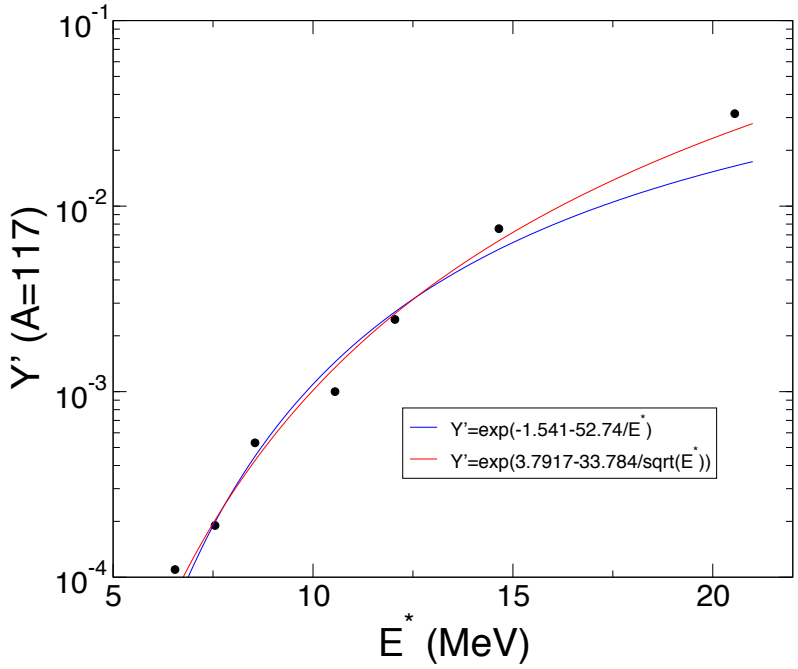

FIGURE 5.19: *Correlation between the mass yield at symmetry corrected for the attenuation factor and the excitation energy at fission for Glendenin's data. The correlation is fitted by two types of formulas.*

To summarize, the production yield at symmetry can be described with the expression:

$$Y_s = \frac{1}{\rho} \exp\left(a_0 - \frac{a_1}{\sqrt{E^*}}\right) \tag{5.18}$$

where E^* is the initial excitation energy and ρ is the above defined attenuation factor. The parameters a_0 and a_1 extracted above cannot be used directly because we are using Z distributions instead of A distributions, so that a multiplicating factor comes into the game (ratios of the widths in A versus Z). But we know that equation 5.18 is accurate enough and we can fit the 2 parameters against the data contained in the databases, which are scarcer (3 points) but accurate.

This is shown in figure 5.20 where we plot $Y'_s = Y_s \times \rho$ in the case of data from ENDF/B-VII.1.

Although a formula in the format of equation 5.17 seems to fit better, we stick to formula in the format of equation 5.16 which is more physical and is more representative of the trend of data. So at the end we adopt:

$$Y_{Z=46}(E^*) = \frac{1}{\rho} \exp\left(5.057 - \frac{33.033}{\sqrt{E^*}}\right) \tag{5.19}$$

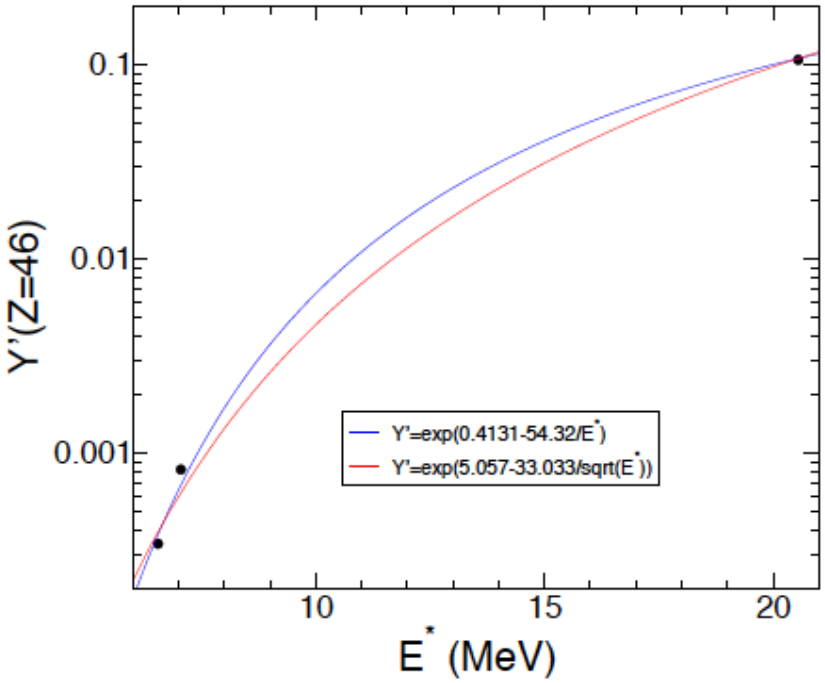

FIGURE 5.20: *Correlation between the elemental yield at symmetry corrected for the attenuation factor and the excitation energy at fission for data from the ENDF/B-VII.1 library. Two types of formulas are used to fit the correlation.*

Expected yield at symmetry for electromagnetic excitation

The electromagnetic excitation spectrum is denoted as $P_{el}(E^*)dE^*$. The expected yield at symmetry ($Z = 46$) is:

$$Y_{th} = \frac{\int Y_{Z=46}(E^*)P_{el}(E^*)dE^*}{\int P_{el}(E^*)dE^*} \tag{5.20}$$

By carrying up the integrals, we get Y_{th} = 0.0106. It is already remarked that this value is close to $Y_{Z=46}(12)$ = 0.011, meaning that $<Y(E^*)>$ fortuitously equals to $Y(<E^*>)$, which was not expected at all due to the steep variation of $Y_{Z=46}$ with the excitation energy.

Now looking at figure 5.21, we see that the elemental yield at symmetry is close to Y_{exp} = 0.02. If we use formula in the format of equation 5.17 in the calculation, the prediction can be increased up to 0.013, but it is still definitely lower than 0.02.

In conclusion, the production at symmetry is higher than predicted from the electromagnetic excitation energy, which is consistent with the excess of emitted neutrons found for the other Uranium isotopes [22]. The reason for this could be that the contribution of the charge-exchange reactions, which have very low cross section with respect to the electromagnetic excitation but can deposit a much higher excitation energy, is not removed in our data. However, it is hard to believe that the yield at symmetry can be increased by a factor of 2 just because of the influence of the charge-exchange reactions. Actually, this significant difference observed between the measurement and the calculation could be caused by the fact that the Coulomb excitation energy is underestimated in our experiment. To verify this idea, further investigations

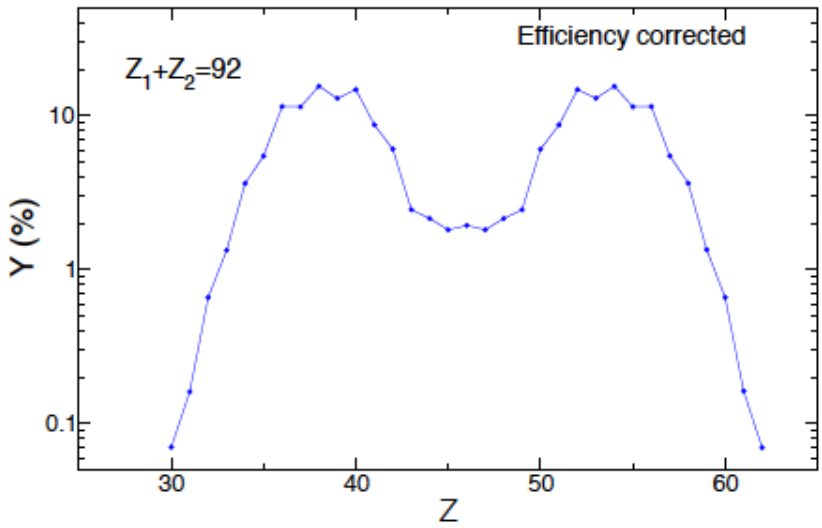

FIGURE 5.21: *Elemental yield of fragments produced by the Coulomb-induced fission of ^{236}U. The efficiency of the setup is already taken into account. The spectrum is shown in the logarithm scale.*

are needed.

Chapter 6

Conclusion

The SOFIA program aims to measure several fission observables — fission yields, the total kinetic energy of the fragments and the prompt neutron multiplicity, for a wide range of actinides and pre-actinides. In the experiment, the pair of fragments produced in the Coulomb-induced fission are identified simultaneously in both mass and nuclear charge on an event-by-event basis, with the use of a relativistic primary beam and the inverse kinematics.

In this paper, all the detectors used in the experimental setup are described extensively. And the analysis based on the associated measurements is explained step by step. It consists of two parts: the isotopic identification of the desired fissioning system (^{236}U here) from the cocktail secondary beam produced by the ^{238}U primary beam, and the nuclear charge identification of the fission fragments. Both identifications are performed on the basis of the ΔE - Bρ - ToF technique. An unprecedented nuclear charge resolution has been achieved for the fragments: 0.35 FWHM for the group of light fragments and 0.39 FWHM for the heavy ones.

Then after subtracting the contribution of the fragmentation fissions, the nuclear charge spectrum of the fragments purely produced by the Coulomb-induced fission of ^{236}U is obtained. Finally, with the efficiency of the setup taken into account, the elemental yield of the fragments over the whole range is extracted with high accuracy (an uncertainty lower than 3.5%, even for the heavy fragments whose measurement is always a challenge for most fission experiments).

To evaluate and interpret the obtained elemental yield, comparisons to some other SOFIA data and the evaluated data from the libraries are performed. It turns out that the elemental yield for the Coulomb-induced fission of ^{236}U is completely consistent with those measured for other Uranium isotopes in the previous SOFIA experiment. Concerning the databases, the comparison with the data from the ENDF/B-VII.1 library shows good consistency, while in view of our result, it seems that the JEFF3.1 library still needs to be improved on the fission yield topic.

In this paper, the mean N-values and the mean-Z values of the heavy fragments are compared among various Uranium isotopes. It shows that passing from ^{234}U to ^{238}U, the increase in the mean N-value of the heavy fragments is smaller than that for the light ones. We regard this as a support for the interpretation that the stabilization of the heavy fragments is influenced by the stability of the neutron shells, because otherwise, the assignment of the added neutrons to the fragments would be simply proportional, resulting that the average neutron number of the heavy fragments increases much more than that of the light ones. Meanwhile, it is seen that a decrease of 0.28 occurs in the proton number of the heavy fragments. This decrease is caused by the fact that the total number of protons for the fragments is constant (92) and the protons have to follow neutrons to keep a reasonable N/Z ratio. However, the value of the decrease is only about half of what the N/Z ratio would suggest, implying that the proton shell may also play a role in the stabilization of the heavy fragments.

Furthermore, it is observed that the elemental yield at symmetry is higher than predicted from the Coulomb excitation energy, which is consistent with the excess of neutron emission

found in the previous SOFIA data. A possible explanation is that the contribution of the charge-exchange reactions which exhibit a much higher excitation energy as compared to the Coulomb excitation is not fully subtracted in our data. However, it is hardly possible that the measured yield at symmetry can be as twice as calculated just because of the influence of the charge-exchange reactions. Actually, the non-negligible difference between the measurement and the calculation may suggest that the Coulomb excitation energy is underestimated in our experiment.

Additionally, some achievements due to the improvement in the detectors and electronics are worth mentioning:

- with the use of the Triple MUSIC, the secondary beam is fully identified in both mass and nuclear charge for all events.
- by using new PMTs in the START scintillation detector placed at S2, the mass resolution of the secondary beam is still satisfying until a counting rate of 3 MHz which is not achievable for most detectors and electronics. The plastic scintillator at S2 being able to bear such a high counting rate is very important to our experiment: in order to finally have enough statistics for the desired fission events in a short time. As the fission probability is low (a few %), the primary beam of a high intensity is needed, implying that large quantity of fragments will arrive at S2 continuously.
- with the vertical segmentation in the Twin MUSIC, the enlargement of the active surface of the ToF wall and the replacement of plastic slats in the ToF wall by those with longer attenuation length, the average efficiency of the setup is improved to as high as 90%.

It is already known that this PhD work ends at the elemental yield of the fragments produced by the Coulomb-induced fission of ^{236}U. However, with the full data acquired in the SOFIA experiment in October 2014, further analysis can still be performed to obtain fission observables of interest. For example, the next step is to identify both fragments in mass simultaneously on an event-by-event basis, and this will lead to the isotopic yield of fission fragments over the whole range. Besides, concerning the Coulomb-induced fission of ^{236}U, the total kinetic energy of the fragments and the multiplicity of the prompt neutron are also expected to be obtained. Then, with all these results, systematic comparisons with microscopic models can be performed.

After dealing with all the existing data, the SOFIA program aims to explore the fission process with more exotic nuclides, which will help to interpret the competition between asymmetric and symmetric fissions, new structure effects, and so on. Then, if we think one step further, there are mainly two long-term goals: one is to conduct fission experiments by using the "dream" beam of ^{242}Pu (if available) as the primary beam in the SOFIA framework. In such experiments, the fission of elements with mass number larger than 238 can be studied. Therefore, the data of fission of Plutonium isotopes and ^{239}U, which are important for the nuclear reactor, will be available, and the results are directly comparable to the GANIL data. As for the other goal, it is to study the electron-induced fission in which the excitation energy can be measured event-by-event.

List of Tables

3.1 Technical information of the Triple MUSIC 40
3.2 Technical information of scintillation detectors 43
3.3 Technical information of MWPCs 46
3.4 Materials in four calibration runs 48
3.5 Charge state distribution of ^{236}U ions at 700 AMeV after penetrating 200 mm of Ar 59
3.6 Charge state distribution of ^{236}U ions at 700 AMeV at the exit of an 80 μm Nb foil 60
3.7 Behaviors of Nb foils with various thicknesses 62
3.8 Evolution of mass resolutions with various counting rates 77

4.1 Technical information of the active target 84
4.2 Technical information of the Twin MUSIC 86
4.3 Technical information of the ToF wall 88
4.4 Technical information of the MWPC2 90
4.5 Energy losses measured before/after the fission location 94

5.1 Mean N-value for the heavy fragments of three U isotopes. 134
5.2 Mean Z-value for the heavy fragments of four U isotopes. 134

List of Figures

1.1 Saddle point shapes for various values of x 6
1.2 Surface, Coulomb, and net deformation energies vs. deformation parameter . . . 7
1.3 Single-neutron energy levels vs. deformation parameter 9
1.4 Scheme of the double-humped fission barrier of actinides 10

2.1 Layout of the GSI facility 21
2.2 Calculation of the excitation-energy distribution at fission 26
2.3 Energy distribution of nuclear-induced excitation of ^{234}U 27

3.1 Setup for the secondary beam identification 32
3.2 Selection process of fragmentation products in FRS, shown on the nuclide chart . 33
3.3 Schematic view of the FRS facility 35
3.4 Picture of the Triple MUSIC 38
3.5 Side view of the Triple MUSIC 40
3.6 Top view of the Triple MUSIC. 40
3.7 Picture of the STOP IB detector 42
3.8 Picture of MWPCs 44
3.9 Structure of a MWPC and the internal electric field 45
3.10 Raw time of flight vs. the inverse of the velocity for the primary beam 49
3.11 Geometric sketch of anodes in the Triple MUSIC 50
3.12 Correlation of vertical positions in two sections of the Triple MUSIC 51
3.13 Sum of energy losses vs. Y for a pair in the Triple MUSIC 52
3.14 Spectra of energy losses in the Triple MUSIC 53
3.15 Drift time selection and energy loss in the Triple MUSIC vs. velocity 54
3.16 Energy loss vs. drift time in the Triple MUSIC 55
3.17 Energy loss vs. horizontal angle in the Triple MUSIC 55
3.18 Spectra of the energy loss in the Triple MUSIC 56
3.19 Equilibrium charge-state distributions vs. projectile energy 57
3.20 Equilibrium charge-state distribution of the U projectile vs. target atomic number 60
3.21 Simplified model used for the calculation of charge state distributions 60
3.22 Correlation of two corrected energy loss measurements in the Triple MUSIC . . . 63
3.23 Spectra of the energy loss given by the Triple MUSIC and by the section 2 64
3.24 Energy loss spectrum of secondary beams, shown in the logarithm scale 65
3.25 Energy loss vs. nuclear charge for secondary beams 65

3.26 Ion's position at Cave C vs. that at S2 . . . 69
3.27 A/q vs. positions at S2 and Cave C for secondary beams . . . 70
3.28 A/q of secondary beam ions before and after corrections . . . 71
3.29 Secondary beam identification map of U and Pa isotopes . . . 73
3.30 Secondary beam identification map for FRS settings of light nuclei . . . 75
3.31 Counting rates at S2 for FRS settings of ^{236}U and ^{187}Tl . . . 76
3.32 Evolution of mass spectra of Thallium isotopes . . . 76
3.33 Mass resolution vs. counting rate at S2 . . . 77

4.1 Schematic view of the setup for the identification of fission fragments . . . 80
4.2 Picture of the active target . . . 82
4.3 Sketch of the side view of the active target . . . 83
4.4 Picture of the Twin MUSIC . . . 85
4.5 Sketches of the top view and side view of the Twin MUSIC . . . 85
4.6 Pictures of the ToF wall . . . 87
4.7 Picture of the MWPC2 . . . 91
4.8 Scheme of the anodes and cathodes in the active target. . . . 93
4.9 Correlation of energy losses measured in anodes 3 and 4 . . . 94
4.10 Drift time spectrum in Twin MUSIC . . . 96
4.11 Example of the position measurement in Twin MUSIC . . . 97
4.12 Correlation between the fit residual and the measured position . . . 98
4.13 Spectra of the fit residual in Twin MUSIC . . . 98
4.14 Example of the incident positions on the ToF wall . . . 100
4.15 Example of the cases of the X and Y positions in the MWPC1 . . . 100
4.16 Geometric model used for the trajectory reconstruction . . . 103
4.17 Energy loss in the Twin MUSIC vs. velocity . . . 107
4.18 Energy loss vs. horizontal position in the Twin MUSIC . . . 107
4.19 Energy loss in the Twin MUSIC vs. horizontal position in the MWPC2 . . . 108
4.20 Energy loss in the Twin MUSIC vs. Y position measured by the MWPC2 . . . 109
4.21 Spectrum of the corrected energy loss of the fission fragments . . . 111
4.22 Energy loss vs. nuclear charge for the fission fragments . . . 111
4.23 Nuclear charge distribution of the fission fragments . . . 112
4.24 Corrected energy loss vs. X position in the Twin MUSIC . . . 112
4.25 Energy loss vs. X position on the other side of the Twin MUSIC . . . 113

5.1 Correlation between measured nuclear charges of both fission fragments . . . 117
5.2 Selection of events in which the total charge of the fragments is equal to 92 . . . 118
5.3 Charge-sum spectra of the fragments in different targets and the ratio of the spectra 120
5.4 Scaled charge-sum spectrum of the fission fragments produced in the Al target . 122
5.5 Nuclear charge spectra of the fission fragments produced in different targets . . . 123
5.6 Vertical position vs. nuclear charge of the fragments for two types of PMTs . . . 125

5.7 Position distribution of the fragments on the MWPC2 126
5.8 Efficiency of the setup vs. nuclear charge of the fragments 127
5.9 Raw and final elemental fission yields 128
5.10 Relative uncertainty on the elemental fission yield vs. Z 131
5.11 Elemental fission yields for various Uranium isotopes 132
5.12 Elemental fission yields for various Uranium isotopes 133
5.13 Comparison of elemental yield to evaluations from the ENDF/B-VII.1 library . . 135
5.14 Comparison of elemental yield to evaluations from the JEFF 3.1 library 136
5.15 Mass yield of fragments of ^{235}U(n, f) at various neutron energies 137
5.16 Mass yield for ^{235}U(n, f) vs. initial excitation energy 138
5.17 Neutron-induced fission cross section vs. excitation energy 138
5.18 Attenuation factor of fission cross section vs. excitation energy 139
5.19 Yield at symmetry vs. excitation energy at fission for Glendenin's data 140
5.20 Yield at symmetry vs. excitation energy at fission for the ENDF/B-VII.1 data . . 141
5.21 Elemental yield for the Coulomb-induced fission of ^{236}U in the log scale 142

A.1 Scheme of the experimental setup in the cave C 159

Bibliography

[1] J. Chadwick. Possible existence of a neutron. *Nature*, 129:312, 1932.

[2] E. Fermi. Possible production of elements of atomic number higher than 92. *Nature*, 133:898–899, 1934.

[3] L. Meitner and O.R. Frisch. Disintegration of uranium by neutrons: a new type of nuclear reaction. *Nature*, 143:239–240, 1939.

[4] Robert Vandenbosch and John R. Huizenga. *Nuclear Fission*. Academic Press, 1973.

[5] Ida Noddack. On element 93. *Zeitschrift fur Angewandte Chemie*, 47:653, 1934.

[6] Pieter H.M. Van Assche. The ignored discovery of the element Z= 43. *Nuclear Physics A*, 480(2):205–214, 1988.

[7] W. Noddack, I. Tacke, and O. Berg. Die ekamangane. *Naturwissenschaften*, 13(26):567–574, 1925.

[8] O. Hahn and F. Straßmann. Über die Entstehung von Radiumisotopen aus Uran durch Bestrahlen mit schnellen und verlangsamten Neutronen. *Naturwissenschaften*, 26(46):755–756, 1938.

[9] O. Hahn and F. Straßmann. Über den Nachweis und das Verhalten der bei der Bestrahlung des Urans mittels Neutronen entstehenden Erdalkalimetalle. *Naturwissenschaften*, 27(1):11–15, 1939.

[10] O.R. Frisch. Physical evidence for the division of heavy nuclei under neutron bombardment. *Nature*, 143(3616):276–276, 1939.

[11] Niels Bohr and John Archibald Wheeler. The mechanism of nuclear fission. *Physical Review*, 56(5):426, 1939.

[12] G. Gamow. Mass defect curve and nuclear constitution. *Proceedings of the Royal Society of London. Series A*, 126(803):632–644, 1930.

[13] C.F.V. Weizsäcker. Zur theorie der kernmassen. *Zeitschrift für Physik A Hadrons and Nuclei*, 96(7):431–458, 1935.

[14] W. Pauli. Über den Zusammenhang des Abschlusses der Elektronengruppen im Atom mit der Komplexstruktur der Spektren. *Zeitschrift für Physik A Hadrons and Nuclei*, 31(1):765–783.

[15] S. Cohen and W.J. Swiatecki. The deformation energy of a charged drop: Part v: Results of electronic computer studies. *Annals of Physics*, 22(3):406–437, 1963.

[16] M.G. Mayer. On closed shells in nuclei. *Physical Review*, 74(3):235, 1948.

[17] M.G. Mayer. Nuclear configurations in the spin-orbit coupling model. i. empirical evidence. *Physical Review*, 78(1):16, 1950.

[18] O. Haxel, J.H.D. Jensen, and H.E. Suess. On the" magic numbers" in nuclear structure. *Physical Review*, 75(11):1766, 1949.

[19] Sven Gösta Nilsson. Binding states of individual nucleons in strongly deformed nuclei. *Kgl. Danske Videnskab. Selskab., Mat.-fys Medd.*, 29, 1955.

[20] V.M. Strutinsky. Shell effects in nuclear masses and deformation energies. *Nuclear Physics A*, 95(2):420–442, 1967.

[21] Cyriel Wagemans. *The nuclear fission process*. CRC press, 1991.

[22] Julie-Fiona Martin. *Coulex fission of ^{234}U, ^{235}U, ^{237}Np and ^{238}Np studied within the SOFIA experimental program*. PhD thesis, Université Paris-Sud, CEA/DAM/DIF Bruyères-le-Châtel, November 2014.

[23] W.J. Maeck. Fission yields : measurement techniques and data status. In *Neutron Standards and Applications: Proceedings of the International Specialists Symposium on Neutron Standards and Applications Held at the National Bureau of Standards, Gaithersburg, MD*, volume 493, page 146, 1977.

[24] S. Prakash and S.B. Manohar. Radiochemical methods of measurements of fission products yields. *Journal of radioanalytical and nuclear chemistry*, 142(1):119–133, 1990.

[25] D.N. Poenaru and W. Greiner. *Experimental techniques in nuclear physics*. Walter de Gruyter, 1997.

[26] A. Oed, P. Geltenbort, R. Brissot, F. Gönnenwein, P. Perrin, E. Aker, and D. Engelhardt. A mass spectrometer for fission fragments based on time-of-flight and energy measurements. *Nuclear Instruments and Methods in Physics Research*, 219(3):569–574, 1984.

[27] D. Dore, F. Farget, F.-R. Lecolley, G. Lehaut, T. Materna, J. Pancin, S. Panebianco, and Th. Papaevangelou. FALSTAFF: A new tool for fission studies. In *EPJ Web of Conferences*, volume 62, page 05005, 2013.

[28] N. Boucheneb, P. Geltenbort, M. Asghar, G. Barreau, T.P. Doan, F. Gönnenwein, B. Leroux, A. Oed, and A. Sicre. High resolution measurements of mass, energy and nuclear charge correlations for ^{229}Th(n_{th}, f) with the Cosi Fan Tutte spectrometer. *Nuclear Physics A*, 502:261–270, 1989.

[29] M.O. Frégeau, S. Oberstedt, Th. Gamboni, W. Geerts, F.-J. Hambsch, and M. Vidali. First results from the new double velocity–double energy spectrometer VERDI. *Nuclear Instruments and Methods in Physics Research Section A: Accelerators, Spectrometers, Detectors and Associated Equipment*, 817:35–41, 2016.

[30] A. Bail, O. Serot, L. Mathieu, O. Litaize, T. Materna, U. Köster, H. Faust, A. Letourneau, and S. Panebianco. Isotopic yield measurement in the heavy mass region for ^{239}Pu thermal neutron induced fission. *Physical Review C*, 84(3):034605, 2011.

[31] D. Rochman, H. Faust, I. Tsekhanovich, F. Gönnenwein, F. Storrer, S. Oberstedt, and V. Sokolov. Isotopic yields from the reaction ^{245}Cm(n$_{th}$, f) at the Lohengrin mass separator. *Nuclear Physics A*, 710(1):3–28, 2002.

[32] Adeline Bail. *Mesures de rendements isobariques et isotopiques des produits de fission lourds sur le spectromètre de masse LOHENGRIN*. PhD thesis, Université Bordeaux 1, 2009.

[33] Olivier Delaune. *Technique de la cinématique inverse pour l'étude des rendements isotopiques des fragments de fission aux énergies GANIL*. PhD thesis, Université de Caen, 2012.

[34] M. Caamaño, O. Delaune, F. Farget, X. Derkx, K.-H. Schmidt, L. Audouin, C.-O. Bacri, G. Barreau, J. Benlliure, E. Casarejos, A. Chbihi, B. Fernández-Domínguez, L. Gaudefroy, C. Golabek, B. Jurado, A. Lemasson, A. Navin, M. Rejmund, T. Roger, A. Shrivastava, and C. Schmitt. Isotopic yield distributions of transfer- and fusion-induced fission from ^{238}U + ^{12}C reactions in inverse kinematics. *Physical Review C*, 88(2):024605, Aug 2013.

[35] Sako Masami. Fission study using SAMURAI spectrometer at Riken. `http://asrc.jaea.go.jp/soshiki/gr/chiba_gr/workshop3/Program3.html`. 16th ASRC International Workshop "Nuclear Fission and Structure of Exotic Nuclei", Mar 2014.

[36] M. Bernas, S. Czajkowski, P. Armbruster, H. Geissel, Ph. Dessagne, C. Donzaud, H.-R. Faust, E. Hanelt, A. Heinz, M. Hesse, C. Kozhuharov, Ch. Miehe, G. Münzenberg, M. Pfützner, C. Röhl, K.-H. Schmidt, W. Schwab, C. Stéphan, K. Sümmerer, L. Tassan-Got, and B. Voss. Projectile fission at relativistic velocities: a novel and powerful source of neutron-rich isotopes well suited for in-flight isotopic separation. *Physics Letters B*, 331(1):19–24, 1994.

[37] C. Donzaud, S. Czajkowski, P. Armbruster, M. Bernas, C. Böckstiegel, P. Dessagne, H. Geissel, E. Hanelt, A. Heinz, C. Kozhuharov, C. Miehé, G. Münzenberg, M. Pfützner, W. Schwab, C. Stéphan, K. Sümmerer, L. Tassan-Got, and B. Voss. Low-energy fission investigated in reactions of 750 AMeV ^{238}U-ions on ^{208}Pb. II: Isotopic distributions. *The European Physical Journal A-Hadrons and Nuclei*, 1(4):407–426.

[38] K.-H. Schmidt, S. Steinhäuser, C. Böckstiegel, A. Grewe, A. Heinz, A.R. Junghans, J. Benlliure, H.-G. Clerc, M. de Jong, J. Müller, M. Pfützner, and B. Voss. Relativistic radioactive beams: A new access to nuclear-fission studies. *Nuclear Physics A*, 665(3–4):221 – 267, 2000.

[39] A. Winther and K. Alder. Relativistic coulomb excitation. *Nuclear Physics A*, 319(3):518 – 532, 1979.

[40] Carlos A. Bertulani and Gerhard Baur. Electromagnetic processes in relativistic heavy ion collisions. *Physics Reports*, 163(5):299 – 408, 1988.

[41] E. Fermi. On the theory of collisions between atoms and electrically charged particles. *Nuovo Cim.*, 2:143–158, 1925.

[42] Eric Pellereau. *Contribution à la mise en place, à la réalisation, et à l'analyse des données de rendements de fission issues de l'expérience SOFIA au GSI*. PhD thesis, Université Paris-Sud, CEA/DAM/DIF Bruyères-le-Châtel, December 2013.

[43] J. Benecke, T. Chou, C.-N. Yang, and E. Yen. Hypothesis of limiting fragmentation in high-energy collisions. *Physical Review*, 188(5):2159, 1969.

[44] P. Armbruster, J. Benlliure, M. Bernas, A. Boudard, E. Casarejos, S. Czajkowski, T. Enqvist, S. Leray, P. Napolitani, J. Pereira, F. Rejmund, M.-V. Ricciardi, K.-H. Schmidt, C. Stéphan, J. Taieb, L. Tassan-Got, and C. Volant. Measurement of a complete set of nuclides, cross sections, and kinetic energies in spallation of ^{238}U 1AGeV with protons. *Phys. Rev. Lett.*, 93:212701, Nov 2004.

[45] H. Geissel, P. Armbruster, K.H. Behr, A. Brünle, K. Burkard, M. Chen, H. Folger, B. Franczak, H. Keller, O. Klepper, B. Langenbeck, F. Nickel, E. Pfeng, M. Pfützner, E. Roeckl, K. Rykaczewski, I. Schall, D. Schardt, C. Scheidenberger, K.-H. Schmidt, A. Schröter, T. Schwab, K. Sümmerer, M. Weber, G. Münzenberg, T. Brohm, H.-G. Clerc, M. Fauerbach, J.-J. Gaimard, A. Grewe, E. Hanelt, B. Knödler, M. Steiner, B. Voss, J. Weckenmann, C. Ziegler, A. Magel, H. Wollnik, J.P. Dufour, Y. Fujita, D.J. Vieira, and B. Sherrill. The GSI projectile fragment separator (FRS): a versatile magnetic system for relativistic heavy ions. *Nuclear Instruments and Methods in Physics Research Section B: Beam Interactions with Materials and Atoms*, 70(1-4):286–297, 1992.

[46] H. Alvarez-Pol, J. Benlliure, E. Casarejos, L. Audouin, D. Cortina-Gil, T. Enqvist, B. Fernández-Domínguez, A. R. Junghans, B. Jurado, P. Napolitani, J. Pereira, F. Rejmund, K.-H. Schmidt, and O. Yordanov. Production of new neutron-rich isotopes of heavy elements in fragmentation reactions of ^{238}U projectiles at 1 A GeV. *Phys. Rev. C*, 82:041602, Oct 2010.

[47] E. Nappi. Charged particle identification via ionization energy loss and time-of-flight measurements. In *INSTRUMENTATION IN ELEMENTARY PARTICLE PHYSICS*, volume 674, pages 18–35, 2003.

[48] G. Charpak, R. Bouclier, T. Bressani, J. Favier, and Č. Zupančič. The use of multiwire proportional counters to select and localize charged particles. *Nuclear Instruments and Methods*, 62(3):262–268, 1968.

[49] Wikipedia. Wire chamber — wikipedia, the free encyclopedia, 2016.

[50] W.R. Leo. *Techniques for nuclear and particle physics experiments: a how-to approach*. Springer Science & Business Media, 2012.

[51] O.B. Tarasov and D. Bazin. Lise++: Radioactive beam production with in-flight separators. *Nuclear Instruments and Methods in Physics Research Section B: Beam Interactions with Materials and Atoms*, 266(19–20):4657 – 4664, 2008. Proceedings of the {XVth} International Conference on Electromagnetic Isotope Separators and Techniques Related to their Applications.

[52] C. Scheidenberger, Th. Stöhlker, W.E. Meyerhof, H. Geissel, P.H. Mokler, and B. Blank. Charge states of relativistic heavy ions in matter. *Nuclear Instruments and Methods in Physics Research Section B: Beam Interactions with Materials and Atoms*, 142(4):441 – 462, 1998.

[53] Hans D. Betz. Heavy ion charge states. *Applied Atomic Collision Physics*, 4, 2013.

[54] C. Scheidenberger, Th. Stöhlker, W.E. Meyerhof, H. Geissel, P.H. Mokler, and B. Blank. GLOBAL. `http://web-docs.gsi.de/~weick/charge_states/`.

[55] C. Scheidenberger, Th. Stöhlker, W.E. Meyerhof, H. Geissel, P.H. Mokler, and B. Blank. CHARGE. `http://web-docs.gsi.de/~weick/charge_states/`.

[56] K. H. Schmidt. AMADEUS (A MAgnet and DEgrader Utility for Scaling). `http://www-win.gsi.de/charms/amadeus.htm`.

[57] Kwong Lau and Jörg Pyrlik. Optimization of centroid-finding algorithms for cathode strip chambers. *Nuclear Instruments and Methods in Physics Research Section A: Accelerators, Spectrometers, Detectors and Associated Equipment*, 366(2):298–309, 1995.

[58] L. Audouin, L. Tassan-Got, P. Armbruster, K.-H. Schmidt, C. Stéphan, and J. Taieb. Recoil spectrometers for heavy-ion identification and secondary-beam production: Pushing the low-energy limit. *Nuclear Instruments and Methods in Physics Research Section A: Accelerators, Spectrometers, Detectors and Associated Equipment*, 548(3):517 – 539, 2005.

[59] M. Caamaño, F. Rejmund, and K.-H. Schmidt. Influence of asymmetry and fissility on even-odd effect in fission-fragment yields. *EPJ Web of Conferences*, 8:03001, 2010.

[60] H.H. Heckman, D.E. Greiner, P.J. Lindstrom, and F.S. Bieser. Fragmentation of ^{14}N Nuclei at 29 GeV: Inclusive Isotope Spectra at 0°. *Physical Review Letters*, 28(14):926, 1972.

[61] A. Kelić, K.-H. Schmidt, T. Enqvist, A. Boudard, P. Armbruster, J. Benlliure, M. Bernas, S. Czajkowski, R. Legraine, S. Leray, B. Mustapha, M. Pravikoff, F. Rejmund, C. Stéphan, J. Taieb, L. Tassan-Got, C. Volant, and W. Wlazło. Isotopic and velocity distributions of $_{83}$Bi produced in charge-pickup reactions of $^{208}_{82}$Pb at 1 A GeV. *Physical Review C*, 70(6):064608, 2004.

[62] Karl-Heinz Schmidt. CONFID - COde for simulating experiments on Nuclear FIssion using a large Dipole. http://www.khs-erzhausen.de/.

[63] K.F. Flynn, E.P. Horwitz, C.A.A. Bloomquist, R.F. Barnes, R.K. Sjoblom, P.R. Fields, and L.E. Glendenin. Distribution of Mass in the Spontaneous Fission of ^{256}Fm. *Physical Review C*, 5(5):1725, 1972.

[64] M.B. Chadwick, M. Herman, P. Obložinskỳ, M.E. Dunn, Y. Danon, A.C. Kahler, D.L. Smith, B. Pritychenko, G. Arbanas, R. Arcilla, R. Brewer, D.A. Brown, R. Capote, A.D. Carlson, Y.S. Cho, H. Derrien, K. Guber, G.M. Hale, S. Hoblit, S. Holloway, T.D. Johnson, T. Kawano, B.C. Kiedrowski, H. Kim, S. Kunieda, N.M. Larson, L. Leal, J.P. Lestone, R.C. Little, E.A. McCutchan, R.E. MacFarlane, M. MacInnes, C.M. Mattoon, R.D. McKnight, S.F. Mughabghab, G.P.A. Nobre, G. Palmiotti, A. Palumbo, M.T. Pigni, V.G. Pronyaev, R.O. Sayer, A.A. Sonzogni, N.C. Summers, P. Talou, I.J. Thompson, A. Trkov, R.L. Vogt, S.C. van der Marck, A. Wallner, M.C. White, D. Wiarda, and P.G. Young. ENDF/B-VII. 1 nuclear data for science and technology: cross sections, covariances, fission product yields and decay data. *Nuclear Data Sheets*, 112(12):2887–2996, 2011.

[65] http://www.oecd-nea.org/janisweb/search/endf.

[66] L.E. Glendenin, J.E. Gindler, D.J. Henderson, and J.W. Meadows. Mass distributions for monoenergetic-neutron-induced fission of ^{235}U. *Physical Review C*, 24(6):2600, 1981.

Appendix A

Scheme of the experimental setup

In figure A.1, the experimental setup in the Cave C is schematically presented, and measured positions for all detectors are also given.

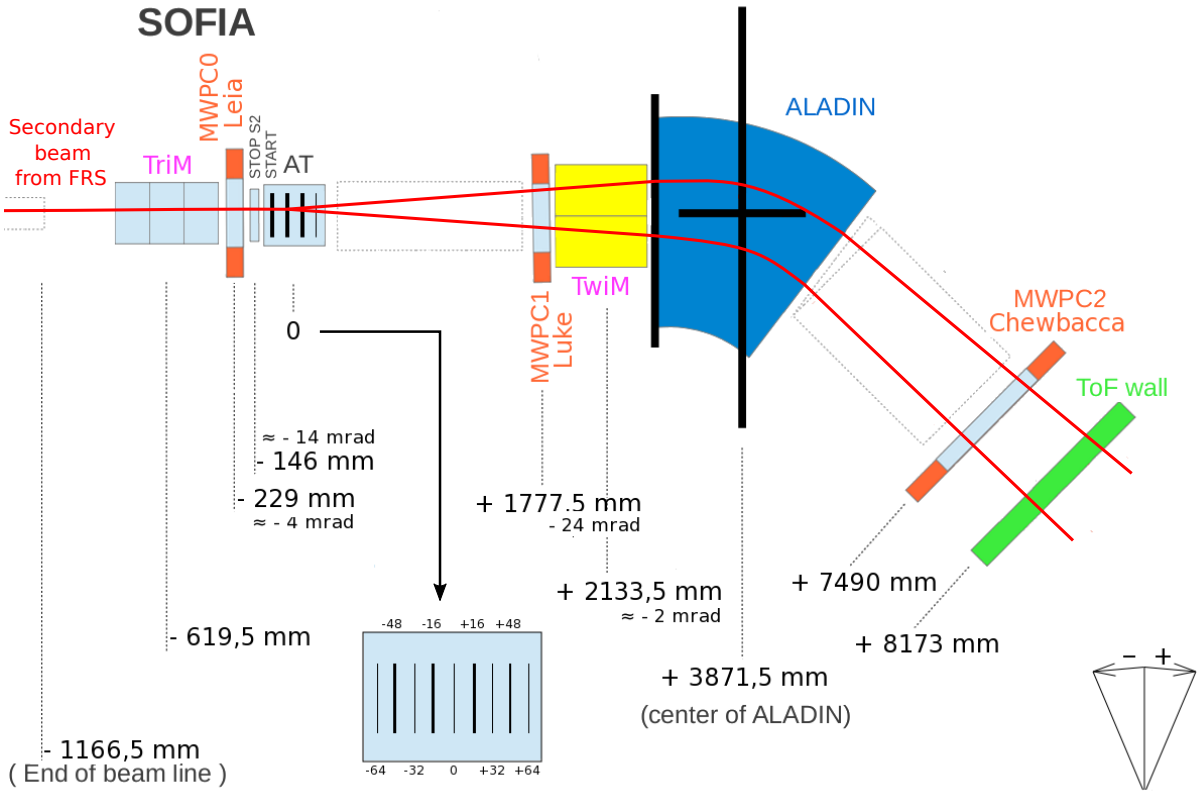

FIGURE A.1: *Scheme of the experimental setup in the cave C, together with measured positions for all the detectors, Court. Thomas Gorbinet.*

Résumé

La fission du noyau atomique est une des réactions nucléaires les plus complexes, durant laquelle le noyau subit une deformation à large échelle, suivie d'une réorganisation complète des nucléons. Afin de caractériser la dynamique de la fission, plusieurs observables ont été proposés. Le programme SOFIA (Studies On FIssion with Aladin) permet d'accéder à certains d'entre eux:

- les taux de production des fragments de fission,
- l'énergie cinétique des fragments émis,
- et la multiplicité des neutrons prompts.

La mesure des taux de production des fragments est motivée par 2 raisons principales:

- d'une part, les taux de production des fragments intéressent à la fois les applications aux réacteurs nucléaires et la théorie des réactions et de la structure du noyau.
  En effet, les fragments de fission sont la source essentielle de la chaleur résiduelle du réacteur, et la source des neutrons retardés. Certains d'entre eux sont responsables de l'empoisonnement du cœur. Il est donc important de connaitre avec précision ces taux de production. De plus, ces taux renseignent sur la structure en couche et sur les modes de fission, et constituent un excellent test des modèles théoriques décrivant la fission.
- d'autre part, les taux de production des fragments prédits par les différents modèles manquent de précision, et les données présentes dans les librairies sont fréquemment en désaccord entre elles. Des données nouvelles et de haute qualité sont donc souhaitables.

Habituellement, les taux de production des fragments sont mesurés au cours d'expériences où la fission est déclenché par l'irradiation d'une cible de matière fissile par des neutrons, des photons ou des particules chargées. Le développement des accélérateurs d'ions lourds a permis de proposer une autre technique : le noyau d'intérêt constitue le faisceau, et la fission est induite en vol par une interaction avec une cible fixe. On parle respectivement de cinématique directe ou de cinématique inverse.

L'utilisation de la cinématique inverse permet de surmonter plusieurs difficultés rencontrées en cinématique directe:

- La fission de noyaux à vie très courte peut être mesurée, puisque la contrainte de disposer des échantillons pour créer une cible n'existe plus. On réduit aussi les contraintes de radioprotection inhérentes à la manipulation de noyaux radioactifs. Enfin la question de la fragilité de la cible et de sa résistance à l'irradiation est également réglée.
- Une même expérience en cinématique directe porte sur un nombre réduit de systèmes fissionants, puisqu'il faut disposer d'une cible pour chacun. En cinématique inverse il est possible de transmettre un faisceau "cocktail" associant jusqu'à une dizaine de noyaux, et donc de couvrir un grand nombre de systèmes en une seule expérience.

- En cinématique directe, les fragments de fission sont émis dos-à-dos, et de manière relativement isotrope, ce qui rend leur détection simultanée délicate. Par contraste, en cinématique inverse, les 2 fragments sont émis dans un cône vers l'avant, ce qui permet d'atteindre une haute efficacité de détection simultanée.
- En cinématique directe, la mesure de la charge nucléaire est limitée au fragment léger et ne se fait qu'avec une résolution réduite. Cela est dû à la très faible énergie cinétique des fragments, qui se traduit par une forte variation d'état de charge. En cinématique inverse, l'énergie cinétique des fragments est bien plus élevée, ce qui permet d'atteindre une bonne voire une excellente résolution en charge pour les 2 fragments.

Il y a principalement 3 grandes installations dans le monde où des faisceaux d'ions lourds de haute énergie sont disponibles, et qui permettent donc d'étudier la fission en cinématique inverse: GANIL en France, RIKEN au Japon et GSI en Allemagne. Ces installations offrent des gammes d'énergie sensiblement différentes: autour de 10 AMeV, 100 AMeV et jusqu'à 1000 AMeV respectivement. Les expériences SOFIA se déroulent à GSI, afin de bénéficier de la plus grande énergie cinétique et de maximiser le gain de la méthode pour la résolution en charge.

En effet, dans les expériences SOFIA, la charge nucléaire des fragments est obtenue à partir de la mesure de leur perte d'énergie dans une chambre d'ionisation. Si les ions n'ont qu'une énergie cinétique limitée, ils vont subir un grand nombre de changements d'état de charge en traversant le gaz. Ces fluctuations rendent très difficiles une mesure précise des charges nucléaires. Dans le cas des fragments de fission, ces fluctuations deviennent négligeables pour des énergies de quelques centaines de MeV par nucléon.

Avec l'augmentation de l'énergie d'excitation, les effets de couche, l'effet pair-impair ou encore la fission asymétrique tendent à disparaitre. Si on souhaite étudier le rôle des effets de couche dans la fission, il est donc primordial de déclencher les fissions à basse énergie. Or il existe 2 mécanismes principaux pour déclencher la fission: une collision nucléaire directe et l'interaction coulombienne. Dans le cas d'un faisceau de plusieurs centaines de AMeV, une collision va le plus souvent créer un système à haute énergie d'excitation - plusieurs dizaines voire plusieurs centaines de MeV. On va donc lui préférer l'interaction coulombienne pour déclencher la fission. Le recours à ce mécanisme ne nous permet pas de déterminer l'énergie d'excitation événement par évènement: seule une distribution globale des énergies d'excitation peut être calculée. Il est intéressant de remarquer que, sauf à utiliser des voies de réaction très particulières comme le transfert ou le (p,2p), le problème de la non-détermination de l'énergie d'excitation se pose également pour la fission induite par collision, et que cette dernière conduit à un spectre d'énergie d'excitation nettement plus étendu que par excitation coulombienne, rendant les résultats d'autant plus difficiles à interpréter. Le mécanisme coulombien est donc bien adapté à l'étude de la fission, d'autant que sa très large section efficace (plusieurs barns) permet de travailler confortablement avec des faisceaux de basse intensité.

Le travail présenté dans cette thèse porte sur l'expérience conduite en octobre 2014, dédiée à l'étude de la fission coulombienne de ^{236}U. Cette réaction présente un intérêt tout particulier

car elle constitue un analogue de la fission induite par neutron de ^{235}U, c'est-à-dire d'une des réactions essentielles ayant lieu dans les réacteurs nucléaires. Dans notre cas, les simulations indiquent que l'excitation coulombienne conduit à une énergie d'excitation moyenne de l'ordre de 12 MeV, ce qui est équivalent à l'énergie du noyau composé après la capture d'un neutron de 6 MeV environ.

Il n'existe pas de faisceau de ^{236}U à GSI: il doit donc être créé par fragmentation du seul faisceau voisin disponible, ^{238}U. Les ions de ^{238}U passent tout d'abord dans l'accélérateur linéaire UNILAC, puis dans le synchrotron SIS-18 où ils sont portés à une énergie de 1 AGeV. Ce faisceau primaire est envoyé sur une cible de Beryllium. Les réactions de fragmentation qui s'y déroulent produisent une très grande variété de noyaux, qui vont être analysés et sélectionnés dans le FRS, un spectromètre de recul à haute résolution.

Le noyau d'intérêt (dans notre cas, ^{236}U) est sélectionné en deux étapes, selon la méthode dite Bρ - ΔE - Bρ. Une première sélection sur la rigidité magnétique Bρ peut être, au premier ordre, assimilée à une sélection sur le rapport masse sur charge. Le passage dans un couche de matière épaisse a pour conséquence une perte d'énergie significative, qui dépend principalement de la charge nucléaire et qui modifie donc fortement la rigidité magnétique. La seconde sélection en rigidité magnétique s'apparente alors, en première approximation, à une sélection en Z. Au final, un nombre réduit de noyaux sont transmis jusqu'en cave C, où se trouve le dispositif SOFIA, formant un faisceau dit "cocktail": il est donc nécessaire d'identifier, événement par événement, le noyau qui va fissioner.

La technique d'identification, dite ΔE - Bρ - ToF, est appliquée successivement au faisceau secondaire et aux fragments produits lors de sa fission. Elle permet l'identification en charge et en masse du noyau. Il s'agit de mesurer à la fois la perte d'énergie dans une chambre d'ionisation, de reconstruire la trajectoire dans un champ magnétique, et de mesurer le temps de vol sur une distance connue. Dans le cas du faisceau secondaire, le champ magnétique est partie intégrante du FRS; pour ce qui est des fragments, SOFIA utilise l'aimant ALADIN (A Large Acceptance DIpole magNet), installé en cave C. Les pertes d'énergie sont mesurées par des MUSIC (MUlti-Sampling Ionization Chamber). L'information sur les trajectoires sont obtenues par des chambres multifils (MWPC, Multi-Wire Proportional Chamber) et également par les chambres d'ionisation, capables de mesurer la position horizontale et l'angle horizontal des noyaux. Les temps de vols sont obtenus grâce à une mesure de temps dans des scintillateurs plastiques.

Il faut remarquer que les ions du faisceau secondaire ont une énergie d'environ 700 AMeV lorsqu'ils fissionent, produisant des fragments de fission d'une énergie cinétique voisine. A ces énergies, la grande majorité des noyaux sont totalement épluchés, ce qui équivaut à une charge atomique (q) égale à la charge nucléaire (Z). Cette dernière peut alors être directement déduite de la perte d'énergie dans une chambre d'ionisation, qui est proportionnelle à q^2. Pour les ions les plus lourds cependant, et particulièrement pour les ions constituant le faisceau secondaire, l'égalité $q = Z$ n'est pas forcément vérifiée et il faut combiner plusieurs mesures indépendantes de la perte d'énergie pour augmenter les chances d'obtenir une mesure réalisée lorsque l'ion

est totalement épluché.

Dans ce document, tous les détecteurs utilisés dans l'expérience sont décrits en détail. L'analyse menant à l'identification isotopique des ions du faisceau secondaire, et à l'identification en charge des fragments, est décrite pas-à-pas.

Comme expliqué plus haut, les expériences SOFIA s'intéressent à la fission induite par excitation coulombienne plutôt qu'aux fissions consécutives à une collision nucléaire. L'interaction coulombienne survient lorsque le projectile passe à proximité d'un noyau cible de charge élevée (dans le cas de SOFIA, de l'uranium), et est modélisée comme un échange de photons virtuels qui conduisent à l'excitation des résonances multipolaires géantes. Le projectile peut alors se désexciter par fission. L'énergie d'excitation est modérée et ne permet pas d'évaporation de proton, ce qui conduit à la formation de deux fragments dont la somme des charges est rigoureusement identique à celle du noyau projectile.

Les fissions induites par collision surviennent également, et leur contribution à la production des fragments doit être supprimée afin d'obtenir des taux de production des fragments par la seule interaction coulombienne. Lors d'une collision, un certain nombre de nucléons sont abrasés du projectile, ce qui implique une forte énergie d'excitation (jusqu'à plusieurs centaines de MeV). Même si des protons n'ont pas été retirés lors de l'abrasion, l'énergie est souvent assez élevée pour entrainer l'évaporation d'un ou plusieurs protons. En conséquence, la charge du système fissionant à la suite d'une collision sera le plus souvent inférieure au Z du projectile. Comparer la somme des charges des fragments à celle du projectile permet de rejeter la très grande majorité des fissions dues à une collision, événement par événement.

Toutefois, une fraction des fissions induites par collision subsiste: celle pour lesquelles seuls des neutrons ont été perdus lors de l'abrasion et/ou de l'évaporation. Celles-ci ne peuvent être rejetées événement par événement, mais leur contribution aux taux de production peut être évaluée. Pour cela, une cible de matériel de faible Z, en l'occurrence de l'aluminium, est utilisée en complément de l'uranium. Comme la section efficace d'interaction coulombienne varie très rapidement avec la charge de la cible, elle devient négligeable dans la cible d'aluminium. Ainsi, 2 jeux de données peuvent être produits: un mêlant fissions nucléaire et coulombienne (cibles d'uranium) et un de fission nucléaire seulement (cible d'aluminium). Il est ainsi possible, via une renormalisation appropriée, de soustraire la contribution nucléaire des résultats obtenus sur les cibles d'uranium.

Dernière étape de l'analyse, l'efficacité de détection du dispositif est évaluée à partir de simulation, pour aboutir à une valeur des taux de production de la fission coulombienne de ^{236}U avec une haute précision.

Pour évaluer et interpréter les taux de production élémentaires obtenus, des comparaisons avec d'autres données produites par SOFIA et les données évaluées disponibles dans les librairies ont été réalisées. Les valeurs obtenues pour la fission coulombienne de ^{236}U sont pleinement cohérentes avec celles mesurées par le même dispositif pour d'autres isotopes de

l'uranium. De manière générale la librairie ENDF/B-VII.1 est en bon accord avec nos données, alors que la librairie JEFF3.1 a besoin d'être améliorée pour cet observable.

Nous avons comparé les valeurs moyennes de N et de Z des fragments formés lors de la fission de divers isotopes de l'uranium. Nous constatons qu'en passant de ^{234}U à ^{238}U, l'augmentation du N moyen est plus faible pour les fragments lourds que pour les fragments légers. Nous relions ce constat à la stabilisation du fragment lourd par un effet de couche neutron, sans lequel l'accroissement de N serait simplement proportionnel à celui du N du noyau d'origine. Dans la même série isotopique, on observe une diminution du nombre moyen de protons des noyaux lourds, interprétée comme une adaptation de la distribution des protons entre les deux fragments sous l'effet des variations de N. Toutefois, cette décroissance est seulement la moitié de que ce phénomène entrainerait, ce qui pourrait laisser penser qu'une couche protons pourrait également avoir un rôle dans la stabilisation des fragments lourds.

De plus, on constate que le taux de fission symétrique est supérieur d'un facteur deux aux prédictions issues de modèles dans lesquels on utilise un spectre d'excitation coulombienne simulé, tout en étant en bon accord avec les données SOFIA précédentes. Les réactions d'échange de charge (formation d'un noyau Z=93 et évaporation d'un proton, suivi d'une fission), qui ne sont pas prises en compte dans l'analyse, pourraient être une raison de ce désaccord. Cette contribution devrait cependant rester mineure et il est difficile de croire qu'elle puisse être seule responsable. C'est donc probablement du côté des calculs d'excitation coulombienne que se trouvent le problème.

Ce travail de thèse s'est terminé par l'obtention des taux de production élémentaires de la fission coulombienne de ^{236}U. Toutefois, l'analyse des données acquises en octobre 2014 devrait être poursuivie pour obtenir l'identification en masse des fragments et donc déduire les taux de production isotopiques. Il est également possible de déterminer l'énergie cinétique totale libérée par la fission et le nombre de neutrons prompts, tout cela événement par événement. Ces jeux de données permettraient des comparaisons nettement plus approfondies avec les modèles.

Le programme SOFIA va se poursuivre avec l'étude de noyaux plus exotiques, qui permettront d'interpréter la compétition entre fission symétrique et fission asymétrique et l'influence des effets de structure. A plus long terme, on peut identifier deux objectifs. Le premier est de réaliser l'étude de la fission en utilisant un faisceau primaire de ^{242}Pu. Cela permettrait de mesurer la fission de systèmes tels que ^{239}U* ou ^{240}Pu*, analogues de réactions essentielles pour les réacteurs nucléaires, et qui pourraient de plus être comparés directement aux résultats obtenus à GANIL sur la fission induite par transfert. Le second objectif est d'utiliser des électrons pour déclencher la fission, ce qui permettrait une mesure de l'énergie d'excitation événement par événement.

université PARIS-SACLAY | ÉCOLE DOCTORALE PHENIICS

Titre : Étude de la fission d'actinides exotiques par réaction relativiste (en français)
Mots clés : fission, cinématique inverse, taux de production des fragments de fission

Résumé : SOFIA (Studies On FIssion with Aladin) est un programme expérimental innovant qui a pour objectif la mesure de plusieurs observables de la fission nucléaire : les taux de production isotopiques des fragments de fission, l'énergie cinétique totale des fragments, et la multiplicité des neutrons prompts. Ces informations sont obtenues pour une large variété d'actinides et de pré-actinides. Le recours à la cinématique inverse (le système fissionnant est le faisceau et non pas la cible) est le seul moyen d'identifier les fragments à la fois en charge et en masse. Le travail de doctorat présenté dans cette thèse porte sur l'expérience menée en Octobre 2014 et dédiée à la mesure de la fission de ^{236}U induite par excitation coulombienne, soit l'analogue de la fission de ^{235}U induite par neutron.
Les expériences SOFIA ont lieu à GSI (Darmstadt, Allemagne), la seule installation au monde capable de délivrer un faisceau d'uranium 238 de 1 GeV par nucléon. Ce faisceau primaire subit une première fragmentation, dont les produits sont sélectionnés par le FRS (FRagment Separator) afin de former un faisceau secondaire du noyau d'intérêt, en l'occurrence ^{236}U, qui est guidé vers l'expérience SOFIA où sa fission est déclenchée.
Certains noyaux proches de ^{236}U sont également transmis par le FRS : il est donc nécessaire de procéder à l'identification en masse et en charge du système fissionnant, puis d'identifier les deux fragments de fission. Dans les deux cas, l'identification, réalisée événement par événement, repose sur la mesure simultanée de la perte d'énergie dans un gaz, de la rigidité magnétique et du temps de vol. Seules les fissions induites par excitation coulombiennes sont pertinentes : la contribution des réactions nucléaires à la production des fragments doit donc être mesurée et soustraite.
L'analyse présentée dans ce document inclut l'identification du faisceau secondaire en masse et en charge, l'identification en charge des fragments de fission, l'estimation de la contribution des réactions nucléaires, et finalement les taux de production des éléments obtenus dans la fission de ^{236}U. Ces résultats sont comparés à ceux d'autres mesures réalisées sur SOFIA, et à des résultats antérieurs obtenus par d'autres techniques.

Title : Study of fission of exotic actinides by relativistic reactions (in English)
Keywords : fission, inverse kinematics, fission fragment yield

Abstract : SOFIA (Studies On FIssion with Aladin) is an innovative experimental program which aims to measure several fission observables — the isotopic fission yields, the total kinetic energy of the fragments and the prompt neutron multiplicity, for a wide range of actinides and pre-actinides. The use of inverse kinematics (the fissioning system is the beam instead of the target) is the only way to fully identify fragments in charge and mass. The PhD work presented in this thesis concerns the experiment conducted in October 2014, and is focused on the Coulomb-induced fission of ^{236}U, which can be regarded as the analog of the neutron-induced fission of ^{235}U.
The SOFIA experiments take place in GSI (Darmstadt, Germany) because it is the sole facility in the world which delivers a beam of ^{238}U at 1 AGeV. This beam is fragmented and the products are selected by the FRS (FRagment separator) in order to deliver a secondary beam of nuclei of interest - ^{236}U in our case, which is then guided to the SOFIA setup where its fission is triggered.
Since some nuclides with close atomic and mass numbers to ^{236}U are also transmitted by the FRS, it is necessary to identify the fissioning system from the secondary beam first, and then identify both the associated fission fragments. All identifications are performed event by event on the basis of measurements of the energy loss, the magnetic rigidity and the time of flight. Since we are only interested in the Coulomb-induced fission of ^{236}U, the contribution of fragmentation fissions on the nuclear charge distribution of fission fragments has to be suppressed.
The analysis in this paper involves the isotopic identification of the fissioning system, the nuclear charge identification of the fission fragments, the estimation of the nuclear contribution, and the extraction of the elemental fission yield. The results are then compared to other measurements performed with the SOFIA setup, as well as previous results obtained by other techniques.

Université Paris-Saclay
Espace Technologique / Immeuble Discovery
Route de l'Orme aux Merisiers RD 128 / 91190 Saint-Aubin, France